



**University of
Nottingham**

UK | CHINA | MALAYSIA

**Electrostatic Theory of Charged
Particle Polarisation:
Applications in Self-Assembly,
Pharmaceutical and
Atmospheric Processes**

Joshua Baptiste

Student Number: 4284541

Thesis submitted to the University of Nottingham
for the degree of Doctor of Philosophy

**Supervised by Prof. Elena Besley (95%) &
Prof. Anthony J. Stace (5%)**

School of Chemistry
University of Nottingham

30th May 2021

To Mum and Dad, couldn't have done it without you.

Acknowledgements

My PhD journey has been a long one, which means I've got a long list of people I need to thank for their help and support throughout my time. First and foremost, I would like to thank my supervisors, Prof. Elena Besley and Prof. Tony Stace, for their massive support during the whole of my time here, ever since I was a young and lost Masters project student, you have helped me to grow as a scientist and I couldn't have asked for better supervisors to learn from. I would also like to extend that to other members of the electrostatics team that has been here over the years for their helpful discussions, including: Dr Ivan Derbenev, Dr Eric Lindgren, Izzy Cooley, Abi Miller, Becky Heaton, Connor Williamson and Maggie Stankiewicz. The rest of Compchem (and those adopted) have also provided the best kind of working environment. I'd like to thank the School of Chemistry and the University of Nottingham for giving me the tools I needed to complete my research. Thank you to Dave, Cheng and Mel at GSK who were great to collaborate with and even better hosts during my visit. Many thanks to Ben, Steffi and Hassan in Aachen too who have all taught me so much about the background and theory of the model that I've been using for so long. I'd also like to thank Prof. Ingrid Mann in Norway for such great discussions on such an interesting project. Particular mention goes to the undergraduate lab technicians: Zena and Tina—who made my life 100% easier while demonstrating; also, the dream team of second year demonstrating—Grace and David—need to be mentioned for making the hours of dealing with the undergrads' inability to turn a plug on go by stress-free. I'd like to thank the whole PGSA football community—especially Monkman, Nick and Fil—for 5 years of an amazingly inclusive footballing experience, with a couple of international trips away mixed in. Thank you to Grandma! Thanks for making my Sunday shifts at Tesco bearable with the best chilli and spag bol, and a special mention to the weekly freshly baked apple crumble!

Finally, I am deeply grateful to my parents for encouraging me at every step to keep learning and doing my best at whatever I do, you've made me in to the person I am today and I couldn't have done it without your love and support.

Abstract

New developments in theoretical approaches to calculating electrostatic interactions between charged polarisable particles are presented and applied to a wide range of charged systems to test the versatility of the solution. Here, the theory behind the expansion of the many-body polarisable electrostatic solution (Lindgren et al., 2018) has been expanded to include non-homogeneous surface charge densities in the form of point charges, and also the introduction of external electric fields. A wide range of trends are explored, along with testing of the implementation of this new development. The model is then applied to applications that test the model against a wide range of experimental data, including: the atmospheric physics involved with cloud formation in the upper atmosphere; the aggregation of bipolar pharmaceutical aerosols found in dry powder inhalers; the self-assembly behaviour of bipatchy microcolloids; and the study of the role of counterions in the spontaneous formation of dimers between hydrophilic macroanions in solution. The model displays its robustness not only by providing solutions to problems on multiple length-scales (nano- and meso-scale in this work), but it also handles a range of mediums with both systems in solution and in vacuum/air are studied. The work is finally concluded, with a host of scenarios provided as possible future work.

List of Publications

1. C. Harris, J. Baptiste, E. B. Lindgren, E. Besley and A. J. Stace, Coulomb fission in multiply charged molecular clusters: Experiment and theory, *J. Chem. Phys.*, **2017**, 146, 164302.
2. F. Naderi Mehr, D. Grigoriev, R. Heaton, J. Baptiste, A. J. Stace, N. Pureskiy, E. Besley and A. Böker, Self-Assembly Behavior of Oppositely Charged Inverse Bipatchy Microcolloids, *Small*, **2020**, 16, 2000442.
3. J. Baptiste, C. Williamson, J. Fox, A. J. Stace, M. Hassan, S. Braun, B. Stamm, I. Mann and E. Besley, Charged particle dynamics in dry powder inhalers: Evidence of particle scavenging, *Atmos. Chem. Phys.*, **2021**, 21(11), 8735–8745.
4. J. Baptiste, C. Pang, D. Prime, E. Besley, M. Hamilton, and A. J. Stace, Charged particle dynamics in dry powder inhalers: Evidence of particle scavenging, *in preparation*.
5. J. Baptiste, I. Derbenev, A. J. Stace, E. Besley, The role of counterions in the initial stage of macroanion self-assembly: An example of the $\{\text{Mo}_{72}\text{Fe}_{30}\}$ polyoxometalate, *in preparation*.
6. M. Hassan, C. Williamson, J. Baptiste, S. Braun, A. J. Stace, B. Stamm, and E. Besley, Manipulating particle interactions with electric field and charges: General electrostatic many-body framework, *in preparation*.

Contents

Acknowledgements	i
Abstract	ii
List of Publications	iii
1 Introduction	1
1.1 Basics of Electrostatic Theory	4
1.2 Polarisation of Dielectric Materials	8
1.2.1 Method of Image Charges	10
1.2.2 Electrostatic analysis of the interactions between charged particles of two dielectric materials	13
1.3 Aims and Objectives	18
2 The many-body electrostatic problem of charged polarisable particles: An extension to point-charge distributions and ex- ternal electric fields	20
2.1 Surface point charge and external electric field solutions	21
2.1.1 Formulation of the Problem	21
2.1.2 Formulation of the problem based on a partial differential equation (PDE)	23
2.1.3 Formulation of the problem based on an integral equation	26
2.1.4 Existing methodology in the absence of surface point- charges and external fields	28
2.1.5 Effects of an external electric field and surface point- charges	33
2.1.6 Energy and forces in the presence of external fields and point charges.	34

2.2	Molecular dynamics	39
3	General numerical results	40
3.1	Interactions between pairs of like-charged particles	40
3.2	Non-Uniform Charge Distributions	50
3.2.1	Gaussian Distribution	51
3.2.2	Point-Charge Distribution	56
3.3	Neutral particles in external electric fields	58
4	The influence of surface charge on dust agglomeration growth in the mesosphere	70
4.1	Introduction	70
4.2	Ionospheric dusty plasma conditions	74
4.3	Framing the problem	76
4.4	Aggregation of oxide and ice particles	83
4.5	Aggregation of oxide particles	85
4.6	Brief discussion of main results and conclusions	90
5	Charged particle dynamics in dry powder inhalers: Evidence of particle scavenging	91
5.1	Introduction	91
5.2	Framing the computational problem	95
5.2.1	Two-body collisions	95
5.3	Electrostatic cohesion of colliding powder particles	99
5.4	Dynamics simulations of charge scavenging mechanisms	105
5.5	Concluding remarks	113
6	Self-assembly behavior of oppositely charged inverse bi-patchy micro-colloids	114
6.1	Introduction	114
6.2	Bi-patchy particles with two oppositely-charged patches	115
6.2.1	Electrostatic interactions between patchy particles	118
6.3	Conclusion and Outlook	124
7	The role of counterions in the initial stage of macroanion self-assembly: An example of the $\{\text{Mo}_{72}\text{Fe}_{30}\}$ polyoxometalate	128

7.1	Introduction	128
7.1.1	Framing the problem	131
7.2	Methodology	133
7.3	Results and Discussion	136
7.3.1	Determination of parameters	136
7.3.2	Dimer interactions	137
7.4	Concluding remarks	144
8	Conclusions and Future Work	146
8.1	Conclusions	146
8.2	Future Work	149
	Bibliography	154
	Appendices	165
A	Theory	165
A.1	Mathematical considerations	165
A.2	Mathematical Proofs	168

List of Tables

1.1	Further developments of the electrostatic model of two particle interactions in vacuum [19].	16
1.2	Applications of the electrostatic solution.	17
3.1	A comparison between point charge and Gaussian solution for benzene results.	57
3.2	Energies of six orientations in Figure 3.22.	67
4.1	Common particulates found in the MLT region which are considered in this study.	74
4.2	Energetic considerations and the percentage of aggregation for SiO ₂ - ice collisions at T = 150 K and C _R = 0.9 (the surface point charge model). SiO ₂ particle has the fixed radius and charge ($a_2 = 0.2$ nm, $q_2 = -1e$), and the size and charge of ice particle is varied. The collision geometry is shown in Figure 4.3a.	84
4.3	Energetic considerations and the percentage of aggregation for FeO - ice collisions at T = 150 K and C _R = 0.9 (the surface point charge model). FeO particle has the fixed radius and charge ($a_2 = 0.2$ nm, $q_2 = -1e$), and the size and charge of ice particle is varied. The collision geometry is shown in Figure 4.3a	84

4.4 Energetic considerations and the percentage of aggregation for MgO - ice collisions at $T = 150$ K and $C_R = 0.9$ (the surface point charge model). MgO particle has the fixed radius and charge ($a_2 = 0.2$ nm, $q_2 = -1e$), and the size and charge of ice particle is varied. The collision geometry is shown in Figure 4.3a 85

4.5 Energetic considerations and the percentage of aggregation for SiO₂ - SiO₂ and FeO - FeO collisions at $T = 150$ K and $C_R = 0.9$ (the surface point charge model). Particle 2 has the fixed radius and charge ($a_2 = 0.2$ nm, $q_2 = -1e$), and the size and charge of particle 1 is varied. The collision geometry is shown in Figure 4.3b. 87

4.6 Energetic considerations and the percentage of aggregation for SiO₂ - SiO₂ and FeO - FeO collisions at $T = 150$ K and $C_R = 0.9$ (the surface point charge model). Particle 2 has the fixed charge ($q_2 = -1e$) and particle 1 is neutral ($q_1 = 0$), and the size of both particles is varied. The collision geometry is shown in Figure 4.3c. 88

5.1 The effect of particle diameter d on the deposition quality of particles within the lungs. [64] 92

5.2 A table showing the size fractions corresponding to each of the compartments within the BOLAR equipment, and also the diameters equal to the midpoint of the size fraction. [68] 94

5.3 A table showing the average charge per particle q_j for the outer detector (OD) and inner detector (ID) for each compartment in the BOLAR[™]. 100

5.4 Mass data obtained from the outer detector (OD) and inner detector (ID) for each compartment in the BOLAR[™]. Averages for the smallest size bin exclude the 0 μ g results. 101

5.5	A table showing $E_{\text{electrostatic}}$ at the point of contact in eV for all possible combinations of oppositely charged particles.	102
5.6	Total number of positive n_+ and negative n_- particles within the pharmaceutical aerosol cloud with radius a	109
5.7	Scavenging particle parameters	110
6.1	The parameters used in the computations of electrostatic interaction energies: k is the dielectric constant, a is the radius, and q is the charge; k_m is 30.05 (90:10 mixture of ethanol and water). A particle graphic representation is also included for clarity. . .	119

List of Figures

1.1	An exaggerated visualisation of a particle composed of a polar molecule in the absence of an electric field (left) and exposed to an electric field (right).	9
1.2	A visualisation of a system involving (a) a point charge with a conducting infinite plate, and (b) the equivalent image charge problem.	11
2.1	Geometric representation of the system comprised of M non-overlapping spherical particles $\Omega_1, \dots, \Omega_M$ with radius a_i , dielectric constant k_i , and centred at x_i , surrounded by a homogeneous medium of dielectric constant k_0	22
3.1	F as a function of s for the interaction between two dielectric particles with $a_1 = 1$ nm, $q_{1,2} = 1e$, $k_i = 20$ and $k_0 = 1$. $a_2 = 1$ nm (solid), 2 nm (dashed) and 5 nm (dotted).	42
3.2	U as a function of s for the interaction between two dielectric particles with $a_1 = 1$ nm, $q_{1,2} = 1e$, $k_i = 20$ and $k_0 = 1$. $a_2 = 1$ nm (solid), 2 nm (dashed) and 5 nm (dotted).	43
3.3	U as a function of s for the interaction between two dielectric particles with $a_{1,2} = 1$ nm, $q_1 = 1e$, $k_i = 20$ and $k_0 = 1$. $q_2 = 1e$ (solid), $2e$ (dashed) and $5e$ (dotted).	44

- 3.4 A contour plot showing the electrostatic force (in pN) between a pair of like-charged spheres, with dielectric constants $k_1 = k_2 = 10$. The force is plotted as a function of size ratio a_2/a_1 and the charge ratio q_2/q_1 , with $s = 0.1$ nm, $a_1 = 1$ nm and $q_1 = 1e$. The regions of attraction are displayed as in red whereas the regions with repulsive forces are represented in blue. 45
- 3.5 A geometric representation of various two sphere systems between s^* values of 0 and 1. separated by 1 nm. The radii of the spheres in the examples are: (i) $a_1 = a_2 = 5$ cm, (ii) $a_1 = 0.5$ nm and $a_2 = 0.75$ nm, and (iii) $a_1 = a_2 = 5$ pm. The range of values of s^* from 0 to 1 corresponds to a continuum of the values for all possible combinations of sphere size and separation distances. 46
- 3.6 A contour plot showing the electrostatic force (in pN) between a pair of equal-sized, like-charged spheres, with dielectric constants $k_1 = k_2 = 20$. The force is plotted as a function of the scaled surface-to-surface separation s^* and the charge ratio q_2/q_1 , with $a_1 = a_2 = 1$ nm and $q_1 = 1e$. The regions of attraction are displayed in red whereas the regions with repulsive forces are represented in blue. 47
- 3.7 The interaction in a vacuum ($k_0 = 1$) between two particles with varying dielectric constants. Shown are **(a)** U and **(b)** F between a pair of charged dielectric particles: $q_1 = 1e$, $q_2 = 2e$, $a_1 = 0.63$ nm, $a_2 = 0.84$ nm, with dielectric constants $k_i = 1.1, 2, 4, 6, 8, 10, 20$ represented by black, red, orange, yellow, green, blue and purple respectively. 48

- 3.8 Charge density σ as a function of sweeping angle for two equally charged spheres at a separation of 0.1 nm. The solid lines indicate the values of σ for particle 1, with the dashed line indicating the values for particle 2. $k_i = 1$ (black), 2 (orange), 4 (yellow), 8 (green), $a_1 = 0.63$ nm, $a_2 = 0.84$ nm, $q_1 = q_2 = 1.0$ e. On each particle $\beta = 0$ is the point on the surface of the particle closest to the other sphere. 49
- 3.9 Higher order Gaussian distributions using Equation (3.8) where $\tau = 1$ and $(\mu_x, \mu_y) = (0, 0)$ for a range of P values. 53
- 3.10 A plot of σ as a function of β for a single non-polarisable particle $a = 1.0$ nm with a Gaussian distribution of charge $q_g = 1e$ with (a) $\tau = 0.4$ nm and (b) $\tau = 1.0$ nm. 54
- 3.11 A plot of U as a function of τ_{rel} for a normal Gaussian distribution (solid, $P = 1$) and a higher order Gaussian distribution (dashed, $P = 5$). The interaction energy between two point-charges at this separation is displayed as the dotted line to show the expected value. 55
- 3.12 Visual representations of the surface charge density on the surface of two non-polarisable spheres ($a = 1.0$ nm) with Gaussian surface charge density distributions with $\tau = 0.4$ nm and $q_g = 1e$. (a) is a normal Gaussian ($P = 1$) and (b) is a higher order Gaussian ($P = 5$). 55
- 3.13 U as a function of s for the interaction between two non-polarisable dielectric particles ($k = k_0 = 1$, $a_1 = a_2 = 5$ nm) with point charges ($q_1 = 1e$, $q_2 = 2e$ (solid), $q_2 = 1e$ (dotted)) positioned in the same direction as the vector between the particles (a), and the equivalent calculation using Coulomb's law (b). Here $s = h_p - 2a_2$, where h_p is the distance between the point charge locations. 57

- 3.14 σ_{ext} as a function of θ for a 5 μm particle ($k = 10$) in a vacuum $k_0 = 1$ exposed to a uniform external electric field with a strength of 200,000 V/m. 59
- 3.15 Interaction energy as a function of s between two neutral dielectric particles ($k = 10$, $a = 5 \mu\text{m}$) in a vacuum in a uniform electric field with a strength of 200 kV m^{-1} . The solid lines indicate the energies calculated using the dielectric particle model, whereas the dotted lines indicate the results using Equation (3.12). The particles are aligned parallel (red) or perpendicular (blue) to the electric field vector. 60
- 3.16 A comparison of the energy profiles for the interaction between a pair of 5 μm polarisable particles with radii with $k_p = 10$ and $k_0 = 1$ in external electric field strengths of 100 kV m^{-1} (red) and 200 kV m^{-1} (black) using Equation 3.12 (a) and the dielectric particle model (b). The particles are either aligned parallel (solid) or perpendicular (dotted) to the electric field vector. 61
- 3.17 Interaction energy as a function of k_p in a system containing two neutral dielectric particles with radii 5 μm suspended in a dielectric medium ($k_0 = 1000$), separated by a surface-to-surface separation of 5 μm calculated using our model (solid) and 3.12 (dotted) 62
- 3.18 Interaction energy as a function of k_0 in a system containing two neutral dielectric particles ($k_p = 100$) with radii $a = 5 \mu\text{m}$ suspended in a dielectric medium, separated by a surface-to-surface separation of 5 μm calculated using our model (solid) and Equation 3.12 (dotted) 63

- 3.19 Interaction energy U as a function of θ for two neutral dielectric particles with a surface-to-surface separation of $5 \mu\text{m}$. $a = 5 \mu\text{m}$. $k_0 = 10$, $k = 20$ (solid), $k = 5$ (dashed), $k_1 = 20$, $k_2 = 5$ (dotted). $E_\infty = 200 \text{ kV m}^{-1}$. θ is the angle between the electric field vector and inter-particle vector. 64
- 3.20 A normalised plot of the force vectors for $\theta = 0^\circ\text{-}90^\circ$ for two neutral dielectric particles with radii $a = 2.5 \mu\text{m}$ separated by a surface-to-surface separation of $5 \mu\text{m}$ and an external electric field \mathbf{E} in the positive x-axis. Shown are the cases where both the particles are (a) more polarisable and (b) less polarisable than the medium. (c) is the case where one particle is more polarisable than the medium, whereas the other is less polarisable. 65
- 3.21 Screen-shot of the final structure after 75 s of simulation time produced by a molecular dynamics simulation of 50 randomly positioned dielectric particles ($k = 20$) with $a = 5 \mu\text{m}$ and speeds of 1 m s^{-1} in a dielectric medium ($k_0 = 10$). The particles are exposed to an external electric field in the positive x direction with $E_\infty = 200 \text{ kV m}^{-1}$ 66
- 3.22 A simplified visualisation of a collection of 6 local geometries seen at the end of the molecular dynamics simulation in Figure 3.21. Shown are **(a,b)** a pair of three-body configurations, **(c,d,e)** three four-body configurations, and **(f)** a seven-body hexagonal configuration. 68
- 3.23 U_{add} for a linear arrangement of M neutral particles with $a = 5 \mu\text{m}$, $k = 20$, $k_0 = 10$ for values of M from 3-50 in an electric field strength $E_\infty = 200 \text{ kV m}^{-1}$ parallel to the chain axis. 69

- 4.1 Possible outcomes for a collision between like charged particles. The total energy is schematically split into two components: the electrostatic interaction energy (solid) and the relative kinetic energy (dashed). The electrostatic interaction energy profile is calculated for a collision between ice particle ($a_1 = 3$ nm) and SiO₂ particle ($a_2 = 0.5$ nm) both carrying the charge of $q_1 = q_2 = -1e$ 79
- 4.2 Aggregation probability, indicated by the shaded area, for a collision between SiO₂ particle ($a_2 = 0.2$ nm, $q_2 = -1e$) and ice particle ($a_1 = 30$ nm) as defined by the Maxwell-Boltzmann distribution of the relative velocity at $T = 150$ K: (a) the case of neutral ice particle ($q_1 = 0$), the probability of aggregation is one as $P(v_{\text{rel}})$ is integrated in the velocity range of $[0,1192]$ ms⁻¹; (b) $q_1 = -1e$, the probability of aggregation is 0.293 as $P(v_{\text{rel}})$ is integrated in the velocity range of $[295,1219]$ ms⁻¹; (c) $q_1 = -2e$, the probability of aggregation is 0.034 as $P(v_{\text{rel}})$ is integrated in the velocity range of $[450,1260]$ ms⁻¹. The values of $v_{\text{rel}}^{\text{min}}$ and $v_{\text{rel}}^{\text{max}}$ are taken from Table 4.2 79
- 4.3 Position of the point charge on the surface of colliding particles depicted by a small open circle: (a) ice particle (1) and small oxide particulate (2); (b) and (c): both particles (1 and 2) are oxides. 80

4.4	Electrostatic interaction energy as a function of the separation distance between an ice particle and a SiO ₂ particle ($a_2 = 0.2$ nm, $q_2 = -1e$) in the geometry shown in Figure 4.3a, as calculated by the point charge model analogous to Filippov et al. [##]. Horizontal lines indicate the value of the Coulomb energy barrier obtained using the uniform surface charge model: (a) the charge of the ice particle is $q_1 = -1e$, and the radius varies as $a_1 = 10$ nm (line 1), 20 nm (line 2) and 30 nm (line 3); (b) the radius of the ice particle is $a_1 = 30$ nm, and the charge varies as $q_1 = -1e$ (line 3), $-2e$ (line 4) and $-5e$ (line 5). Note the change of scale on the y -axis.	82
4.5	Aggregation probability, presented as percentage, for a collision between SiO ₂ particle ($a_2 = 0.2$ nm, $q_2 = -1e$) and ice particle ($q_1 = -1e$ and $q_1 = -2e$) whose size varies from $a_1 = 1$ nm to 100 nm.	86
5.1	Schematic of the Dekati [®] BOLAR [™] . [67]	93
5.2	Dekati [®] BOLAR [™] internal components. [67]	94
5.3	A visualisation of the relative sizes of particle with diameters of 9.43 μ m, 5.73 μ m, 3.39 μ m, 1.78 μ m and 0.48 μ m from left to right.	95
5.4	A visual representation of a collision between two particles with opposite charges (negative = blue, positive = red) and different radii. Each particle has linear speed v_j travelling at an angle θ either side of the y -axis moving in the direction of the arrows shown.	97
5.5	$E_{\text{electrostatic}}$ as a function of the number of terms used N for two charged lactose particles where $k_{1,2} = 2.9$, $a_{1,2} = 1.0$ μ m, $q_1 = +100e$, $q_2 = -100e$ interacting in air ($k_0 = 1.0$).	99

- 5.6 Charge data from a BOLAR™ run showing the total positive (red), negative (blue) and net (green) charge for lactose particles in each size fraction within the BOLAR™. 101
- 5.7 A plot showing the internal kinetic energy of the system E_{IK} as a function of θ for the collision between the largest ($a_1 = 4.72 \mu\text{m}$) and smallest ($a_2 = 0.24 \mu\text{m}$) particles with $v_j = 6 \text{ m s}^{-1}$ (black line). Also shown is $E_{\text{electrostatic}}$ for the interactions between particles where $q_1 = -6575 \text{ aC}$ and $q_2 = +20.24 \text{ aC}$ (red) and $q_1 = +7097 \text{ aC}$ and $q_2 = -5.85 \text{ aC}$ (blue). The inset data shows the region where the 3 plots are comparable in magnitude, indicated by the green rectangle on the main plot. 103
- 5.8 2D plots of E_{IK} as a function of v_j and θ for 4 different colliding systems. The interactions presented are those between the smallest **(a)**, most asymmetric **(b)** and **(c)**, and largest **(d)** lactose particles. For each interaction, $E_{\text{electrostatic}}$ is represented for each plot as the black contour line, cohesive collisions are indicated by the red/yellow region, whereas the blue region indicates separation. 104
- 5.9 A comparison of the 2D plots for 2 systems containing a pair of colliding asymmetrically-sized lactose particles ($a_1 = 4.72 \mu\text{m}$, $a_2 = 0.24 \mu\text{m}$, $q_1 = +7097 \text{ aC}$, $q_2 = -5.85 \text{ aC}$). The systems are identical with the exception of the coefficient of restitution C_R . The white horizontal and vertical dashed lines are placed in identical positions in each subfigure for constant v_j and θ respectively. 105

- 5.10 2D plots of E_{IK} as a function of v_j and θ for 2 systems containing colliding lactose particles. The interactions presented are those between symmetrically- and asymmetrically-sized lactose particles. The yellow markers correspond to the input values for v_j and θ in the two dynamic simulations performed for each collision. 106
- 5.11 Screenshots of dynamic simulations at (a) 0 and (b) 20 μs for the dynamic simulations of the system described in Figure 5.10a ($a_{1,2} = 0.24 \mu\text{m}$, $q_1 = +20.24 \text{ aC}$, $q_2 = -5.85 \text{ aC}$, $v = 6.5 \text{ m s}^{-1}$, $\theta = 5^\circ$). Screenshots at (c) 0 and (d) 8 μs for the dynamic simulations of the system described in Figure 5.10b ($a_1 = 0.24 \mu\text{m}$, $a_2 = 4.72 \mu\text{m}$, $q_1 = +20.24 \text{ aC}$, $q_2 = -6575 \text{ aC}$, $v = 6.5 \text{ m s}^{-1}$, $\theta = 10^\circ$). 107
- 5.12 Screenshots at various timestamps for the dynamic simulation of a small two-body cluster ($a_{1,2} = 0.24 \mu\text{m}$, $q_1 = +20.24 \text{ aC}$, $q_2 = -5.85 \text{ aC}$) being impacted by the impact of a larger particle ($a_3 = 4.72 \mu\text{m}$, $q_3 = -6575 \text{ aC}$) with an initial velocity of 1 m s^{-1} . 108
- 5.13 Aggregation data over the entire 200 μs dynamic simulations of a cloud of 300 aerosol particles passing over scavenging particle I ($a = 10 \mu\text{m}$, $q = -38.5 \text{ fC}$). Shown is the data for the (a) number and (b) percentage of aerosol particles coalesced on the scavenging particle with radii of $0.24 \mu\text{m}$ (blue), $0.89 \mu\text{m}$ (red) and $1.70 \mu\text{m}$ (green), as well as the (c) total number of particles coalesced and the (d) total cluster charge. Each plot shows the mean and standard deviation for the sample size. 111

- 5.14 A comparison of percentage aggregation of the smallest particles over the entire 200 μs dynamic simulations ($a = 0.24 \mu\text{m}$) between scavenging particles with $a = 10 \mu\text{m}$ **(a)** I ($q = -38.5 \text{ fC}$, blue) and II ($q = -19.3 \text{ fC}$, red), and **(b)** I ($q = -38.5 \text{ fC}$, blue) and III ($q = -46.3 \text{ fC}$, red). Each plot shows the mean and standard deviation for the sample size. 112
- 6.1 a) Scheme of the generation of oppositely charged patches on the surface of an MF particle made of prelabeled PMVEMA and PEI with Rhodamine 6G and FITC, respectively. b) SFM height image of a PMVEMA patch. c) SEM image of a PEI patch. d) SEM image and e,f) fluorescence and the overlaid microscope images of bipatchy MF particles with patches made of PMVEMA and PEI that are coloured red and green, respectively. Scale bars: $1 \mu\text{m}$ 117
- 6.2 a) Fluorescence and b) optical microscope images of the self-assembly of bipatchy particles. c) Six possible connection types which could be formed via random interactions between patchy and nonpatchy surfaces of particles, together with statistics of experimentally observed connections in the aggregates formed by MF bipatchy particles. The fraction of PEI patch interactions is larger than the fraction of PMVEMA interactions due to the higher yield of PEI patches. 120
- 6.3 Overlay of fluorescence and optical microscope images of a) the branched, b) bent, and c) linear chains, which are formed via electrostatic attraction between oppositely charged PMVEMA and PEI patches. For a better visualization, connections between bipatchy particles are represented with white lines, PMVEMA and PEI patches are additionally highlighted with red and green colored half-circles, respectively. Scale bars: $10 \mu\text{m}$ 122

- 6.4 Overlay of the optical and fluorescence microscope images of the bipatchy particles a) before and b) after addition of a solution of NaCl. The elimination of self-aggregation can also be observed by the unaided eye. In solution, the white sediment of the large aggregates at the bottom of the Eppendorf tube (inset (a)) converts upon increase of the ionic strength to a turbid dispersion of small aggregates and single particles (inset (b)). c) Statistics for long and short chains as well as single particles in a dispersion of bipatchy particles before and after addition of the NaCl solution in comparison with the statistics obtained for a sample of untreated MF particles. Scale bars: 25 μm 123
- 6.5 The calculated electrostatic interaction energy (in fJ) as a function of the surface-to-surface separation between a pair of colloids: solid lines correspond to the interaction between bi-patchy particles shown in the figure; dashed lines correspond to the interaction between a bi-patchy particle and a mono-patchy particle with the outer patch removed (in case C, negative PMVMEA patch shown in red is removed); dash-dotted line corresponds to case C with the (green) positive PEI patch removed 124
- 6.6 Calculated rotational barriers for re-orientation from the repulsive PEI-PEI connection (bottom right) to the stable the PMVEMA-PEI configuration (left). Images at the bottom of the figure show the calculated distribution of the surface charge on the particles and patches. 125
- 6.7 Electrostatic interaction energy (in fJ) as a function of the surface-to-surface separation between: a) two bipatchy particles and b) bipatchy and monopatchy particles. PMVEMA and PEI patches are highlighted by red and green colors, respectively. . . 126

7.1	A geometric representative of a system containing two spherical macroions with a counterion between them.	133
7.2	Fractional concentrations of $\{\text{Mo}_{72}\text{Fe}_{30}\}^{i-}$ where i is the number of deprotonations for pHs of 2.5 (blue/solid) and 3.0 (orange/dotted).	137
7.3	Interaction energy as a function of s between $\{\text{Mo}_{72}\text{Fe}_{30}\}^-$ and $\{\text{Mo}_{72}\text{Fe}_{30}\}^{7-}$ in a vacuum ($k_0 = 1$).	138
7.4	Interaction energy as a function of s between $\{\text{Mo}_{72}\text{Fe}_{30}\}^-$ and $\{\text{Mo}_{72}\text{Fe}_{30}\}^{7-}$ in water ($k_0 = 80$).	139
7.5	Interaction energy as a function of s for a range of POM-counterion interactions. (a) shows the interaction between a Mg^{2+} counterion with $\{\text{Mo}_{72}\text{Fe}_{30}\}^i$ with $i = -1e$ (solid), $-3e$ (dash), $-5e$ (dash-dot) and $-7e$ (dot) in water ($k_0 = 80$). (b) shows the interaction between a Mg^{2+} counterion with $\{\text{Mo}_{72}\text{Fe}_{30}\}^{7-}$ in a range of polar mediums. $k_0 = 80$ (solid), 40 (dash) and 20 (dash-dot).	141
7.6	The effect of the dielectric constant of the medium on the binding energy between a pom and a counterion. $\{\text{Mo}_{72}\text{Fe}_{30}\}^{3-} + \text{K}^+$ (solid) and $\{\text{Mo}_{72}\text{Fe}_{30}\}^{3-} + \text{Mg}^{2+}$ (dashed) interaction, k_0 shown, $k_{POM} = 10$, $k_c = k_0 = 80$	142
7.7	A contour plot of the electrostatic interaction energy as a function of Mg^{2+} counterion position in a system containing two $\{\text{Mo}_{72}\text{Fe}_{30}\}^{7-}$ ions separated by a surface-to-surface separation of 1.5 nm in water ($k_0 = 80$).	143
7.8	Fraction concentrations of $[\text{Mg}_x^{2+}\{\text{Mo}_{72}\text{Fe}_{30}\}^{i-}]^z$ for pHs of 2.5 (orange/dotted) and 3.0 (blue/solid).	144
7.9	Energy as a function of s (left) for the 4 dimer systems considered (right).	145

Chapter 1

Introduction

Electromagnetism is the branch of physics concerned with the study of the electromagnetic force—the physical interaction that occurs between electrically charged particles. The electromagnetic force is propagated via the electromagnetic field, which includes contributions from both electric and magnetic fields. The electric field component is generated by the presence of static charges in the system (electrostatics) whereas the magnetic component comes from the presence of moving charges (electrodynamics). The electrical phenomenon is the result of a fundamental property: the presence of electric charge in matter. While most matter is generally neutral, it is possible for it to gain electric charge through atoms either possessing a deficit (positive) or excess (negative) of electrons. The electromagnetic interaction is the interaction acting between electrically charged particles and, along with gravity, governs the majority of interactions seen in day-to-day life.

Electric phenomena have been observed and been the cause of wonder for millenia, with examples such as thunder and lightning, caused by a huge build up of charge in clouds, being thought to be caused by the weapons of angry gods such as Zeus's thunderbolt to punish ancient Greeks [1] or Thor's hammer, Mjölfnir, in Norse mythology [2]. Due to the perception of lightning being caused by a higher power, these events were considered to be sacred; this led

to many holy sites across the globe being constructed at the place of lightning strikes.

The effects of electric charges at rest (electrostatics) have been known about for much longer than electric currents (electrodynamics). Credit for the coining of the terminology can be traced back to the times of Thales of Miletus in ancient Greece (c. 600 B.C.), who is the earliest known person to document the effects of static electricity [3, 4]. The word “electricity” is derived from the word “elektron”, the Greek word for amber. He noted that when a piece of amber is rubbed with cloth or wool, it would begin to attract small, light objects such as dust or hair. He also noted that trying to remove these fibres generally made the situation worse, leading early philosophers to wonder about the cause.

In the 17th century, Jean-Antoine Nollet—as well as discovering the phenomenon of osmosis in natural membranes—produced a wide range of experimental demonstrations which gave a deeper insight in to the effects and behaviour of electricity; one such demonstration was his experiment named “Electric boy”, where a young man was suspended from the ceiling using an insulation material (such as silk cords) and electrified [5]. It caused the man’s body to accumulate charge, causing objects to become attracted to him, and close proximity to a grounded person would lead to sparks. He also performed an experiment in 1746 to test the speed of the propagation of electricity. He gathered around two hundred monks in a circle with a circumference of about a mile, connected each with pieces of iron wire, and then discharged a battery of Leyden jars through this human chain; each man reacted to the electric shock at practically the same time, leading to his conclusion that the speed was “very high” [6]. Nollet was also the first to report on the electro spraying phenomenon in 1750, when he noted the aerosolisation of water flowing from a vessel when the vessel is electrified and placed near electrical ground [7]. He took this observation further and also noted that “a person, electrified by

connection to a high-voltage generator, would not bleed normally if he were to cut himself; blood would spray from the wound”.

Around the same time across the Atlantic Ocean, big steps in the understanding of electrical phenomena were being undertaken by US Founding Father Benjamin Franklin. Prior to the American Revolutionary War, Franklin was theorising about the nature of electricity and famously established that lightning is electricity by using kites during thunderstorms to collect electrical charge in Leyden jars [8]. He was a strong advocate of a ‘single fluid’ model of electric charge which states that an object with an excess of fluid would have one charge, whereas a deficit would lead to the opposite charge. The other model was a ‘two fluid’ model, which had positive and negative fluids moving around. The debate eventually was settled to side with Franklin over a century later [9]. He was also responsible for a range of electrical terms still in use today: battery, charge, conductor, positively, negatively, among others.

One notable example of electrostatic effects in nature occurred in the US during the Dust Bowl in the 1930s during the Great Depression [10, 11]. The Dust Bowl was a period of time where a series of severe dust storms devastated a 150,000 square mile region spanning across Oklahoma, the Texas Panhandles, and parts of Colorado, Kansas, and New Mexico. In the decade following World War I, new gasoline-powered machinery allowed farmers to increase their workload substantially. This increase in the work of the land, and poor farming practices led to the over-ploughing of the topsoil which, in conjunction with one of the most severe droughts in centuries, resulted in the desertification of farm land across the south. This produced the perfect conditions for huge dust clouds to form—sometimes miles in height—and travel over the multiple states. The dust particles within the cloud gained charge due to triboelectric effects, leading to huge amounts of static electricity building up between the dust and the ground; this led to situations where people with cars drove with a

chain dragging behind, and mothers hugging their children could be met with a static shock rendering both unconscious. The fine nature of the particles also caused a huge amount of health issues, with residents exhibiting signs of silicosis.

1.1 Basics of Electrostatic Theory

Coulomb's Law

Charles-Augustin de Coulomb was a French physicist who discovered the experimental law that describes the force between two electrically charged particles. The law—named after him as Coulomb's law—was discovered in 1785, and states that:

“The magnitude of the electrostatic force of attraction or repulsion between two point charges is directly proportional to the product of the magnitudes of charges and inversely proportional to the square of the distance between them.” — Charles-Augustin de Coulomb (1785) [12]

This is shown in the scalar form, where the magnitude of the force between two point charges q_1 and q_2 separated by the distance r is

$$|\mathbf{F}| = K \frac{|q_1 q_2|}{r^2}, \quad (1.1)$$

where K is the constant of proportionality in Coulomb's law, known as Coulomb's constant and is equal to $1/(4\pi\epsilon_0)$, where ϵ_0 is the electric permittivity of free space, $K \approx 8.987\,551\,792 \times 10^9 \text{ N m}^2 \text{ C}^{-2}$ [13]. While this gives only the magnitude of the interaction, taking the sign of the product $q_1 q_2$ reveals whether the interaction is attractive ($q_1 q_2 < 0$) or repulsive ($q_1 q_2 > 0$). In vector form, a system with 2 point charges ($i = 1, 2$) in a vacuum, each with their own charge q_i and position \mathbf{r}_i , experiences an electrostatic force \mathbf{F}_1 on

point charge 1 equal to

$$\mathbf{F}_1 = \frac{q_1 q_2}{4\pi\epsilon_0} \frac{\mathbf{r}_1 - \mathbf{r}_2}{|\mathbf{r}_1 - \mathbf{r}_2|^3} = \frac{q_1 q_2}{4\pi\epsilon_0} \frac{\hat{\mathbf{r}}_{12}}{|\mathbf{r}_{12}|^2} \quad (1.2)$$

where $\mathbf{r}_{12} = \mathbf{r}_1 - \mathbf{r}_2$ and $\hat{\mathbf{r}}_{12} = \frac{\mathbf{r}_{12}}{|\mathbf{r}_{12}|}$, a unit vector from point charge 2 to point charge 1. The force between two charges acts along the vector between the two and—obeying Newton’s third law of motion—is equal in magnitude and in opposite directions on each charge ($\mathbf{F}_2 = -\mathbf{F}_1$).

The Coulomb force \mathbf{F} on any charged particle can also be seen as being equal to the product of the electric field \mathbf{E} and the charge of the particle q , and is given as

$$\mathbf{F} = q\mathbf{E}. \quad (1.3)$$

The electric field \mathbf{E}_i generated at an arbitrary position \mathbf{r}_0 by point charge q_i at position \mathbf{r}_i is given by

$$\mathbf{E}_i(\mathbf{r}_0) = K \frac{q_i}{|\mathbf{r}_0 - \mathbf{r}_i|^2} \hat{\mathbf{r}}_{0i}. \quad (1.4)$$

Coulomb’s law can be extended to many-body problems including multiple point charges as it follows the law of superposition, and can be written as a linear addition of functions ($f(x + y + \dots) = f(x) + f(y) + \dots$). Using the superposition principle, the total electric field \mathbf{E} at an arbitrary position \mathbf{r}_0 in a system with M point charges is

$$\mathbf{E}(\mathbf{r}_0) = K \sum_i^M \frac{q_i}{|\mathbf{r}_0 - \mathbf{r}_i|^2} \hat{\mathbf{r}}_{0i}. \quad (1.5)$$

This leads to the electrostatic force acting on point charge q_i \mathbf{F}_i positioned at

\mathbf{r}_i in a system with M point charges in the form

$$\mathbf{F}_i(\mathbf{r}_i) = q_i \mathbf{E}(\mathbf{r}_i) = q_i K \sum_{j \neq i}^M \frac{q_j}{|\mathbf{r}_i - \mathbf{r}_j|^2} \hat{\mathbf{r}}_{ij}. \quad (1.6)$$

Up until now, the charges have been treated as discrete point charges, whereas it is generally more appropriate to consider these charges as continuous charge distributions. There are 3 ways of representing total charge as a continuous distribution:

$$q = \int \lambda d\ell' \quad \lambda = \text{linear charge density} \quad (1.7)$$

$$q = \int \sigma da' \quad \sigma = \text{surface charge density} \quad (1.8)$$

$$q = \int \rho d\tau' \quad \rho = \text{volume charge density} \quad (1.9)$$

where $d\ell'$, da' and $d\tau'$ are the infinitesimal elements of length, surface and volume respectively. Taking the volume charge density ρ as an example, we gain a description of the electric field \mathbf{E} at an arbitrary position \mathbf{r}_0 produced by M volume charge distributions:

$$\mathbf{E}(\mathbf{r}_0) = K \sum_i^M \int_{R_i} \frac{\rho_i(\mathbf{r}_i(\tau)) d\tau}{|\mathbf{r}_0 - \mathbf{r}_i(\tau)|^2} \hat{\mathbf{r}}_{0i}, \quad (1.10)$$

where R_i is a region containing all the points where $\rho_i > 0$, $\mathbf{r}_i(\tau)$ is the vector describing τ . These equations allow for the electric field to be solved for systems where all of the charge distributions are known.

Maxwell's equation for the divergence of such a field is given as: [14]

$$\nabla \cdot \mathbf{E} = \frac{\rho}{\epsilon_0}. \quad (1.11)$$

As electric potential Φ is a scalar function, calculating Φ has advantages over directly calculating the electric field. \mathbf{E} can then be directly calculated from

Φ , given that electric fields are the negative gradient of the electric potential ($\mathbf{E} = -\nabla\Phi$). Using this relationship, Equation (1.11) can be rewritten as a Poisson equation in the form

$$\begin{aligned}\nabla \cdot (-\nabla\Phi) &= \frac{\rho}{\varepsilon_0}, \\ \nabla^2\Phi &= -\frac{\rho}{\varepsilon_0}.\end{aligned}\tag{1.12}$$

This is fine for non-polarisable distributions, but once polarisation occurs (such as in conductors and dielectrics) the charge density distribution is no longer known and needs to be solved for.

While the Poisson equation is extensively used in electrostatic models, the study of charged particles in an electrolyte solution requires an extension that takes into account the charge density and electric potential generated by a distribution of electrolyte ions. The freedom of movement of the ions in solution is well described by Maxwell-Boltzmann statistics, with a local ion density c defined by

$$c = c_0 \cdot \exp\left(\frac{-U}{k_B T}\right),\tag{1.13}$$

where c_0 is the bulk ion concentration, U is the potential energy of an ion brought to the surface ($q\Phi$), k_B is the Boltzmann constant, and T is the temperature in Kelvins [15].

When c_0 is the bulk concentration of ions, the densities of the positive ions c^+ and negative ions c^- are given by

$$c^+ = c_0 \exp\frac{-q_p\Phi}{k_B T}\tag{1.14}$$

and

$$c^- = c_0 \exp \frac{q_n \Phi}{k_B T}, \quad (1.15)$$

where q_p and q_n are the charge of the positive and negative ions respectively. Substituting Equations (1.14) and (1.15) into the local charge density ρ_e as

$$\rho_e = q_e(c^+ - c^-) = q_e c_0 \left(\exp \frac{-q_p \Phi}{k_B T} - \exp \frac{q_n \Phi}{k_B T} \right), \quad (1.16)$$

which can be used as the charge distribution in the Poisson equation (1.12) to find the potential Φ generated by the electrolyte solution.

1.2 Polarisation of Dielectric Materials

In nature, there are two main classes of materials with distinct properties: conductors and insulators (also known as dielectrics). A material is considered an electrical conductor when there are charge carriers within the material that are free to move in one or more directions through the bulk of the material when exposed to an electric field. Dielectrics, on the other hand, have their charges bound to the atoms within the material, meaning that they are electrically insulating and poor conductors of electric charge. In a dielectric material, the charge is split into two types of charges, “free” and “bound”. Free charge is the charge that is present in excess and can move into electrostatic equilibrium. Bound charge, on the other hand, is due to the polarisation of atoms or reorientation of polar molecules to create a series of dipoles aligned within a field, as shown in Figure 1.1.

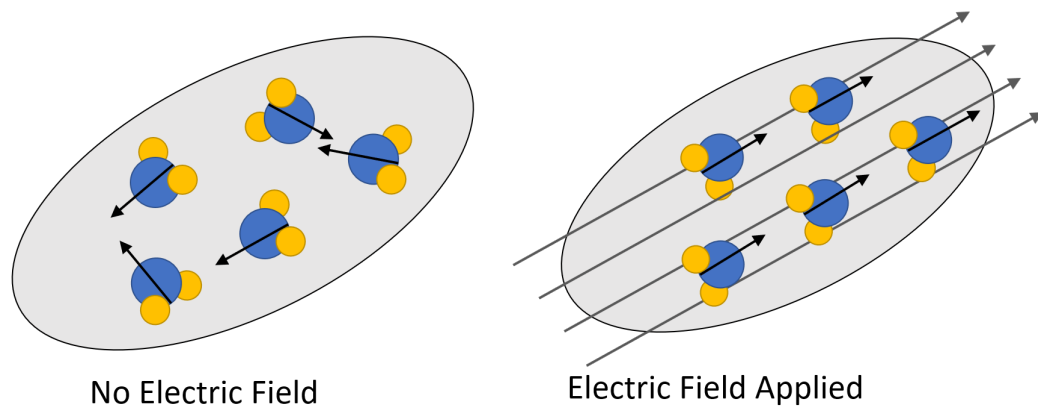


Figure 1.1: An exaggerated visualisation of a particle composed of a polar molecule in the absence of an electric field (left) and exposed to an electric field (right).

Polarisation in a dielectric material comes in 4 main forms:

- **Electronic** - The production of atomic dipoles composed of positive nuclei and negative electron clouds.
- **Ionic** - The displacement of positive and negative ions under the influence of a field in an ionic crystal.
- **Orientalional** - The alignment of molecular dipoles with the field (as in Figure 1.1).
- **Interfacial/Space Charge** - An electric field causing the aggregation of charge between two different regions within a material or at the interface between two materials.

One of the earliest recorded observations of electrostatic interactions between dielectric materials was in the late 16th/early 17th century when William Gilbert—while investigating a description of the behaviour of magnetic and electrostatic phenomena—noticed that when in the presence of a charged piece of amber, a droplet of water distorted into a cone. This early observation showed evidence of the effect of electric fields on dielectric materials [16].

The atomic quantity described as the polarisability α is the tendency of the charge density of an atom to be distorted from its natural shape by the presence of an external electric field. α is defined by the relationship between the magnitude of an induced dipole moment \mathbf{p} and the electric field \mathbf{E} causing the induction.

The Clausius-Mossotti relation describes the bulk quantity of dielectric constant k (relative permittivity ε_r) in terms of the atomic quantity of polarisability α [17, 18]:

$$\left(\frac{k-1}{k+2}\right) = \frac{N\alpha}{3\varepsilon_0}, \quad (1.17)$$

where N is the number density of the atoms/molecules and k is the dielectric constant ($\varepsilon/\varepsilon_0$).

The electric susceptibility χ_e is a dimensionless constant of proportionality that gives an indication towards the degree of polarisation of a dielectric material when exposed to an electric field \mathbf{E} , where $\chi_e = k - 1$ ($\chi_e = 0$ for a vacuum). χ_e relates the electric field \mathbf{E} to the induced dielectric polarisation density \mathbf{P} by:

$$\mathbf{P} = \varepsilon_0\chi_e\mathbf{E}. \quad (1.18)$$

The electric displacement field \mathbf{D} within a dielectric material is related to \mathbf{P} by

$$\mathbf{D} = \varepsilon_0\mathbf{E} + \mathbf{P} = \varepsilon_0(1 + \chi_e)\mathbf{E} = k\varepsilon_0\mathbf{E} \quad (1.19)$$

where, following Gauss's law, $\nabla \cdot \mathbf{D} = \rho_f$.

1.2.1 Method of Image Charges

One of the earliest developed methods to deal with the interactions between charged particles and polarisable interfaces is the method of image charges. The method is a mathematical tool for the solving of differential equations, and gets its name from the domain of the sought function (Φ) being extended by the addition of its mirror image across the interface [13].

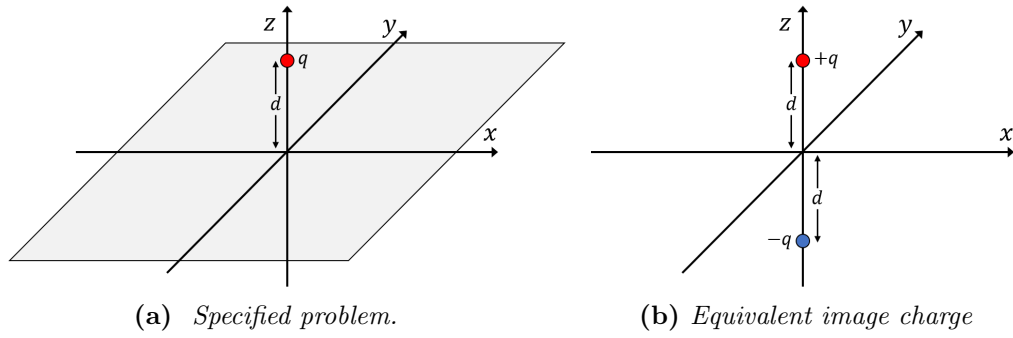


Figure 1.2: A visualisation of a system involving (a) a point charge with a conducting infinite plate, and (b) the equivalent image charge problem.

Consider a system with a point charge q at a distance d above an infinite grounded conducting plane. The problem involves solving Poisson's equation in the region $z > 0$, with a point charge q at $(0, 0, d)$ (see Figure 1.2a), obeying the boundary conditions:

1. $V = 0$ at $z = 0$ (since the conducting plane is grounded), and
2. $V \rightarrow 0$ at large distances from the charge.

The first uniqueness theorem, which states that:

“The solution to Laplace's equation in some volume \mathcal{V} is uniquely determined if Φ is specified on the boundary surface \mathcal{S} ” - David J. Griffiths [13],

guarantees only one function that meets these requirements, and all that's needed to find this function is either a trick or a clever guess; the trick, in this case, is to completely disregard the actual problem and study a different one. This new configuration contains the original point charge $+q$ at $\mathbf{r}_1 = (0, 0, d)$ and a point charge with the opposite charge $-q$ at $\mathbf{r}_2 = (0, 0, -d)$ and the absence of the conducting plane all together (see Figure 1.2. In this case, the computation of the potential Φ at an arbitrary point \mathbf{r}_0 is simple, with

$$\Phi(\mathbf{r}_0) = \frac{1}{4\pi\epsilon_0} \left[\frac{q}{|\mathbf{r}_0 - \mathbf{r}_1|} - \frac{q}{|\mathbf{r}_0 - \mathbf{r}_2|} \right], \quad (1.20)$$

which also follows the conditions:

1. $V = 0$ at $z = 0$,
2. $V \rightarrow 0$ for $|\mathbf{r}_0 - \mathbf{r}_{1,2}| \gg d$,

and the only charge present in the system $z > 0$ is the charge $+q$ at $(0, 0, d)$. These three conditions are identical to those of the system discussed earlier, leading to the system with two point charges happening to produce the exact same potential in the region of interest ($z > 0$). While it's different for $z < 0$, this doesn't matter as it doesn't represent any region of space we're interested in. This allows us to conclude that the potential of a point charge q above an infinite grounded conductor is equal to Equation (1.20) when $z \geq 0$. The surface charge density σ at position $(x, y, 0)$ on a conducting plane in the vicinity of a point charge q at $(0, 0, d)$ is given by:

$$\sigma(x, y) = \frac{-qd}{2\pi(x^2 + y^2 + d^2)^{3/2}}. \quad (1.21)$$

When the plane is no longer conducting and dielectric in nature, the method of image charges is still valid.

When the plane is dielectric—as opposed to conducting—it can be treated almost in the same way with slight differences. In this case, charge of the image q' produced by a point charge q is no longer $-q$, and is determined by the permittivity of both the plane k_1 and the medium that encompasses the point charge k_0 , using the relationship

$$q' = \frac{k_0 - k_1}{k_0 + k_1}q. \quad (1.22)$$

Using this relationship, we can deduce that there are 3 possible interactions. The first is an attractive interaction, where the plate is more polarisable than the medium ($k_1 > k_0$) leading to an opposite-charge interaction. If the opposite is true, and the medium is more polarisable than the plate ($k_0 > k_1$), the image

charge q' becomes the same sign as the source charge q and the interaction with the plate becomes repulsive. When the polarisabilities of the medium and plate are equal ($k_0 = k_1$), q' becomes 0 leading to no interaction with the plate.

The method of image charges works extremely well for simple systems with one polarisable boundary, but even increasing the complexity to two polarisable boundaries leads to an infinite set of image charges being needed to compute Φ . This makes increasing the complexity to many-body interactions increasingly inefficient with a high computational cost.

1.2.2 Electrostatic analysis of the interactions between charged particles of two dielectric materials

In 2010 Bichoutskaia et al. [19] published a general solution to the problem of calculating the electrostatic force between charged dielectric particles, which is based upon a multipole expansion in Legendre polynomials using spherical coordinates. The solution considers the interaction between two dielectric spheres ($i = 1, 2$) suspended in a dielectric medium k_0 , each with their own charge q_i , radius a_i and dielectric constant k_i , separated by a surface-to-surface separation s ($s = h - a_1 - a_2$ where h is the centre-to-centre separation). The model treats the free charge of a dielectric particle to be uniformly distributed on the surface of the particle— $\sigma_f = q/(4\pi a^2)$ —where there is no charge present in the volume of the sphere.

In addition to the condition that the electric potential Φ vanishes at infinity, there are 3 additional boundary conditions applied in this model. The first is that the tangential component of the electric field is continuous at the surface due to the continuity of the electric potential on the surface of each sphere

$$\hat{\mathbf{n}} \times \left(\mathbf{E}_{r_i=a_i^+} - \mathbf{E}_{r_i=a_i^-} \right) = 0. \quad (1.23)$$

The normal component of the electric field is discontinuous at boundary due to the presence of a total charge density on the surface of each sphere

$$\hat{\mathbf{n}} \cdot \left(\mathbf{E}_{r_i=a_i^+} - \mathbf{E}_{r_i=a_i^-} \right) = \frac{\sigma}{\epsilon_0}. \quad (1.24)$$

The normal component of the electric displacement field is discontinuous due to the presence of a free charge on the surface of each sphere

$$\hat{\mathbf{n}} \cdot \left(\mathbf{D}_{r_i=a_i^+} - \mathbf{D}_{r_i=a_i^-} \right) = \sigma_f. \quad (1.25)$$

where $\hat{\mathbf{n}}$ is a unit vector perpendicular to a point on the surface of a sphere, and the subscripts a_i^+ and a_i^- denote radial positions on the outside and the inside of the sphere, respectively.

The electrostatic force between two spheres \mathbf{F}_{12} with the presence of surface charge on each is calculated from a generalisation of Equation (1.2) and is given by

$$\mathbf{F}_{12} = K \int dq_1(\mathbf{r}_1) \int dq_2(\mathbf{r}_2) \frac{\hat{\mathbf{r}}_{12}}{|\mathbf{r}_1 - \mathbf{r}_2|^2}, \quad (1.26)$$

where \mathbf{r}_1 and \mathbf{r}_2 are position vectors at the surface of spheres 1 and 2 respectively, K is Coulomb's constant, and $dq_1(\mathbf{r}_1)$ and $dq_2(\mathbf{r}_2)$ are the corresponding charge elements. The first term $\int dq_1(\mathbf{r}_1)$ accounts for the charge on sphere 1, as in Equations (1.7) to (1.9), whereas the rest of the equation accounts for the electric field generated by the charge on sphere 2, similar to Equation (1.4). From this, the electrostatic force \mathbf{F}_{12} is evaluated using a Legendre polynomial expansion of the electric potential Φ generated by each sphere as they interact. The total surface charge distribution is evaluated as a function of h . Integrating the charge over the the surface leads to an analytical expression for the force

in the form

$$\mathbf{F}_{12} = -\frac{1}{K} \sum_{l=0}^{\infty} A_{1,l} A_{1,l+1} \frac{(k_1 + 1)(l + 1) + 1}{(k_1 - 1)a_1^{2l+3}}, \quad (1.27)$$

where a negative value for \mathbf{F}_{12} indicates attraction, and repulsion for positive values. The multipole moment coefficients $A_{1,l}$ account for the dependence of \mathbf{F}_{12} on h , and also describe the mutual polarisation of interacting spheres as a function of their charges (q_1/q_2), dielectric constants (k_1/k_2) and radii (a_1/a_2), with the equations describing $A_{1,l}$ deduced in Bichoutskaia et al. [19], and leading to the force being expressed as

$$\begin{aligned} \mathbf{F}_{12} = & K \frac{q_1 q_2}{h^2} - q_1 \sum_{m=1}^{\infty} \sum_{l=0}^{\infty} A_{1,l} \frac{(k_2 - 1)m(m + 1)}{(k_2 + 1)m + 1} \\ & \times \frac{(l + m)!}{l!m!} \frac{a_2^{2m+1}}{h^{2m+l+3}} - \frac{1}{K} \sum_{l=1}^{\infty} A_{1,l} A_{1,l+1} \frac{(k_1 + 1)(l + 1) + 1}{(k_1 - 1)a_1^{2l+3}}. \end{aligned} \quad (1.28)$$

The first term in Equation (1.28) accounts for the monopole-monopole interaction, which is functionally equivalent to Coulomb's law with the interaction between point charges at the centre of each particle. The second and third terms account for the mutual polarisation of the charge densities of the particles, and is always attractive in vacuum, with the magnitude of the interaction being a function of the dielectric constant k . In the case of like-charged particles, particular combinations of q , a , and k can cause attractive polarisation interactions that overcome the repulsion of the coulombic interactions sufficiently so that the overall force is attractive between like-charged particles.

In the 11 years since the publication of this two-body solution, there has been a large amount of development to the model, increasing its versatility and range of applications, shown in Table 1.1.

Table 1.1: Further developments of the electrostatic model of two particle interactions in vacuum [19].

Development	Methodology Description	Reference
Particle-Plane Interactions	A solution to this problem using a bispherical coordinate system; this solution has greater versatility than using spherical coordinates, with the capability to model particle-planar interactions, although the drawback to this is slower convergence.	[20]
Interactions in Electrolyte Solution	Accounts for interactions in a polarisable medium that's a dilute solution of a strong electrolyte, solving within the Debye-Hückel approximation using the boundary condition of constant potential, with the solution being finalised in 2018.	[21, 22]
Inhomogeneous Surface Charge Density	An expansion to include a new definition of the surface charge density, providing a solution to the interaction between two particles with inhomogeneous surface charge distributions, represented as point charges on the surface. The point charges are represented as Dirac-delta functions and the options for multiple orientations allows for a more in-depth analysis of interactions.	[23]
Interactions Between Spheroidal Particles	Theory for the interaction between particles with spheroidal geometries with the particles now also being able to take the shape of oblate or prolate spheroids. The model gives the expected charge density distributions from analytical solutions for isolated particles, while also matching the expected interactions between the limiting cases involving rods (prolate limit) and disks (oblate limit).	[24]
Generalisation to Many-Body Interactions	A many-body generalisation of the two-body solution was produced that used an integral equation approach to be able to calculate the interaction between an arbitrary number of particles in three-dimensional space, with the algorithmic complexity being only linearly scaling with respect to the number of particles in the system through the use of a modified fast multipole method.	[25]
Many-Body Dynamics	Implementation of the many-body solution as the force field in dynamics simulations. The set of differential equations representing the classical equations of motion have been integrated previously using the Euler method and more recently with the Verlet method.	[26]

Table 1.2: Applications of the electrostatic solution.

Application	Description	Reference
Coulomb Fission	Use of the two-body solution to model the behaviour of like-charged dielectric spheres in conditions similar to those found in the Coulomb fission process present in the electrospray phenomenon. Kinetic energy releases were determined experimentally and confirmed using computational simulations.	[23, 27, 28]
Aerosol Aggregation on Titan	A study into the aggregation of negatively-charged particles in the atmosphere of Saturn's moon Titan. The aggregation of polar and non-polar materials is compared, with the energy barriers for polar molecules calculated to be $\sim kT$ for asymmetric systems.	[25]
Polyoxometalate (POM) Adsorption	A study into the effect of the solvent on the interaction between a neutral POM and a charged plane. Solvents with high polarisability lead to a repulsive polarisation interactions between charged and neutral species.	[29]
Microparticle Aggregation	Two series of dynamics simulations investigating experimental studies. The first relates to experiments on the assembly of polymer particles subjected to tribocharging with the simulations successfully reproducing many of the observed patterns of behaviour. A second study explores events observed following collisions between single particles and small clusters composed of charged particles derived from a metal oxide composite.	[26]
Bipatchy Microcolloid Self-Assembly	Analysis of the interaction between particles with pairs of oppositely charged patches on the surface. The calculations show that chain formation is driven by a combination of attractive electrostatic interactions between oppositely charged patches.	[30]
Cloud Microphysics	A study of the coalescence between like-charged dust and ice particles in the upper mesosphere to lower thermosphere (MLT) region of the atmosphere using point-charge descriptions of the charge.	[31]
Superlattice Stability	A series of studies looking at the many-body polarisation effects in superlattices. The first investigates the electrostatic interaction energy for varying particle size combinations for a range of structures, from AB-type to AB ₁₃ -type. The second looks into a binary collection of X@C ₆₀ endohedral fullerenes in many types of AB and AB ₂ lattice structures.	In prep.

1.3 Aims and Objectives

The work in this thesis presents a deep investigation into the interactions between polarisable particles and pushes the theory developed in 2018 by Lindgren et al. [32] to a wider range of applications. The work begins in Chapter 2 with the theory behind the expansion of the many-body solution to include non-homogeneous surface charge densities in the form of point charges, and also the introduction of external electric fields.

Following this, numerical tests are performed in Chapter 3 to demonstrate the full range of capabilities of the many-body model and its expansions. Two-body phenomena, such as like-charge attraction, are followed by tests of many-body arrangements. Also presented are tests of non-uniform charge distributions in the form of two-dimensional Gaussian distributions on the surface of the particles and an investigation into the limitations to the size of the Gaussian and also analysis of higher-order distributions. The point-charge solution is then tested against Coulomb's law, as well as used to reproduce the results in 2019 by Filippov et al. [23]. A very small Gaussian is then used and compared with the results from the point charge distribution to test whether a small Gaussian width can be used to replicate the results from the point charge solution.

Chapter 4 presents the work produced in Baptiste et al. [31] which is an investigation of the processes behind the aggregation of nanoscale dust and ice particles in the mesosphere to lower thermosphere (MLT) region of the atmosphere. The interactions between the particles are modelled using the newly-developed point charge solution from Chapter 2, with the point charge oriented either in the same direction or away from each other. The project looks into the effect of particle size and composition on the likelihood of aggregation based on the size of the electrostatic energy barrier for the collision and the

energy well of the aggregation.

Chapter 5 is a study into the effects of bipolar charge on the electrostatic cohesion of pharmaceutical particles, and investigates the effects of particle size and charge on the charge-scavenging nature of particles in an aerosol airflow. The pair interactions are primarily studied, with large scale dynamic simulations being used to investigate the effectiveness of the scavenging of particles of varying size.

Chapter 6 presents the work produced in Naderi Mehr et al. [30] which is a study into the self-assembly behaviour of oppositely charged inverse bi-patchy micro-colloids. The patches on the particles in these calculations are represented by smaller spheres, and the energy is analysed for a range of orientations of monopatch and bipatchy particles.

Finally, Chapter 7 studies the role of counterions in the self-assembly of polyoxometalates into macroanionic “Blackberry” structures. Here the focus is on the formation of a dimer, with the interactions being between POMs with charges within a specified range of charges expected based on the pH, with discrete counterions stabilising the interaction. In this chapter the effect of the polarisability of the solvent is also investigated, with the aim of providing a theoretical explanation for experimental observations.

Chapter 2

The many-body electrostatic problem of charged polarisable particles: An extension to point-charge distributions and external electric fields

Included in this chapter are new developments in the many-body electrostatic theory developed in 2018 by Lindgren et al. [25] which extend the solution to consider non-homogeneous surface charge densities in the form of smooth analytical functions and as a point charge. Also included in this section is the implementation of an external electric field into the model. The developments included have been developed as part of a collaboration with Prof. Benjamin Stamm and Dr. Stefanie Braun at RWTH Aachen University and, Dr. Muhammad Hassan now of Sorbonne Université.

2.1 Surface point charge and external electric field solutions

There are a large number of applications where a uniform surface charge density is not an appropriate representation of the charge present in a system. When the charge on a particle is of the order of $\pm 1e$, or charge given by a small cluster of metal ions on the surface of the particle, the charge density is best represented by the singularity of a point charge distribution. A patch of charge imprinted onto the surface of a neutral particle as in Naderi Mehr et al. [30] is an example of a distribution unsuitably modelled by a uniform distribution, with a more suitable representation being that of Gaussian or Kent distributions, or that of a step function.

2.1.1 Formulation of the Problem

We consider a physical system of M non-intersecting dielectric spherical particles, defined by their radii $\{a_i\}_{i=1}^M$, centers $\{\mathbf{x}_i\}_{i=1}^M$, and dielectric constants $\{k_i\}_{i=1}^M$, immersed in a background medium (solvent) which has dielectric constant $k_0 \geq 1$.

For the purpose of this article, we will view the physical system at a particular snapshot in time so that, in effect, the physical system is considered at rest. The spherical particles are described as open balls denoted by $\{\Omega_i\}_{i=1}^M$ with surfaces $\{\Gamma_i\}_{i=1}^M$. The surfaces of the dielectric particles represent the boundary Γ between the interior Ω^- and the exterior Ω^+ of the particles. Note that the global values for both the boundaries Γ_0 and the particles Ω_0 are defined as

$$\begin{aligned}\Gamma_0 &= \Gamma_1 \cup \dots \cup \Gamma_M, \\ \Omega_0 &= \Omega_1 \cup \dots \cup \Omega_M.\end{aligned}$$

We assume that this surface Γ carries a given free charge distribution σ_f and that there is no charge in the interior of the particles, i.e., in Ω^- . (See Ap-

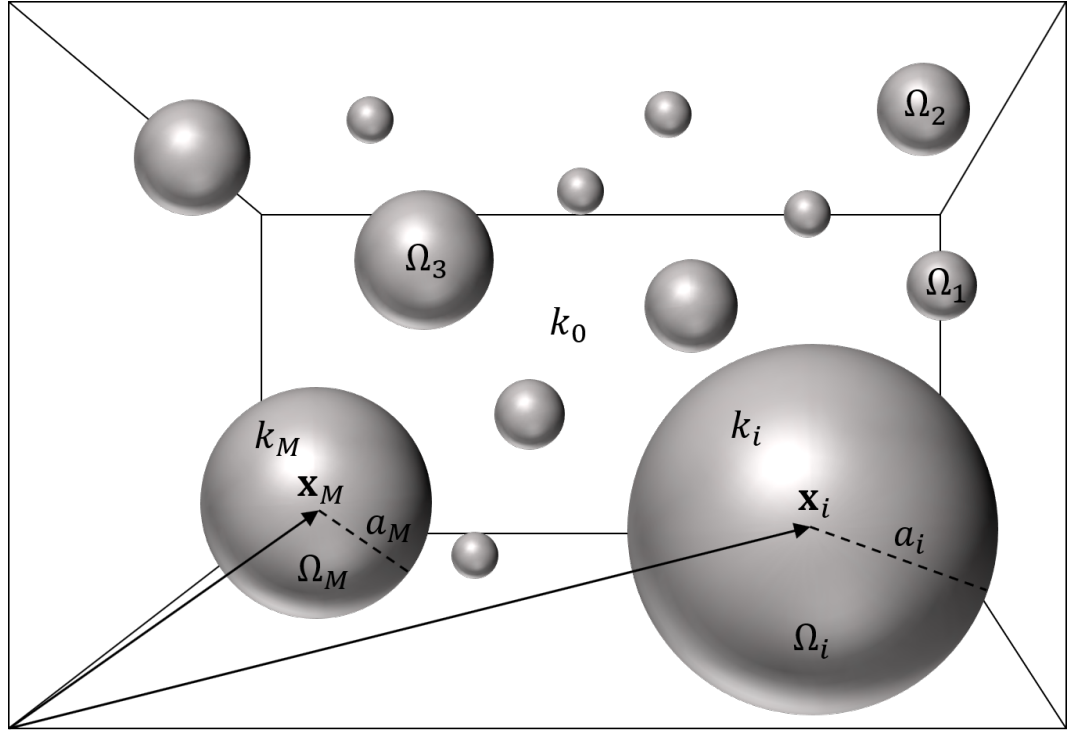


Figure 2.1: Geometric representation of the system comprised of M non-overlapping spherical particles $\Omega_1, \dots, \Omega_M$ with radius a_i , dielectric constant k_i , and centred at x_i , surrounded by a homogeneous medium of dielectric constant k_0 .

pendix A.1 for a precise mathematical description of these quantities).

To account for the point-charge contribution to the surface free charge, the free charge σ_f is split into two contributions

$$\sigma_f = \sigma_s + \sigma_p. \quad (2.1)$$

Here σ_s corresponds to the square-integrable part of the surface charge, whereas σ_p is the point-charge contribution to the free charge represented by a linear combination of n_p Dirac delta distributions δ per particle:

$$\sigma_p = \sum_{i=1}^M \sum_{j=1}^{n_{p,i}} q_{i,j} \delta_{\mathbf{z}_{i,j}}, \quad \text{where } \mathbf{z}_{i,j} \in \Gamma_i \text{ and for all } j = 1, \dots, n_{p,i}. \quad (2.2)$$

Next, we define an external potential Φ_{ext} with associated external electric field $\mathbf{E}_{\text{ext}} := -\nabla\Phi_{\text{ext}}$, and we do not impose the constraint that $\Phi_{\text{ext}}(\mathbf{x}) \rightarrow 0$ as $|\mathbf{x}| \rightarrow \infty$. We consider the external potential to be harmonic, i.e. $\Delta\Phi_{\text{ext}} = 0$,

so that we do not describe the charges creating the external field within the considered system but we do not restrict the external electric field \mathbf{E}_{ext} to be uniform. Finally, we assume that the system of dielectric particles does not affect the external field \mathbf{E}_{ext} , for instance, through polarisation, which justifies the use of our terminology external.

Our aim is to now to determine the net surface charge on each dielectric particle after taking into account both the free charge σ_f as well as the bound charges resulting from polarisation effects due to the presence of charged neighbouring particles and the effect of the external electric field. Using the net surface charge, we will be able to deduce the other physical quantities of interest, namely, the electrostatic forces and energy resulting from the interaction of the M charged dielectric spheres both with each other and with the external electric field.

In order to determine the net surface charge, we will first derive governing equations for the net electrostatic potential. As we shall see, the net electrostatic potential can be used to deduce the required net surface charge as well as the subsequent physical quantities of interest. The main challenges in achieving our aim are to work with the singular nature of the point-charges σ_p and the external potential Φ_{ext} which does not necessarily decay to zero at infinity.

2.1.2 Formulation of the problem based on a partial differential equation (PDE)

The problem of electrostatic interaction between M charged dielectric spheres can be described by a PDE-based transmission problem. Here, we define the total potential $\Phi_{\text{tot}} = \Phi_{\text{ext}} + \Phi$ and the corresponding total electric field $\mathbf{E}_{\text{tot}} := \mathbf{E}_{\text{ext}} + \mathbf{E}$, where \mathbf{E} is the perturbation of \mathbf{E}_{ext} due to the presence of the dielectric charged spheres, and Φ is the corresponding perturbation potential

so that $\mathbf{E} = -\nabla\Phi$. As in Section 1.2.2, standard arguments from the theory of electrostatics in dielectric media imply that the total potential Φ_{tot} satisfies the following conditions:

$$\Delta\Phi_{\text{tot}} = 0 \quad \text{in each } \Omega_i, \quad (2.3)$$

$$[[\Phi_{\text{tot}}]] = 0 \quad \text{on } \Gamma_0, \quad (2.4)$$

$$[[k\nabla\Phi_{\text{tot}}]] = \sigma_f \quad \text{on } \Gamma_0. \quad (2.5)$$

Here, Ω^+ denotes the space outside the particles, k is the dielectric function which takes value k_i on the ball $\bar{\Omega}_i$ and value k_0 on Ω^+ , and $[[\Phi_{\text{tot}}]]$ and $[[k\nabla\Phi_{\text{tot}}]]$ are jump discontinuities defined by

$$[[\Phi_{\text{tot}}]]|_{\Gamma_i}(\mathbf{z}) := \Phi_{\text{tot}}(\mathbf{z})|_{\Omega_i}\eta(\mathbf{z}) - \Phi_{\text{tot}}(\mathbf{z})|_{\Omega^+}\eta(\mathbf{z}), \quad (2.6)$$

$$[[k\nabla\Phi_{\text{tot}}]]|_{\Omega_i}(\mathbf{z}) := k_i\nabla\Phi_{\text{tot}}(\mathbf{z})|_{\Omega_i} \cdot \eta(\mathbf{z}) - k_0\nabla\Phi_{\text{tot}}(\mathbf{z})|_{\Omega^+} \cdot \eta(\mathbf{z}), \quad (2.7)$$

where $\eta(\mathbf{z})$ is the normal unit vector at $\mathbf{z} \in \Gamma_0$ pointing towards the exterior of the particles.

In general, Equations (2.3)-(2.5) are ill-posed as can be seen, for instance, by observing that if $\sigma_f \equiv 0$, then any constant function Φ_{tot} will satisfy this equation. In order to obtain the correct total potential Φ_{tot} , we make use of the relation $\Phi_{\text{tot}} = \Phi_{\text{ext}} + \Phi$ and first derive a well-posed equation for the electrostatic potential Φ . Using decomposition (2.1), elementary algebra yields

Φ that satisfies the following transmission problem

$$\Delta\Phi = 0 \quad \text{in each } \Omega_i, \quad (2.8)$$

$$[[\Phi]] = 0 \quad \text{on } \Gamma_0, \quad (2.9)$$

$$[[k\nabla\Phi]] = \sigma_s + \sigma_p - (k - k_0)\partial_n\Phi_{\text{ext}} \quad \text{on } \Gamma_0, \quad (2.10)$$

$$|\Phi| \rightarrow 0 \quad \text{as } |\mathbf{x}| \rightarrow \infty, \quad (2.11)$$

where $\partial_n\Phi_{\text{ext}}$ denotes the normal derivative of Φ_{ext} on the boundary Γ_0 . PDEs similar to the transmission problem (2.8)-(2.11) have been previously considered in the literature (see, e.g., [33, 34]), however the key novelty of Equations (2.8)-(2.11) is in the addition of contributions due to the external electric field and the presence of point-charges on the surface of the dielectric particles. These additional terms require a significant modification of the earlier definitions [34–36] of the electrostatic forces and interaction energy for the M -body charged dielectric spheres, and they present additional challenges in the efficient numerical implementation.

In addition to the presence of the highly non-regular point-charge term σ_p , another difficulty in solving the transmission problem (2.8)-(2.11) is the fact that the equation is posed on the entire space \mathbb{R}^3 . Indeed, since the potential Φ a priori decays only as $|\mathbf{x}|^{-1}$, a naive truncation of the computational domain in an effort to use classical algorithms such as the finite element method leads to significant errors. The usual approach to circumventing this problem is to appeal to the theory of integral equations and reformulate the transmission problem (2.8)-(2.11) as a so-called boundary integral equation (BIE) posed on the interface Γ_0 . This is the subject of the next subsection.

2.1.3 Formulation of the problem based on an integral equation

In order to describe the integral equation-based approach to the problem of electrostatic interaction between M charged dielectric spheres we require some additional notions. First, we define the single layer potential of σ , denoted $\mathcal{S}\sigma$, as the mapping with the property that

$$(\mathcal{S}\sigma)(\mathbf{x}) := \int_{\Gamma} \frac{\sigma(\mathbf{y})}{4\pi|\mathbf{x} - \mathbf{y}|} d\mathbf{y}, \quad \forall \mathbf{x} \in \Omega_0 \wedge \mathbf{x} \neq \mathbf{y}, \quad (2.12)$$

which also satisfies the following conditions

$$[[\mathcal{S}\sigma]] = 0; \quad [[\nabla\mathcal{S}\sigma]] = \sigma.$$

As a consequence, it is possible to consider the restriction of the single layer potential defined through Equation (2.12) on the boundary Γ and thereby define the so-called single layer boundary operator, denoted \mathcal{V} as the improper integral

$$(\mathcal{V}\sigma)(\mathbf{z}) := \int_{\Gamma} \frac{\sigma(\mathbf{z}')}{4\pi|\mathbf{z} - \mathbf{z}'|} d\mathbf{z}', \quad \forall \mathbf{z} \in \Gamma_0 \wedge \mathbf{z} \neq \mathbf{z}'.$$

Note, that occasionally it will be necessary to consider the “local” single layer potential and boundary operators defined on an individual sphere Ω_i . We will denote these as \mathcal{S}_i and \mathcal{V}_i respectively.

The surface electrostatic potential λ is now described by the following boundary integral equation:

$$\lambda - \mathcal{V} \left(\frac{k_0 - k}{k_0} \text{DtN}\lambda \right) = \frac{1}{k_0} \mathcal{V}(\sigma_s + \sigma_p) + \frac{k_0 - k}{k_0} \mathcal{V}(\partial_n \Phi_{\text{ext}}). \quad (2.13)$$

Here, the notation DtN is used to denote the local Dirichlet-to-Neumann (DtN)

map on the surface Γ (see Appendix A.1 for further details).

An equivalent reformulation of the BIE (2.13) for the induced surface charge can be achieved by applying \mathcal{V}^{-1} to both sides of the equation, and defining $\sigma := \mathcal{V}^{-1}\lambda$ which yields the following BIE

$$\sigma - \frac{k_0 - k}{k_0} \text{DtN}\mathcal{V}\sigma = \frac{1}{k_0}(\sigma_s + \sigma_p) + \frac{k_0 - k}{k_0}(\partial_n \Phi_{\text{ext}}). \quad (2.14)$$

In Equation (2.14), the quantity of interest σ , which we often call the induced surface charge, represents (up to a scaling factor) the total surface charge on each dielectric particle after taking into account both the free charge σ_f as well as the bound charges resulting from polarisation effects due to the presence of charged neighbouring particles and the effect of the external electric field.

More precisely,

- σ_f represents the free charge on each particle;
- $\sigma_b := (k_0 - k)(\text{DtN}\mathcal{V}\sigma + \partial_n \Phi_{\text{ext}})$ represents the bound charge on each particle;
- $k_0\sigma = \sigma_f + \sigma_b$ represents the total charge on each particle.

A simple manipulation of Equation (2.14) yields the following relation between the surface charge σ and the surface electrostatic potential λ :

$$\sigma = \frac{k_0 - k}{k_0} \text{DtN}\lambda + \frac{1}{k_0}(\sigma_s + \sigma_p) + \frac{k_0 - k}{k_0}(\partial_n \Phi_{\text{ext}}). \quad (2.15)$$

Equation (2.15) implies that once λ is known, the charge distribution σ can be computed using the purely local DtN map.

We also remark here that the relation between the PDE (2.8)-(2.11) and the BIE (2.13) representations of the electrostatic potential can be clearly established since λ is simply the restriction (more precisely the Dirichlet trace)

of the electrostatic potential Φ on the boundary Γ . Thus, for any point $\mathbf{x} \in \Omega$, we have $\Phi(\mathbf{x}) = (\mathcal{S}\mathcal{V}^{-1}\lambda)(\mathbf{x}) = (\mathcal{S}\sigma)(\mathbf{x})$, and we therefore also have $\Phi_{\text{tot}}(\mathbf{x}) = \Phi_{\text{ext}}(\mathbf{x}) + (\mathcal{S}\sigma)(\mathbf{x})$.

As emphasised above, an important technical difficulty in the analysis of Equation (2.13) is the presence of the low-regularity point-charge term σ_p , which requires special treatment in the design of efficient numerical methods. Previously, the BIE (2.13) has been the subject of extensive analysis in the much simpler case when both point-charges and the external field are absent, i.e., when $\sigma_p \equiv 0$ and $\Phi_{\text{ext}} \equiv 0$. We first briefly summarise the existing methodology and explain how the BIE (2.13) can be solved in this simple case before turning our attention to the more complex problem (Section 3) describing surface point-charges and an external electric field.

2.1.4 Existing methodology in the absence of surface point-charges and external fields

In the absence of the point-charge contribution to the surface free charge and an external electric field, the boundary integral Equation (2.13) reads as

$$\tilde{\lambda} - \mathcal{V} \left(\frac{\kappa_0 - \kappa}{\kappa_0} \text{DtN} \tilde{\lambda} \right) = \frac{1}{\kappa_0} \mathcal{V} \sigma_s. \quad (2.16)$$

Equation (2.16) is solved using a Galerkin discretisation with an approximation space constructed from the span of finite linear combinations of local spherical harmonics on each sphere Ω_i (exact definitions of the spherical harmonics and the approximation space W^N can be found in Appendix A.1). More precisely, the Galerkin discretisation of the integral Equation (2.16) reads as follows: let N be a fixed discretisation parameter, we seek the Galerkin solution $\tilde{\lambda}_N$ which

satisfies for all test functions ψ_N the equation

$$\left(\tilde{\lambda}_N - \mathcal{V} \left(\frac{\kappa_0 - \kappa}{\kappa_0} \text{DtN} \tilde{\lambda}_N \right), \psi_N \right)_{L^2(\Gamma)} = \frac{1}{\kappa_0} (\mathcal{V} \sigma_s, \psi_N)_{L^2(\Gamma)}. \quad (2.17)$$

The Galerkin solution $\tilde{\lambda}_N$ and the test function ψ_N can be expanded as a finite linear combination of basis functions. This ansatz allows us to reduce the Galerkin discretisation (2.16) to a linear system of equations for the unknown expansion coefficients of $\tilde{\lambda}_N$. More precisely, Equation (2.16) yields the linear system

$$\mathbf{A} \tilde{\boldsymbol{\lambda}} = \tilde{\boldsymbol{f}}, \quad (2.18)$$

where the solution matrix \mathbf{A} and the vector $\tilde{\boldsymbol{f}}$ are defined as

$$\begin{aligned} [\mathbf{A}_{ij}]_{\ell\ell'}^{mm'} &:= \left(\mathcal{Y}_{\ell'm'}^j - \mathcal{V} \left(\frac{\kappa_0 - \kappa}{\kappa_0} \text{DtN} \mathcal{Y}_{\ell'm'}^j \right), \mathcal{Y}_{\ell m}^i \right)_{L^2(\Gamma_i)}, \\ [\mathbf{f}_i]_{\ell}^m &:= \frac{1}{\kappa_0} (\mathcal{V} \sigma_s, \mathcal{Y}_{\ell m}^i)_{L^2(\Gamma_i)}, \end{aligned} \quad (2.19)$$

where $\mathcal{Y}_{\ell m}^i$ denotes the spherical harmonic of degree ℓ and order m on the sphere Ω_i and the indices $i, j \in \{1, \dots, M\}$, $\ell, \ell' \in \{0, \dots, N\}$ and $|m| \leq \ell$, $|m'| \leq \ell'$. A more detailed definition of $\mathcal{Y}_{\ell m}^i$ can be found in Appendix A.1.

A detailed explanation of how to compute the entries in the solution matrix \mathbf{A} and vector $\tilde{\boldsymbol{f}}$ can be found in Lindgren et al. [25]. Here, we simply remark that apart from the diagonal terms ($i = j$), computing the entries of the solution matrix requires evaluating a double integral on the unit sphere while computing the entries of the vector requires evaluating a single integral on the unit sphere. Both cases typically require the use of numerical quadrature, for which purpose Lebedev grid points are used.

It is also possible to use a modification of the classical Fast Multipole Method

(FMM) to speed up the computation of the vector $\tilde{\mathbf{f}}$ and matrix-vector products involving the dense solution matrix \mathbf{A} . Essentially, the FMM allows computing the action of the single layer boundary operator \mathcal{V} on an arbitrary element of the approximation space in linear scaling computational cost (with respect to M). In view of the fact that the DtN map is a purely local operator (and in fact diagonal in the basis of local spherical harmonics), the solution matrix \mathbf{A} does not need to be explicitly computed and stored, and its action on an arbitrary vector can be calculated in linear scaling cost. Further details on the FMM implementation can be found in [25, 36].

Once the vector $\tilde{\mathbf{f}}$ has been computed and the solution matrix \mathbf{A} set up, the linear system (2.18) can be solved using a Krylov subspace solver such as GMRES (see [35] for a detailed convergence analysis of GMRES as applied to this linear system). We can now turn our attention to the calculation of the discrete electrostatic energy and forces. Indeed, the approximate electrostatic interaction energy of the M -body system is given by

$$\tilde{U}_{\text{int}}^N := \frac{1}{2}(\sigma_s, \tilde{\lambda}_N)_{L^2(\Gamma)} - \frac{1}{2} \sum_{j=1}^M (\sigma_{s,j}, \tilde{\lambda}_N^{jj})_{L^2(\Gamma_j)}, \quad (2.20)$$

where $\sigma_{s,j} = \sigma_s|_{\Gamma_j}$ and $\tilde{\lambda}_N^{jj} \in W^N(\Gamma_j)$ is the approximate, so-called self-potential generated by the free charge $\sigma_{s,j}$ only on the sphere Γ_j in the absence of the other spheres. It is defined as the solution to the local Galerkin discretisation

$$\left(\tilde{\lambda}_N^{jj} - \mathcal{V}_j \text{DtN}_j \left(\frac{\kappa_0 - \kappa_j}{\kappa_0} \tilde{\lambda}_N^{jj} \right), \psi_N^{jj} \right)_{L^2(\Gamma_j)} = \left(\frac{1}{\kappa_0} \mathcal{V}_j \sigma_{s,j}, \psi_N^{jj} \right)_{L^2(\Gamma_j)}.$$

Consider Definition (2.20) of the electrostatic interaction energy. The first term in Equation (2.20) can be interpreted as the total electrostatic energy of the system whilst the second term, involving the summation, can be seen as the self energy.

Next, we derive an expression for the discrete electrostatic forces. As a first step, if $\tilde{\lambda}_N$ denotes the solution to the Galerkin discretisation (2.17) for a given free charge σ_s , then we define the approximate induced surface charge $\tilde{\sigma}_N$ as the unique element of the approximation space W^N (defined in Appendix A.1) that satisfies

$$(\mathcal{V}\tilde{\sigma}_N, \psi_N)_{L^2(\Gamma)} = (\tilde{\lambda}_N, \psi_N)_{L^2(\Gamma)}. \quad (2.21)$$

In other words, σ_N is simply an approximation of the exact induced surface charge σ , which we remind the reader physically represents the net charge on the dielectric spheres that includes polarisation effects. We will therefore use σ_N to derive an expression for the discrete electrostatic forces acting on the dielectric particles.

In practice, $\tilde{\sigma}_N$ is not determined using Equation (2.21), which requires the computationally expensive inversion of the single layer boundary operator \mathcal{V} . Instead, a careful examination of the Galerkin discretisation (2.17) reveals that $\tilde{\sigma}_N$ satisfies the relation (c.f., Equation (2.15))

$$\tilde{\sigma}_N = \frac{\kappa_0 - \kappa}{\kappa_0} \text{DtN} \tilde{\lambda}_N + \frac{1}{\kappa_0} \sigma_s^N, \quad (2.22)$$

where σ_s^N is the best approximation (in the L^2 -sense) of σ_s in the approximation space W^N . Consequently, once the linear system (2.18) has been solved, only purely local operations involving the Dirichlet-to-Neumann operator are required to obtain $\tilde{\sigma}_N$.

The discrete approximation to the electrostatic force acting on the dielectric particle is now given by

$$\mathbf{F}_i^N := \kappa_0 (\tilde{\sigma}_N, \mathbf{E}_{\text{exc}}^i)_{L^2(\Gamma_i)}. \quad (2.23)$$

Here, $\mathbf{E}_{\text{exc}}^i$ is the i -excluded electric field generated by the approximate induced surface charge σ_N , i.e., the vector field given by

$$\mathbf{E}_{\text{exc}}^i(\mathbf{x}) = -\nabla(\mathcal{S}\sigma_N)(\mathbf{x}) - \nabla(\mathcal{S}_i\sigma_{i,N})(\mathbf{x}), \quad (2.24)$$

where $\sigma_{i,N} := \sigma_N|_{\Gamma_i}$, and ∇ denotes the usual gradient taken with respect to Cartesian coordinates. The i -excluded electric field $\mathbf{E}_{\text{exc}}^i$ is the part of the total electric field generated by the approximate induced charge σ_N that interacts with (i.e., exerts a net electrostatic force on) the dielectric particle Ω_i .

Consider Definitions (2.20) and (2.23) of the discrete electrostatic interaction energy and forces respectively. A key result in [36, Supplementary material] establishes that these are related by the identity

$$-\nabla_{\mathbf{x}_i} U_{\text{int}}^N = \mathbf{F}_i^N,$$

where $\nabla_{\mathbf{x}_i}$ denotes the the gradient taken with respect to the location of the center \mathbf{x}_i of the sphere Ω_i .

The Galerkin nature of the method we have presented allows for a precise mathematical analysis in terms of accuracy with respect to N and complexity with respect to M as presented in the series of articles [34–36]. This model, however, is limited to the assumptions we made at the beginning of Section 2.1.4. In particular, it does not account for the presence of surface point-charges and the effect of an external electric field. This extension and generalisation is the subject of the following section.

2.1.5 Effects of an external electric field and surface point-charges

We now turn our attention to the boundary integral Equation (2.13), central to this study, which describes the electrostatic interaction of the dielectric spheres in the presence of both an external electric field and a point-charge contribution to the free charge residing on the particle surface.

Galerkin discretisation in the presence of point-charges and external fields

We define the external charge as $\sigma_{\text{ext}} := -(k - k_0)\partial_n \Phi_{\text{ext}}$, which is simply the external electric field contribution to the right-hand side of the BIE (2.13). The Galerkin discretisation of the integral equation (2.13) can be written as

$$\begin{aligned} & \left(\lambda_{\ell_{\max}} - \mathcal{V} \left(\frac{k_0 - k}{k_0} \text{DtN} \lambda_{\ell_{\max}} \right), \psi_{\ell_{\max}} \right)_{L^2(\Gamma_0)} \\ & = \frac{1}{k_0} (\mathcal{V}(\sigma_s + \sigma_{\text{ext}} + \sigma_p), \psi_{\ell_{\max}})_{L^2(\Gamma_0)}. \end{aligned} \quad (2.25)$$

As before, the Galerkin discretisation (2.25) yields a linear system of equations for the unknown local spherical harmonics expansion coefficients of $\lambda_{\ell_{\max}}$, and the resulting linear system reads as

$$\mathbf{A}\boldsymbol{\lambda} = \mathbf{f}, \quad (2.26)$$

where the solution matrix \mathbf{A} is defined precisely as before through Equation (2.19) and

$$[\boldsymbol{\lambda}_i]_{\ell}^m := (\lambda_{\ell_{\max}}, \mathcal{Y}_{\ell m}^i)_{L^2(\Gamma_i)}, \quad (2.27)$$

where $\ell \in \{0, \dots, \ell_{\max}\}$ and $|m| \leq \ell$. On the other hand, determining the new right-hand side vector \mathbf{f} requires some additional work due to the presence of the point-charge term σ_p .

To this end, let $\mathbf{z}_j \in \Gamma_j \subset \Gamma_0$ be fixed and consider the Dirac delta function $\delta_{\mathbf{z}_j}$. The definition of the single layer boundary operator \mathcal{V} implies that for any $q \in \mathbb{R}$ and all \mathbf{x} in Γ_0 with $\mathbf{x} \neq \mathbf{z}_j$ we have

$$\mathcal{V}(q\delta_{\mathbf{z}_j})(\mathbf{x}) = \int_{\Gamma_j} \frac{q\delta_{\mathbf{z}_j}(\mathbf{y})}{|\mathbf{x} - \mathbf{y}|} d\mathbf{y} = \frac{q}{|\mathbf{x} - \mathbf{z}_j|},$$

and hence,

$$\mathcal{V}(\sigma_p)(\mathbf{x}) = \sum_{j=1}^M \sum_{k=1}^{n_p^k} \frac{q_{j,k}}{|\mathbf{x} - \mathbf{z}_{j,k}|},$$

and therefore the right-hand side vector \mathbf{f} in Equation (2.26) can be defined as

$$[\mathbf{f}_i]_\ell^m := \frac{1}{k_0} (\mathcal{V}(\sigma_s + \sigma_{\text{ext}}) + \mathcal{V}(\sigma_p), \mathcal{Y}_{\ell m}^i)_{L^2(\Gamma_i)}. \quad (2.28)$$

Since the solution matrix \mathbf{A} is exactly as before (see Section 2.1.4), one can use the same linear solver routine to approximate the solution to Equation (2.26). Having solved the underlying linear system, we can now turn our attention to computing other (discrete) physical quantities of interest.

2.1.6 Energy and forces in the presence of external fields and point charges.

The approximate total electrostatic interaction energy of the system is given by

$$\begin{aligned} U_{\text{int}}^N &:= \frac{1}{2} (\sigma_s + \sigma_p + \sigma_{\text{ext}}, \lambda_N)_{L^2(\Gamma)} + (\sigma_s + \sigma_p, \lambda_{\text{ext}}^N)_{L^2(\Gamma)} \\ &\quad + \frac{1}{2} (\sigma_{\text{ext}}, \lambda_{\text{ext}}^N)_{L^2(\Gamma)} - \frac{1}{2} \sum_{j=1}^M (\sigma_{s,j} + \sigma_{p,j}, \lambda_N^{j,j})_{L^2(\Gamma_j)}, \end{aligned} \quad (2.29)$$

where we denote $\sigma_{s,j} = \sigma_s|_{\Gamma_j}$, $\sigma_{p,j} := \sigma_p|_{\Gamma_j}$, and we write λ_{ext}^N for the best approximation of $\lambda_{\text{ext}} := \Phi_{\text{ext}}|_{\Gamma}$ and $\lambda_N^{j,j} \in W^N(\Gamma_j)$ for the approximate self-potential only on the sphere Γ_j in the absence of the external field \mathbf{E}_{ext} and all

other spheres, which is formally defined as the solution to the local Galerkin discretisation

$$\begin{aligned} & \left(\lambda_N^{jj} - \mathcal{V}_j \text{DtN}_j \left(\frac{k_0 - k_j}{k_0} \lambda_N^{jj} \right), \psi_N^{jj} \right)_{L^2(\Gamma_j)} \\ & = \left(\frac{1}{k_0} (\mathcal{V}_j \sigma_{s,j} + \sigma_{p,j}), \psi_N^{jj} \right)_{L^2(\Gamma_j)}. \end{aligned}$$

It is important to emphasise that total electrostatic interaction energy we define here through Equation (2.29) includes both the energy due to the interaction between the dielectric particles themselves as well as the energy arising from the interaction of the particles with the external electric field.

Consider again the formal definition (2.29) of the electrostatic interaction energy. The combination of the first three terms in Equation (2.29) can be interpreted as the total electrostatic energy of the system whilst the fourth term, involving the summation can be seen as the self electrostatic energy of the system. We emphasise that, due to the presence of the point-charge contribution σ_p , both the total energy and the self-energies are infinite as in the case of fixed Coulomb point-charges. However, when writing the interaction energy as

$$\begin{aligned} U_{\text{int}}^N & := \frac{1}{2} \sum_{j=1}^M (\sigma_{s,j} + \sigma_{p,j}, \lambda_N - \lambda_N^{jj})_{L^2(\Gamma_j)} + \frac{1}{2} (\sigma_{\text{ext}}, \lambda_N)_{L^2(\Gamma)} \\ & + (\sigma_s + \sigma_p, \lambda_{\text{ext}}^N)_{L^2(\Gamma)} + \frac{1}{2} (\sigma_{\text{ext}}, \lambda_{\text{ext}}^N)_{L^2(\Gamma)}, \end{aligned}$$

each of the terms is finite and thus the interaction energy is a well-defined quantity.

It is possible to rewrite Equation (2.29) for the electrostatic interaction energy in a more physically intuitive form in terms of the electric fields that appear in the PDE formulations (2.3)-(2.5) and (2.8)-(2.11) leading to the following.

Let λ_{ext} denote the restriction of Φ_{ext} on Γ , and let λ denote the solution to the boundary integral Equation (2.13) for a given free charge $\sigma_f = \sigma_s + \sigma_p$ and external electric field \mathbf{E}_{ext} . Then for any open ball \mathbb{B}_a of radius $a > 0$ which is large enough to contain Ω^- , the exact electrostatic interaction energy of the system, denoted U_{int} , satisfies the relation

$$\begin{aligned}
 U_{\text{int}} &:= \frac{1}{2}(\sigma_s + \sigma_p + \sigma_{\text{ext}}, \lambda)_{L^2(\Gamma)} + (\sigma_s + \sigma_p, \lambda_{\text{ext}})_{L^2(\Gamma)} \\
 &\quad + \frac{1}{2}(\sigma_{\text{ext}}, \lambda_{\text{ext}})_{L^2(\Gamma)} - \frac{1}{2} \sum_{j=1}^M (\sigma_{s,j} + \sigma_{p,j}, \lambda^{jj})_{L^2(\Gamma_j)} \quad (2.30) \\
 &= \frac{1}{2} \int_{\mathbb{B}_a} k(\mathbf{x}) \mathbf{E}_{\text{tot}}(\mathbf{x}) \cdot \mathbf{E}_{\text{tot}}(\mathbf{x}) \, d\mathbf{x} - \frac{1}{2} \sum_{j=1}^M \int_{\mathbb{B}_a} k(\mathbf{x}) \mathbf{E}^{jj}(\mathbf{x}) \cdot \mathbf{E}^{jj}(\mathbf{x}) \, d\mathbf{x} \\
 &\quad - \frac{1}{2} \int_{\mathbb{B}_a} k_0 \mathbf{E}_{\text{ext}}(\mathbf{x}) \cdot \mathbf{E}_{\text{ext}}(\mathbf{x}) \, d\mathbf{x} - \int_{\partial\mathbb{B}_a} k_0 \partial_n \Phi(\mathbf{x}) \Phi_{\text{ext}}(\mathbf{x}) \, d\mathbf{x} \\
 &\quad - \frac{1}{2} \int_{\partial\mathbb{B}_a} k_0 \left(\partial_n \Phi(\mathbf{x}) \Phi(\mathbf{x}) - \sum_{j=1}^M \partial_n \Phi^{jj}(\mathbf{x}) \Phi^{jj}(\mathbf{x}) \right) \, d\mathbf{x}. \quad (2.31)
 \end{aligned}$$

Here, λ^{jj} is the exact self-potential only on the sphere Γ_j in the absence of the external field \mathbf{E}_{ext} and all other spheres, and it is defined as the solution to the local BIE

$$\lambda^{jj} - \mathcal{V}_j \text{DtN}_j \left(\frac{k_0 - k_j}{k_0} \lambda^{jj} \right) = \frac{1}{k_0} (\mathcal{V}_j \sigma_{s,j} + \sigma_{p,j}),$$

and \mathbf{E}^{jj} is the “self electric field” of the j -th dielectric particle, i.e., the electric field produced only due to the sphere Γ_j in the absence of both the external field \mathbf{E}_{ext} as well as the other spheres.

The five terms in Equation (2.31) which constitute U_{int} all have physical interpretations. Indeed, the first integral can be seen as the total electrostatic energy associated with the electric field \mathbf{E}_{tot} , and the second integral can be interpreted as the self-energy associated with the free charge $\sigma_f = \sigma_s + \sigma_p$ on the particle surface. The third term is the self energy of the external electric

field \mathbf{E}_{ext} . Finally, the last two terms can be interpreted as the boundary terms that, in general, may not vanish if one takes the limit $a \rightarrow \infty$ but yield an expression independent of a and accounts for the arbitrary choice of a .

Essentially, the above theorem establishes that in the exact case, i.e., when we take the discretisation parameter $N \rightarrow \infty$, the definition of the interaction energy derived from the integral equation formalism and given by Equation (2.29) coincides with the definition of the interaction energy (up to some additional boundary terms) in any open ball \mathbb{B}_a that is large enough to contain Ω^- as derived from the PDE picture and given through Equation (2.31).

Next, we turn our attention to the discrete electrostatic forces. To this end, if λ_N denotes the solution to the Galerkin discretisation (2.25) for a given free charge $\sigma_f = \sigma_s + \sigma_p$ and external electric field \mathbf{E}_{ext} , then we define the approximate induced surface charge σ_N that generates the surface electrostatic potential λ_N as

$$(\mathcal{V}\sigma_N, \psi_N)_{L^2(\Gamma)} = (\lambda_N, \psi_N)_{L^2(\Gamma)}. \quad (2.32)$$

In practice, σ_N can be determined again using the following relation (c.f., Equation (2.22)), which can be deduced from the Galerkin discretisation (2.25):

$$\sigma_N = \frac{k_0 - k}{k_0} \text{DtN}\lambda_N + \frac{1}{k_0} (\sigma_s^N + \sigma_p^N + \sigma_{\text{ext}}^N), \quad (2.33)$$

where σ_s^N, σ_p^N , and σ_{ext}^N are the best approximations or projections (in the L^2 -sense) of σ_s, σ_p , and σ_{ext} in the approximation space W^N defined in Appendix A.1. The approximate net electrostatic force acting on the dielectric particle described by the open ball Ω_i is now given by

$$\mathbf{F}_i^N := k_0 (\sigma_N, \mathbf{E}_{\text{exc}}^i + \mathbf{E}_{\text{ext}})_{L^2(\Gamma_i)}. \quad (2.34)$$

Consider Definitions (2.29) and (2.34) of the discrete electrostatic interaction energy and forces respectively. As before in Section 2.1.4, it is possible to demonstrate that the electrostatic forces are indeed realised as the negative sphere-centered gradients of the interaction energy. Indeed, we have the following theorem.

Let U_{int}^N denote the discrete interaction energy and \mathbf{F}_i^N , denote the discrete electrostatic force acting on the dielectric particle Ω_i as given by Definitions (2.30) and (2.34) respectively. Then it holds that

$$-\nabla_{\mathbf{x}_i} U_{\text{int}}^N = \mathbf{F}_i^N, \quad (2.35)$$

where $\nabla_{\mathbf{x}_i}$ denotes the the gradient taken with respect to the location of the center \mathbf{x}_i of the sphere Γ_i .

2.2 Molecular dynamics

In this work, the electrostatic solution presented in the previous section has been implemented as the force field for molecular dynamics simulations. The Verlet method was used to integrate Newton's equations of motion in this work over the Euler method previously used in Lindgren et al. [26] due to its second order accuracy. The use of dynamic simulations allows for the identification of features within a system that can better help to gain a qualitative understanding of processes involved with self-assembly mechanisms. In order to avoid any accumulated errors, timestep sizes were kept small relative to overall simulation times, with all simulations having at least 40000 timesteps per simulation—enough for the time-frame to cover the desired observations. The computational routine also included a collision handler to ensure that particles did not overlap. A coefficient of restitution C_R is incorporated into the equations of motion in order to facilitate the self-assembly behaviour; it is included such that linear momentum is conserved, but some portion of the kinetic energy is lost to the system. C_R is defined as:

$$C_R = \frac{\text{relative speed post-collision}}{\text{relative speed pre-collision}}$$

The velocities of the particles in all systems simulated are negligible in comparison with the speed of light c so the magnetic component to the total electromagnetic interactions have been ignored. The systems modelled using dynamic simulations are mesoscale, therefore there are no considerations of the system constituting a canonical (NVT) ensemble through the assignment of a temperature; this was justified by the fact that in these simulations, in the interactions between the charged particles $U \gg k_B T$ where k_B is the Boltzmann constant and T is a temperature. All simulations were performed in the absence of any external forces (i.e. gravity, drag, etc.).

Chapter 3

General numerical results

In this chapter, fundamental aspects of the model are tested, displaying the trends that we see throughout the work in this thesis. New implementations (non-homogeneous charge densities and external electric fields) are tested to ensure correct implementation, and robustness of the model.

3.1 Interactions between pairs of like-charged particles

The electrostatic interaction between two like-charged dielectric particles in a vacuum over a range of separations can be generalised into two main contributions; the repulsive interaction which dominates at longer ranges, and the attractive interactions which have the biggest effect on the electrostatic nature at short separation. The magnitude of the attractive interactions between two like-charged polarisable spheres is dependent upon four major variables: the ratio of the sizes of the two spheres, a_1/a_2 ; the ratio of the charges in the spheres, q_1/q_2 ; the separation between the surfaces of the two spheres, s ; and the dielectric constants of the spheres, k_i . The attraction between two like-charged spheres when one sphere has a larger surface charge density than the other occurs due to the mutual polarisation causing a redistribution of surface charge densities sufficiently large enough to create regions of opposite

charge on the sphere with a lower surface charge density, inducing an attractive interaction. The magnitude of the repulsive interaction is dependent only on the charges (q_1 and q_2) and centre-to-centre separation, $h = a_1 + a_2 + s$.

Here, the preferred size and charge ratios that lead to attraction between like-charged dielectric spheres are explored. The surface charge density of one of the spheres will be altered in two different ways. The first is by increasing the size of one of the spheres, and the other is by increasing the charge of one of the spheres. Figure 3.1 shows the calculated electrostatic force between two dielectric particles with a dielectric constant k_i of 20. The charges of both spheres ($q_{1,2} = 1e$) and the radius of sphere 1 ($a_1 = 1$ nm) in all plots are kept consistent, with the only variable between the plots being the radius of sphere 2. The plot where $a_1 = a_2$ (solid) shows a purely repulsive force with no attractive regime due to symmetric nature of the interaction. The dashed and dotted plots in Figure 3.1 show an increase in the attractive contribution at short separation as the size of a_2 increases. This is due to the asymmetry of the two spheres increasing which causes the surface charge density on the larger sphere to reduce, making it much more susceptible to polarisation. The stability of the system at zero separation can be determined from plots present on the electrostatic interaction energy graph in Figure 3.2. These three plots relate to the same three systems in Figure 3.1 but show how increasing asymmetry of the system affects the total energy of the system at the point of contact.

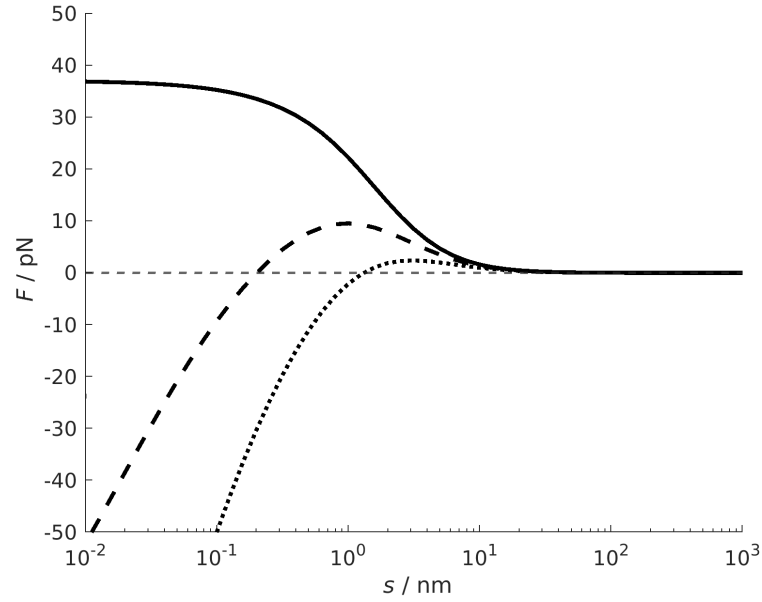


Figure 3.1: F as a function of s for the interaction between two dielectric particles with $a_1 = 1$ nm, $q_{1,2} = 1e$, $k_i = 20$ and $k_0 = 1$. $a_2 = 1$ nm (solid), 2 nm (dashed) and 5 nm (dotted).

Unstable (solid) – No attraction, always separates.

Metastable (dashed) – There is a local minimum at the point of contact.

Stable (dotted) – This is where the energy of the system at the point of contact is more energetically favourable than the separated system.

Unlike increasing a_2 , which only increases the magnitude of the attractive contribution to the force, increasing the charge of q_2 increases both the attractive multipolar contribution—due to the increase in polarisation from the increased charge density—and also the repulsive contribution to the electrostatic force ($q_1 q_2 / h^2$). These effects lead to similar overall results when compared to the varying particle size results, although the increased repulsion leads to a much larger energy barrier for the particles to come together, as shown in Figure 3.3.

The nature of the electrostatic force between two dielectric spheres over a range of combinations of size and charge ratios at a fixed dielectric constant and separation is presented in Figure 3.4. The figure presents a contour plot of a series of calculations for the force as a function of both a_2/a_1 , from 0.1 to

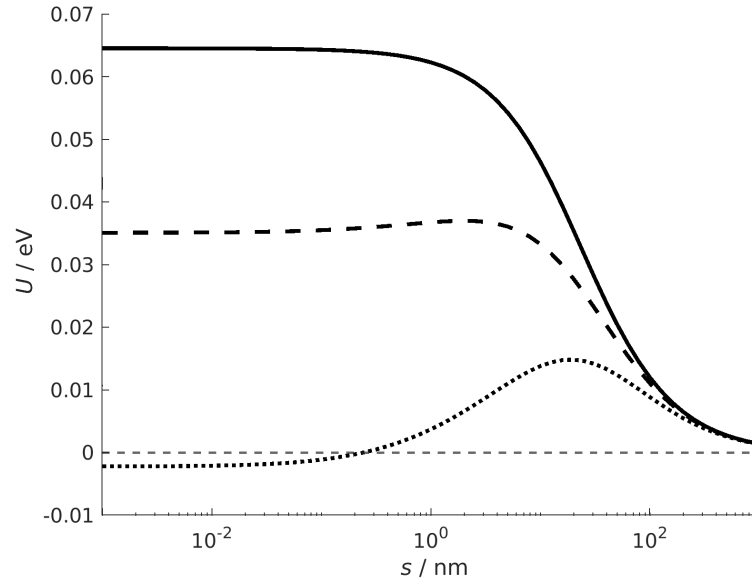


Figure 3.2: U as a function of s for the interaction between two dielectric particles with $a_1 = 1$ nm, $q_{1,2} = 1e$, $k_i = 20$ and $k_0 = 1$. $a_2 = 1$ nm (solid), 2 nm (dashed) and 5 nm (dotted).

10, and q_2/q_1 , from 0 to 10.

The nature of the interaction is determined by the colour of the area on the plot, with the redder areas signifying an attractive interaction between spheres, whereas the bluer areas represent configurations with a repulsive interaction.

The plot can be roughly split into three major zones:

i) The light red area which covers the majority of the top half of Figure 3.4 where $a_2 \gg a_1$. This area is only lightly attractive, with interaction forces between 0 pN and -100 pN, and accounts for the configurations where both a_2 and q_2 are both much larger than a_1 and q_1 respectively. This light attraction is present as the surface charge density on the sphere 1 is still sufficiently high in comparison to the surface charge density on sphere 2 to induce polarisation, even when the total charge on sphere 2 approach 10 times that of the charge of sphere 1.

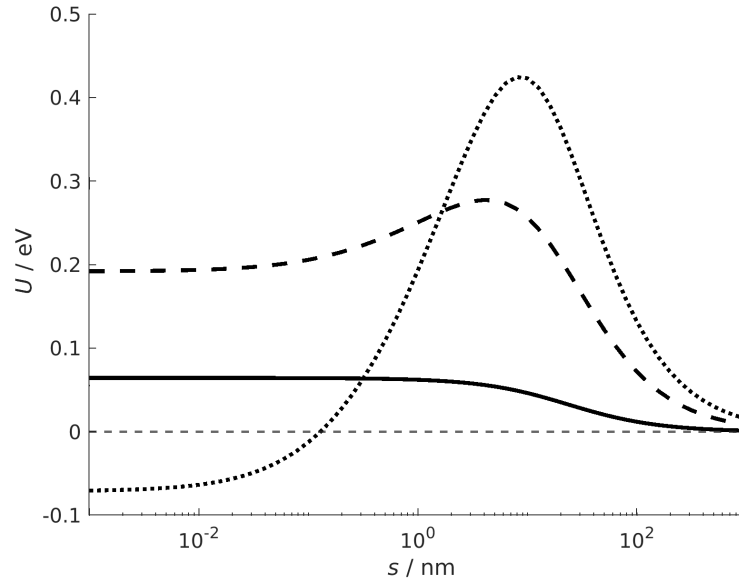


Figure 3.3: U as a function of s for the interaction between two dielectric particles with $a_{1,2} = 1$ nm, $q_1 = 1e$, $k_i = 20$ and $k_0 = 1$. $q_2 = 1e$ (solid), $2e$ (dashed) and $5e$ (dotted).

ii) The blue region which covers the majority of the middle portion of the plot where $a_2 \approx a_1$. In this area, the surface charge density of the two spheres are similar and therefore the magnitude of the polarisation contribution begins to diminish, leaving the contribution due to Coulomb repulsion as the dominant component of the net force.

iii) The final region is the darker red region positioned below region (ii) where a_2 is similar in size to or smaller than a_1 , and has a much bigger total charge, q_2 , in comparison. The configurations within this region represent a strong attractive interaction ($F < -500$ pN) between the spheres, with the very high surface charge density on sphere 2 causing the polarisation effects to dominate the nature of the interaction between the sphere.

The combinations of radius and charge ratios in region (iii) are the configurations which tend to lead to the biggest magnitude for the attractive terms and thus show the most preferred combinations for strong attraction.

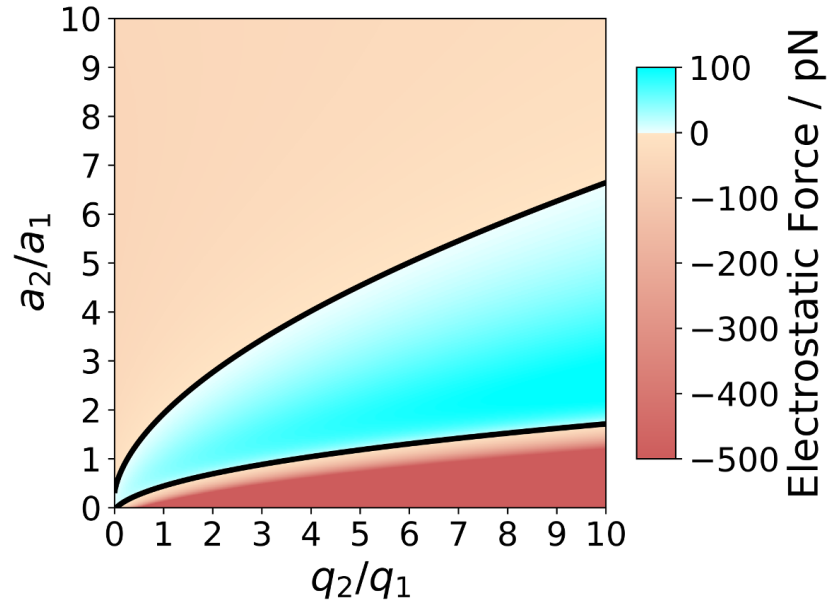


Figure 3.4: A contour plot showing the electrostatic force (in pN) between a pair of like-charged spheres, with dielectric constants $k_1 = k_2 = 10$. The force is plotted as a function of size ratio a_2/a_1 and the charge ratio q_2/q_1 , with $s = 0.1$ nm, $a_1 = 1$ nm and $q_1 = 1e$. The regions of attraction are displayed as in red whereas the regions with repulsive forces are represented in blue.

The nature of the electrostatic interaction between two like-charged dielectric spheres at a specific surface-to-surface separation, s , is predominantly governed by the size of the spheres in relation to their separation. This effect that system geometry has on the interactions between like-charged particles was explored in 2014 [20]; the paper proposes that a dimensionless geometric parameter, s^* , can be calculated to give a good idea to the nature of the electrostatic interactions

$$s^* \equiv \frac{s}{2a}, \quad (3.1)$$

where s is the surface-to-surface separation of the spheres and $2a$ is the distance between two inverse points in a bispherical coordinate system [37].

From this, we can deduce that if the separation s becomes much bigger than the radii of the spheres, $s^* \rightarrow 1$ and the interactions within the system begin to start behaving like the interactions present between point charges, where the monopolar terms dominate the sphere-to-sphere interactions; conversely,

when the separation of the spheres becomes much smaller than the radii of the spheres, $s^* \rightarrow 0$, with the system tending to behave like two charged planes or two large spheres in close proximity, where the multipolar terms have a huge contribution to the overall interaction. Figure 3.5 shows a visual representation of the physical nature of the interactions between spheres as a function of s^* .

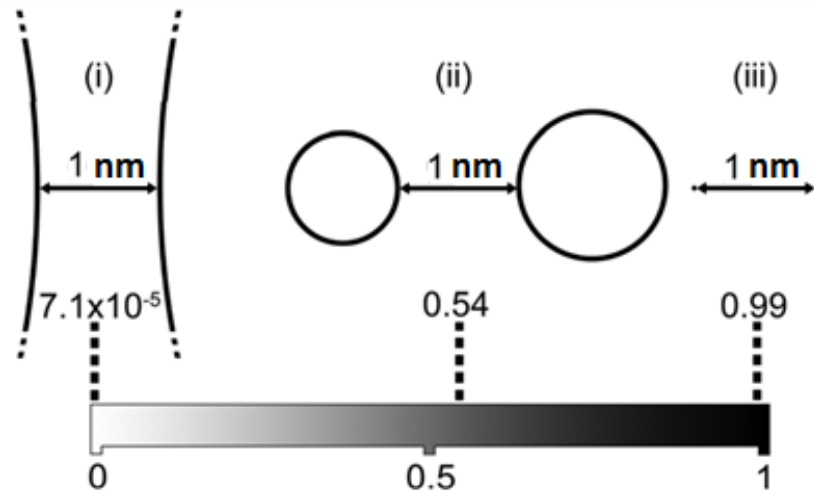


Figure 3.5: A geometric representation of various two sphere systems between s^* values of 0 and 1, separated by 1 nm. The radii of the spheres in the examples are: (i) $a_1 = a_2 = 5$ cm, (ii) $a_1 = 0.5$ nm and $a_2 = 0.75$ nm, and (iii) $a_1 = a_2 = 5$ pm. The range of values of s^* from 0 to 1 corresponds to a continuum of the values for all possible combinations of sphere size and separation distances.

Figure 3.6 is a contour plot showing the electrostatic force (in pN) between a pair of equal-sized ($a_1 = a_2 = 1$ nm), like-charged dielectric spheres, with dielectric constants ($k_1 = k_2 = 20$). The force is plotted as a function of the scaled surface-to-surface separation (s^*) and the charge ratio (q_2/q_1) with the interactions always being positive at larger separation. The plot shows that as the charge ratio increases, the larger the separation can be in order for the polarisation terms to still be the dominant factors in the force equation.

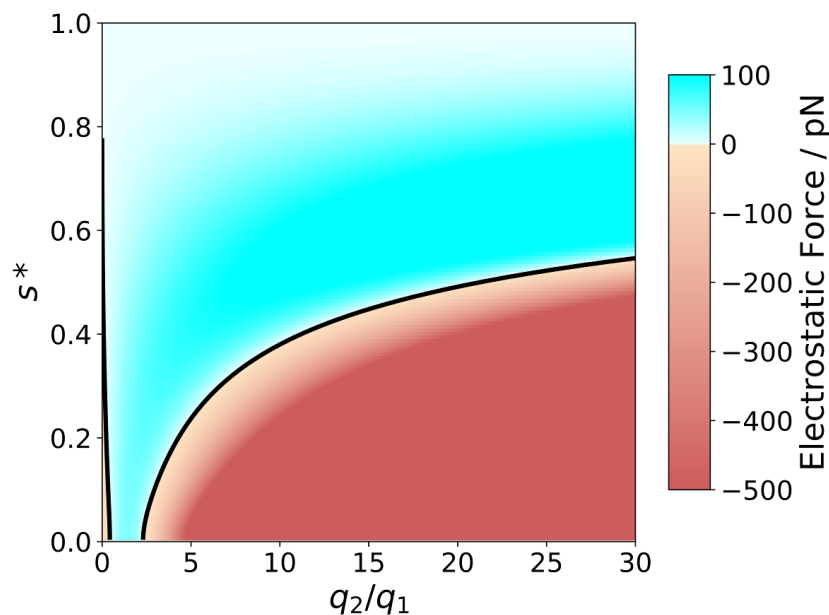


Figure 3.6: A contour plot showing the electrostatic force (in pN) between a pair of equal-sized, like-charged spheres, with dielectric constants $k_1 = k_2 = 20$. The force is plotted as a function of the scaled surface-to-surface separation s^* and the charge ratio q_2/q_1 , with $a_1 = a_2 = 1$ nm and $q_1 = 1e$. The regions of attraction are displayed in red whereas the regions with repulsive forces are represented in blue.

The dielectric constant k is defined as the permittivity of the material ε relative to permittivity of a vacuum $\varepsilon_0 = 8.854\,187\,817\,6 \times 10^{-12}$ F m $^{-1}$

$$k = \frac{\varepsilon}{\varepsilon_0}.$$

This value is generally governed by the polarity of the molecule, for example, the large dipole moment in the O-H bonds of water cause the molecule to be sizeably polarisable, leading to an overall bulk dielectric constant k_i of 80, whereas a non-polar molecule such as benzene, which essentially has no overall dipole moment has a dielectric constant of just 2.3. A slight issue with using the dielectric constant, is that the value represents the extent that a bulk material concentrates electric flux, which loses significance when scaling down away from bulk to the level of nanoclusters, although the value can be used as a parameter that suggests the overall polarisability of the cluster.

The size of the dielectric constant of a molecule has a significant effect on the magnitude of the polarisation of dielectric spheres in this study, with materials that have higher dielectric constants being more susceptible to polarisation, inducing a greater contribution to the attractive force caused by the multipole coefficient terms.

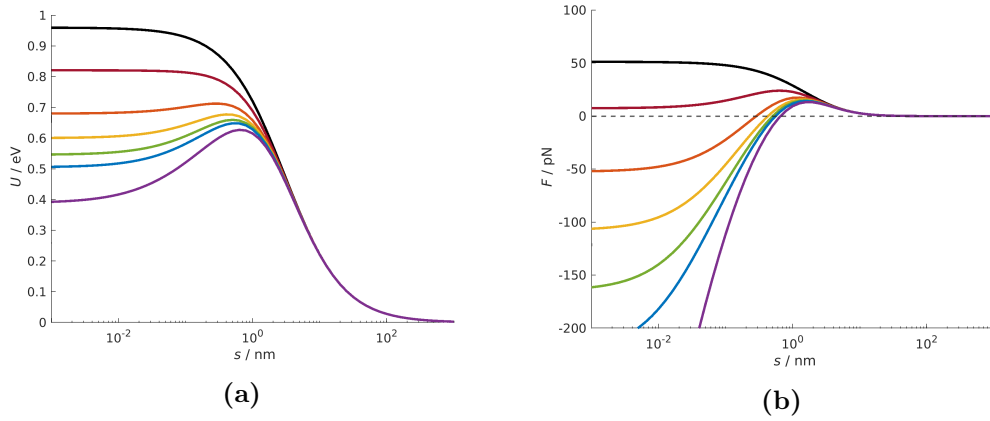


Figure 3.7: The interaction in a vacuum ($k_0 = 1$) between two particles with varying dielectric constants. Shown are (a) U and (b) F between a pair of charged dielectric particles: $q_1 = 1e$, $q_2 = 2e$, $a_1 = 0.63$ nm, $a_2 = 0.84$ nm, with dielectric constants $k_i = 1.1, 2, 4, 6, 8, 10, 20$ represented by black, red, orange, yellow, green, blue and purple respectively.

This relationship can be seen in Figure 3.7 with a clear relationship being shown between the magnitude of the dielectric constant and the polarisability of the sphere. This is evident as on the $k_i = 1.1$ plot which looks very similar to interaction between point charges due to the low dielectric constant leading to a negligible contribution from polarisation effects. Increasing values of k_i lead to more attractive/less repulsive plots as a whole.

The lack of polarisation of the surface charged density, even at very short separation due to a low dielectric constant can be seen in Figure 3.8 which shows the charge density distributions at a separation of 0.1 nm for a range of dielectric constants.

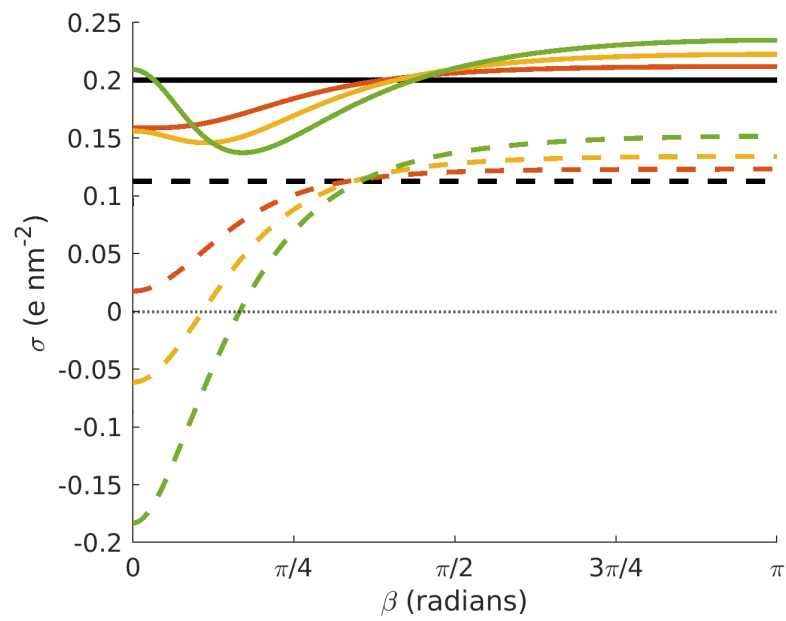


Figure 3.8: Charge density σ as a function of sweeping angle for two equally charged spheres at a separation of 0.1 nm. The solid lines indicate the values of σ for particle 1, with the dashed line indicating the values for particle 2. $k_i = 1$ (black), 2 (orange), 4 (yellow), 8 (green), $a_1 = 0.63$ nm, $a_2 = 0.84$ nm, $q_1 = q_2 = 1.0$ e. On each particle $\beta = 0$ is the point on the surface of the particle closest to the other sphere.

3.2 Non-Uniform Charge Distributions

In its lowest energy form, the free charge of a particle q is spread over the surface of the particle to give a uniform free charge density σ_s in the form

$$\sigma_s = \frac{q}{4\pi a^2}. \quad (3.2)$$

Despite this, there are many situations where a uniform distribution is an unsuitable representation of a charged system; here we introduce the application of non-uniform surface charge densities to the particles in the forms of both point charge distributions and Gaussian distributions.

The point charge distribution is a many-body generalisation of the two-body solution introduced in 2019 by Filippov et al. [23] and is used to replicate the kinetic energy release values from that paper. The model is also verified against Coulomb's law to test the basic accuracy of the implementation.

The Gaussian distribution is tested using both standard and higher order distributions to find the limit of the standard deviation of the distribution, and then a small width Gaussian is also used as an approximate representation of a point charge and tested against the point charge solution.

3.2.1 Gaussian Distribution

If charge is localised to a specific region of the surface, the distribution is no longer uniform. In cases like this, functions such as Gaussian distributions can be used to describe the shape and magnitude of the charge density distribution.

In 1 dimension, a Gaussian distribution $f(x)$ is

$$f(x) = \frac{1}{\tau_x \sqrt{2\pi}} \exp\left(-\frac{1}{2} \frac{(x - \mu_x)^2}{\tau_x^2}\right) \quad (3.3)$$

where τ in this section is the standard deviation (usually denoted by σ) and μ is the expected value [38]. When placing a Gaussian on a surface, the distribution becomes elliptical and the product of two individual 1-dimensional Gaussians ($P(x, y) = P(x)P(y)$), each with their own individual expected values (μ_x, μ_y) and standard deviations (τ_x, τ_y).

$$f(x, y) = \frac{1}{\tau_x \sqrt{2\pi}} \exp\left(-\frac{1}{2} \frac{(x - \mu_x)^2}{\tau_x^2}\right) \frac{1}{\tau_y \sqrt{2\pi}} \exp\left(-\frac{1}{2} \frac{(y - \mu_y)^2}{\tau_y^2}\right). \quad (3.4)$$

If $\tau = \tau_x = \tau_y$, the distribution gains circular symmetry. When this is the case, the distribution can be simplified to

$$f(d) = \frac{1}{2\pi\tau^2} \exp\left(-\frac{d^2}{\tau^2}\right) \quad (3.5)$$

where d is the distance from the expected coordinate (μ_x, μ_y) .

To transform this normalised distribution into a Gaussian surface charge density distribution σ_g , the distribution is scaled by the total charge q_g of the distribution.

$$\sigma_{g,i}(d) = \frac{q_g}{2\pi\tau^2} \exp\left(-\frac{d^2}{\tau^2}\right) \quad \text{on } \Gamma_i. \quad (3.6)$$

For a particle i with $n_{g,i}$ Gaussian distributions, the surface charge density at a point on the surface $\sigma_{g,i}(\mathbf{z})$ due to multiple Gaussian distributions is

$$\sigma_{g,i}(\mathbf{z}) = \sum_{k=1}^{n_{g,i}} \frac{q_{g,k}}{2\pi\tau_k^2} \exp\left(-\frac{d_k^2}{\tau_k^2}\right) \quad \text{on } \Gamma_i. \quad (3.7)$$

where $d_k = |\mathbf{z} - \boldsymbol{\mu}_k|$, where $\boldsymbol{\mu}_k = (\mu_{x,k}, \mu_{y,k})$.

The shape of the Gaussian distribution can be adjusted by using a modified version of the Gaussian in the form

$$f(d) = \frac{1}{2\pi\tau^2} \exp\left(-\left(\frac{d^2}{\tau^2}\right)^P\right), \quad (3.8)$$

where $P = 1$ for standard Gaussians, and increasing P leads to an increasingly more flat-topped Gaussian distribution [39]. When $P \neq 1$, the integral of the distribution deviates from the normalised value, and therefore the distribution needs to be corrected by dividing $f(x, y)$ by its own surface integral $\iint_s f(x, y) dS$. The effect of increasing P is shown clearly in Figure 3.9.

As the Gaussian function is designed for flat surfaces, rather than spherical surfaces, the solution can only be solved within the diameter of the sphere ($0 \leq d \leq 2a$). In order to ensure that all of q_g is being placed on the particle, it is important to make sure that $f(d)$ is negligible at $d = 2a$, otherwise, the amount of charge present on the particle will not equal the charge expected by the integral of the Gaussian function. Placing a Gaussian distribution designed for a flat 2D surface on a sphere also leads to deviations from the expected value due to the curved nature of the surface, although this effect is negligible for distributions with widths smaller than the particle's radius.

As τ increases, the distribution become wider, and the value for σ at $f(2a)$

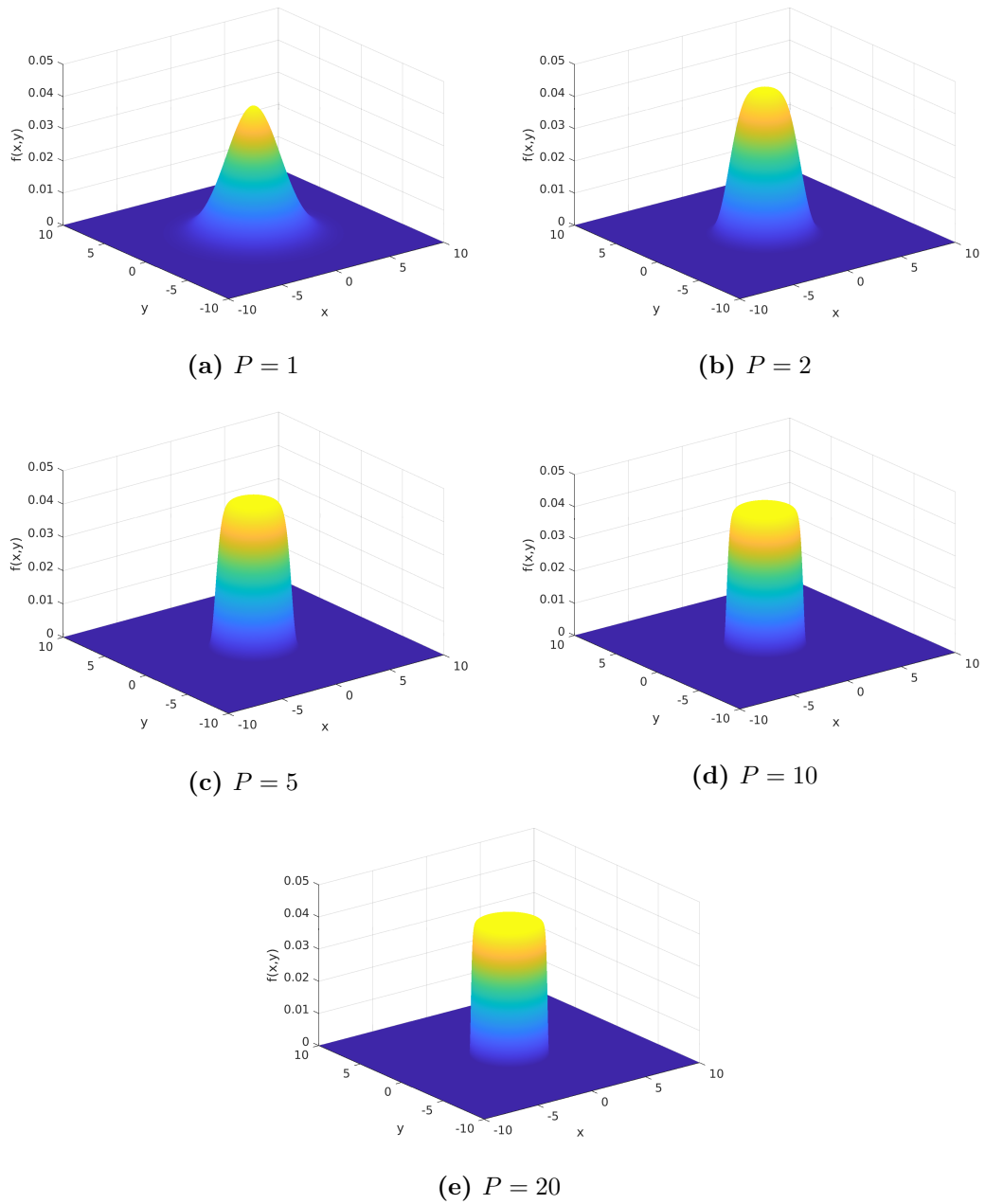


Figure 3.9: Higher order Gaussian distributions using Equation (3.8) where $\tau = 1$ and $(\mu_x, \mu_y) = (0, 0)$ for a range of P values.

becomes more significant, up until a point where it is no longer negligible, as in Figure 3.10b. This distribution has a large value where $\beta = \pm 180^\circ$ —the point where $d = 2a$.

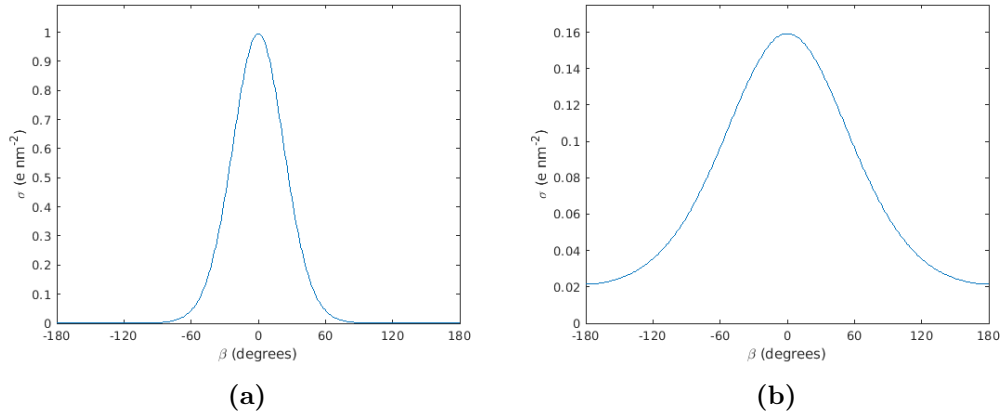


Figure 3.10: A plot of σ as a function of β for a single non-polarisable particle $a = 1.0$ nm with a Gaussian distribution of charge $q_g = 1e$ with (a) $\tau = 0.4$ nm and (b) $\tau = 1.0$ nm.

Figure 3.11 shows the interaction between two non-polarisable particles ($a_{1,2} = 1$ nm), one carrying a Gaussian distribution of charge $q = 1e$ and the other uniform $q = -1e$, separated by a surface-to-surface separation $s = 1000$ nm. The Gaussian distribution on particle 1 is centred pointing towards particle two, and τ is varied from 0.1 to 2. Here, $\tau_{\text{rel}} = \tau/a_1$, and gives a generalised limit of τ relative to the size of the particle.

From Figure 3.11, in the case of a normal Gaussian ($P = 1$), τ_{rel} is limited to a maximum value of ~ 0.5 , whereas a higher order Gaussian ($P = 5$) is able to more than double this while still keeping its charge. It is clear to see why this is the case in Figure 3.12, there the patch in 3.12a shows a much more diffuse distribution than in 3.12b. The higher order distribution allows for the ability to create patches of charge on the surface of a particle with a more uniform distribution of charge within the patch's radius, as opposed to the more diffuse nature of the normal Gaussian.

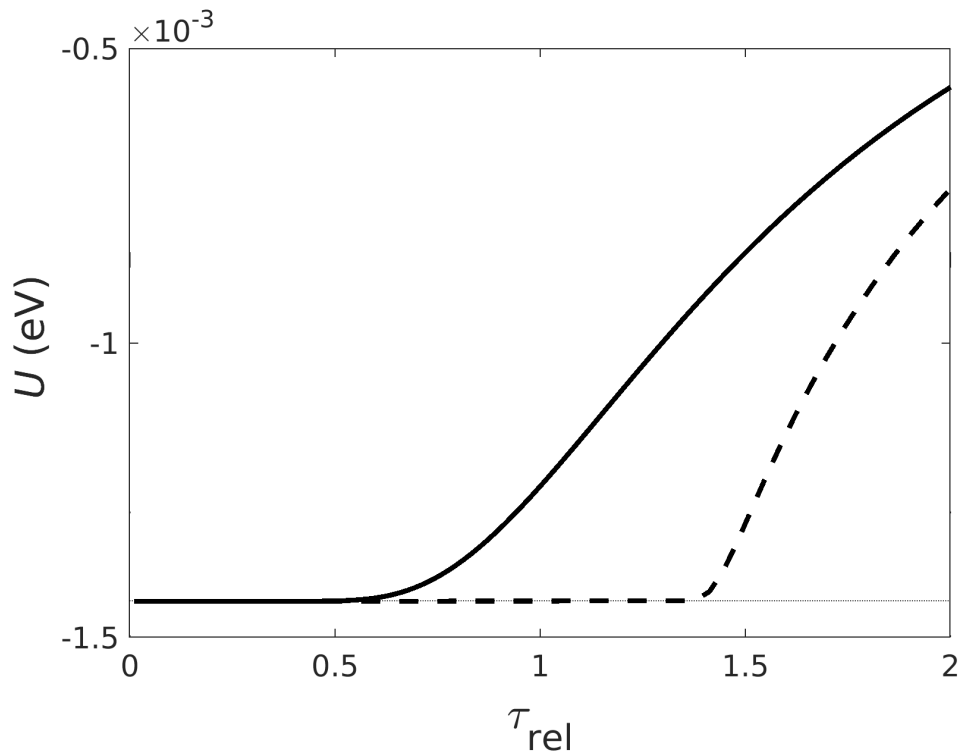


Figure 3.11: A plot of U as a function of τ_{rel} for a normal Gaussian distribution (solid, $P = 1$) and a higher order Gaussian distribution (dashed, $P = 5$). The interaction energy between two point-charges at this separation is displayed as the dotted line to show the expected value.

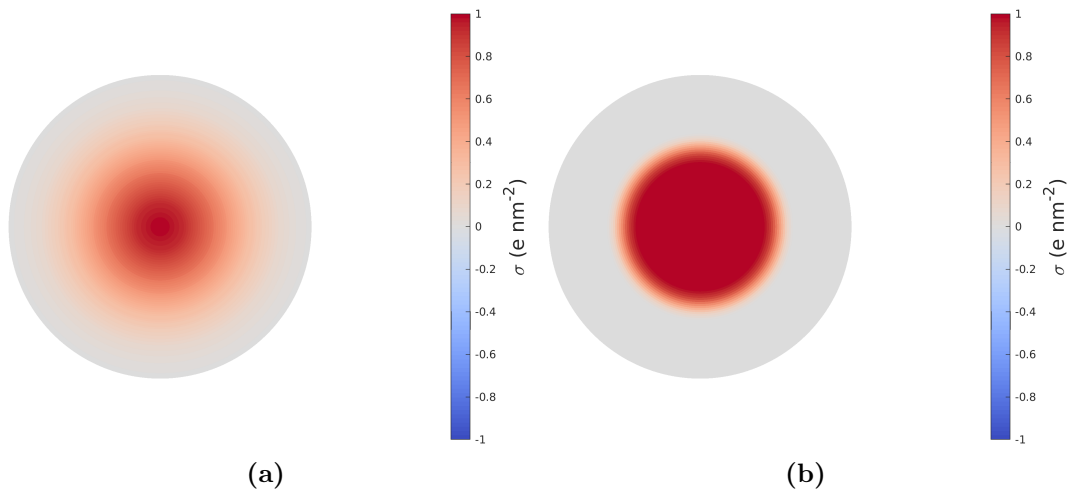


Figure 3.12: Visual representations of the surface charge density on the surface of two non-polarisable spheres ($a = 1.0 \text{ nm}$) with Gaussian surface charge density distributions with $\tau = 0.4 \text{ nm}$ and $q_g = 1e$. (a) is a normal Gaussian ($P = 1$) and (b) is a higher order Gaussian ($P = 5$).

3.2.2 Point-Charge Distribution

There are times where the charge present on a sphere is best represented as a localised point on its surface, such as when $q = \pm 1e$ or the charge is situated on metal ions deposited on a point of the surface. In this section that accuracy of the model is investigated against a Coulomb's law and a previous implementation of the solution.

In order to validate the point charge solution implementation, it is tested against Coulomb's law. Here, the two dielectric spheres with radii $a = 5$ nm have dielectric constants $k = 1$ and are placed in a vacuum $k_0 = 1$ with point charges positioned on the boundary in the same direction along the vector between the centres of the particles. The particles' permittivity being equal to that of the medium allows us to look purely at the interactions between the point charges without polarisation contributions to the interaction energy U . The energy between these two particles should be equal to the equivalent set up using Coulomb's law. The agreement shown in Figure 3.13 indicates that our implementation perfectly matches the expected results, and allows us to move forward to more intensive tests.

In order to validate the point-charge implementation, a comparison with similar work is presented. In 2019, a solution to the problem of representing non-homogeneous surface charge density as a point charge was developed by Filippov et al. [23]. This model was used to further investigate the electrospray problem in Harris et al. [28], where the experimental kinetic energies released (KER) during the Coulomb fission process were predicted using the maximum value in the energy-separation profile. The model was used to include an orientational analysis of the process, leading to a range of energy profiles with differing characteristics. Here we calculated values of kinetic energy release using the dielectric particle model point charge implementation. The systems chosen were

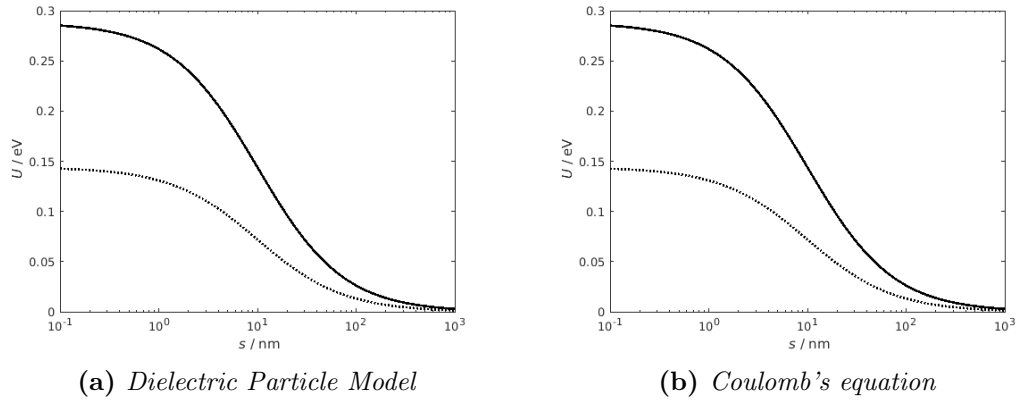


Figure 3.13: U as a function of s for the interaction between two non-polarisable dielectric particles ($k = k_0 = 1$, $a_1 = a_2 = 5$ nm) with point charges ($q_1 = 1e$, $q_2 = 2e$ (solid), $q_2 = 1e$ (dotted)) positioned in the same direction as the vector between the particles (a), and the equivalent calculation using Coulomb's law (b). Here $s = h_p - 2a_2$, where h_p is the distance between the point charge locations.

Table 3.1: A comparison between point charge and Gaussian solution for benzene results.

Orientation	Point Charge Model KER (eV)	Gaussian Distribution KER (eV)	Difference (%)
II	0.571	0.571	0
III	0.714	0.714	0
IV	47.432	46.424	2.12
V	0.831	0.830	0.01

the system in Figure 5 in Filippov et al. [23] looking at a low dielectric material in benzene ($k = 2.28$). The corresponding values for each arrangement of the point charges is shown in Table 3.1. When compared with the calculated values from Filippov et al., the values consistently differ by $\sim 0.1\%$ for all calculations. While the values should match exactly, this small difference is likely a consequence of the precision used for constants in calculations being slightly different.

Table 3.1 also shows the difference between using the point charge solution and a very small Gaussian ($\tau = 1$ pm) to simulate a point charge. Here it shows that even in an extreme case, such as in orientation IV, where the point charges are directed towards each other at a separation of 10 pm, the biggest error is just 2%, with most cases $< 0.01\%$, indicating that a small Gaussian is a very good approximation of a point charge distribution.

3.3 Neutral particles in external electric fields

Here the validity of the implementation of the external electric field solution to the model is tested. It is tested for neutral particles against the expected results from the literature for the induction of a dipole and subsequent interactions between these induced dipoles against the solution in Stone [18].

The problem considers the interaction between two neutral dielectric particles ($i = 1, 2$) suspended in a dielectric medium separated by a surface-to-surface distance s being exposed to a uniform external electric field.

The electric dipole moment \mathbf{p} of two oppositely-charged point charges is

$$\mathbf{p} = q\mathbf{d} \quad (3.9)$$

where q is the magnitude of the charge of the point charges, and \mathbf{d} is the vector between the point charges from negative to positive. When a neutral dielectric particle is placed in a uniform electric field, there is a redistribution of charge density on the surface of the particle. This redistribution can be represented as a dipole in the direction of the applied field in the form

$$\mathbf{p} = 4\pi\epsilon_0 \left(\frac{\kappa - 1}{\kappa + 2} a^3 \right) \mathbf{E} \quad (3.10)$$

where \mathbf{E} is the external field vector, a is the radius of the sphere and κ is the relative permittivity of the particle with respect to the medium ($\kappa = k_p/k_0$).

The surface charge density on the sphere due to the presence of a uniform external electric field σ_{ext} is given by

$$\sigma_{\text{ext}} = 3\epsilon_0 \left(\frac{\kappa - 1}{\kappa + 2} \right) E_{\infty} \cos \theta = \frac{1}{V} \mathbf{p} \cdot \hat{\mathbf{R}} \quad (3.11)$$

where E_{∞} is the magnitude of the electric field strength, θ is the angle on

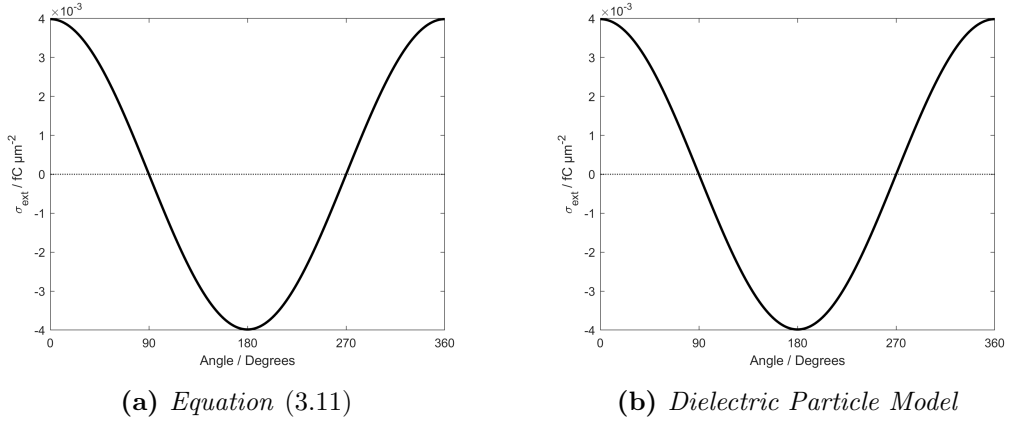


Figure 3.14: σ_{ext} as a function of θ for a $5 \mu\text{m}$ particle ($k = 10$) in a vacuum $k_0 = 1$ exposed to a uniform external electric field with a strength of $200,000 \text{ V/m}$.

the sphere relative to the electric field vector and $\hat{\mathbf{R}}$ is the unit vector in the direction of the electric field.

Although the redistribution of surface charge density of a single neutral dielectric particle by a uniform field leads to no overall force on the particle, the presence of a second particle can lead to interaction energies and forces between the two. From Stone [18], interaction energy between two dipoles $E_{\mathbf{pp}}$ is given by

$$E_{\mathbf{pp}} = \frac{R^2 \mathbf{p}_1 \cdot \mathbf{p}_2 - 3(\mathbf{p}_1 \cdot \mathbf{R}_{12})(\mathbf{p}_2 \cdot \mathbf{R}_{12})}{4\pi\epsilon_0 k_0 R^5} \quad (3.12)$$

where R is the distance between the centres of the two dipoles, \mathbf{R}_{12} is the vector between the two and k_0 is the dielectric constant of the medium.

Using Equation (3.11) we can calculate the theoretical values for σ_{ext} as a function of θ and compare it with the σ_{ext} produced using our model, as shown in Figure. 3.14a. The particle is a $5 \mu\text{m}$ radius dielectric particle with a dielectric constant of 10 suspended in a vacuum ($k_0 = 1$) exposed to a uniform external electric field with a strength of $200,000 \text{ V/m}$. We see a perfect agreement to theory in our test of the model's ability to predict σ_{ext} . \mathbf{E} and the particle's radius a can be used in Equation (3.10) to gain a theoretical value for \mathbf{p} which, in this particular case, gives a value of $2.0862 \text{ fC}\cdot\mu\text{m}$. In Equation (3.11) we

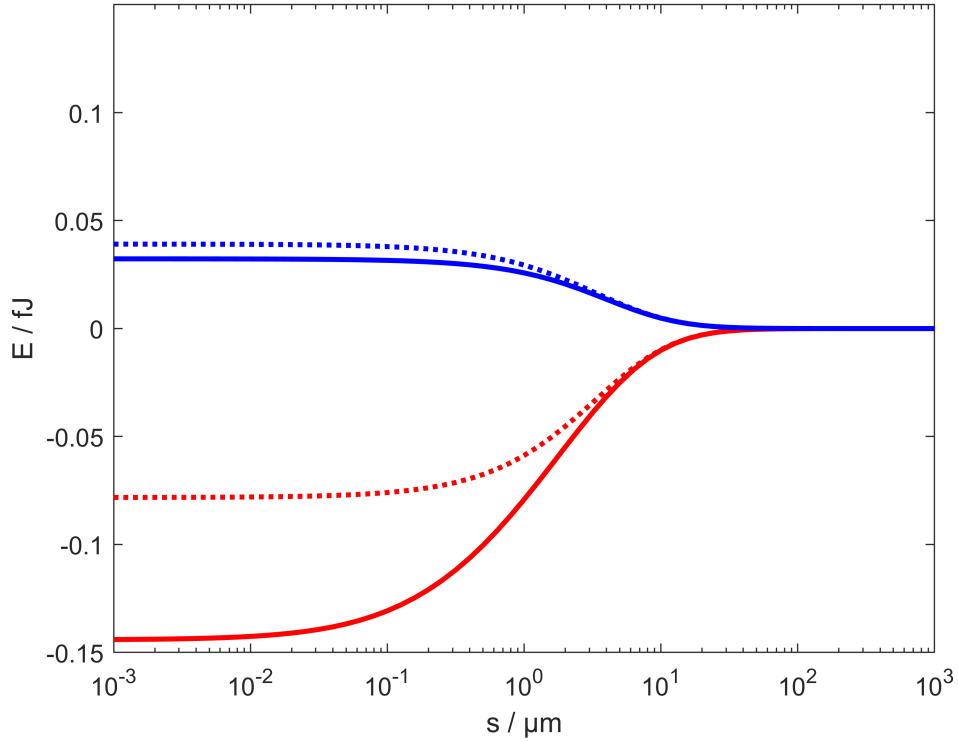


Figure 3.15: Interaction energy as a function of s between two neutral dielectric particles ($k = 10$, $a = 5 \mu\text{m}$) in a vacuum in a uniform electric field with a strength of 200 kV m^{-1} . The solid lines indicate the energies calculated using the dielectric particle model, whereas the dotted lines indicate the results using Equation (3.12). The particles are aligned parallel (red) or perpendicular (blue) to the electric field vector.

can use the maximum value of σ_{ext} to find a calculated value of \mathbf{p} of $2.0862 \text{ fC}\cdot\mu\text{m}$, matching the theoretical value.

As stated in earlier in this Section, adding another particle to the system leads to an interaction between the two. This effect can be seen in Figure 3.15 where the polarisable electrostatic model is compared against the analytical solution in Equation (3.12) for the interaction between two of the particles previously discussed ($k = 10$, $a = 5 \mu\text{m}$) in vacuum.

The difference between our model and the theoretical model in Figure 3.15 is due to the dielectric particle model accounting for dipole-induced multipole on the particles, whereas Equation (3.12) accounts for the pure interaction between dipoles. It demonstrates the need to consider the polarisation of the

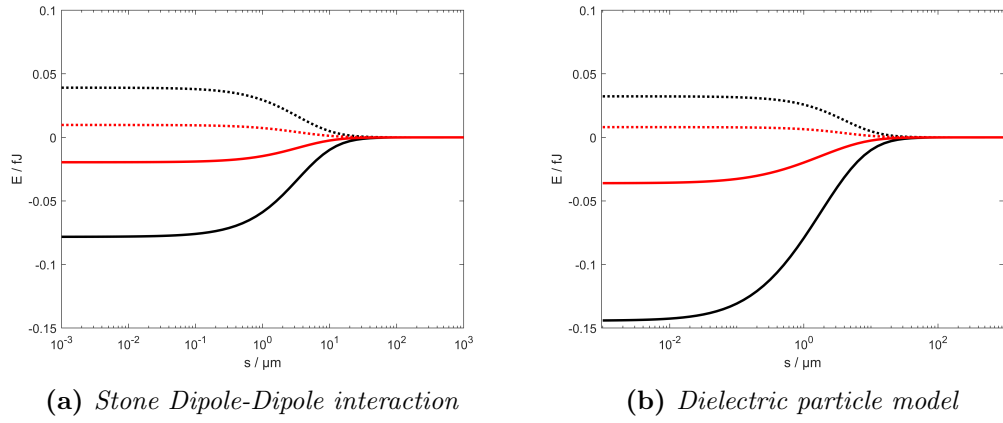


Figure 3.16: A comparison of the energy profiles for the interaction between a pair of $5 \mu\text{m}$ polarisable particles with radii with $k_p = 10$ and $k_0 = 1$ in external electric field strengths of 100 kV m^{-1} (red) and 200 kV m^{-1} (black) using Equation 3.12 (a) and the dielectric particle model (b). The particles are either aligned parallel (solid) or perpendicular (dotted) to the electric field vector.

particles, as opposed to just looking at the dipole-dipole interaction, as even when the dielectric constant is only 10, the interaction can be increased by $\sim 90\%$ in the parallel orientation.

From Equation (3.10), we can see that the size of the dipole \mathbf{p} is directly proportional to the magnitude of the external electric field E_∞ . Consequently we should expect the energy calculated from Equation (3.12) to be proportional to E_∞^2 . Figure 3.16 shows this effect for both our model and the results calculated using Equation (3.12), as when the field strength is halved, the interaction energy is reduced by a factor of exactly 4 in both cases, as expected.

The dielectric constant of both the particles and the medium play a critical role in the nature of the interaction. The relationship between k_i and k_0 can be defined as κ where $\kappa = k_i/k_0$. When looking at just a single particle we can use Equation (3.10) to find the limits of \mathbf{p} , which are:

- i) When $k_p \gg k_0$, $\kappa \rightarrow \infty$, $\mathbf{p} \rightarrow 4\pi\epsilon_0\mathbf{E}$
- ii) When $k_p \ll k_0$, $\kappa \rightarrow 0$, $\mathbf{p} \rightarrow -2\pi\epsilon_0\mathbf{E}$
- iii) When $k_p = k_0$, $\kappa = 1$, $\mathbf{p} = 0$

This effect can be seen in Figure 3.17, as when $k_p = 1$ and $\kappa = 10^{-3}$, the theoretical value for the energy is roughly 1/4 of the value where $k_p = 10^6$ and $\kappa = 10^3$, indicating that the magnitude of the individual dipoles are doubled as κ increases from 10^{-3} to 10^3 . The difference in the energies between the calculations using our code and those using Equation 3.12 is due to the effects from polarisation, which are explained in Lindgren et al. [29].

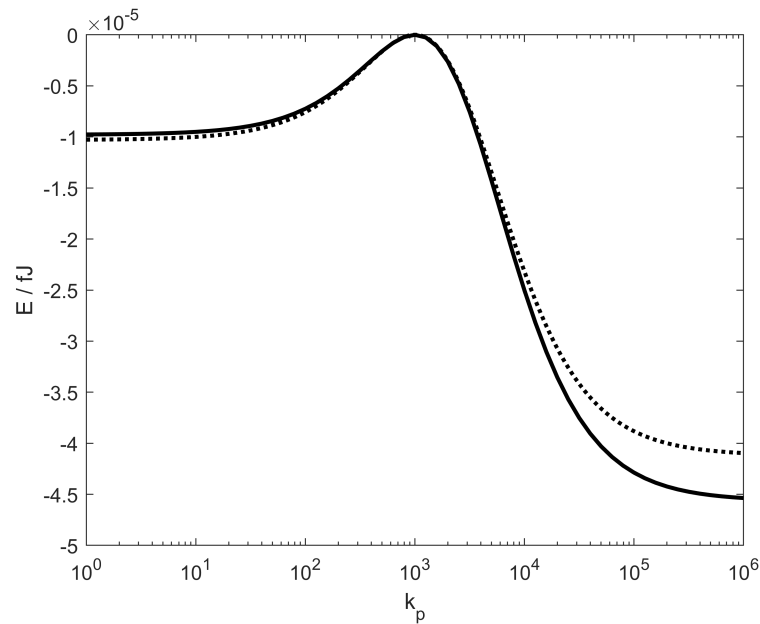


Figure 3.17: Interaction energy as a function of k_p in a system containing two neutral dielectric particles with radii $5 \mu\text{m}$ suspended in a dielectric medium ($k_0 = 1000$), separated by a surface-to-surface separation of $5 \mu\text{m}$ calculated using our model (solid) and 3.12 (dotted)

Figure 3.18 shows the effect of keeping k_p constant and changing k_0 . This has two effects: the first is where κ influences the magnitude and direction of the dipole; the second is the effect of the screening from the polarisable medium on the magnitude of the interactions, as the energies are proportional to $1/k_0$, as when k_0 increases, the magnitude of the interaction is heavily reduced. The same energy differences between the dielectric particle model and theory can be seen due to the same effects in Lindgren et al. [29].

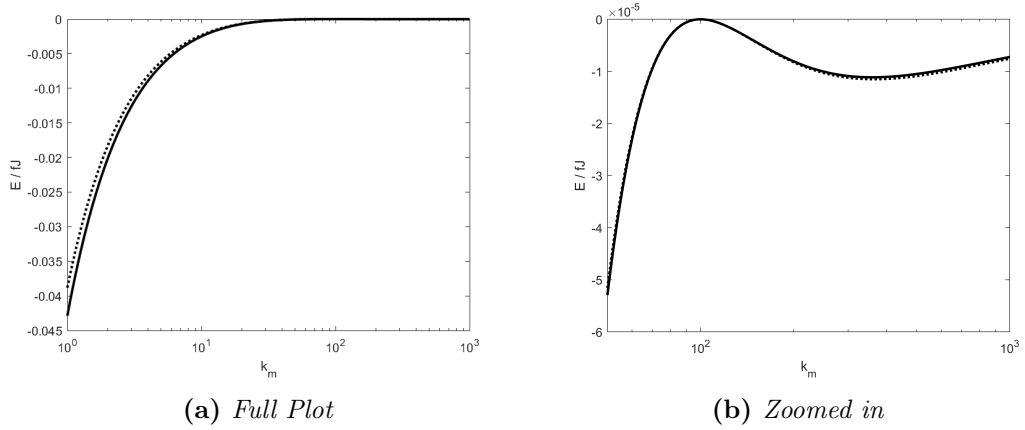


Figure 3.18: Interaction energy as a function of k_0 in a system containing two neutral dielectric particles ($k_p = 100$) with radii $a = 5 \mu\text{m}$ suspended in a dielectric medium, separated by a surface-to-surface separation of $5 \mu\text{m}$ calculated using our model (solid) and Equation 3.12 (dotted)

The angle between the vectors of the inter-particle displacement and external electric field θ has a strong effect on the nature of the interaction between the particles. Previously, the particles were similar in nature (both particles' dielectric constant k_p either above or below k_0). In these cases, if the alignment of the particles is parallel to the field ($\theta = 0^\circ, 180^\circ$), the interaction is attractive due to the head to tail orientation of the dipoles, whereas if the particles are aligned perpendicularly ($\theta = 90^\circ$), the interaction is repulsive due to a parallel orientation. This can be seen in Figure 3.19 where the energy when the dipoles are parallel the field is exactly twice the magnitude of the energy of the perpendicular case for the pure dipole-dipole interaction, with our model deviating slightly due to increased attraction from polarisation effects.

When the particles are dissimilar in nature ($\kappa_1 > 1, \kappa_2 < 1$) as seen in the dotted case Figure 3.19, we get the same relationship in the relative magnitudes of interactions as we got in the similar case, but the sign is flipped. When the particles are aligned parallel with the field, the dipoles are oriented head-to-head, leading to a strong, repulsive interaction. In the perpendicular orientation they are aligned anti-parallel next to each other, leading to a weaker, attractive interaction.

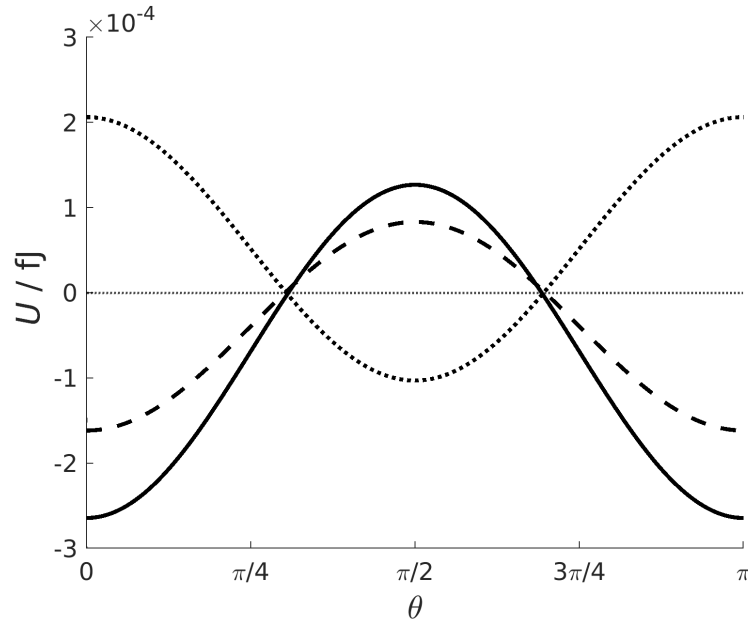


Figure 3.19: Interaction energy U as a function of θ for two neutral dielectric particles with a surface-to-surface separation of $5 \mu\text{m}$. $a = 5 \mu\text{m}$. $k_0 = 10$, $k = 20$ (solid), $k = 5$ (dashed), $k_1 = 20$, $k_2 = 5$ (dotted). $E_\infty = 200 \text{ kV m}^{-1}$. θ is the angle between the electric field vector and inter-particle vector.

The direction and relative magnitude of the force for the three systems in Figure 3.19 are shown in Figure 3.20, where the relative magnitude is normalised against the interaction with the largest magnitude. Here we see the influence on the nature of the interactions based on the relative polarisabilities of the particles and the medium. In each case, the electric field vector \mathbf{E} is directed in the positive x -axis, and the dielectric constant of the medium is kept as 10, with the particles either being 20 or 5, leading to values of κ equal to 2 or 0.5 respectively. In Figure 3.20, (a) and (b) show similar trends, although the relative strength of the repulsive interaction when the particles are aligned perpendicular to the field give slight variations. This is due to the trend seen in Lindgren et al. [29] where mediums more polarisable than the particles leads to a repulsive charge-induced interaction; this leads to the trend in Figure 3.20b where the stronger attractive interaction is reduced and the weaker repulsive interaction is increased. As mentioned before, Figure 3.20c gives the expected result, where the most repulsive interaction in when the dipoles are pointed

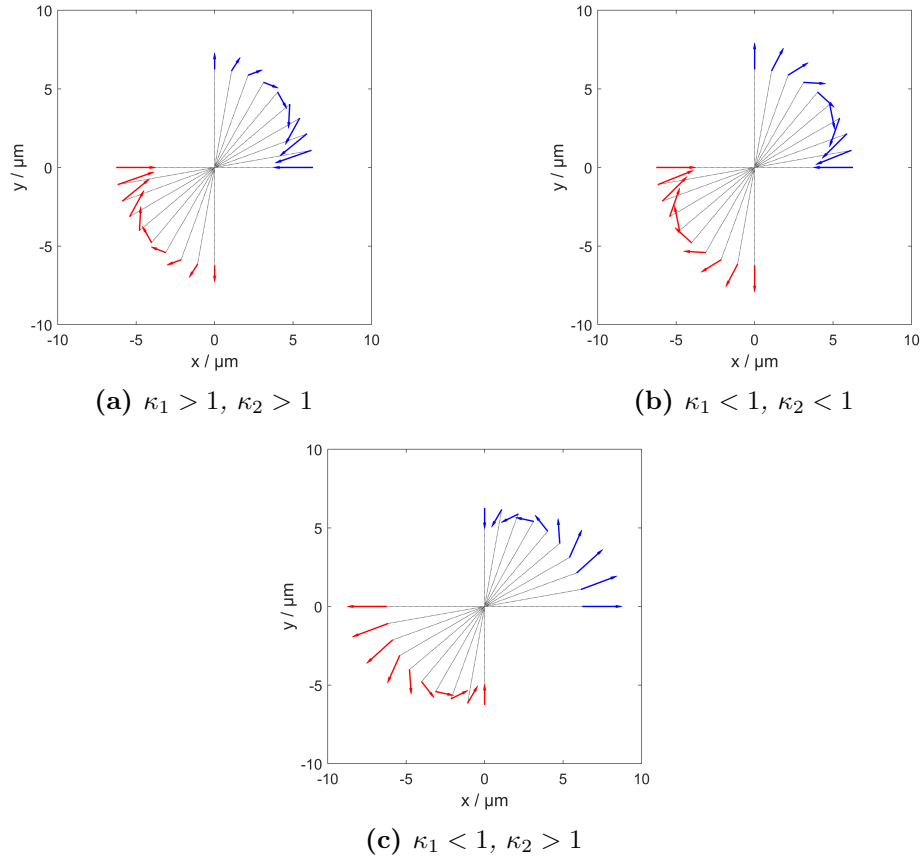


Figure 3.20: A normalised plot of the force vectors for $\theta = 0^\circ$ - 90° for two neutral dielectric particles with radii $a = 2.5 \mu\text{m}$ separated by a surface-to-surface separation of $5 \mu\text{m}$ and an external electric field \mathbf{E} in the positive x -axis. Shown are the cases where both the particles are (a) more polarisable and (b) less polarisable than the medium. (c) is the case where one particle is more polarisable than the medium, whereas the other is less polarisable.

towards each other; the normalised magnitude of the interaction when $\theta = 90^\circ$ is between those of (a) and (b) due to the conflicting effects of the attractive contribution for the particle with $\kappa > 1$ and the repulsive contribution for the particle with $\kappa < 1$ cancelling each other.

Dynamic Simulation of Neutral Particles in an External Electric Field

A two-dimensional dynamics simulation was performed of 50 polarisable particles ($k = 20$) with radii $a = 5 \mu\text{m}$ in a polarisable medium ($k_0 = 10$) in random positions within a square simulation box with $150 \mu\text{m}$ length walls.

The particles have a coefficient of restitution C_R of 0.6 in collisions with each other and $C_R = 1$ in collisions with the wall. Each particle began the simulation with a speed of 1 m s^{-1} in a randomised direction. The particles are exposed to a static external electric field directed in the positive x direction with a field strength of 200 kV m^{-1} . In this study, only 1 simulation was performed, and the final geometry was obtained after 75 s of simulation time and is shown in Figure 3.21. As the system was losing kinetic energy after each collision, the speeds of the particles slowed down fairly rapidly, allowing for the time-step length to be increased periodically.

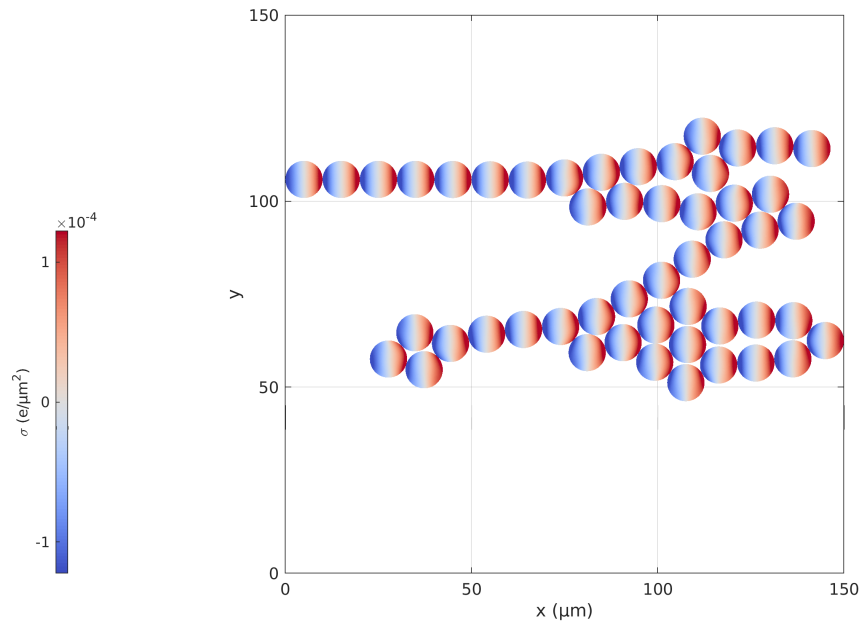


Figure 3.21: Screen-shot of the final structure after 75 s of simulation time produced by a molecular dynamics simulation of 50 randomly positioned dielectric particles ($k = 20$) with $a = 5 \text{ } \mu\text{m}$ and speeds of 1 m s^{-1} in a dielectric medium ($k_0 = 10$). The particles are exposed to an external electric field in the positive x direction with $E_\infty = 200 \text{ kV m}^{-1}$.

In this figure, we see a range of local geometries, with the general trend being a strong affinity for the particles being in a linear geometry aligned with the electric field vector \mathbf{E} . 6 local geometries are shown in Figure 3.22, with a set of three-body (I and II), four-body (III, IV and V) and seven-body (VI) structures. The interaction energy of each of these local structures is shown in Table 3.2. Structures II and VI are orientations where their energies have no

dependence on the rotational angle of the particle with respect to \mathbf{E} , whereas III and IV are the same geometry, but with their major axis aligned either parallel (III) or perpendicular (IV) to \mathbf{E} , leading to a rotational dependence on the energy. Going from structure II to structure III or IV is achieved by the addition of a particle in a position either parallel (III) or perpendicular (IV) to \mathbf{E} . The energies in Table 3.2 suggest the reasoning for the prevalence of structure III over structure IV in the simulations; the energy of structure III is lower in energy than structure II, whereas structure IV is higher in energy.

Table 3.2: Energies of six orientations in Figure 3.22.

Local Structure	U (aJ)
I	-2.20
II	-0.81
III	-2.25
IV	-0.51
V	-3.44
VI	-3.50

By far the most common orientation of particles is a linear arrangement parallel with the direction of the external field. As shown in Figures 3.19 and 3.20, when the particles are similar in composition, the strongest interaction is when the particles are aligned parallel with the field due to the dipoles created on the particles all being aligned in the same direction with respect to each other.

Figure 3.23 shows the energy associated with adding a particle to the end of a linear chain, where $U_{\text{add}}(M) = U(M) - U(M - 1)$. The justification for accounting for the many-body effects is clearly displayed here, as the energy of adding a third particle to the chain is $\sim 10\%$ lower than that of adding a 50th particle. This clearly shows the many-body effect of adding a particle to the end of a shorter chain as opposed to a longer chain, as longer chains can redistribute the effects over a longer chain, almost to the point where the many-body effects can be neglected for long chains.

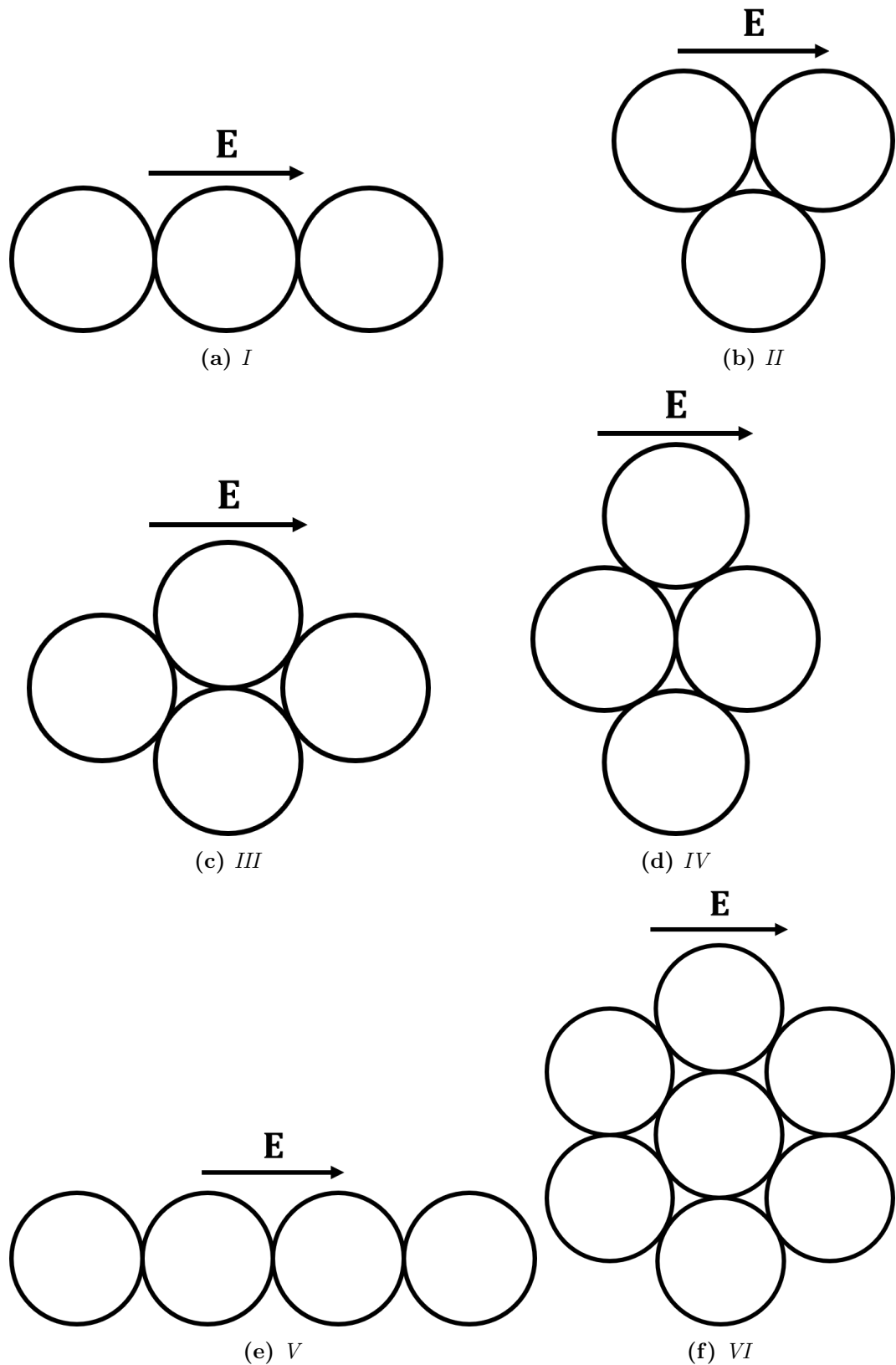


Figure 3.22: A simplified visualisation of a collection of 6 local geometries seen at the end of the molecular dynamics simulation in Figure 3.21. Shown are (a,b) a pair of three-body configurations, (c,d,e) three four-body configurations, and (f) a seven-body hexagonal configuration.

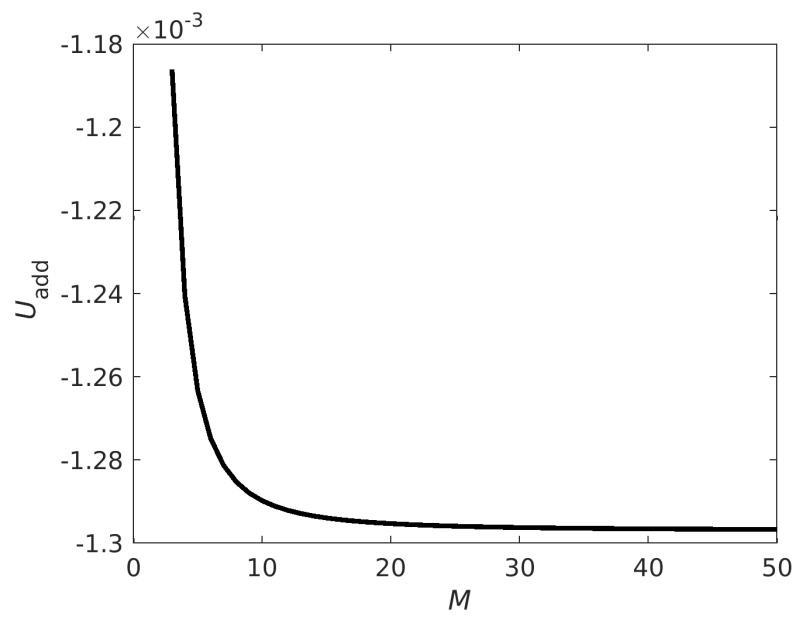


Figure 3.23: U_{add} for a linear arrangement of M neutral particles with $a = 5 \mu\text{m}$, $k = 20$, $k_0 = 10$ for values of M from 3-50 in an electric field strength $E_\infty = 200 \text{ kV m}^{-1}$ parallel to the chain axis.

Chapter 4

The influence of surface charge on dust agglomeration growth in the mesosphere

The work in this chapter was performed as part of a collaboration with Astrophysicist Prof. Ingrid Mann at UiT The Arctic University of Norway. A presentation given at an ISSI team meeting on the “Electrostatic Aggregation of Dust in the Lunar Regolith” in Bern sparked discussions about whether this could be expanded to the dust and ice particles in the higher reaches of the atmosphere, more specifically in the upper mesosphere and lower thermosphere region.

4.1 Introduction

A significant fraction of the cosmic dust and meteoroid material that hits the Earth remains in the atmosphere for extended periods of time and is a source of solid dust particles, denoted as meteoric smoke particles (MSP) [40, 41] MSP are formed by an ablation process, whereby meteoroids colliding with atmospheric particles experience strong deceleration and are heated to evaporation temperatures. Meteoric and atmospheric species form an expanding

column of partially ionised gas behind the meteoroid, which is observed as a meteor, see e.g. [42]. Part of the meteoroid material vaporises, and the released small solid particles and gaseous species are incorporated into the atmosphere where they grow further to form MSP, see e.g. [40, 43]. The coalescence or condensation mechanisms leading to dust agglomerates is considered to be an important aspect of atmospheric physics and chemistry. A better understanding of these mechanisms could help to establish the significance of particles containing refractory materials that are present in the upper mesosphere and lower thermosphere, in short, the MLT region of 60 to 130 km. These small solid particles could also play a role in the formation of ice clouds by providing a core for heterogeneous condensation that is more effective than homogeneous nucleation. During summer, at high and mid latitudes the temperature near the mesopause reaches a minimum and can fall below the freezing point of water [44], and clouds of ice particles, polar mesospheric clouds (PMC), can form at heights of 80 to 85 km [45]. These are also observed from Earth after sunset and are known as noctilucent clouds (NLC). Because NLC may be an indicator of climate change [46], it is important to understand the possible role of meteoric smoke in the coalescence of ice particles, although the growth of the meteoric smoke is an interesting topic of research in itself.

Models of coagulation [40, 43, 47] take into consideration the convection of dust particles in global atmospheric circulation, the influence of gravitational force, and Brownian motion. The models also assume that particles stick together after a collision, which is not always the case. The outcome can depend on the relative velocity of the colliding particles and the elasticity of a collision as defined by the coefficient of restitution, which can vary according to the composition of a particle. Dust charging, which can cause particles to experience either strong attractive or repulsive forces, could also play a role in the growth process. This consideration has not previously been included in modelling the collisional dust growth in the MLT, but has been studied for

droplets in tropospheric clouds [48].

In this chapter the influence of surface charge on particle agglomeration processes is studied. The point charge development in Chapter 2 is used to represent the ice, metal oxide and silica particles. This model can be combined with other theories to predict collision outcomes according to the variables of particle size, charge, dielectric constant, relative kinetic energy, collision geometry and the coefficient of restitution. The presence of negative, positive and neutral particles in the MLT region implies that Coulomb forces between oppositely charged objects are the main attractive component of any electrostatically-driven dust agglomeration process. However, in addition to the strong attractive interaction between oppositely charged particles, attractive interactions between particles of the same sign of charge can also take place at small separation distances, leading to the formation of stable aggregates. This attractive force is governed by the polarisation of surface charge, leading to regions of negative and positive surface charge density close to the point of contact between colliding particles [49]. The strength of the resulting attractive electrostatic force depends on particle composition as the value of the dielectric constant determines the extent of polarisation of bound surface charge. Previously, the model has successfully explained the effects of like-charge attraction in a range of coalescence processes such as agglomeration of single particles and small clusters derived from a metal oxide composite [32], aerosol growth in the atmosphere of Titan [50] and self-assembly behaviour of charged micro-colloids [30]. Interactions between pairs of neutral and charged particles also depend on the polarisation of surface charge, but these take place in the absence of a Coulomb barrier (see below). In atmospheric science, the method of image charges (described in Section 1.2.1) is routinely used to study collision outcomes if particles can be approximated by conducting spheres (or having the dielectric constant greater than 80).

The focus of this work is on aggregation processes relevant to mesospheric

conditions and in particular at high latitudes. The MLT region offers unique conditions in terms of the electrostatic environment, composition and physical parameters such as temperature and pressure. The pressure at 60 km is less than 1 hPa and decreases further with increasing altitude; therefore, particles interact essentially in vacuum, and, consequently, in these simulations the dielectric constant of the surrounding medium is taken to be one. To investigate the growth of meteoric smoke particles, we consider charged and neutral metal oxides particles with radii ranging from 0.2 nm to 5 nm as shown in Table 4.1. To simulate the growth of ice onto the meteoric smoke, we examine the interactions between metal oxide particulates and large ice particles ranging in size from 10 nm to 100 nm and with charges 0 to $-5e$. As these particles typically possess a low charge (or single charge arising, for example, from either a photoionisation event that removes a single electron from a molecule on the particle or the attachment of an ambient air ion) the charge distribution is best represented by a point free charge residing on the surface. For this case, we have extended the numerical method developed in Lindgren et al. [25] to allow for description of particle charge in the form of point charge(s) residing on its surface, similar to a solution proposed in Filippov et al. [23] but based on a numerical method. Comparisons with a uniform distribution of free surface charge, as described in Bichoutskaia et al. [19], shows that for particles with radii greater than 10 nm, the choice of a specific form of surface charge distribution does not affect the calculated electrostatic energy between particles; however, the difference does become important for sub-nanometer particles.

The remaining parts of the chapter are organised as follows. In Section 4.2, we describe the ionospheric dusty plasma in the region where we study dust growth. In Section 4.3, the range of relative velocities for collisions leading to aggregation is calculated for all collision scenarios that are considered suitable to describe the interactions between ice and dust particles in the mesosphere. These velocity ranges are subsequently used to calculate the percentage aggregation

Table 4.1: Common particulates found in the MLT region which are considered in this study.

Particle Composition	Dielectric constant	Density, g cm^{-3}	Size range, nm	Charge, e
Ice, H_2O	100	0.92	3 - 100	0, -1 to -5
Silicon Dioxide, SiO_2	3.9	2.65	0.2 - 5	0, -1, -2
Magnesium Oxide, MgO	9.6	3.58	0.2 - 5	0, -1, -2
Iron Oxide, FeO	14.2	5.74	0.2 - 5	0, -1, -2

outcome. The orientational geometry of the collisions is discussed, and a quantitative estimation of the electrostatic interaction energy profile is presented for collisions between like-charged particles. Section 4.4 focuses on specific cases of aggregation between like-charged dust and ice particles, and Section 4.5 deals with aggregation between small charged dust particulates. A brief discussion of the results is provided separately in Section 4.6.

4.2 Ionospheric dusty plasma conditions

The MLT overlaps with the D-region ionosphere where the major ionisation process under quiet conditions above 80 km is due to solar radiation and geo-coronal UV radiation, and galactic cosmic rays become an important source of ionization below 80 km. At high latitudes, where ice clouds can form, the precipitation of high-energy electrons and protons that form in the Sun-magnetosphere interactions and enter the ionosphere during geo-magnetically perturbed conditions promote further ionisation. This increases the ionization rate by up to several orders of magnitude [51].

The dust particles in the MLT are hence embedded in a low-pressure atmosphere with a small but highly variable degree of ionization. They collect and emit electrons and ions and some of the dust particles acquire a net equilibrium surface charge in a balance when the currents of incoming and outgoing charged particles are equal. The number density of plasma particles is variable. The

impact of photons causes photoelectron emission and the detachment of electrons from negatively charged dust. Photoionising solar X-ray, EUV and UV fluxes can be variable, and other sources of ionising radiation include aurora and geo-corona, as well as elves and sprites formed in the atmosphere [52]. The dust number density is of similar order as that of the free electrons and ions; all particles with charge collectively form a dusty plasma. In model calculations, the dust charge has been simulated by taking into account the capture of plasma particles, photo detachment and photoionization [53, 54]. The time to reach equilibrium charge varies from around 100 s in quiet conditions to less than 1 s in a meteor [42, 55].

Different assumptions have been made regarding the composition of particles. Hervig et al. [56] describe the polar mesospheric cloud particles that are observed with extinction measurements, as a mixture of ice and meteoric smoke and suggest wüstite and magnesiowüstite as possible smoke materials. To simulate dust conditions in the laboratory, Plane et al. [57] consider olivine and pyroxene and Duft et al. [58] iron silicate. A number of laboratory experiments and ion chemistry considerations could also constrain expected MSP dust composition, revealing that FeO and MgO are rapidly oxidized by O_3 and O_2 , and recombine with H_2O and CO_2 [57]. Hence the existence of these oxides as pure particles is unlikely. Bearing this in mind, we chose our sample materials mentioned above as analogues for materials with different dielectric constants. There has been no successful analysis made so far of the composition of collected MSPs, which is because of difficulties in the collection process and because of different sources of contamination [59]. Rapp et al. [41] used in-situ rocket observations to constrain the workfunction of the MSP material and from that inferred Fe and Mg hydroxides as possible initial compounds. Robertson et al. [60] pointed out that rocket measurements of dust particles using charge detection can be misinterpreted when there are approximately equal numbers of positively and negatively charged MSPs; they also point out the importance of charge

interactions for understanding the coagulation process.

4.3 Framing the problem

Temperatures in the MLT region typically fall in the range of 130 K to 150 K, however observational studies have shown this to be variable [44]. Such low temperatures have a significant effect on the nature of water droplets, as according to the appropriate phase diagram [61, 62], ice particles are in a ‘soft ice’ state and may absorb some of the kinetic energy present during a collision. This possibility has implications for the outcome of all collisions between small metal oxide particulates and ice particles, which at short separation distances can exhibit a strong attraction, even when both particles have a charge of the same sign [19]. However, for like-charged particles with low velocities, this attractive region is largely inaccessible due to the presence of a large repulsive Coulomb energy barrier (E_{Coul}) which prevents their aggregation. In addition to the Coulomb barrier, other factors affect aggregation during a collision; these include the binding energy as defined by the interaction energy at the point of contact (E_0), the coefficient of restitution (C_R), the Maxwell-Boltzmann distribution of particle velocities at a defined temperature, and the composition of colliding particles (as defined by the dielectric constant and particle density).

The total kinetic energy of a system containing two colliding particles is the sum of the relative kinetic energy with respect to the centre of mass (K_{rel}) and the kinetic energy of the centre of mass (K_{cm})

$$K_{\text{tot}} = \frac{1}{2}\mu|\mathbf{v}_{\text{rel}}|^2 + \frac{1}{2}M\mathbf{v}_{\text{cm}}^2 \quad (4.1)$$

where $\mu = \frac{m_1 m_2}{m_1 + m_2}$ is the reduced mass of the colliding particles, $M = m_1 + m_2$, $\mathbf{v}_{\text{rel}} = \mathbf{v}_1 - \mathbf{v}_2$, and $\mathbf{v}_{\text{cm}} = \frac{\sum m_j \mathbf{v}_j}{M}$ ($j = 1, 2$). The kinetic energy of the centre of

mass is unaffected by changes in the inter-particle interaction energy. However, due to the law of conservation of energy, the loss or gain of electrostatic interaction energy between the colliding particles leads to corresponding changes in the relative kinetic energy. At the point where the electrostatic interaction energy is at the maximum (the Coulomb barrier, E_{Coul}), the relative kinetic energy of the colliding pair is at the minimum. Once over the barrier and immediately before the collision the kinetic energy is at its highest, i.e. $K_{\text{rel}}^{\text{before}} = K_{\text{rel}}^{\text{initial}} - E_0$, and in an inelastic collision, it is reduced to $K_{\text{rel}}^{\text{after}} = C_R^2 \times K_{\text{rel}}^{\text{before}}$. If $C_R = 1$, the collision is elastic and the kinetic energy does not change during the collision. The minimum relative initial velocity colliding particles require to overcome the Coulomb barrier is therefore

$$v_{\text{rel}}^{\text{min}} = \sqrt{\frac{2E_{\text{Coul}}}{\mu}}. \quad (4.2)$$

If the loss of kinetic energy during a collision ($K_{\text{rel}}^{\text{before}} - K_{\text{rel}}^{\text{after}}$) is greater than the excess kinetic energy as compared to the Coulomb barrier ($K_{\text{rel}}^{\text{initial}} - E_{\text{Coul}}$), then the particles are trapped behind the barrier. The maximum relative initial velocity ($v_{\text{rel}}^{\text{max}}$), above which coalescence is not possible, is derived from the situation where, during a collision, insufficient kinetic energy is removed through the action of the coefficient of restitution and the particles fly apart. This maximum initial velocity is given by:

$$v_{\text{rel}}^{\text{max}} = \sqrt{\frac{2[(E_{\text{Coul}} - E_0)/C_R^2 + E_0]}{\mu}}. \quad (4.3)$$

The above collision scenarios are illustrated in Figure 4.1 based on an example case of a small SiO_2 particle colliding with a larger ice particle both carrying a negative charge of $q_1 = q_2 = -1e$. Three possible outcomes are described. If the relative kinetic energy of the colliding particles is smaller than the height of the

Coulomb barrier (case 1) then the particles always repel one another without energy loss. If the particles collide inelastically with a relative kinetic energy sufficient to overcome the Coulomb barrier, the loss of kinetic energy during a collision may prevent their subsequent separation and lead to the formation of a stable, or metastable, aggregate (case 2). If the energy loss during such a collision is not sufficient to stabilise the pair, the particles rebound and separate (case 3). The latter case may be applicable in warmer regions of the atmosphere where particles move with higher velocities. In this work, we consider a wide range of particle velocities in order to identify a wide range of possible collision outcomes. The probability distribution for the relative velocity of two colliding particles in the form of a Maxwell-Boltzmann distribution at temperature T is given by

$$P(v_{\text{rel}}) = \sqrt{\frac{2}{\pi}} \left(\frac{\mu}{kT} \right)^{3/2} v_{\text{rel}}^2 e^{-\frac{\mu v_{\text{rel}}^2}{2kT}}. \quad (4.4)$$

In Figure 4.2, representative examples for the Maxwell-Boltzmann distribution of the relative velocities are shown for collisions between SiO_2 particles carrying a charge of $q_2 = -1e$ and ice particles with $q_1 = 0, -1e,$ and $-2e$ at $T = 150$ K. If the surface charge is represented by a point charge residing on the particle's surface then the orientational geometry of a collision becomes important. Figure 4.3 shows the geometries considered in this study, both for collisions between ice particles and small metal oxide particulates (Figure 4.3a) and for collisions between metal oxide particles (Figures 4.3b and 4.3c).

Previous studies by Bichoutskaia et al. [19] have shown conclusively that, between like-charged particles, attraction is strongly size-dependent, such that particles carrying the same amount of charge should have dissimilar sizes. This effect becomes more noticeable with the increase of the ratio of particle radii, a_1/a_2 ; as the ratio increases, surface charge polarisation becomes more

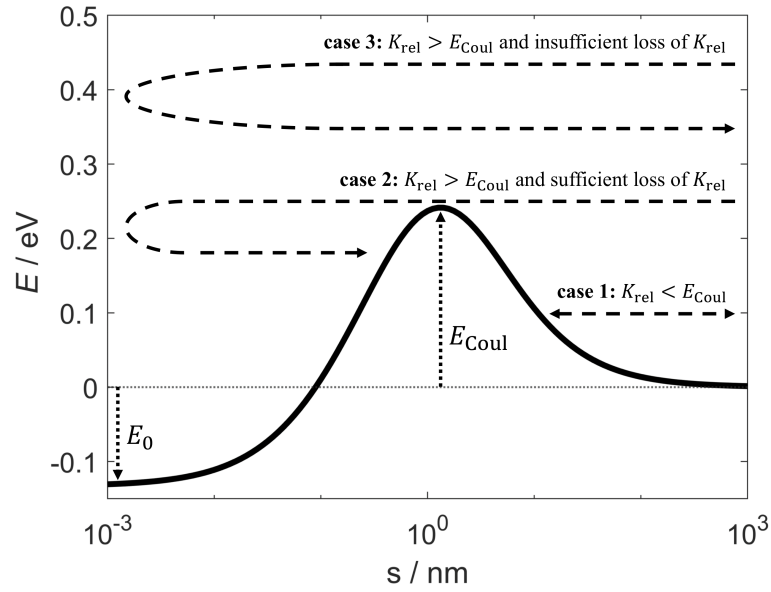


Figure 4.1: Possible outcomes for a collision between like charged particles. The total energy is schematically split into two components: the electrostatic interaction energy (solid) and the relative kinetic energy (dashed). The electrostatic interaction energy profile is calculated for a collision between ice particle ($a_1 = 3$ nm) and SiO_2 particle ($a_2 = 0.5$ nm) both carrying the charge of $q_1 = q_2 = -1e$.

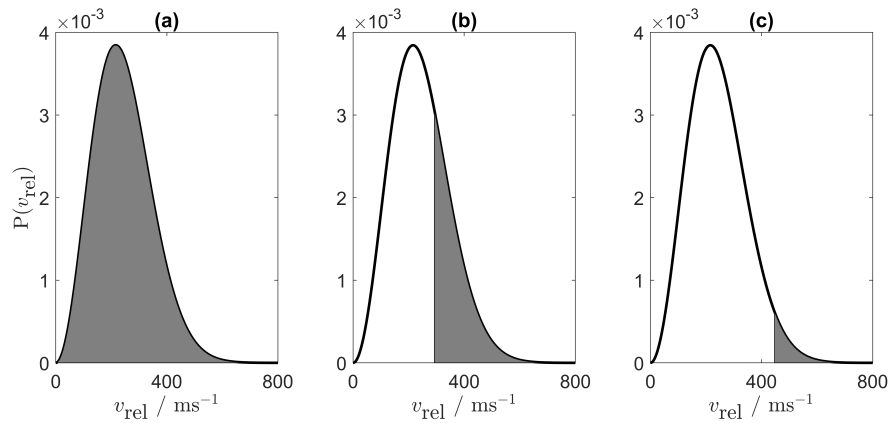


Figure 4.2: Aggregation probability, indicated by the shaded area, for a collision between SiO_2 particle ($a_2 = 0.2$ nm, $q_2 = -1e$) and ice particle ($a_1 = 30$ nm) as defined by the Maxwell-Boltzmann distribution of the relative velocity at $T = 150$ K: (a) the case of neutral ice particle ($q_1 = 0$), the probability of aggregation is one as $P(v_{\text{rel}})$ is integrated in the velocity range of $[0, 1192]$ ms^{-1} ; (b) $q_1 = -1e$, the probability of aggregation is 0.293 as $P(v_{\text{rel}})$ is integrated in the velocity range of $[295, 1219]$ ms^{-1} ; (c) $q_1 = -2e$, the probability of aggregation is 0.034 as $P(v_{\text{rel}})$ is integrated in the velocity range of $[450, 1260]$ ms^{-1} . The values of $v_{\text{rel}}^{\text{min}}$ and $v_{\text{rel}}^{\text{max}}$ are taken from Table 4.2

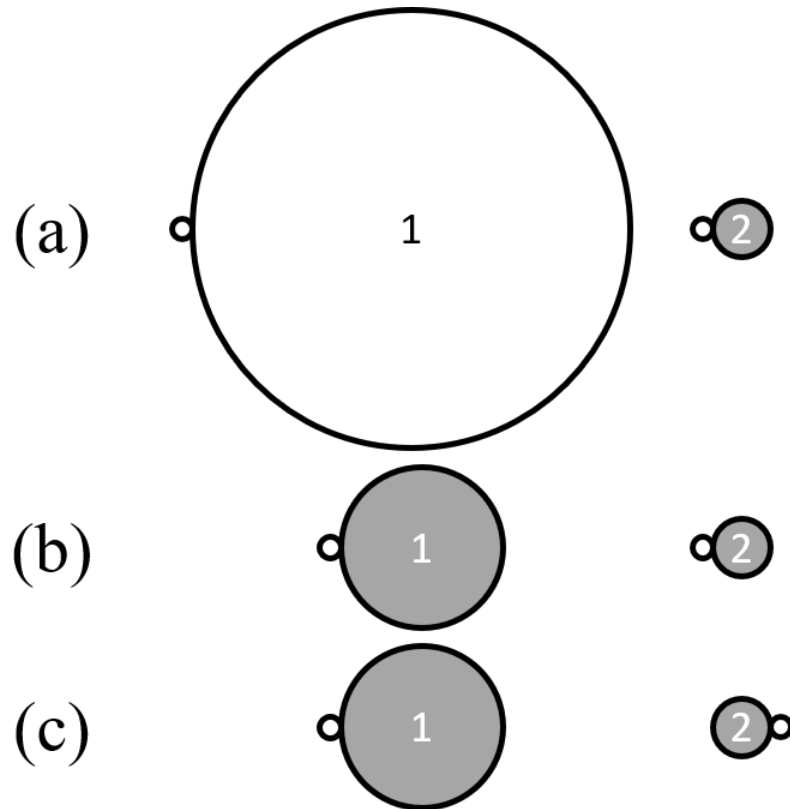


Figure 4.3: Position of the point charge on the surface of colliding particles depicted by a small open circle: (a) ice particle (1) and small oxide particulate (2); (b) and (c): both particles (1 and 2) are oxides.

pronounced, leading to strong attraction at short separation distances and a reduction of the Coulomb barrier. This effect is illustrated in Figure 4.4a, which shows electrostatic interaction energy profiles as a function of separation distance for collisions between like charged ice and SiO₂ particles ($q_1 = q_2 = -1e$) as the size of the ice particle varies between $a_1 = 10$ nm, 20 nm and 30 nm. As the ice particle becomes larger, the height of the Coulomb barrier decreases, which in turn can affect the outcome of a collision. Note that Figure 4.4 refers to a collision geometry shown in Figure 4.3a which favours the attractive interaction between two particles, each with a point charge located on their surface.

In this example, the SiO₂ particle approaches the ice particle from the direction opposite the location of the point charge on the latter, and this collision corresponds to the least repulsive interaction. An equivalent scenario has been considered assuming a uniform distribution of surface charge on both particles, following the approach described in Bichoutskaia et al. [19]. The height of the Coulomb barrier obtained using a uniform distribution of surface charge is depicted in Figure 4.4 by horizontal lines. For the size of particles considered in this work, these two approximations give very similar results. Although the height of the Coulomb barrier is strongly influenced by the size of the large ice particle (Figure 4.4a), it shows no change with variation in sizes of SiO₂ particles considered here. The height of the Coulomb barrier is affected even more greatly when the charge of colliding particles is changed. In the case considered in Figure 4.4b, the charge on ice particle was increased from $q_1 = -1e$ to $-5e$ to show almost linear dependence of the barrier on charge variation, in accordance with the leading Coulomb energy term $E \propto \frac{q_1 q_2}{h}$. The variation of the electrostatic energy with particle size shown in Figure 4.4a is a more subtle effect related to surface charge polarisation (note in Figure 4.4b the change of scale along y -axis).

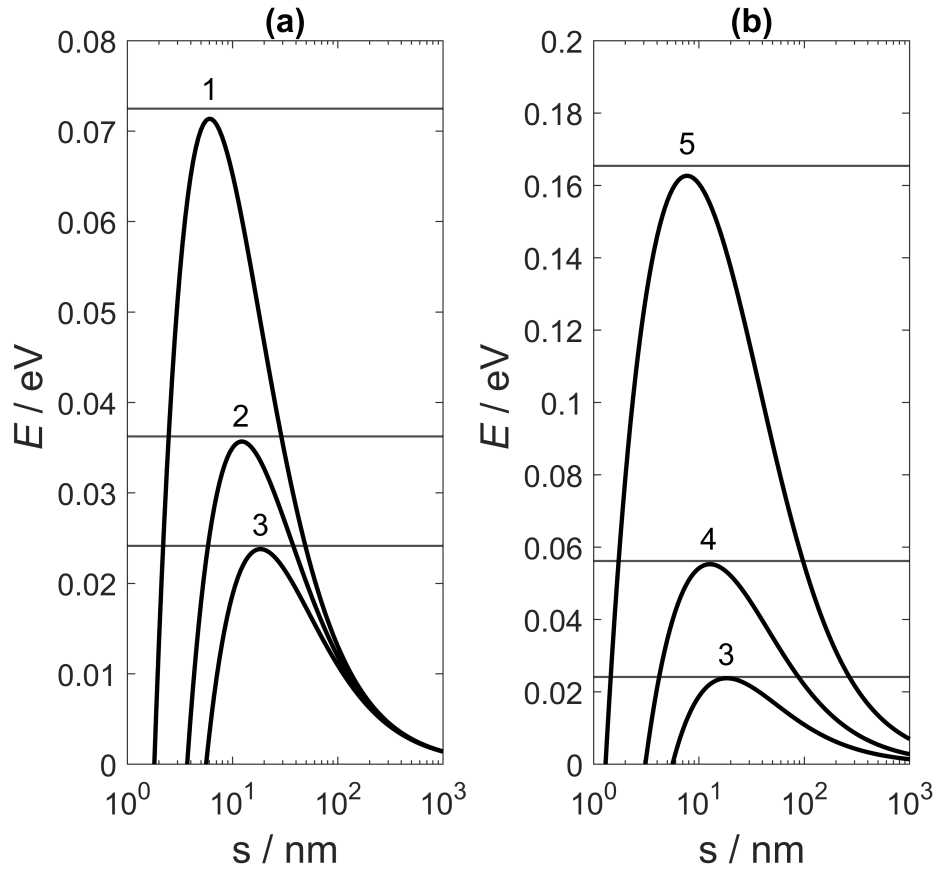


Figure 4.4: Electrostatic interaction energy as a function of the separation distance between an ice particle and a SiO_2 particle ($a_2 = 0.2$ nm, $q_2 = -1e$) in the geometry shown in Figure 4.3a, as calculated by the point charge model analogous to Filippov et al. [##]. Horizontal lines indicate the value of the Coulomb energy barrier obtained using the uniform surface charge model: (a) the charge of the ice particle is $q_1 = -1e$, and the radius varies as $a_1 = 10$ nm (line 1), 20 nm (line 2) and 30 nm (line 3); (b) the radius of the ice particle is $a_1 = 30$ nm, and the charge varies as $q_1 = -1e$ (line 3), $-2e$ (line 4) and $-5e$ (line 5). Note the change of scale on the y-axis.

4.4 Aggregation of oxide and ice particles

Consider first the aggregation of negatively charged metal oxide and ice particles. Table 4.2 shows values of $v_{\text{rel}}^{\text{min}}$ and $v_{\text{rel}}^{\text{max}}$ calculated using equations (2) and (3) with $C_R = 0.9$. Integrating the probability distribution shown in Figure 4.2 between these limits gives the probability of aggregation, and the results are presented in Table 4.2, where aggregation is expressed as a percentage of all collisions. Table 4.2 summarises results for the aggregation of a metal oxide particle, with a fixed size and charge, with ice particles of varying size and charge. These data show that large ice particles with low charge have the highest probability of coalescence with like-charged metal oxide particles. However, in many cases the Coulomb barrier prevents aggregation of particles with the kinetic energies typically found in the MLT region ($kT = 12.9$ meV at $T = 150$ K), assuming that thermal motion is the predominant contribution to velocity. The barrier can be overcome by a small number of high kinetic energy particles found in the tail of the Maxwell-Boltzmann distribution of molecular speeds at 150 K. For these particular interactions, the free charge on the surface of both colliding particles is described by a point charge with the geometry shown in Figure 4.3a, and the change in electrostatic interaction energy is due to a redistribution of bound charge (polarisation effects). Note that for ice particles with higher charges, a uniform distribution of free charge might be more appropriate. As mentioned previously, if the initial relative velocity of the incoming particles is smaller than $v_{\text{rel}}^{\text{min}}$ the two like charged particles repel (case 1 shown in Figure 4.1), however if it is greater than $v_{\text{rel}}^{\text{max}}$ the particles do not coalesce but instead fly apart due to the residual excess kinetic energy (case 3). Therefore, only collisions with a relative initial velocity greater than $v_{\text{rel}}^{\text{min}}$ and smaller than $v_{\text{rel}}^{\text{max}}$ lead to coalescence. In these examples, a change of the coefficient of restitution would not affect the probability of aggregation as C_R only reduces $v_{\text{rel}}^{\text{max}}$, and values of the latter that fall within the temperature range appropriate for these calculations have extremely low probabilities.

Table 4.2: Energetic considerations and the percentage of aggregation for SiO₂ - ice collisions at T = 150 K and C_R = 0.9 (the surface point charge model). SiO₂ particle has the fixed radius and charge ($a_2 = 0.2$ nm, $q_2 = -1e$), and the size and charge of ice particle is varied. The collision geometry is shown in Figure 4.3a.

ice particle	Coulomb barrier, E_{Coul} , meV	$v_{\text{rel}}^{\text{min}}$, m s ⁻¹	$v_{\text{rel}}^{\text{max}}$, m s ⁻¹	agg, %
$a_1 = 30$ nm; $q_1 = 0$	0	0	1192	100
$a_1 = 30$ nm; $q_1 = -1e$	23.8	293	1219	29.9
$a_1 = 30$ nm; $q_1 = -2e$	55.3	447	1260	3.57
$a_1 = 20$ nm; $q_1 = 0$	0	0	1235	100
$a_1 = 20$ nm; $q_1 = -1e$	35.7	361	1275	13.7
$a_1 = 20$ nm; $q_1 = -2e$	82.9	547	1333	0.50
$a_1 = 10$ nm; $q_1 = 0$	0	0	1251	100
$a_1 = 10$ nm; $q_1 = -1e$	71.3	511	1330	1.15
$a_1 = 10$ nm; $q_1 = -2e$	165.8	780	1441	0

Table 4.3: Energetic considerations and the percentage of aggregation for FeO - ice collisions at T = 150 K and C_R = 0.9 (the surface point charge model). FeO particle has the fixed radius and charge ($a_2 = 0.2$ nm, $q_2 = -1e$), and the size and charge of ice particle is varied. The collision geometry is shown in Figure 4.3a

ice particle	Coulomb barrier, E_{Coul} , meV	$v_{\text{rel}}^{\text{min}}$, m s ⁻¹	$v_{\text{rel}}^{\text{max}}$, m s ⁻¹	aggregation, %
$a_1 = 30$ nm; $q_1 = 0$	0	0	1007	100
$a_1 = 30$ nm; $q_1 = -1e$	23.7	199	987	34.7
$a_1 = 30$ nm; $q_1 = -2e$	55.3	303	1012	5.2
$a_1 = 20$ nm; $q_1 = 0$	0	0	1094	100
$a_1 = 20$ nm; $q_1 = -1e$	35.7	244	1059	17.4
$a_1 = 20$ nm; $q_1 = -2e$	82.9	372	1092	0.91
$a_1 = 10$ nm; $q_1 = 0$	0	0	1267	100
$a_1 = 10$ nm; $q_1 = -1e$	71.3	345	1165	1.91
$a_1 = 10$ nm; $q_1 = -2e$	165.9	526	1225	0

Figure 4.5 shows coalescence results where the size of the ice particle has been increased to 100 nm. These data reinforce the fact that, for like-charge collisions, an increase in the size of the ice particle from 10 nm to 100 nm can lead to an order of magnitude increase in the probability of aggregation. Also given in Figure 4.5 are data calculated for a charge of $-2e$ on the ice particle. In this case, the probability of aggregation is increased from zero (for $a_1 < 20$ nm) to more than 40% (for $a_1 \approx 100$ nm), thus providing a mechanism whereby ice

Table 4.4: Energetic considerations and the percentage of aggregation for MgO - ice collisions at $T = 150$ K and $C_R = 0.9$ (the surface point charge model). MgO particle has the fixed radius and charge ($a_2 = 0.2$ nm, $q_2 = -1e$), and the size and charge of ice particle is varied. The collision geometry is shown in Figure 4.3a

ice particle	Coulomb barrier, E_{Coul} , meV	$v_{\text{rel}}^{\text{min}}$, m s ⁻¹	$v_{\text{rel}}^{\text{max}}$, m s ⁻¹	aggregation, %
$a_1 = 30$ nm; $q_1 = 0$	0	0	1341	100
$a_1 = 30$ nm; $q_1 = -1e$	23.7	252	1311	29.9
$a_1 = 30$ nm; $q_1 = -2e$	55.3	384	1340	3.57
$a_1 = 20$ nm; $q_1 = 0$	0	0	1481	100
$a_1 = 20$ nm; $q_1 = -1e$	35.7	309	1425	13.7
$a_1 = 20$ nm; $q_1 = -2e$	82.9	470	1465	0.50
$a_1 = 10$ nm; $q_1 = 0$	0	0	1776	100
$a_1 = 10$ nm; $q_1 = -1e$	71.3	436	1607	1.15
$a_1 = 10$ nm; $q_1 = -2e$	165.9	665	1676	0

particles can increase their charge, but still participate in aggregation processes.

4.5 Aggregation of oxide particles

The abundant presence of metal oxide and silica particles in meteoric smoke in the MLT region [57] leads to a possibility that these may also aggregate, and with radii ranging from 0.2 nm to 5 nm, these are amongst the smallest particles found in this region of atmosphere. Their size means that if the point charge approximation is used to describe the surface charge, then the exact location of the point charge on the surface of each colliding particle becomes very important because, as shown previously by Filippov et al. [23], collision geometry can alter the strength of the electrostatic interaction. This statement does not apply to most like-charged interactions because, as shown in Table 4.5, the height of the Coulomb barrier prevents very small like-charged particles (less than 5 nm radius) from aggregating. Note that collisions between like-charged silica particles have lower energy barriers than those calculated for collisions between iron oxide particles. For collisions involving larger particles ($a_1 = 5$ nm), despite the lower energy barriers the minimum initial velocity ($v_{\text{rel}}^{\text{min}}$) required to overcome the barriers for SiO₂ are still higher than

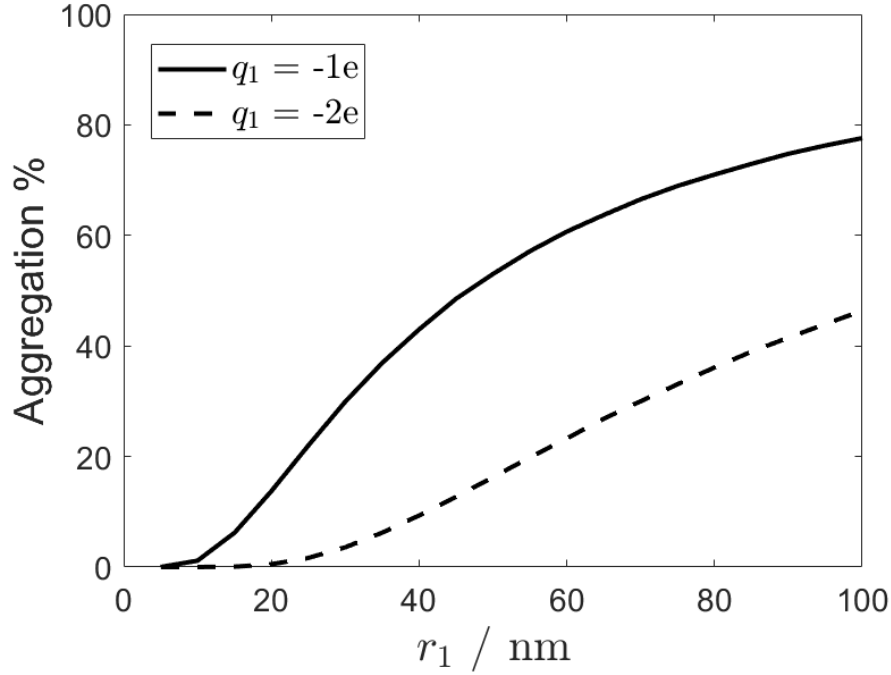


Figure 4.5: Aggregation probability, presented as percentage, for a collision between SiO_2 particle ($a_2 = 0.2 \text{ nm}$, $q_2 = -1e$) and ice particle ($q_1 = -1e$ and $q_1 = -2e$) whose size varies from $a_1 = 1 \text{ nm}$ to 100 nm .

those for FeO particles. These effects arise from differences in density and mass.

For collisions between charged and neutral particles the Coulomb barrier is always zero, and their aggregation is driven by polarisation effects. Again, orientation of the particles becomes important and here two limiting cases are considered. Table 4.5 corresponds to the case where the point charge on the surface of particle 2 faces the neutral particle 1 (geometry shown in Figure 4.3b, but we now assume that particle 1 is neutral). In this configuration, there is strong attraction as the point charge approaches the neutral particle leading to a re-distribution (polarisation) of surface charge on the latter. This leads to a significant increase in the binding energy between the particles (E_0) and results in coalescence through the subsequent action of the coefficient of restitution. Irrespective of particle composition, the absence of a Coulomb barrier results in aggregation for all of the examples examined in Table 4.5.

Table 4.5: Energetic considerations and the percentage of aggregation for SiO₂ - SiO₂ and FeO - FeO collisions at T = 150 K and C_R = 0.9 (the surface point charge model). Particle 2 has the fixed radius and charge (a₂ = 0.2 nm, q₂ = -1e), and the size and charge of particle 1 is varied. The collision geometry is shown in Figure 4.3b.

SiO ₂ - SiO ₂	Coulomb barrier, E _{Coul} , meV	v _{rel} ^{min} , (m s ⁻¹)	v _{rel} ^{max} , (m s ⁻¹)	agg, %
a ₁ = 0.2 nm; q ₁ = 0	0	0	8112	100
a ₁ = 1.0 nm; q ₁ = 0	0	0	3914	100
a ₁ = 5.0 nm; q ₁ = 0	0	0	2187	100
a ₁ = 0.2 nm; q ₁ = -1e	2889	4566	9168	0
a ₁ = 1.0 nm; q ₁ = -1e	622	1504	4156	0
a ₁ = 5.0 nm; q ₁ = -1e	125	671	2273	0.02
FeO - FeO				
a ₁ = 0.2 nm; q ₁ = 0	0	0	2876	100
a ₁ = 1.0 nm; q ₁ = 0	0	0	1811	100
a ₁ = 5.0 nm; q ₁ = 0	0	0	1307	100
a ₁ = 0.2 nm; q ₁ = -1e	3056	3175	4150	0
a ₁ = 1.0 nm; q ₁ = -1e	679	1068	2055	0
a ₁ = 5.0 nm; q ₁ = -1e	136	476	1376	0.03

The data displayed in Table 4.6 correspond to the case least favourable to aggregation between neutral and charged particles. Here, the point charge on the surface of particle 2 faces away from the neutral particle 1 (geometry shown in Figure 4.3c but particle 1 is neutral). In this orientation, collisions with the smallest charged particles (a₂ = 0.2 nm) strongly favour aggregation often resulting in a 100% coalescence outcome, even though the maximum relative initial velocity of colliding particles required for coalescence is significantly lower. When the charged particle is very small, the interaction resembles a point charge - neutral particle case which is always attractive. Note that the aggregation remains almost complete (100%) even when both charged and neutral particles are extremely small (a₁ = a₂ = 0.2 nm) and highly polarisable (FeO, MgO). In general, there are distinct differences between the aggregation outcomes for SiO₂ particles and the more polarisable FeO particles, with the FeO collisions consistently having higher percentage aggregation and MgO particles lie somewhere between the two. For the geometry shown in Figure 4.3c, the aggregation percentage drops very significantly as the size of the charged

Table 4.6: Energetic considerations and the percentage of aggregation for SiO₂ - SiO₂ and FeO - FeO collisions at T = 150 K and C_R = 0.9 (the surface point charge model). Particle 2 has the fixed charge (q₂ = -1e) and particle 1 is neutral (q₁ = 0), and the size of both particles is varied. The collision geometry is shown in Figure 4.3c.

	SiO ₂ - SiO ₂		FeO - FeO		MgO - MgO	
	$v_{\text{rel}}^{\text{max}}$, m/s	aggregation,%	$v_{\text{rel}}^{\text{max}}$, ms ⁻¹	aggregation,%	$v_{\text{rel}}^{\text{max}}$, ms ⁻¹	aggregation,%
$a_2 = 0.2$ nm; $a_1 = 0.2$ nm	364	58.3	445	96.0	495	93.1
$a_2 = 0.2$ nm; $a_1 = 1.0$ nm	569	99.7	625	100	714	100
$a_2 = 0.2$ nm; $a_1 = 5.0$ nm	737	100	748	100	869	100
$a_2 = 1.0$ nm; $a_1 = 0.2$ nm	34.2	0.29	29.8	0.49	29.3	0.29
$a_2 = 1.0$ nm; $a_1 = 1.0$ nm	14.6	9.75	18.0	36.3	20	30.4
$a_2 = 1.0$ nm; $a_1 = 5.0$ nm	22.8	57.2	25.2	91.4	28.7	88.4
$a_2 = 5.0$ nm; $a_1 = 0.2$ nm	9.00	0.01	0.0*	0.0*	0.0*	0.0*
$a_2 = 5.0$ nm; $a_1 = 1.0$ nm	1.42	0.02	1.15	0.04	1.24	0.03
$a_2 = 5.0$ nm; $a_1 = 5.0$ nm	0.59	1.01	0.72	4.78	0.80	3.81

* zero within the accuracy of our calculations

particle 2 grows. This is because any surface polarisation response on the neutral particle due to the presence of a point charge on the surface of particle 2 is now hindered by the volume of the charged particle itself. Finally, when the charged particle is large and the neutral one is very small, the surface polarisation effects on the neutral particle are negligible and aggregation does not occur. This can be illustrated by comparing two examples: if $a_2/a_1 = 10$ (radius of charged particle is ten time bigger than that of neutral particle) the aggregation is 0%, and if $a_1/a_2 = 10$ (radius of neutral particle is ten time bigger than that of charged particle) the aggregation is 100% (Table 4.6).

Finally, if the results given in Tables 4.5 and 4.6 for percentage aggregation are compared, it can be seen that there are differences that depend on how the point charges are orientated on these particles, all of which have comparatively low dielectric constants. In all instances where a charge is pointing towards a large polarisable particle (Table 4.5, when $q_1 = 0$ and $q_2 = -1e$), aggregation is 100%. However, when in Table 4.6 the charge is located at 180° from the adjacent particle (case 4.3c in Figure 4.3), aggregation drops to 58% when in the least polarisable particle pair, SiO_2 , the neutral particle has a radius of 0.2 nm. As the dielectric constant increases on moving to MgO and FeO the particles become more polarisable and the percentage aggregation increases.

4.6 Brief discussion of main results and conclusions

This work is focused on the description of basic principles underpinning the coalescence of ice and dust particles in thermal motion. Specific examples considered in this study examine coalescence between particles, commonly found in the mesosphere, at the temperature $T = 150$ K which is typical to this region of atmosphere. Pair interactions of charged particulates follow the Coulomb law with an additional contribution from the attraction between like-charged and neutral-charged pairs driven by induced polarisation of the particle surface charge. The latter interactions can be significant at short separation distances between interacting particles. Low temperatures in the MLT region imply that the colliding particles are not very energetic, and for a like-charged pair, the relative kinetic energy is often insufficient to overcome the Coulomb barrier. However, the high energy tail of the Maxwell-Boltzmann distribution of the relative velocity at $T = 150$ K provides an adequate amount of collisions leading to aggregation both between like-charged particles of ice and dust and between dust particulates themselves.

The like-charged attraction is more common (and stronger) between particles with low charge. This collision scenario can be described by a localised, point surface charge model and one where the charge is assumed to be uniformly distributed over the entire surface of a particle. An earlier study by Filippov et al. [23] of the interaction between positively charged particles, showed that, for particles with low dielectric constants, there is a difference in predicted behaviour between these two models. As the dielectric constant increases in value, results from the two models became equivalent. Similarly, differences in orientational geometry of a collision (extreme scenarios are shown in Figures 4.3b and 4.3c) were also found to be evident at low dielectric constants; but again these disappeared as the value of the dielectric constant increased.

Chapter 5

Charged particle dynamics in dry powder inhalers: Evidence of particle scavenging

The work in this chapter is a collaboration with the Inhaled Delivery team at GSK (Dr. David Prime, Cheng Pang and Melanie Hamilton) in Ware. The study focuses on the electrostatic cohesion of pharmaceutical aerosols by investigating aggregation pathways via both static and dynamic analysis.

5.1 Introduction

Drug delivery to the lungs in the form of aerosolised fine particles has significant advantages over other forms of administration. The lungs present a large permeable membrane where the active ingredients can be readily absorbed, meaning that, in comparison to other delivery systems, lower doses can be as effective. Delivery is achieved through a metered dose inhaler (MDI) or dry powder inhaler (DPI), within which the particulate drug becomes aerosolised and carried into the lungs by the human breath. However, it is recognised that in order to achieve the desired result, the particles—consisting of a mixture of the active pharmaceutical ingredient (API) and excipients (lactose)—are

required to have diameters in the range 0.5 μm to 10 μm . Any smaller than 0.5 μm and the particles are exhaled and those larger than 10 μm become lodged in the throat and never reach the lungs [63].

Table 5.1: The effect of particle diameter d on the deposition quality of particles within the lungs. [64]

d (μm)	Outcome
$d > 10$	Impaction with throat
$0.5 < d < 10$	Deposition in lungs
$d < 0.5$	Expelled upon exhalation

The powder particles within a DPI inherently possess bipolar charge due to triboelectrification in the manufacturing process. This bipolar charge is both a blessing and a curse, with the charge increasing the quality of deposition within the lungs, but also increasing the likelihood of aggregation of particles into larger clusters which are less able to make it to the lungs [64, 65].

The overall aim of this project is to be able to use computational methods to accurately represent—both statically and dynamically—the interactions present in the airflow of particles shortly after the particles exit the blisters within the manifold of a DPI in order to gain an insight into the aggregation patterns between charged pharmaceutical powder particles. The aim is to achieve this using data collected from experiments conducted using the Dekati[®] BOLAR[™] device in collaboration with the many-body electrostatic model to create models for various systems, including systems ranging in size from 2 body interactions to systems with over 300 particles.

BOLAR[™]

The Dekati[®] Bipolar Charge Meter, or BOLAR[™], (shown in Figures 5.1 and 5.2 [66]) measures the bipolar charge of aerosolised particles as a function of

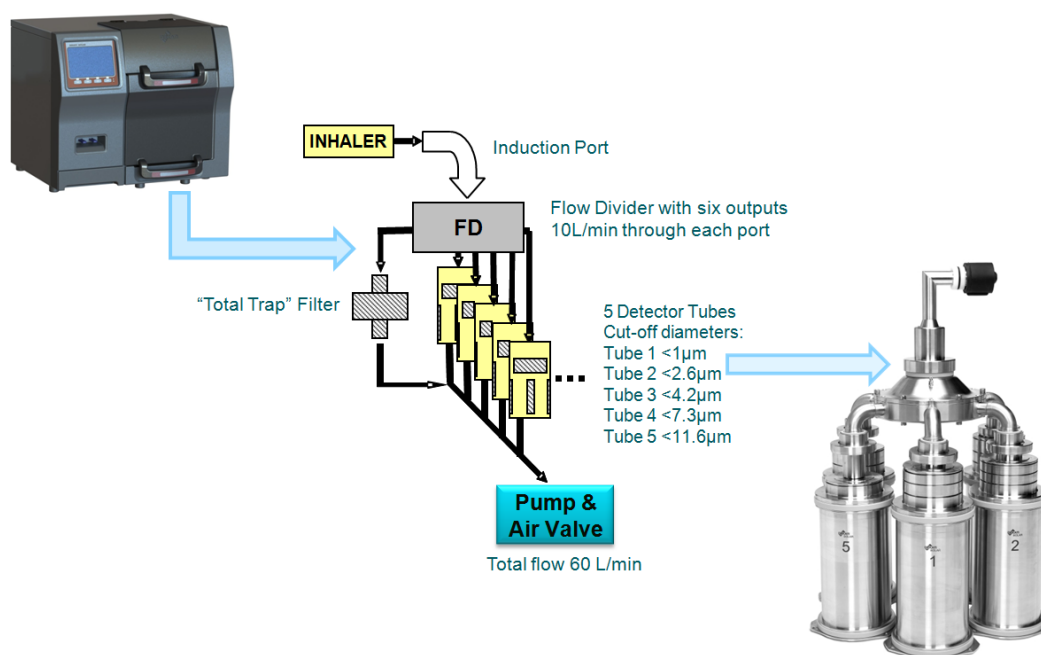


Figure 5.1: Schematic of the Dekati[®] BOLAR[™]. [67]

particle size. Inhaled drug product is aerosolised at 60 L/min flow rate; the dose is then divided six ways by the flow divider and aerodynamically sized prior to entering a detector tube below the impactor stages. The impactor arrangement with differing size cut-offs determines the size of the particles reaching the detector. Five detectors measure positive and negative charge for the various size fractions (Table 5.2), whilst the sixth detector which acts similarly to a Faraday Pail measures the net charge and serves as a control. The inner surfaces are positively charged to +1 kV which attract negatively charged particles and the outer detectors, held at ground potential, attract positively charged particles. Furthermore, the BOLAR technique allows mass recovery of the formulation components (APIs and excipients) to determine the charge to mass ratios [67].

The action of manufacturing and processing pharmaceutical powders cause the particles to collide both with each other and their containers, causing the powder to gain electrical charge via the triboelectric effect. The charge carried by inhalation aerosols has been found to have an effect on both the

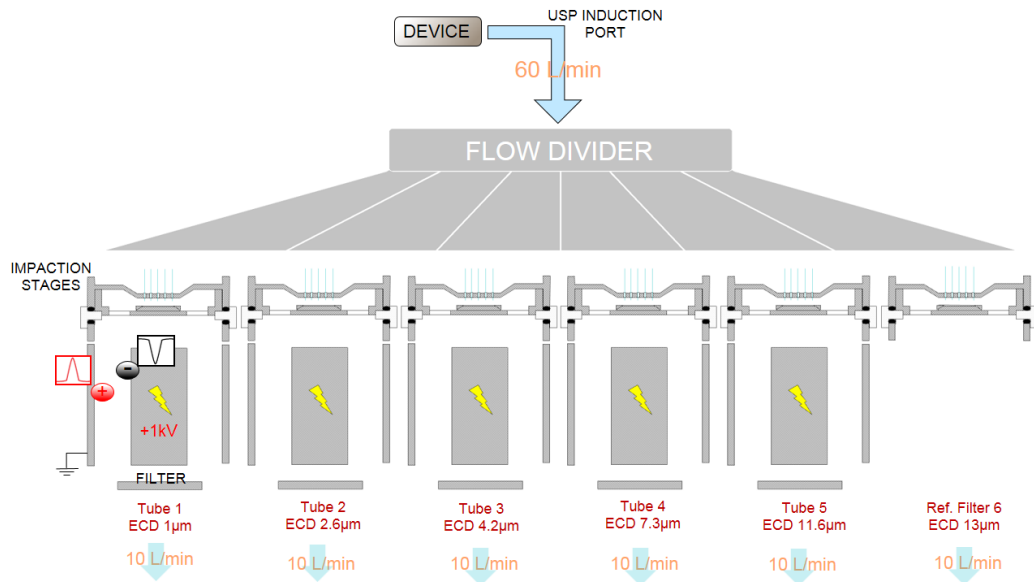


Figure 5.2: Dekati[®] BOLAR[™] internal components. [67]

performance of the inhaler device itself and—as previously stated—deposition of particles within the lungs due to the aggregation of powder particles into larger aggregates, lessening their ability to flow effectively down the airways [68]. The BOLAR is an instrument designed to replicate the inhalation of powders at a controllable flow rate and is used to measure the mass and the amount of bipolar electrical charge for the range of particle size fractions shown in Table 5.2 [67].

Table 5.2: A table showing the size fractions corresponding to each of the compartments within the BOLAR equipment, and also the diameters equal to the midpoint of the size fraction. [68]

Detector Tube	Size Fraction (μm)	Average Particle Diameter (μm)
1	$d < 0.95$	0.48
2	$0.95 < d < 2.60$	1.78
3	$2.60 < d < 4.17$	3.39
4	$4.17 < d < 7.29$	5.73
5	$7.29 < d < 11.57$	9.43

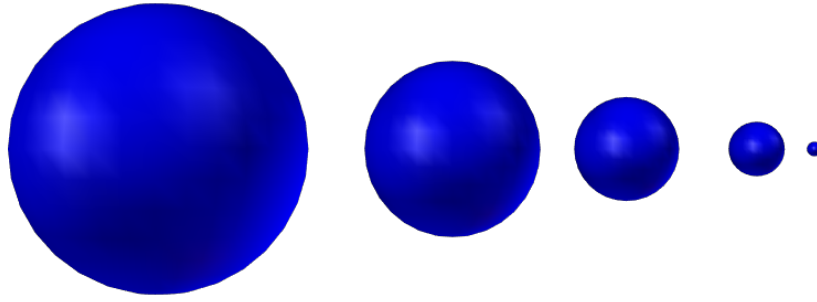


Figure 5.3: A visualisation of the relative sizes of particle with diameters of $9.43 \mu\text{m}$, $5.73 \mu\text{m}$, $3.39 \mu\text{m}$, $1.78 \mu\text{m}$ and $0.48 \mu\text{m}$ from left to right.

The average particle diameter in Table 5.2 is calculated by assuming an equal distribution of particle sizes passing through each of the size fractions, therefore taking the midpoint of each size fraction as the average particle diameter. The relative sizes for typical particles from each of the size fractions are shown in Figure 5.3.

5.2 Framing the computational problem

5.2.1 Two-body collisions

Consider the problem of two oppositely charged powder particles colliding and subsequently separating in a constant airflow, where the Coulombic attraction of the charged particles works against the kinetic energy of the separation immediately after collision. This system is analogous to escape velocities in physics, where gravitational forces between two bodies oppose the kinetic energy of an escaping object; if the object has an initial velocity faster than the escape velocity v_e it will overcome the gravitational pull of the larger body. v_e can be calculated for when the kinetic energy of the object is equal to the total gravitational potential energy at the surface of the larger body. This

relationship is shown by

$$\begin{aligned} E_{\text{K}} &= E_{\text{GP}} \\ \frac{1}{2}mv_e^2 &= \frac{GMm}{r} \\ v_e &= \sqrt{\frac{2GM}{r}} \end{aligned}$$

where E_{K} is the kinetic energy of the escaping object, E_{GP} is the gravitational potential energy on the surface, G is the gravitational constant, M is the mass of the larger object, m is the mass of the escaping object and r is the radius of the larger object. In our case, E_{K} is replaced by the internal kinetic energy of the separating particles immediately after the collision E_{IK} and the attraction due to the gravitational potential energy is exchanged with the electrostatic interaction energy at the point of contact $E_{\text{electrostatic}}$. The outcome of a collision between particles is dependent upon the relationship between the magnitudes of both E_{IK} and $E_{\text{electrostatic}}$, where

$$\text{if } |E_{\text{IK}}| > |E_{\text{electrostatic}}|; \text{ No coalescence,} \quad (5.1)$$

$$\text{if } |E_{\text{IK}}| < |E_{\text{electrostatic}}|; \text{ Particles will coalesce.} \quad (5.2)$$

$E_{\text{electrostatic}}$ is the electrostatic interaction energy calculated at the point of contact where the surface-to-surface separation $s = 0 \text{ }\mu\text{m}$, and is calculated using the uniform model proposed in 2018 by Lindgren et al. [32].

The internal kinetic energy of a system E_{IK} is the kinetic energy of the individual components of a many-body system in the centre of mass reference frame. In the case of two particles with the same speed colliding, E_{IK} depends on 4 parameters: the particles initial speed v_j ; the mass of each particle m_j ; the angle between the velocity vectors of the particles 2θ ; and the coefficient of restitution of the particles C_{R} . Calculating the internal kinetic energy requires knowledge of the momentum of the collision. In the case considered here (shown

in Figure 5.4), the particles are travelling at the same velocity in the y-axis, so the only contribution to the collision's momentum is due to the differences of the velocities in the vector of collision, where the initial particle velocities in this vector $\mathbf{v}_{j,i}$ depend on v_j and θ .

$$\mathbf{v}_{1,i} = v_1 \sin(\theta) \quad (5.3)$$

$$\mathbf{v}_{2,i} = -v_2 \sin(\theta) = -\mathbf{v}_{1,i} \quad (5.4)$$

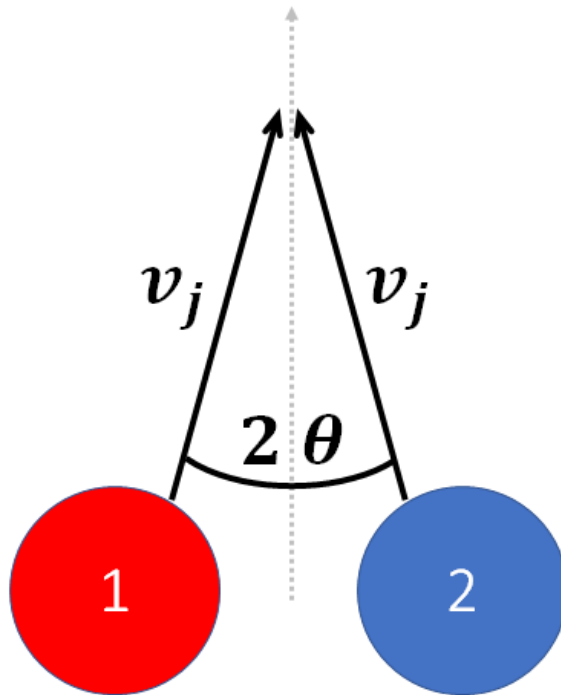


Figure 5.4: A visual representation of a collision between two particles with opposite charges (negative = blue, positive = red) and different radii. Each particle has linear speed v_j travelling at an angle θ either side of the y-axis moving in the direction of the arrows shown.

These initial velocities can be used to calculate the overall momentum of the colliding system. The law of conservation of momentum states that the overall momentum of the system does not change as shown in (5.5).

$$m_1 \mathbf{v}_{1,i} + m_2 \mathbf{v}_{2,i} = m_1 \mathbf{v}_{1,f} + m_2 \mathbf{v}_{2,f} \quad (5.5)$$

In order to be able to calculate the velocities in the collision vector after the

impact for each particle $\mathbf{v}_{j,f}$, the kinetic energy lost in the collision also needs to be accounted for. This is resolved by considering the coefficient of restitution C_R , where

$$C_R = \frac{\mathbf{v}_{2,f} - \mathbf{v}_{1,f}}{\mathbf{v}_{1,i} - \mathbf{v}_{2,i}} \quad (5.6)$$

with $C_R \approx 0.5\text{--}0.8$ for pharmaceutical powders [69]. Combining (5.5) and (5.6) gives solutions to $\mathbf{v}_{1,f}$ and $\mathbf{v}_{2,f}$ in terms of m_1 , m_2 , $\mathbf{v}_{1,i}$, $\mathbf{v}_{2,i}$ and C_R .

$$\mathbf{v}_{1,f} = \frac{m_1 \mathbf{v}_{1,i} + m_2 \mathbf{v}_{2,i} - m_2 C_R (\mathbf{v}_{1,i} - \mathbf{v}_{2,i})}{m_1 + m_2} \quad (5.7)$$

$$\mathbf{v}_{2,f} = \frac{m_1 \mathbf{v}_{1,i} + m_2 \mathbf{v}_{2,i} + m_1 C_R (\mathbf{v}_{1,i} - \mathbf{v}_{2,i})}{m_1 + m_2} \quad (5.8)$$

In order to calculate the internal kinetic energy of the system, the velocity of each particle needs to be considered in relation to the system's centre of mass velocity \mathbf{v}_{CM} .

$$\mathbf{v}_{\text{CM}} = \frac{1}{M} \sum_{j=1,2} m_j \mathbf{v}_{j,f} \quad (5.9)$$

Knowledge of \mathbf{v}_{CM} leads to a solution for E_{IK} in the form

$$E_{\text{IK}} = \frac{1}{2} \sum_{j=1,2} m_j (\mathbf{v}_{j,f} - \mathbf{v}_{\text{CM}})^2 \quad (5.10)$$

By using this approach, it is possible to evaluate the internal kinetic energy of the interaction over a range of initial speeds v_j and incoming angles θ for collisions between particles of any given mass. This data can then be used to predict whether or not a collision between two charged particles will aggregate by using $E_{\text{electrostatic}}$ as a reference point. Once E_{IK} has been calculated (5.1) and (5.2) can be used to determine the outcome of the interaction.

The molecular dynamic simulations in this Chapter were all run with a timestep of 0.05 ns for total simulation times ranging from 15 to 200 μs using the method

described in Section 2.2.

5.3 Electrostatic cohesion of colliding powder particles

The data analysed in this section looks at the interaction between particles consisting solely of particles composed of lactose. Experimental BOLAR™ data used in this section was produced by the Inhaled Delivery team at GSK. The interaction considered from this data consists of lactose particles with bipolar charge with a dielectric constant k_j of 2.9, of radius a_j and charge q_j , colliding in air ($k_0 = 1$). The coefficient of restitution C_R is given a values of 0.8 and 0.5 for relevant calculations.

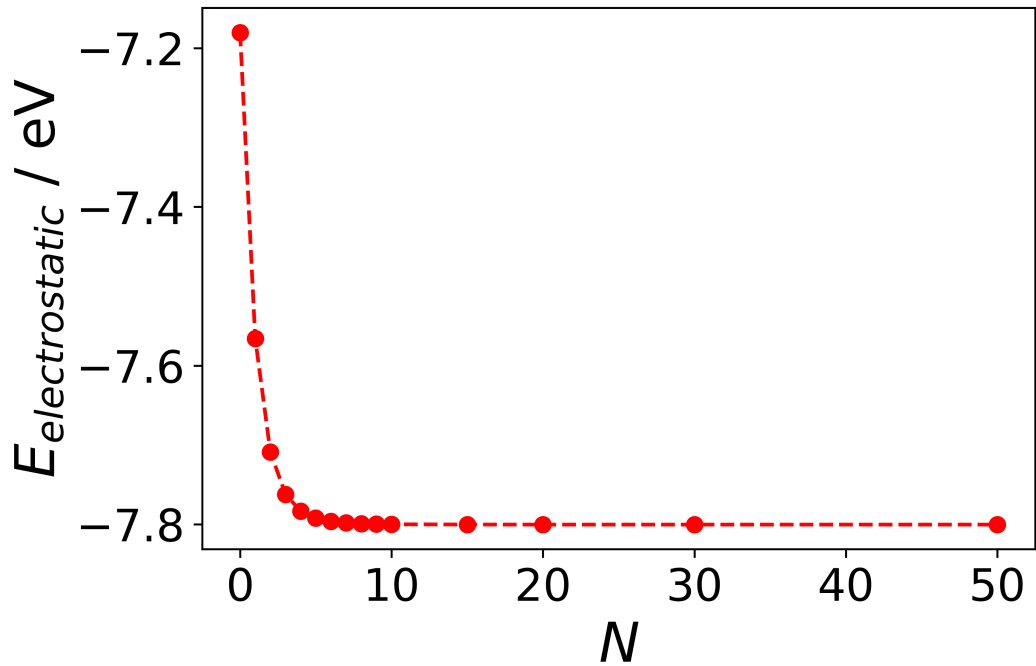


Figure 5.5: $E_{\text{electrostatic}}$ as a function of the number of terms used N for two charged lactose particles where $k_{1,2} = 2.9$, $a_{1,2} = 1.0 \mu\text{m}$, $q_1 = +100e$, $q_2 = -100e$ interacting in air ($k_0 = 1.0$).

The low dielectric constant of lactose may lead to the assumption that the pure non-polarisable coulombic interactions would be sufficient to represent the

electrostatic interactions between the spheres. Looking at an example of an electrostatic interaction between two oppositely-charged lactose particles—as shown in Figure 5.5—the monopolar interaction between non-polarisable particles ($N = 0$) gives an interaction energy of -7.18 eV. Introducing just a single term to the model ($N = 1$) to represent the charge-induced dipole interactions results in an interaction energy of -7.57 eV—a 5% increase in the interaction energy—with the interaction converging to within 1 meV at just 8 terms to an increase in the interaction energy of 8%. This rapid convergence in $E_{\text{electrostatic}}$ allows for the use of a low number of terms while still retaining a high level of accuracy.

The amount of charge present on the surface of the particles in each size fraction q_j was calculated by dividing the total charge for a compartment—shown in Figure 5.6—by the number of particles for each compartment.

The number of particles for each compartment is found by dividing the total

Table 5.3: A table showing the average charge per particle q_j for the outer detector (OD) and inner detector (ID) for each compartment in the BOLAR™.

Compartment	q_j ($\times 10^{-3}$ fC)	Compartment	q_j ($\times 10^{-3}$ fC)
OD1	+20.24	ID1	-5.85
OD2	+626.28	ID2	-521.68
OD3	+1315.05	ID3	-1136.76
OD4	+2930.00	ID4	-2101.45
OD5	+7096.67	ID5	-6575.20

mass of each size fraction by the mass density of lactose (1520 kg m^{-3}) to find the total volume of lactose present and then dividing this total volume by the volume of a single spherical particle using the diameters from Table 5.2. The values of q_j for particles in each compartment are shown in Table 5.3. The raw mass data used to calculate these values is presented in Table 5.4.

$E_{\text{electrostatic}}$ at the point of contact is calculated for each combination of oppo-

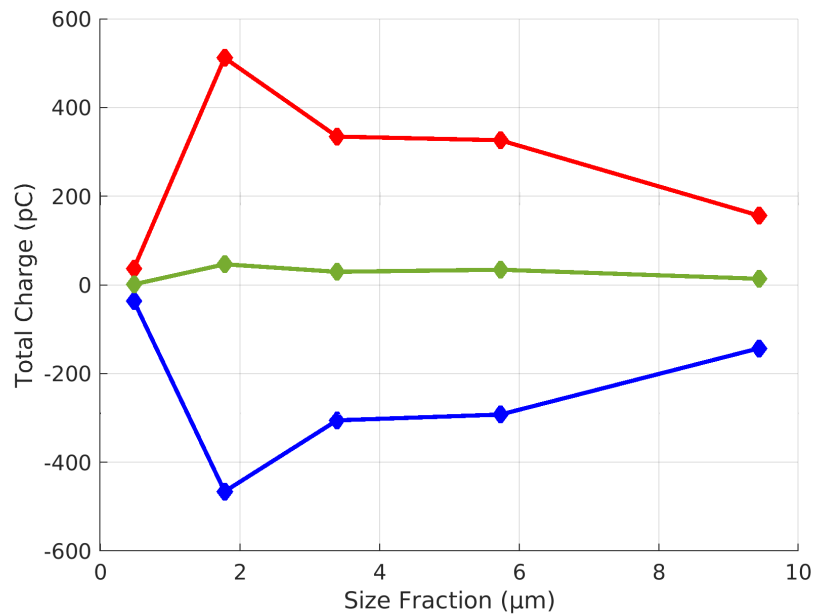


Figure 5.6: Charge data from a BOLAR™ run showing the total positive (red), negative (blue) and net (green) charge for lactose particles in each size fraction within the BOLAR™.

Table 5.4: Mass data obtained from the outer detector (OD) and inner detector (ID) for each compartment in the BOLAR™. Averages for the smallest size bin exclude the 0 μg results.

Prep	Mass per compartment / μg									
	OD1	OD2	OD3	OD4	OD5	ID1	ID2	ID3	ID4	ID5
1	0.19	3.83	8.06	16.05	17.35	0.00	4.38	8.21	18.30	18.96
2	0.14	4.18	8.41	18.98	15.93	0.54	3.86	9.25	28.25	12.13
3	0.00	2.74	5.97	14.44	12.28	0.00	3.03	6.57	15.07	14.16
4	0.20	3.82	9.28	17.10	13.51	0.00	4.68	9.04	23.31	12.65
Ave.	0.18	3.64	7.93	16.64	14.77	0.54	3.99	8.27	21.23	14.47

sitely charged particles and shown in Table 5.5. These are the values used as the baseline for the determination of the outcome of a collision between two particles—as stated in Equations (5.1) and (5.2)—with the relative magnitude of E_{IK} in relation to the magnitude of $E_{\text{electrostatic}}$ determining the outcome of the collision.

A plot of E_{IK} as a function of θ for the two most asymmetrically-sized particles with radii of 0.24 and 4.72 μm and $C_R = 0.8$ travelling with linear velocities $v_j = 6 \text{ m s}^{-1}$ is shown below in Figure 5.7. The plot displays a value for E_{IK}

Table 5.5: A table showing $E_{\text{electrostatic}}$ at the point of contact in eV for all possible combinations of oppositely charged particles.

	OD1	OD2	OD3	OD4	OD5
ID1	-16	-224	-244	-325	-481
ID2	-563	-11198	-16079	-24367	-38792
ID3	-693	-16837	-26857	-44193	-74946
ID4	-786	-21411	-36975	-65543	-118872
ID5	-1528	-43619	-80827	-153836	-299633

for a head on collision ($\theta = 90^\circ$) of around 25 keV which is around 20-50 times the magnitude of $E_{\text{electrostatic}}$ for the relevant interactions shown in Table 5.5. This is a clear example of a collision with too much energy that would lead to a complete separation of the particles. A closer look at the plot given inset in Figure 5.7 that shows the regions where E_{IK} is more comparable to $E_{\text{electrostatic}}$. This region clearly shows points of intersection between E_{IK} and $E_{\text{electrostatic}}$ that signify the critical angles (θ_{crit}) where where any deviation from this angle will alter the outcome of the collision for two particles with this speed. For the interaction between particles from OD1 and ID5 (red plot, $E_{\text{electrostatic}} = -1528$ eV), θ_{crit} is around 15° , whereas for the weaker interaction for particles from OD5 and ID1 (blue plot, $E_{\text{electrostatic}} = -482$ eV) has a much lower value for θ_{crit} of 8° .

The contour plots in Figure 5.8 show E_{IK} for a range of colliding systems. In each of the figures, the collisions resulting in a value of E_{IK} lower than $E_{\text{electrostatic}}$ are coloured yellow or red, whereas those above this value are in the blue region. The interactions between similarly sized particles are shown in Subfigures 5.8a and 5.8d; these interactions show very small critical angles even at lower velocities v_j of 5 m/s ($\theta_{\text{crit}} < 3^\circ$), indicating a very low probability of particles aggregating in the event of a collision.

In contrast, the interactions between asymmetrically sized particles, presented

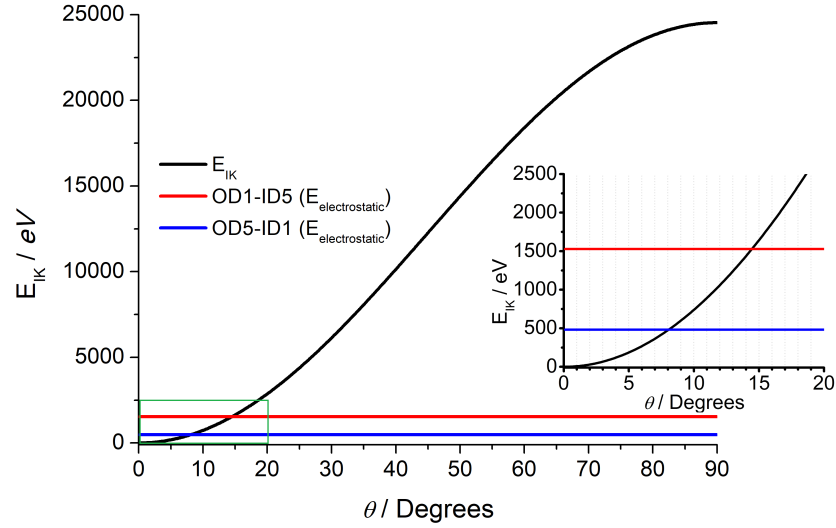


Figure 5.7: A plot showing the internal kinetic energy of the system E_{ik} as a function of θ for the collision between the largest ($a_1 = 4.72 \mu\text{m}$) and smallest ($a_2 = 0.24 \mu\text{m}$) particles with $v_j = 6 \text{ m s}^{-1}$ (black line). Also shown is $E_{\text{electrostatic}}$ for the interactions between particles where $q_1 = -6575 \text{ aC}$ and $q_2 = +20.24 \text{ aC}$ (red) and $q_1 = +7097 \text{ aC}$ and $q_2 = -5.85 \text{ aC}$ (blue). The inset data shows the region where the 3 plots are comparable in magnitude, indicated by the green rectangle on the main plot.

in Subfigures 5.8b and 5.8c, show much larger values of θ_{crit} with fairly significant values ($\theta_{\text{crit}} \geq 5^\circ$) even at larger values of v_j up to 20 m/s. This observation supports the idea that larger charged particles will be more likely to scavenge a collection of smaller particles across its surface after a series of collisions. As the dielectric properties of the APIs used in the inhalers are comparable with those of lactose, it can be assumed that API/Lactose containing mixtures will behave in similar ways. The particle sizes for each of the APIs are generally smaller than those of lactose implying that, after a series of collisions within the inhaler's manifold, smaller API particles will typically be deposited across the surface of larger lactose particles.

The coefficient of restitution is speed of separation of two colliding particles relative to the speed of approach as shown in (5.6). Analysis of both the critical angles θ_{crit} and critical velocities v_{crit} for constant v_j and θ respectively for two systems that are identical with the exception of their values for C_R are shown

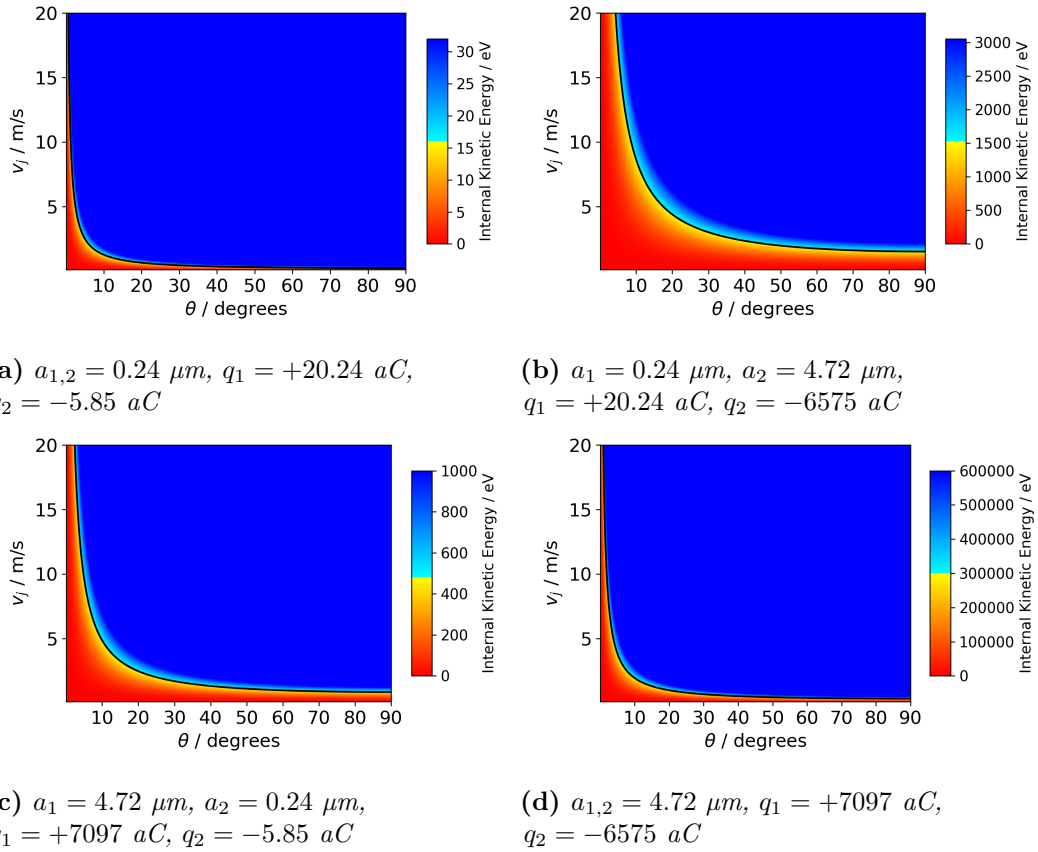


Figure 5.8: 2D plots of E_{IK} as a function of v_j and θ for 4 different colliding systems. The interactions presented are those between the smallest (a), most asymmetric (b) and (c), and largest (d) lactose particles. For each interaction, $E_{\text{electrostatic}}$ is represented for each plot as the black contour line, cohesive collisions are indicated by the red/yellow region, whereas the blue region indicates separation.

in Figure 5.9, with the plots shown in Subfigures 5.9a and 5.9b showing the results for C_R values of 0.8 and 0.5 respectively.

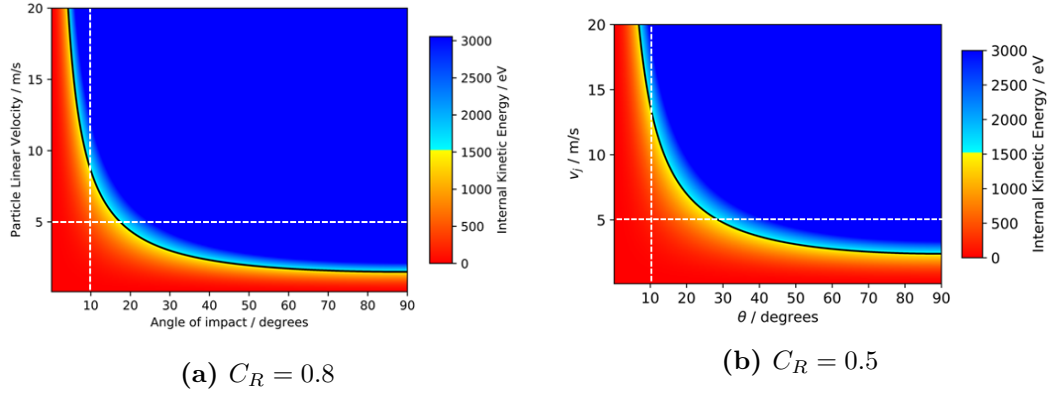


Figure 5.9: A comparison of the 2D plots for 2 systems containing a pair of colliding asymmetrically-sized lactose particles ($a_1 = 4.72 \mu\text{m}$, $a_2 = 0.24 \mu\text{m}$, $q_1 = +7097 \text{ aC}$, $q_2 = -5.85 \text{ aC}$). The systems are identical with the exception of the coefficient of restitution C_R . The white horizontal and vertical dashed lines are placed in identical positions in each subfigure for constant v_j and θ respectively.

At a first glance the two plots look extremely similar, but a closer look at the plots show a clear difference in the points of intersection between the dashed lines and the black contour line for $E_{\text{electrostatic}}$. The horizontal dashed lines in Figure 5.9 represent E_{IK} for when $v_j = 5 \text{ m s}^{-1}$, where the intersection point with the black line indicates the value of θ_{crit} in each case; when $C_R = 0.8$, $\theta_{\text{crit}} \approx 18^\circ$, whereas when C_R is given a lower value of 0.5, θ_{crit} increases to $\sim 30^\circ$. A similar pattern is observed with the vertical dashed lines at $\theta = 10^\circ$, revealing critical velocities of $\sim 8 \text{ m s}^{-1}$ and $\sim 13 \text{ m s}^{-1}$ for C_R values equal to 0.8 and 0.5 respectively.

5.4 Dynamics simulations of charge scavenging mechanisms

Dynamic analysis was performed to verify the observations made in Section 5.3. Both systems in this section have linear velocities v_j of 6.5 m s^{-1} , but the particles involved and values for θ are varied.

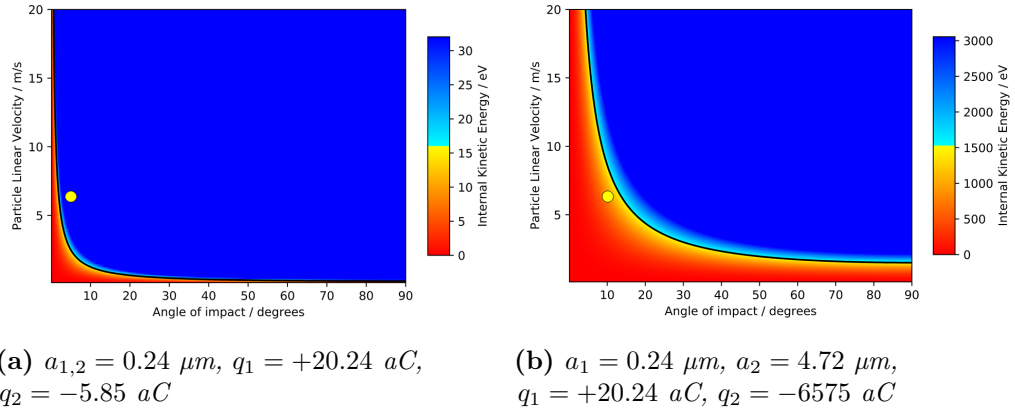


Figure 5.10: 2D plots of E_{IK} as a function of v_j and θ for 2 systems containing colliding lactose particles. The interactions presented are those between symmetrically- and asymmetrically-sized lactose particles. The yellow markers correspond to the input values for v_j and θ in the two dynamic simulations performed for each collision.

In the first simulation, the interaction is between the two smallest particles from OD1 and ID1 with $v_j = 6.5 \text{ m s}^{-1}$ and $\theta = 5^\circ$; here, the two particles collide and then separate with no aggregation. This result agrees with the results shown in Figure 5.10a, where the values used in this simulation correspond to a point in the blue region of the plot, above θ_{crit} .

The second simulation displays the interaction between two asymmetrically sized particles from OD1 and ID5 with $\theta = 10^\circ$; despite the increase in the angle, the particles still aggregate after the collision. This result also agrees with the results shown in Figure 5.10b, where the values used in this simulation corresponds to a result in the red region, below θ_{crit} .

In an airflow of particles, turbulence is likely to occur causing an increase in collision frequency of particles within the aerosol. Some of these collisions can lead to the formation of small charged aggregations. These aggregates are larger in size than their components, and therefore have a larger collision cross-section and leads to a higher likelihood of being impacted by another particle. In a collision between an aggregate and another particle, there are a range of possible outcomes: the particle can coalesce with the aggregate; the particle can completely break up the aggregate; or the particle can break part

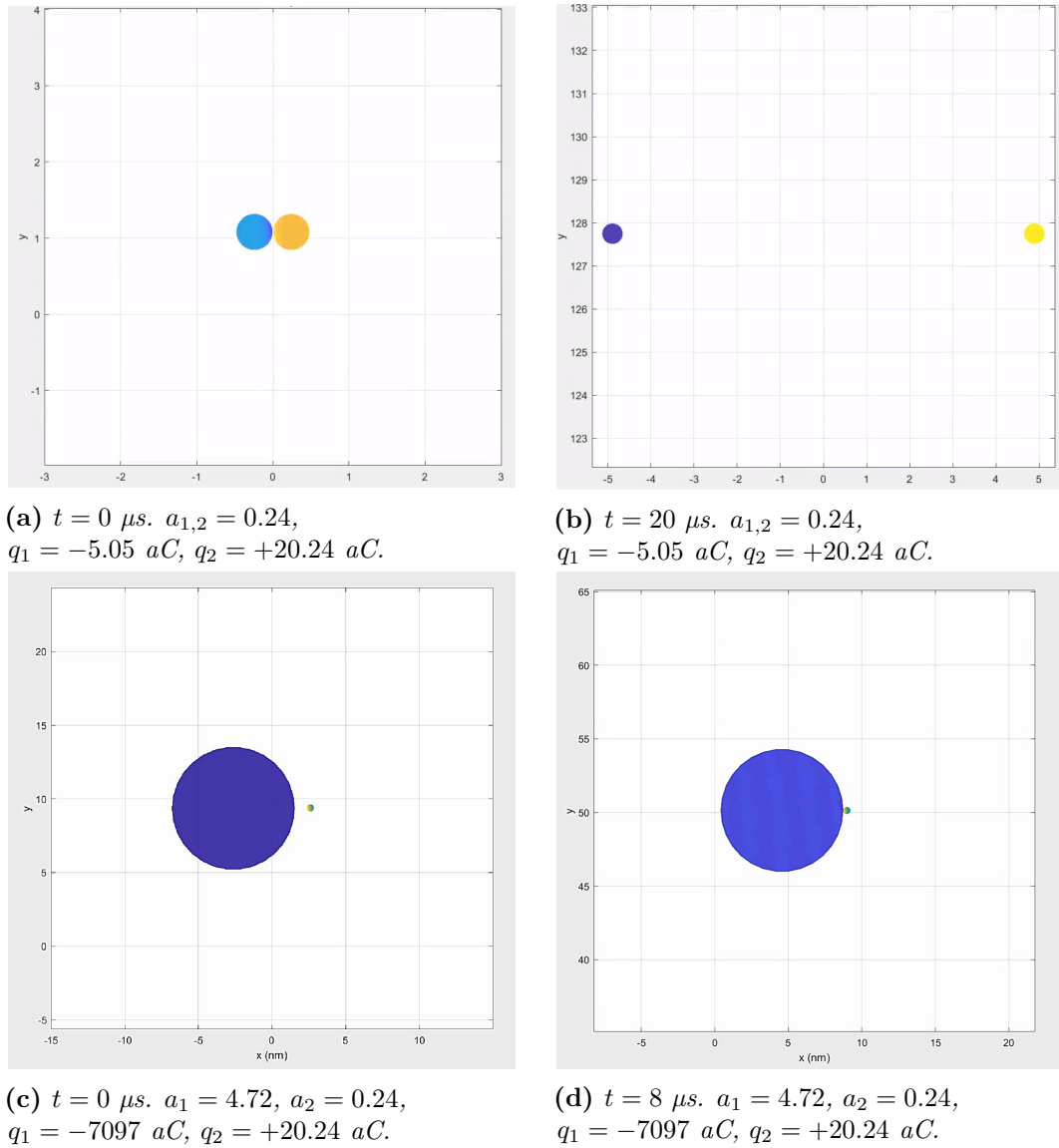


Figure 5.11: Screenshots of dynamic simulations at (a) 0 and (b) 20 μs for the dynamic simulations of the system described in Figure 5.10a ($a_{1,2} = 0.24 \mu\text{m}$, $q_1 = +20.24 \text{ aC}$, $q_2 = -5.85 \text{ aC}$, $v = 6.5 \text{ m s}^{-1}$, $\theta = 5^\circ$). Screenshots at (c) 0 and (d) 8 μs for the dynamic simulations of the system described in Figure 5.10b ($a_1 = 0.24 \mu\text{m}$, $a_2 = 4.72 \mu\text{m}$, $q_1 = +20.24 \text{ aC}$, $q_2 = -6575 \text{ aC}$, $v = 6.5 \text{ m s}^{-1}$, $\theta = 10^\circ$).

of the aggregate off and coalesce with the remainder. A dynamic simulation of a system containing a particle from compartment ID5 impacting an aggregated pair of particles from OD1 and ID1 was performed for a total simulation time of 15 μs .

Figure 5.12 shows the direct impact of the particle on the cluster results in the aggregated particles initially moving away from the impacting particle, although after around 5.5 μs the aggregate separates, with the positively charged particle

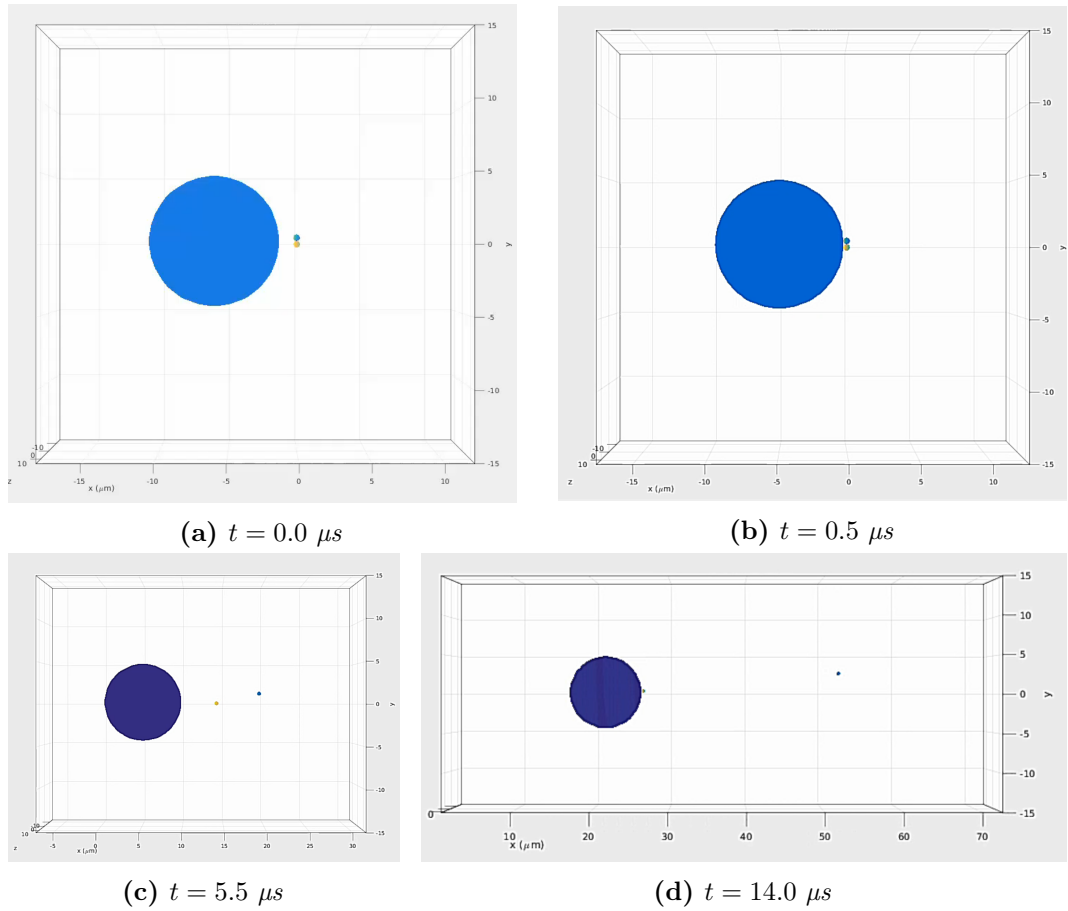


Figure 5.12: Screenshots at various timestamps for the dynamic simulation of a small two-body cluster ($a_{1,2} = 0.24 \mu m$, $q_1 = +20.24 aC$, $q_2 = -5.85 aC$) being impacted by the impact of a larger particle ($a_3 = 4.72 \mu m$, $q_3 = -6575 aC$) with an initial velocity of $1 m s^{-1}$.

being attracted back towards the larger particle, eventually aggregating with the larger particle. This supports the results shown in Figure 5.8, where the likelihood of an aggregation of asymmetric particles is higher than that of similarly-sized particles.

The scavenging of small aerosolised droplets and particles via the presence of a larger charged particle has been observed throughout nature, for example in cloud formation and in charged volcanic ash clouds, as well as commonly used in industrial processes. Due to the size range of the particles in a DPI, this same phenomenon can be assumed to be present within the particle airflow, with larger charged particles travelling slower within the airflow and being overtaken by smaller, bipolarly charged particles. In order to simulate this scav-

Table 5.6: Total number of positive n_+ and negative n_- particles within the pharmaceutical aerosol cloud with radius a .

a (μm)	n_+	n_-
0.24	100	100
0.89	40	40
1.70	10	10

enging, the aerosol cloud requires a large number of particles ($M > 100$). For a system of this size, the fast multipole method (FMM) technique—mentioned in Section 2.1.4—is ideal for reducing the computational cost of the simulations, and so was used for the following larger systems.

The simulations of the charge-scavenging process run in this study were of an aerosolised cloud of 300 lactose particles with bipolar charge passing over a singular larger particle with a diameter around twice that of the particles from largest size fraction in the BOLAR™, with $a = 10 \mu\text{m}$. The cloud contains particles from each compartment in the 3 smallest size fractions randomly positioned within the volume of a cube with edge length of $73.1 \mu\text{m}$, with the number of each type of particle shown in Table 5.6. The size and charge of each particle are taken from Tables 5.2 and 5.3 respectively. Based on the numbers of particles calculated from the mass data in Table 5.4, a uniform density of particles within this volume would expect to contain just 1 or 2 particles, although the regions in the DPI manifold close to the powder blister location contain areas of high turbulence which allow for increased particle densities.

Each dynamics simulation was run for a total simulation time of $200 \mu\text{s}$ with a time step of 0.05 ns using the Verlet integration method. The scavenging particle was placed $5 \mu\text{m}$ from the cloud in the positive x -direction with a velocity of 5.5 m s^{-1} in the same direction. The particles within the cloud were

all given the same velocity of 6.5 m s^{-1} in the positive x -direction. C_R in the simulations is 0.8. The only interactions in the simulations were electrostatically driven, with no influence from air resistance and gravity. Due to the random placement of aerosol particles within the initial cloud, 99 simulations were run for each of the scavenging particles in Table 5.7 to gain an average over multiple simulations. The charges assigned to particles I and III in Table 5.7 were assigned to be in line with the surface charge densities seen for the negative and positive particles in Table 5.3 respectively, whereas scavenging particle II is half the charge of particle I.

Table 5.7: Scavenging particle parameters

Scavenging Particle	a (μm)	q (fC)
I	10	-38.5
II	10	-19.3
III	10	+46.3

Figure 5.13 shows the aggregation data for the simulations run for scavenging particle I. In all simulations for this particle, no negatively-charged particles were observed as being scavenged, ruling out the theory of any like-charged attraction present in the system between the lactose particles; this is due to the very low dielectric constant of 2.9 for lactose and also the similarity of the surface charge densities of the particles. Figure 5.13a gives the expected result, where the aerosol particles from compartment 1 are most numerous and will therefore have the largest aggregation by numbers, and the cloud particles from compartment 3 have the smallest. When this same value is considered as a percentage (Figure 5.13b) of the particles of that size within the cloud, the results for particles from compartments 1 and 2 give similar percentages at the end of the simulation, with the main difference being the fact that the larger particles of the two take longer to reach this value. This is explained simply by the higher charge per mass ratio q/m of the smaller particles, with the q/m for particles from tube OD1 being ~ 1.6 times that of particles from tube

OD2, and ~ 5.5 times that of particles from tube OD3. The overall charge of the scavenging particle and its aggregates is shown in Figure 5.13d, where the scavenging of oppositely-charged particles leads to a decrease in the magnitude of the cluster charge.

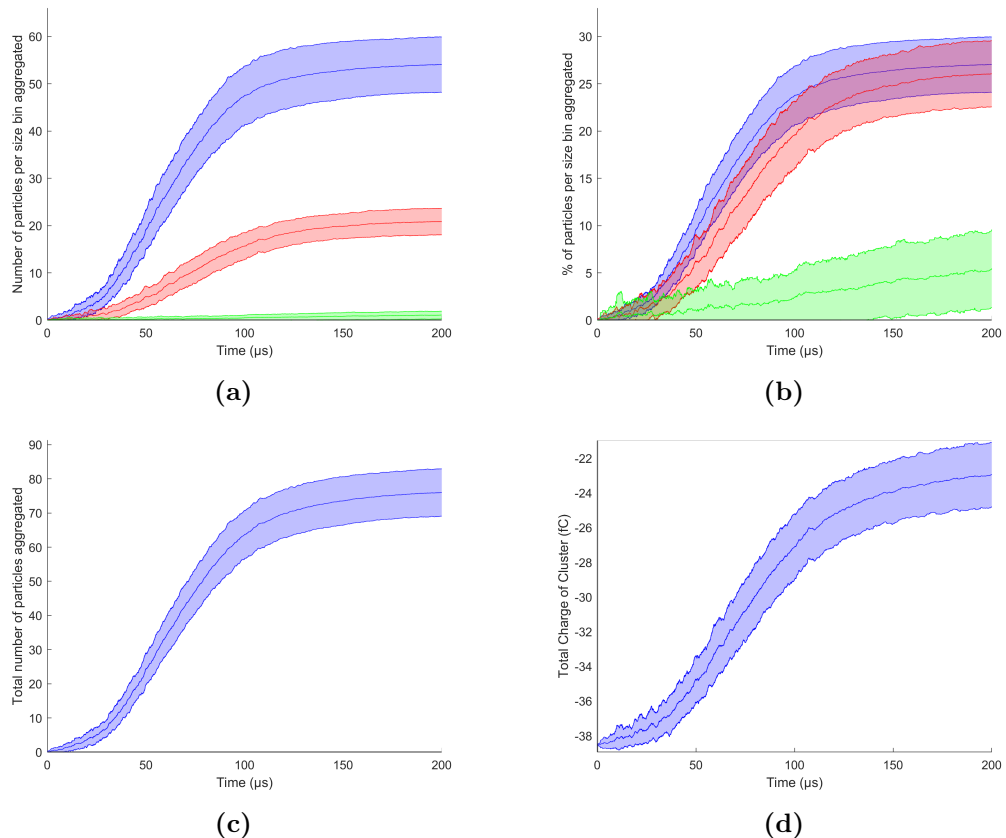


Figure 5.13: Aggregation data over the entire 200 μs dynamic simulations of a cloud of 300 aerosol particles passing over scavenging particle I ($a = 10 \mu\text{m}$, $q = -38.5 \text{ fC}$). Shown is the data for the (a) number and (b) percentage of aerosol particles coalesced on the scavenging particle with radii of 0.24 μm (blue), 0.89 μm (red) and 1.70 μm (green), as well as the (c) total number of particles coalesced and the (d) total cluster charge. Each plot shows the mean and standard deviation for the sample size.

Figure 5.14 shows the comparison between the percentage aggregation data of aerosol particles from compartment 1 for scavenging particles I and II (Figure 5.14a), and I and III (Figure 5.14b) for identical aerosol clouds. The influence of the magnitude of the charge of the scavenging particle on its ability to scavenge aerosol particles is shown in Subfigure 5.14a, where the only difference between the two systems is that particle II possesses 50% of

the charge of particle I. The total aggregation at the end of the simulation for particle II is around half of that of particle I, which is expected from a particle with half the charge. In these calculations, the maximum scavenging rate (obtained from the steepest gradient) of particle I is around 2.5 times that of particle II.

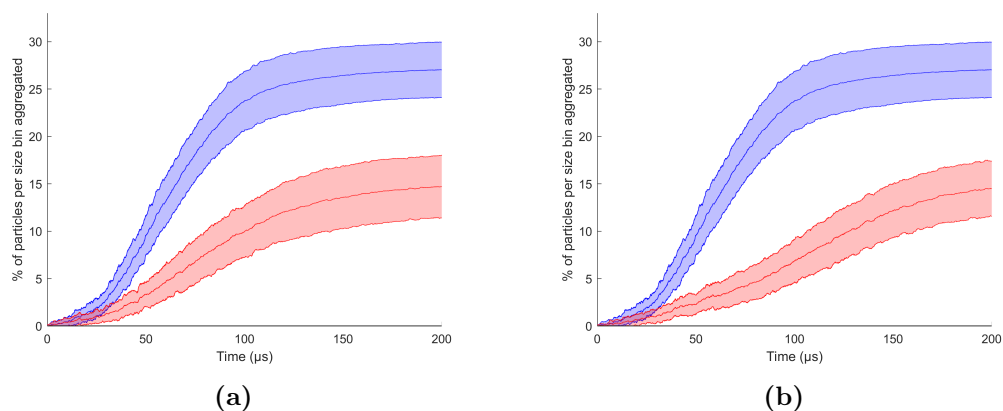


Figure 5.14: A comparison of percentage aggregation of the smallest particles over the entire 200 μs dynamic simulations ($a = 0.24 \mu\text{m}$) between scavenging particles with $a = 10 \mu\text{m}$ (a) I ($q = -38.5 \text{ fC}$, blue) and II ($q = -19.3 \text{ fC}$, red), and (b) I ($q = -38.5 \text{ fC}$, blue) and III ($q = -46.3 \text{ fC}$, red). Each plot shows the mean and standard deviation for the sample size.

Figure 5.6 shows a consistent net positive charge at all sizes detected. The effect of this asymmetry in the bipolar charge within the aerosol is studied in Figure 5.14b, where scavenging particles I and III are compared. Despite particle III having a larger magnitude of charge than particle I, Figure 5.14b shows particle I as having a higher maximum scavenging rate and larger overall aggregation of the smallest particles ($a = 0.24 \mu\text{m}$). This trend is due to these positive aerosol particles being higher in charge than the equivalent negative particles where the positive particles are almost quadruple that of the negative (Table 5.3) and have much stronger interactions with oppositely-charge particles (Table 5.5).

5.5 Concluding remarks

In this chapter the effect of bipolar charge on the aggregation of lactose particles has been studied. The static analysis indicates that asymmetry in particle size tends to produce the most likely aggregates, indicating a charge scavenging mechanism, whereas the dynamics simulations gave further context into the mechanisms, highlighting that the scavenging is driven towards the scavenging of particles with a high charge-to-mass ratio.

Chapter 6

Self-assembly behavior of oppositely charged inverse bi-patchy micro-colloids

The work in this chapter represents a collaborative project with Prof. Alexander Böker, Dr. Dmitry Grivoriev and the rest of the Multifunctional Colloids and Coatings team at the Fraunhofer Institute for Applied Polymer Research (IAP) in Potsdam-Golm, Germany. This chapter focuses more on the theoretical calculations associated with the project; more detailed description of the experimental method and techniques performed by our collaborators associated with characterising the particles and finding yields can be found in Naderi Mehr et al. [30].

6.1 Introduction

A directed attractive interaction between pre-defined “patchy” sites on the surfaces of anisotropic microcolloids can provide them with the ability to self-assemble in a controlled manner to build target structures of increased complexity. An important step towards the controlled formation of a desired superstructure is to identify reversible electrostatic interactions between patches

which allow them to align with one another. The formation of bi-patchy particles with two oppositely charged patches fabricated using sandwich microcontact printing is reported. These particles spontaneously self-aggregate in solution, where a diversity of short and long chains of bi-patchy particles with different shapes, such as branched, bent and linear, are formed. Calculations show that chain formation is driven by a combination of attractive electrostatic interactions between oppositely charged patches and the charge-induced polarization of interacting particles.

In this work, sandwich microcontact printing was used to produce bi-patchy melamine formaldehyde (MF) microparticles with oppositely charged patches consisting of either poly (methyl vinyl ether-alt-maleic acid) (PMVEMA) or polyethylenimine (PEI). The successful attachment of these polymers to the particle poles is demonstrated by different microscopic methods, where the measurements show that the yield of bi-patchy particles was improved. Here, we concentrate on the study of the self-aggregation behaviour of the patchy particles in solution. From a comprehensive statistical analysis of variable chains, such as short and long, branched, bent and linear, we can show that chain formation through the connections between patches is due to electrostatic attractions between oppositely charged patchy particles. These interactions can be weakened or even eliminated by increasing the ionic strength of the medium.

6.2 Bi-patchy particles with two oppositely-charged patches

Multivalent, oppositely charged polymers, PMVEMA as well as PEI, can be attached to the surfaces of MF particles as the isoelectric point (IEP) of the latter has been found to have approximately neutral pH [70]. A localized

change in the pH to either acidic or basic at the contact surface of the MF particles and the polymeric inks leads to their attachment through electrostatic attraction (Figure 6.1a).

For sandwich μ CP, two stamps were spin-coated with water solutions of PMVEMA and PEI, respectively. A monolayer of particles, prepared by drop-casting a dispersion of MF particles on a glass substrate, was pressed against the first stamp, which was spin-coated with PMVEMA. To generate second patches made of PEI on the opposite side of MF particles, the second stamp was pressed against the first stamp with particles immersed in PMVEMA layer. Finally, bi-patchy particles were released in acetone from the second stamp.

Patchy particles, as particular types of anisotropic microcolloid, are increasingly attracting attention due to their non-uniformity, often asymmetric shape, and characteristic properties. They are designed for controlled self-assembly allowing a diversity of complicated target superstructures, such as chains and rings, as well as two-dimensional (2D) and three-dimensional (3D) structures, such as squares, pyramids, tetrahedra, twisted shapes and even diamonds [71–73]. Since not all of these structures have been achieved experimentally, considerable interest is focused on the mechanism of their formation and on the corresponding interactions between patchy particles. Size, number and spatial distribution of patches play a crucial role in the formation of the final constructs; this stimulates computational simulations aimed at predicting the form and three-dimensionality of the resulting structures by changing the patch parameters [74–76]. Simulations by Guo and co-workers [77, 78] have shown that DNA strand-like helices could be generated through the assembly of tri-patchy particles, and the distribution of patches defines the diameter of the final helix. Furthermore, a simpler model has been developed for the formation of polymer-like chains of bi-patchy particles with patches at the

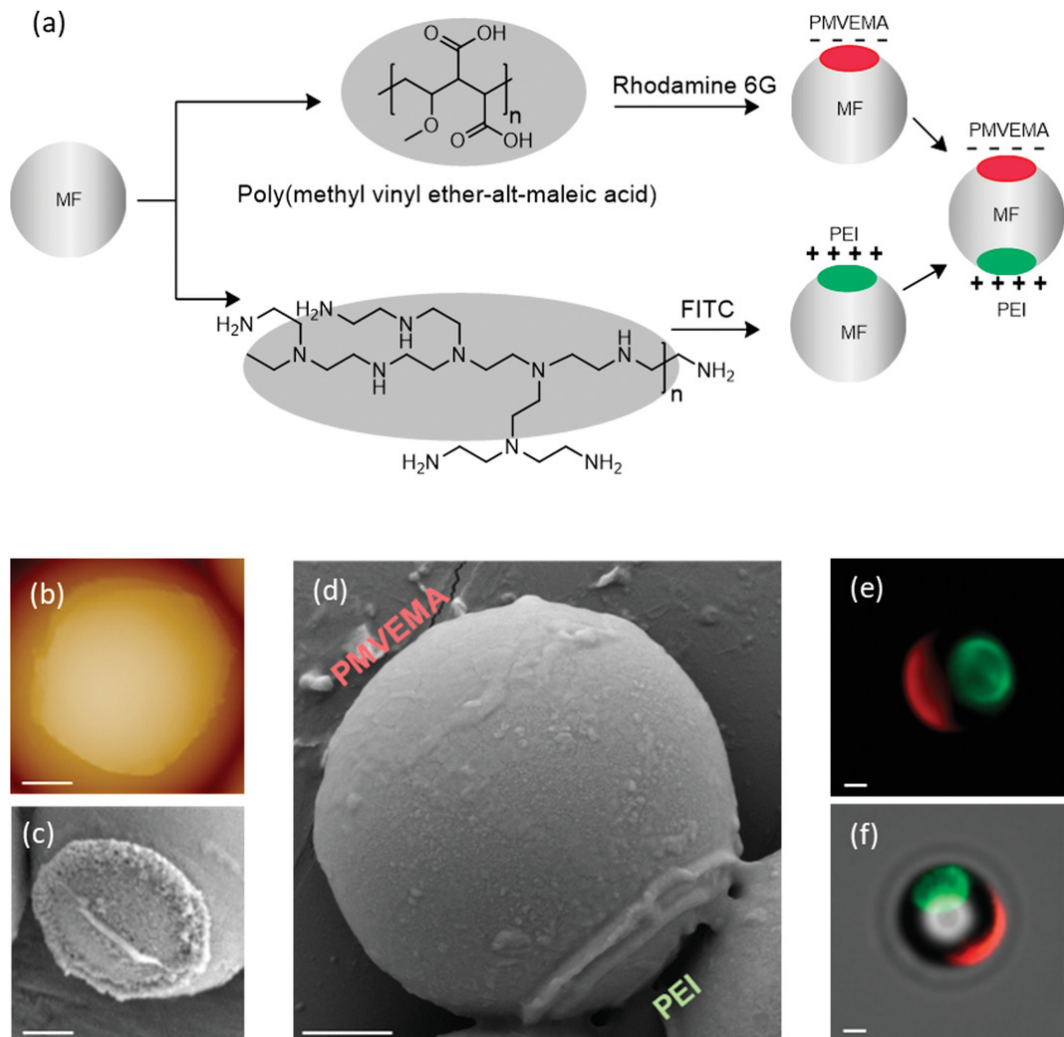


Figure 6.1: a) Scheme of the generation of oppositely charged patches on the surface of an MF particle made of pre-labeled PMVEMA and PEI with Rhodamine 6G and FITC, respectively. b) SFM height image of a PMVEMA patch. c) SEM image of a PEI patch. d) SEM image and e, f) fluorescence and the overlaid microscope images of bipatchy MF particles with patches made of PMVEMA and PEI that are coloured red and green, respectively. Scale bars: 1 μm

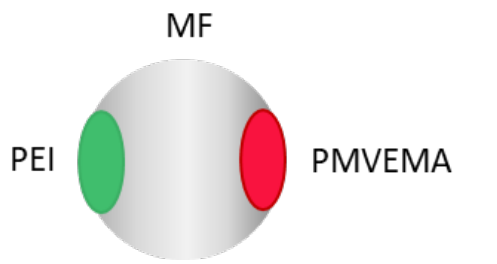
particle poles [79]. In addition to these computational simulations, patchy particles with two (Janus particles) or more patches have also been prepared in recent experimental work [80, 81]. However, self-assembly of these particles into chains or helices has not been reported [80, 82]. Patchy colloids with more than two patches can be produced by the colloidal fusion of a liquid core out of a pressure-deformed cluster of particles [80]. The chemistry of the patches on the particles can be used to control the strength and the directionality of the interactions between colloidal building blocks [83] when symmetrical clusters made from just a few spherical colloidal particles (called as “colloidal molecules”, CMs) are created.

The patchy particles were characterized by various microscopy methods (Figure 6.1b-f). To achieve a clear visualization of the patches for fluorescence microscopy, the polymers PMVEMA and PEI were labelled with Rhodamine 6G and Fluorescein isothiocyanate (FITC) tags, respectively. Information about the morphology and surface properties of the patches was obtained by scanning electron (SEM) and scanning force microscopy (SFM). As one can clearly see (Figures 6.1b–6.1d), there are distinct borders between the patches and the bare surface of particles, enabling an exact measurement of the patch size. Using several tens of SEM and SFM images, the following values for patch size were obtained: $2.33 \pm 0.16 \mu\text{m}$ and $2.4 \pm 0.2 \mu\text{m}$ for PEI and PMVEMA patches, respectively.

6.2.1 Electrostatic interactions between patchy particles

Self-aggregation of patchy particles can be better understood through the accurate evaluation of the electrostatic interaction energy between pairs of charged patchy particles in different relative orientations. In the general case of

Table 6.1: The parameters used in the computations of electrostatic inter-action energies: k is the dielectric constant, a is the radius, and q is the charge; k_m is 30.05 (90:10 mixture of ethanol and water). A particle graphic representation is also included for clarity.



Substance	k	$a / \mu\text{m}$	q / fC
MF	8.0	2.59	0
PEI	3.8	1.295	+0.734
PMVEMA	3.5	1.295	-0.923

a two-body electrostatic interaction between polarisable (dielectric) particles, electric charge on one of the particles creates an electric field that induces a redistribution of surface charge and the polarisation of bound charge on a second particle, which, in turn, generates its own electric field, prompting complementary polarisation effects on the first particle. This iterative process results in an equilibrium state where both particles acquire a static charged configuration that can lead to either an attractive or repulsive force between the interacting particles, which can be readily calculated analytically [19].

In the considered case of particles having patches of different charge and dielectric constant, the many-body solution presented in Chapter 2 has been used. In this work, each bi-patchy particle is represented by three spheres: the central sphere corresponding to the MF carrier and two smaller ones on either side representing the patches. The input parameters, summarised in Table 6.1, were either measured experimentally (sizes of patches and particles) or derived on the basis of well-established theoretical concepts using the data from the literature (e.g. charges on patches were calculated from the data on electrophoretic mobility or zeta-potential according to the Smoluchowski approximation, see [70] and references therein). These parameters were used in computation of the

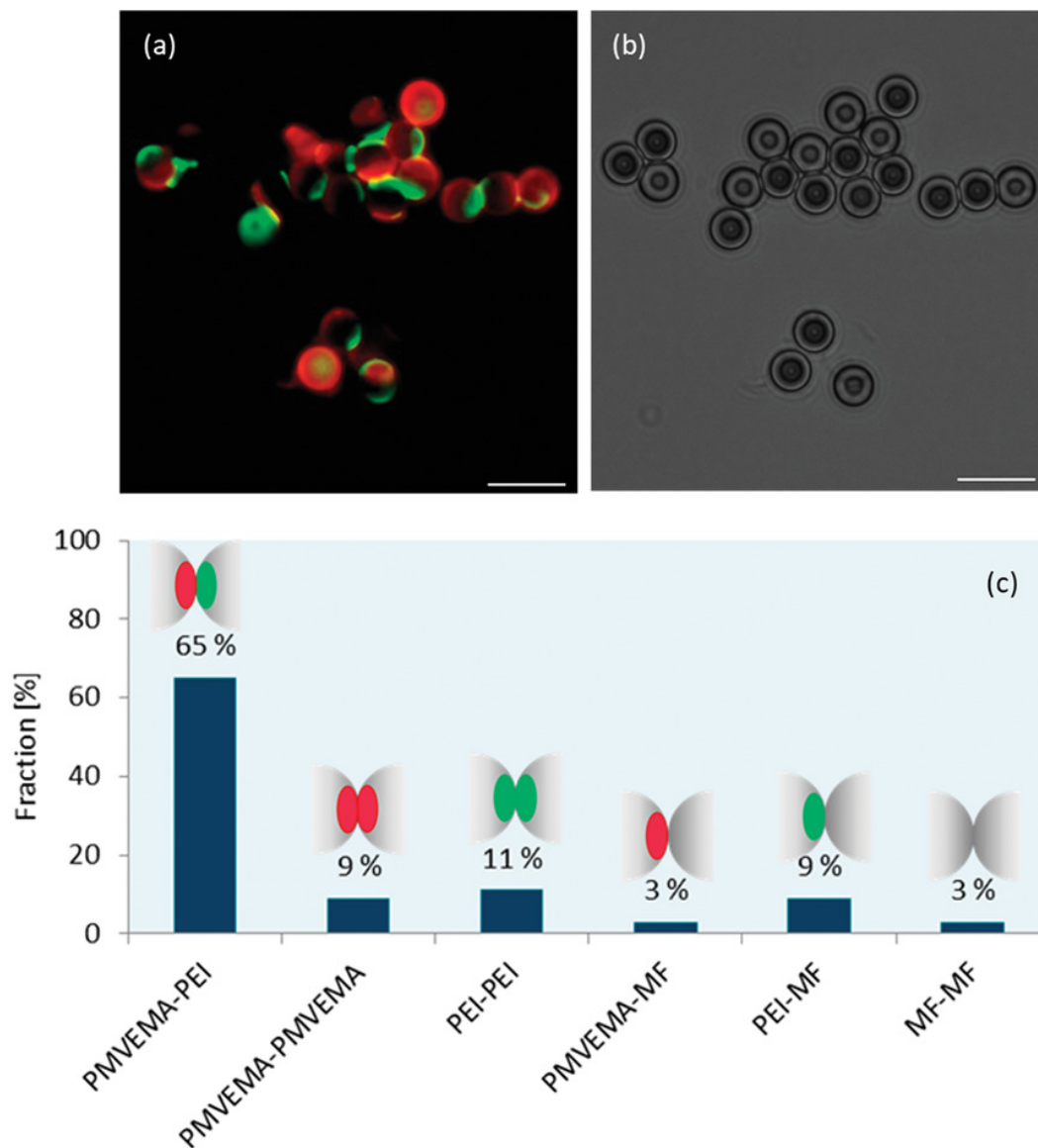


Figure 6.2: a) Fluorescence and b) optical microscope images of the self-assembly of bi-patchy particles. c) Six possible connection types which could be formed via random interactions between patchy and nonpatchy surfaces of particles, together with statistics of experimentally observed connections in the aggregates formed by MF bi-patchy particles. The fraction of PEI patch interactions is larger than the fraction of PMVEMA interactions due to the higher yield of PEI patches.

surface charge distribution on the particles and the electrostatic interaction forces driving their self-aggregation at all relative orientations and separations. The action of charges under their mutual polarisation influence is obtained from Gauss's law that couples uniquely the surface potential with the distribution and magnitude of electrical charge on the surface of the particles. The effect of the surface charge is integrated to numerically obtain the electrostatic force acting on the particles at arbitrary separations and orientations using a Galerkin approximation of an integral equation formulation [32]. The effect of the solvent on the self-assembly behaviour is captured by the dielectric constant of the ethanol:water (90:10) medium, taken to be 30.05, as no charge screening is present in the solution (large Debye screening length). The effect of an increased ionic strength on self-aggregation behaviour of patchy particles has been studied previously in [70] by adding a saturated solution of NaCl in ethanol/water (90:10).

The strongest attractive interaction energy, below -0.05 fJ at short separation distances, is predicted for a pair of bi-patchy particles with the PMVEMA-PEI connection type (Figure 6.7a); this interaction is dominated by a Coulomb attractive force between patches of opposite charge, which constitutes 65% of the overall interaction outcomes found experimentally (see Figure 6.2c). Similar electrostatic behaviour is observed if a mono-patchy and a bi-patchy particle interact directly through either PMVEMA-PMVEMA, PEI-PEI or PMVEMA-PEI connections (Figure 6.5). Much weaker attractive interactions (Figure 6.7b), attenuated by polarisation of neutral MF particles by the charged patches and polarisation effects of the solvent [29], account for a further 12% of the attractive interaction outcomes observed in the experiment (Figure 6.2c). Note that this attractive regime only occurs if the patches on the opposite (outer) sides of the interacting pair are identical. The overall interaction between a bi-patchy particle and a mono-patchy particle remains repulsive if the outer patches have different sign of charge and chemical composition, which

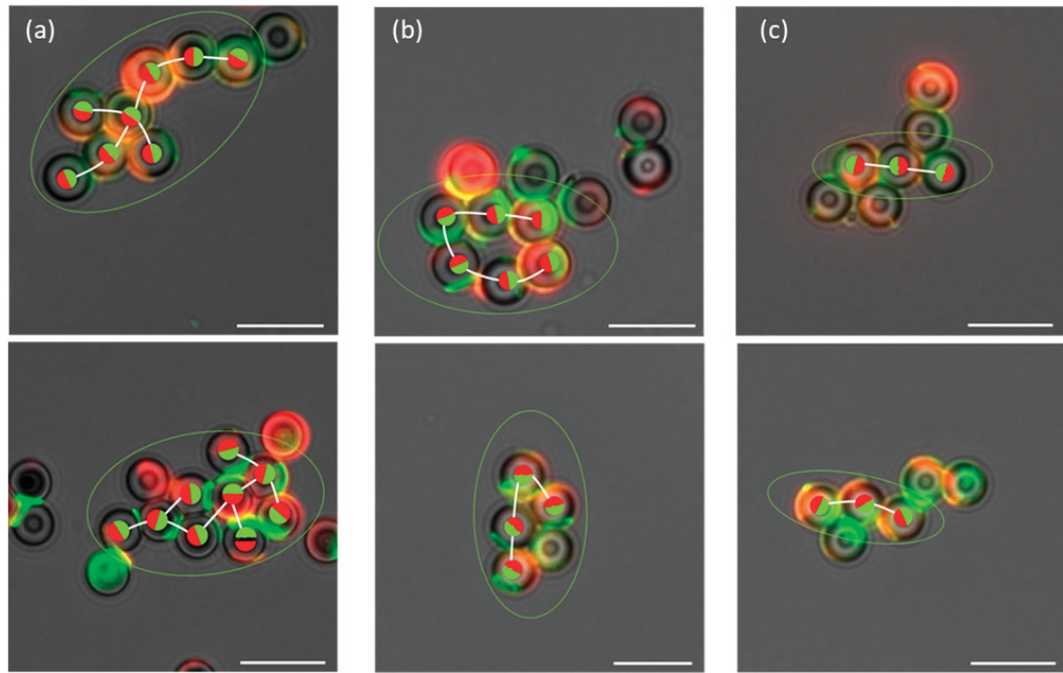


Figure 6.3: *Overlay of fluorescence and optical microscope images of a) the branched, b) bent, and c) linear chains, which are formed via electrostatic attraction between oppositely charged PMVEMA and PEI patches. For a better visualization, connections between bipatchy particles are represented with white lines, PMVEMA and PEI patches are additionally highlighted with red and green colored half-circles, respectively. Scale bars: 10 μm .*

affects the value of the dielectric constant and hence the strength of the total electrostatic force and charge induced polarisation.

Although electrostatic interactions between two individual bi-patchy particles with PMVEMA-PMVEMA and PEI-PEI patch contacts are always repulsive, these connections might be still observed experimentally in small self-assembled clusters, such as those shown in Figure 6.3. Such connections could arise from the complexity of subtle changes in the density of charge residing on the surface of each particle as a consequence of charge-induced polarisation effects, as seen in many-body systems [26, 49]. An attraction between objects carrying the same sign of charge is even possible in the pairwise interaction and results from a mutual polarisation of charge density close to the region where they are in contact [49]. To generate an attractive interaction between like-charged objects it is not only necessary for one object with a high charge density to polarise

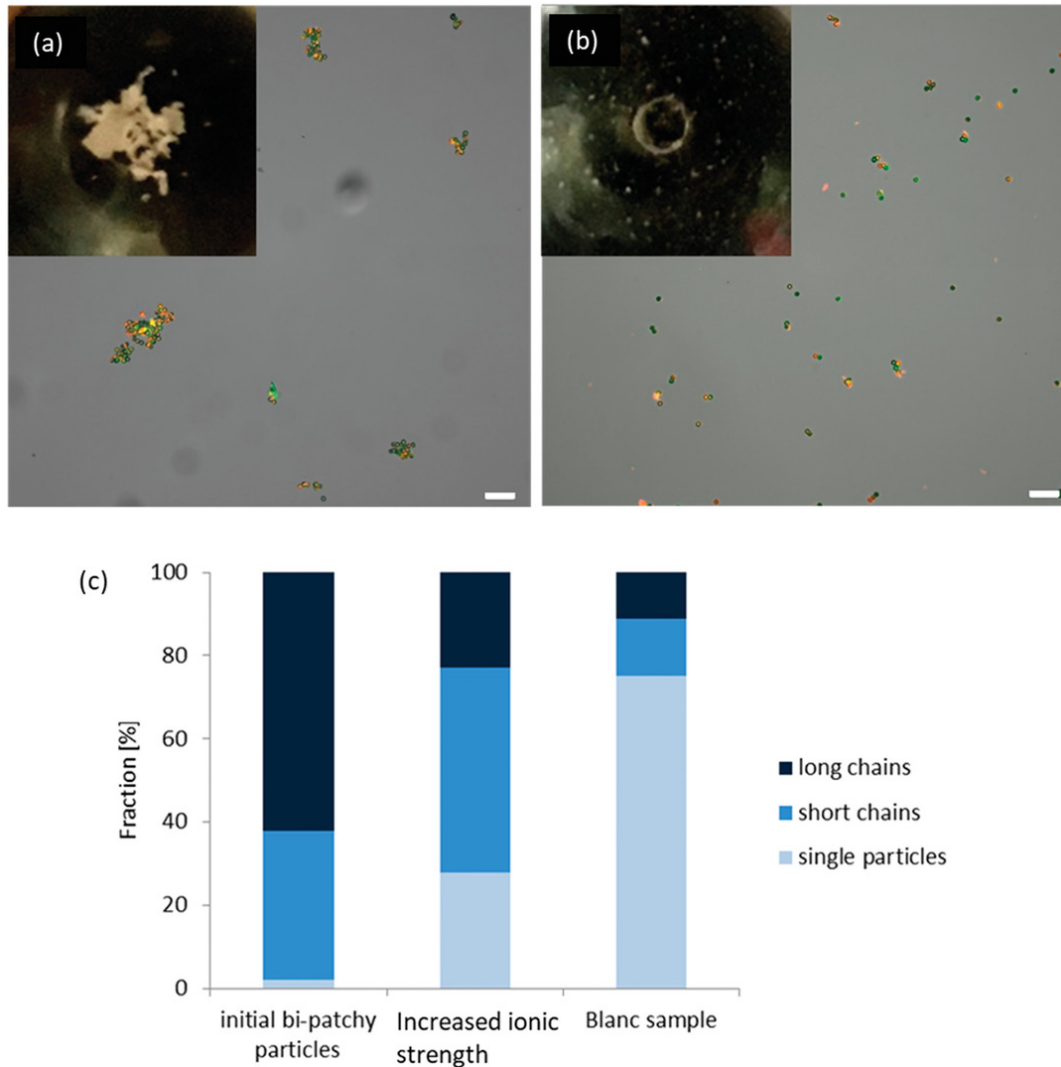


Figure 6.4: *Overlay of the optical and fluorescence microscope images of the bi-patchy particles a) before and b) after addition of a solution of NaCl. The elimination of self-aggregation can also be observed by the unaided eye. In solution, the white sediment of the large aggregates at the bottom of the Eppendorf tube (inset (a)) converts upon increase of the ionic strength to a turbid dispersion of small aggregates and single particles (inset (b)). c) Statistics for long and short chains as well as single particles in a dispersion of bi-patchy particles before and after addition of the NaCl solution in comparison with the statistics obtained for a sample of untreated MF particles. Scale bars: 25 μm .*

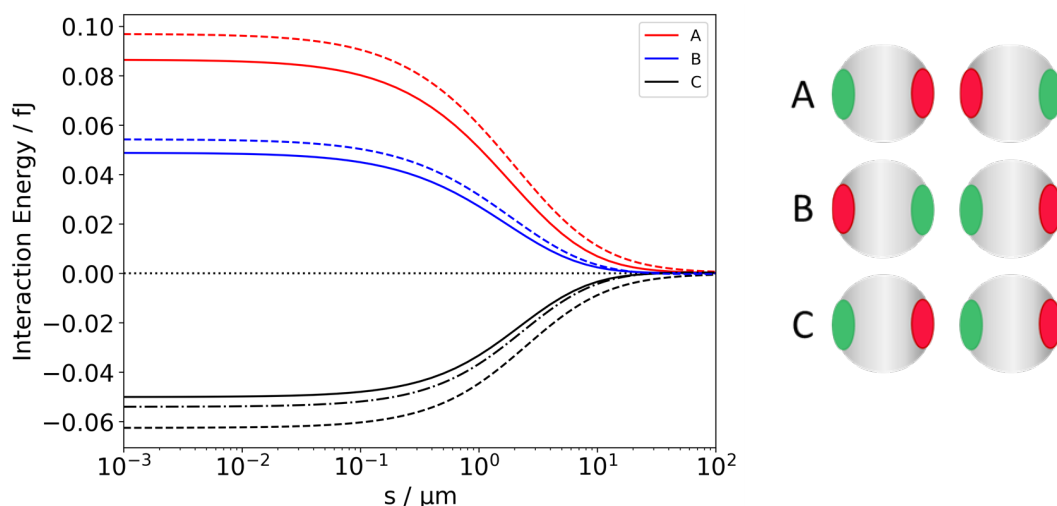


Figure 6.5: *The calculated electrostatic interaction energy (in fJ) as a function of the surface-to-surface separation between a pair of colloids: solid lines correspond to the interaction between bi-patchy particles shown in the figure; dashed lines correspond to the interaction between a bi-patchy particle and a mono-patchy particle with the outer patch removed (in case C, negative PMVMEA patch shown in red is removed); dash-dotted line corresponds to case C with the (green) positive PEI patch removed*

another, but there has to be a reciprocal displacement of density on the second object, too [49]. In the case of small clusters (many-body systems) as observed here, the polarisation of charge density and its mutual redistribution is essentially more complex, leading finally to the induction of an opposite charge on the location close to or within one of the apparently equally charged patches [49].

The rotational barrier between the repulsive PMVEMA-PMVEMA and PEI-PEI orientations and the stable the PMVEMA-PEI orientation decreases with distance between the interacting particles, but remains higher than 0.04 fJ even when the surface-to-surface separation distance reaches 4 μm (Figure 6.6). Such a high barrier eliminates the possibility of a thermally induced rotation of particles in the ethanol-water medium during self-assembly.

6.3 Conclusion and Outlook

Oppositely charged polymeric patches on the surfaces of polymer MF particles have successfully been fabricated with a reasonable yield. The effect of the

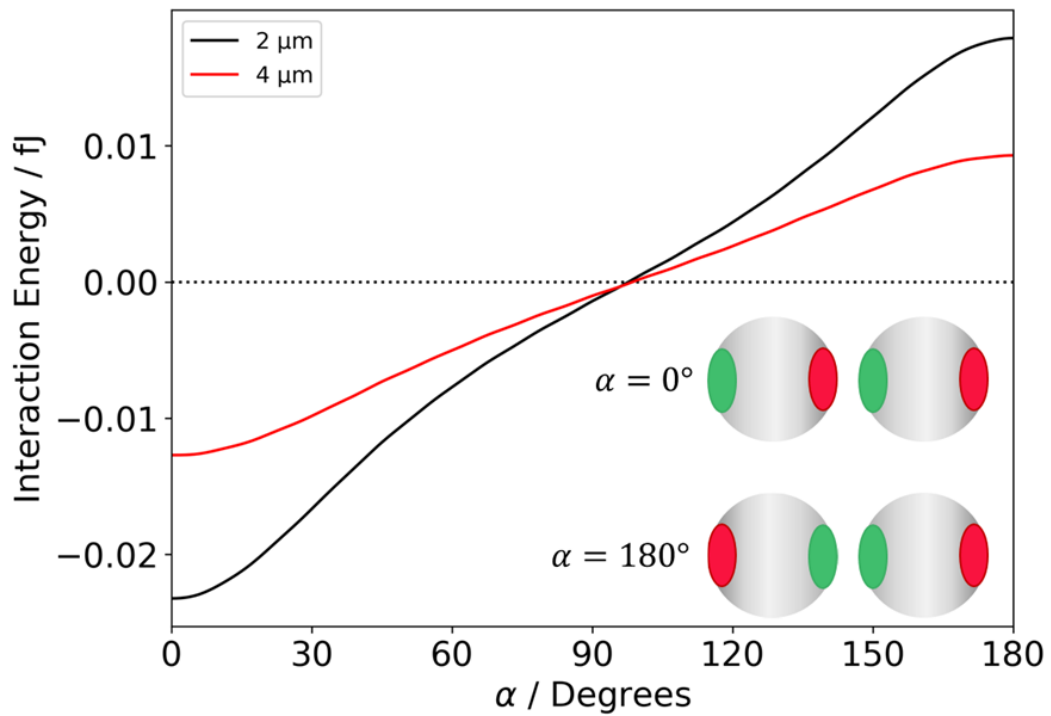


Figure 6.6: Calculated rotational barriers for re-orientation from the repulsive PEI-PEI connection (bottom right) to the stable the PMVEMA-PEI configuration (left). Images at the bottom of the figure show the calculated distribution of the surface charge on the particles and patches.

concentration of the polyelectrolyte ink on the yield of the bi-patchy particles has been studied, and a standard concentration of 2 wt% has been chosen for further investigation. In solution, the bi-patchy particles spontaneously self-aggregated and mostly connect via PMVEMA and PEI interactions. As a result, a variety of short and long chains of bi-patchy particles grew, which could be branched, bent or linear. In addition to electrostatically driven attraction between patches of opposite charge, attractive forces also arise through charge-induced polarization interactions between charged patches and the neutral surfaces of particles; the latter amounts to 12% of the interaction outcomes, for connection types PMVEMA-MF and PEI-MF. These attractive forces are driven by an instantaneous re-distribution of charge on the neutral surfaces of interacting particles due to the presence of a charged patch in close proximity; however, these forces are significantly weaker (up to an order of magnitude) than those due to opposite charge attraction. Moreover, 20% of the observed interactions are connections between initially equally charged patches

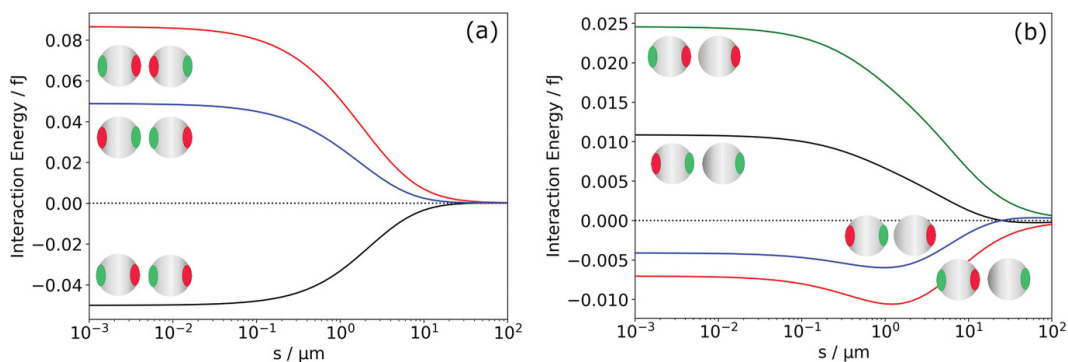


Figure 6.7: Electrostatic interaction energy (in fJ) as a function of the surface-to-surface separation between: a) two bipatchy particles and b) bipatchy and monopatchy particles. PMVEMA and PEI patches are highlighted by red and green colors, respectively.

PMVEMA-PMVEMA and PEI-PEI and are a consequence of charge-induced polarisation and charge re-distribution effects in many-body systems.

To understand further the relation between electrostatic interactions and the formation of chains, a variety of statistics have been performed, with the reliability of the latter being tested against a known sample size. To examine if the formation of chains via oppositely charged patches is as a result of electrostatic interactions, the ionic strength of the dispersion has been changed through the addition of a saturated solution of NaCl. As a result, self-aggregation was either eliminated or weakened due to reduced electrostatic attraction. However, a comparison of statistics for the latter with a reference sample of MF particles, shows a higher number of short chains even after the addition of the salt. This observation may indicate that there are still other types of interaction between bi-patchy particles, for example hydrogen bonds, which were not influenced by a change in ionic strength.

Almost half of all connections observed in aggregates are connections where directional contacts between oppositely charged patches are absent. This is the most important feature of electrostatic interaction as the main driving force for the self-assembly of patchy particles: polarisation and re-distribution of charge especially in many-body systems leads to a much more complicated

localisation of charge in these systems (not only on the patches) and to a “blurring” of directional interactions. This effect is further enhanced by the relatively large size of patches especially in comparison with the size of patchy particles, causing a more complex spatial distribution of the electric field when compared to point charges. Also, the lower charge density in patches compared to point charges leads to a less expressed polarisation of induced charges and to stronger delocalisation.

A theoretical calculation of electrostatic interactions between patchy microparticles used experimentally demonstrated a significant prevalence of electrostatic energy over the energy of thermal motion (kT), however the barrier is of the same order of magnitude as the kinetic energy of particle movement in, for example, a local laminar flow.

These observations show that bipatchy microparticles with oppositely charged patches, obtained by microcontact printing, are less suitable for directed self-assembly than particles with other types of patch-to-patch binding (covalent, hydrophobic etc.). This conclusion is a consequence of the complicated electrostatic interactions and re-distribution of initial charge and charge induced polarisation found in complex many-body systems. To improve the directional character of particle self-assembly via electrostatics, the size of particles should be decreased to submicrometer to essentially reduce disruption from their kinetic energy due to randomly distributed mechanical noise. In addition, the size of charged patches produced by microcontact printing is too large compared to the particles themselves. These issues can partially be addressed using Gaussian distributions, as shown in Section 3.2.1. The charged patches should be more localised and possess higher charge densities in order to improve the directionality of electrostatically driven interactions.

Chapter 7

The role of counterions in the initial stage of macroanion self-assembly: An example of the $\{\text{Mo}_{72}\text{Fe}_{30}\}$ polyoxometalate

The work in this chapter is an investigation into the driving forces behind the self-assembly behaviour of macroanions in solution. The work is based on the experimental observations widely reported in the literature on the self-assembly of polyoxometalates into “blackberry” macrostructures.

7.1 Introduction

The idea of how systems in nature can—with no external influences—arrange themselves into ordered, functional units has been of great interest for years in the understanding of biological systems, such as in cell boundary formation [84] and the folding of proteins [85–87], and how the phenomenon can be manipulated for use in man-made applications, such as creating a cheap and

versatile way of applying a surface coating using self-assembled mono-layers [88]. A broad definition given for self-assembly is that it is a mechanism where the individual components of a system assemble themselves spontaneously via an interaction to form a larger functional unit. This general description covers a wide range of interactions; therefore, a more concise set of conditions are needed to clarify the set of interactions that are of interest. There are 3 major ideas that underpin these types of interactions. The first idea states that the self-assembled structure must have a higher order than the isolated components; this is generally the opposite of what happens in a chemical reaction, where systems tend to move towards more disordered products due to the second law of thermodynamics. The second idea states that the only interactions involved are weak, excluding covalent, ionic and metallic bonding. This places emphasis on weaker interactions being the driving force, such as hydrogen bonding, pi-pi stacking, hydrophobic effects and van der Waals interactions. The third idea states that the individual building blocks of the self-assembled structures are not just simple molecules or atoms, but cover a wide range of nanostructures with different shapes, chemical compositions, and functionalities.

The interactions involved in colloidal dispersions have long been described in the chemical sciences. The Debye-Hückel theory was developed in the 1920s to account for the non-ideal behaviour of solutions of electrolytes and plasmas, even at low concentrations [89]. Debye-Hückel theory is a good approximation for simple systems where the electrolytes are low in concentration, charge and are spherical in nature [90]. The DLVO theory is a more robust solution to the problem of describing colloidal dispersions in electrolyte solutions and has found an increase in popularity in recent years due to its applicability in emerging fields, like in the behaviour of nanoparticles such as fullerenes. This theory provides an explanation for the aggregation of aqueous dispersions in a quantitative way and describes the force as a combination of both van der Waals forces, and the double layer force. DLVO theory has its shortcomings in

describing systems where addition forces play a role in processes, such as the behaviour and stability of colloidal crystals [91]. The approach in this Chapter looks purely at the electrostatic interactions between POMs in solution in the presence of discrete hydrated counterions, as opposed to the averaging of the effect of electrolytes in the system used in both Debye-Hückel and DLVO theories.

The self-assembling system considered in this Chapter is that seen in the behaviour of polyoxometalates (POMs). POMs consist of a large group of metal oxide clusters and have broad applications in the fields of photoelectronic materials [92], biologically active materials in drug delivery [93] and in catalysis [94–96]. It has been observed that, despite their hydrophilicity, POMs in aqueous solutions will self-assemble over time to form hollow vesicle macrostructures known as “blackberries”. This behaviour has led to much speculation as to the driving forces involved in their aggregation. The individual POM building blocks are typically a few nanometres in diameter and can carry up to 30 units of negative charge. POM nanostructures are formed via the linkage of orthometalates in the form MO_x^{z+} , where M is a high oxidation metal centre (usually Mo, W, V or Nb) generally with a d^0 electron configuration and x accounts for the number of oxygen atoms coordinated around the metal centre (usually in the range of 4-7). Due to the versatility of the choices, chemists can use a variety of combinations of initial orthometalates to create POMs with a range of sizes, shapes and topologies [97]. POMs have a well-defined molecular structure with a uniform shape and although they are highly charged molecules, the intramolecular charges do not interact with each other, this makes them ideal to use in the understanding of macroionic solutions such as those found in biomacromolecular systems (e.g., DNA and proteins interacting in the formation of virus capsids). An example of a notable group of POMs are a spherical and symmetrical subset of polyoxometalates known as Keplerates. Keplerates in chemistry get their name due to their similarities in structure to the mathematical structures of the same name which contain both Platonic and

Archimedean solids, one inside the other. Examples of these geometries range from simple structures such as tetrahedrons and cubes, to larger structures such as icosahedrons. Most notable of these Keplerales is an icosahedral polyoxomolybdate with a simplified formula of $\{\text{Mo}_{72}\text{Fe}_{30}\}$ [98]. The 72 molybdenum metal centres of $\{\text{Mo}_{72}\text{Fe}_{30}\}$ are split into 12 pentagonal $\{(\text{Mo})\text{Mo}_5\}$ subunits with each subunit placed at the vertices of an icosahedron. The 30 iron centres are placed on each of the 30 edges of the icosahedron, with each of these iron centres acting as singular deprotonation sites, leading to a total of 30 deprotonation sites on each $\{\text{Mo}_{72}\text{Fe}_{30}\}$. Due to an excess of oxo ligands surrounding the metal centres, POMs generally have a high negative charge which lead to the macrostructures to be soluble in solution. The amount of charge present is tuneable with a variation of the pH of the solution. Despite this large negative charge, aqueous POM macroions can slowly come together—sometimes over the course of months [97, 99–105]—to self-assemble into supramolecular structures, such as the ‘blackberry’ structures seen in Yin et al. [97]. For this self-assembly to occur, there needs to be driving force for the attraction between the two like-charged nanostructures.

7.1.1 Framing the problem

The overall aim of this Chapter is to develop a realistic model that can provide an explanation for the self-assembling nature of $\{\text{Mo}_{72}\text{Fe}_{30}\}$ ions from single macroanions to the huge hollow blackberry structures found in conditions that are seemingly counter-intuitive due to factors such as their high charges and solubility, and the occurrence of blackberry structures at very low POM concentrations ($< 10 \text{ mg mL}^{-1}$) [101]. Developing a quantitative understanding of the growth of these assemblies is desirable as it may lead to the possibility of fine-tuning the process to produce structures with well-defined surface or magnetic properties.

In this work, the source of the attractive interaction between the POMs in solution is investigated to determine the role of counterions in the formation of blackberry structures. The interactions studied in this Chapter are the most primitive interactions in the formation of “blackberries”—the formation of a dimer; the problems studied consider interactions that follow the basic form:



Each set of results looks at a different type of dimer system. The initial set of results consider the purely electrostatic interactions between two $\{\text{Mo}_{72}\text{Fe}_{30}\}$ macroions in both a vacuum and in water, and the effect that polarisation has on the electrostatic force at short separation in each of these cases. The remainder of the Chapter introduces counterions to the system to investigate the effect the presence of ionic species in the solution has on the interaction between POMs.

A couple of key assumptions have been made in the calculations in this project. The major assumption is the use of a dielectric continuum model for the solvent system which removes the computational cost of modelling each individual solvent molecule, at the cost of losing the solvent-structural information, and assuming that they can be modelled simply by an equilibrium average of the effects from each of the individual solvent molecules to have a dielectric constant equal to that of the bulk material.

A second assumption made is that there is no chemical interaction between POM structures and the counterions. In realistic situations, it is possible for some of the larger counterions – which have smaller hydrated radii due to their smaller solvation shells – to be able to displace hydrogen atoms at the deprotonation sites on the POM. This problem is reduced as much as possible by only looking at systems including the smaller counterions least affected by

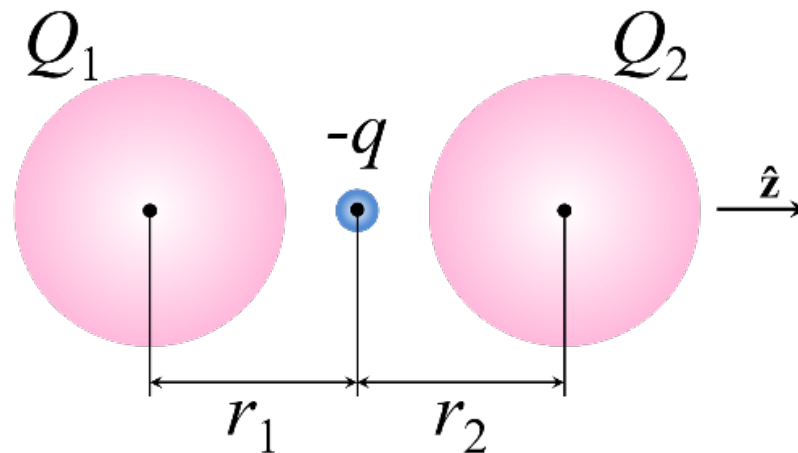


Figure 7.1: A geometric representative of a system containing two spherical macroions with a counterion between them.

this issue. While we don't have any considerations for the chemical interactions involved, it is well-established that electrostatic interactions are the dominating driving force in the aggregation of POMs into blackberry structures [106]. Also neglected are any van der Waals interactions; these are ignored due to the lack of blackberry formation in systems comprised solely neutral POMs [97, 106].

7.2 Methodology

Simple Model

POM association is mediated by the presence of counterions; we therefore consider a simple model with two POMs and a counterion in between them. In case of non-polarisable particles, the position of the single counterion on the z -axis going through the centres of POMs is intuitively clear as it corresponds to the minimum of energy. In case of polarisable particles and ionised surrounding the localisations of counterions will be discussed later.

Therefore, the force acting on the first POM F_1 is proportional to the following

expression:

$$F_1 \propto \frac{Q_1 q}{k_0 r_1^2} - \frac{Q_1 Q_2}{k_0 (r_1 + r_2)^2} \quad (7.1)$$

where $k_0 = \varepsilon_m / \varepsilon_0$. When $r_1 = r_2 = r$, $Q_1 = Q_2 = Q$ and $F = 0$, $4qr^2 = Qr^2$. When the r^2 terms cancel we get an attractive force when $4q > Q$, where the force is attractive when its projection on the z -axis is positive. (7.1) gives some qualitative explanation for observations of the effects that increasing counterion charge has on the aggregation of POMs in the formation of blackberries.

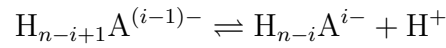
While the simple model gives some qualitative explanation for trends experimentally observed, it is unable to account for some of the more complex interactions present in the system, such as the effects of polarisation on the interactions between the molecules and the medium. These effects have previously been investigated by Lindgren et al. [29], where a charged POM in the vicinity of an oppositely charged plate can experience a repulsive interaction with an when interacting in a highly polarisable medium. We have used the same polarisable force field to investigate the interactions between POMs and counterions.

Charge State Determination

The building blocks of many self-assembling nanoparticles, such as POMs, contain functionalised acid groups on their surface that, when placed in a polar medium such as water, release protons. This causes the nanoparticles to acquire a structure with a net negative charge. Due to this dissociation of H^+ when placed in solution, POMs can be treated to behave as polyprotic acids; this means that the amount of deprotonation, and therefore negative charge present, of each building block is dependent upon a range of variables, such as: the pH of the solution, the number of acid sites present on the particles surface and the dissociation constant. Due to the nature of the acid groups in polyoxometalates,

they can be treated to be weak acids, with a dissociation constant K of around $10^{-5} - 10^{-4}$ [97]. The dissociation of a polyprotic acid with n -acid sites follows a multistep proton loss process and can be described in terms of a sequence of equilibria, with each proton loss i being characterised by a dissociation constant K_i with each successive proton loss having a smaller constant than the previous.

Individual dissociations are given by [107]:



with associated dissociation constants K_i taking the form:

$$K_i = \frac{[\text{H}_{n-i}\text{A}^{i-}] [\text{H}^+]}{[\text{H}_{n-i+1}\text{A}^{(i-1)-}]}$$

For a polyprotic acid with n -acid sites that has dissociated i -times, the fractional concentration α of acid $\text{H}_{n-i}\text{A}^{i-}$ is given by:

$$\alpha_{\text{H}_{n-i}\text{A}^{i-}} = \frac{[\text{H}^+]^{n-i} \prod_{j=0}^i K_j}{\sum_{i=0}^n \left[[\text{H}^+]^{n-i} \prod_{j=0}^i K_j \right]}$$

Here, approximations of K_i are done on a purely statistical basis, with the deprotonating acid sites present on the surface assumed to be both identical to each other and independent of one another. The negative charge produced from the release of protons is assumed to have no influence on the release of further protons. These considerations lead to an equation for K_i in the form:

$$K_i = \frac{(n-i+1)}{i} K$$

where n is the number of acid sites present on the surface, i is the dissociation step number and K is the intrinsic dissociation constant. $K_1 = nK$ which represents that the first dissociation step is equal to the number of acid sites

available for deprotonation multiplied by intrinsic dissociation constant and $K_n = K/n$ which reflects the total number of sites available for protonation.

7.3 Results and Discussion

7.3.1 Determination of parameters

As stated before, one of the first considerations that needs to be made before any calculations are performed is the range of the charges that are available to the POMs depending on its dissociation constant and the pH of the medium. A pH of 3 was chosen to determine the charge states present, due to the largest macrostructures in literature being produced at lower pHs [97, 99–101, 106, 108]. The pK_a of the POM in question, $\{\text{Mo}_{72}\text{Fe}_{30}\}$, has been calculated to be 3.9 [108], and the number of available charge states on the surface of this POM is known to be 30, with each of the 30 iron centres being coordinated to a water molecule that can act as a possible point of deprotonation [101, 109]. This combination of dissociation constant, number of charge states and pH gives a range of charges of between 0 and $-10e$ for the interacting particles as shown in Figure 7.2. This knowledge of the range of charges present in the solution is used as the guideline for the values of the charges of the POMs.

The values for the radii and dielectric constant for both the POM, $\{\text{Mo}_{72}\text{Fe}_{30}\}$, and the counterions K^+ and Mg^{2+} , are kept consistent for all calculations considered in this Chapter. The radius used for the counterions are 0.33 nm (K^+) and 0.4 nm Mg^{2+} respectively, values consistent with their hydrated radii [17]. The dielectric constant of the counterion k_c was given to be equal to that of the medium k_0 to be treated as a non-polarisable point charge at the centre of the hydrated sphere, with the medium being water unless otherwise stated ($k_0 = 80$). The radius of the POM used is that of the experimentally known value of 1.25 nm [97]. A value of 10 was used for the dielectric constant of

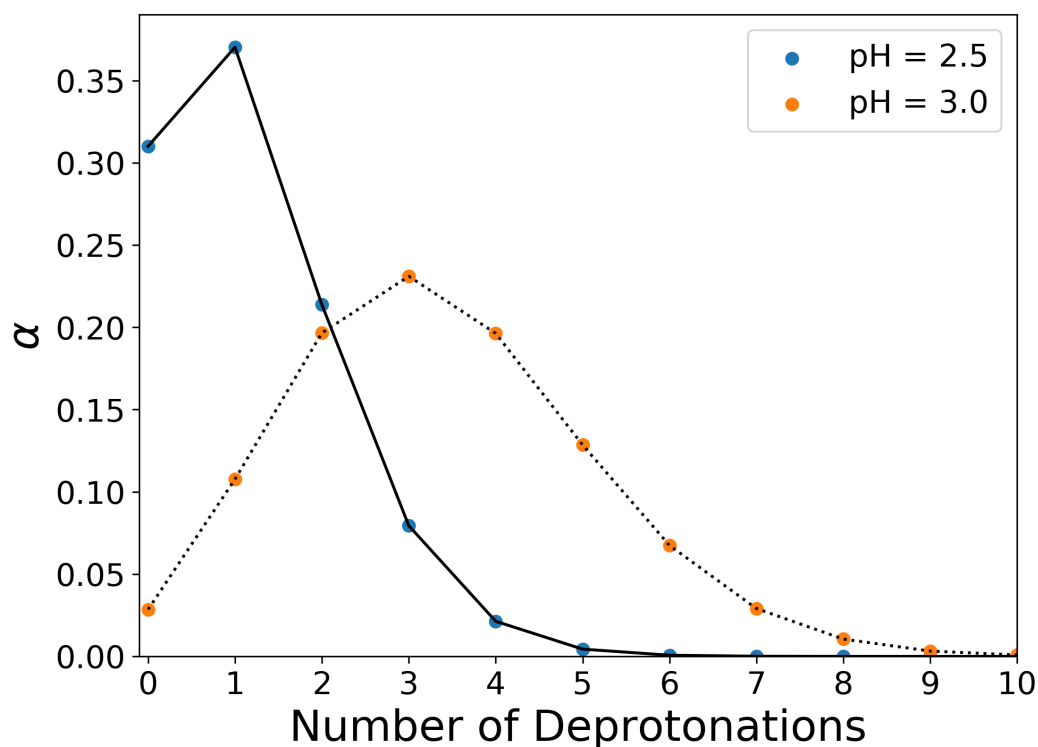


Figure 7.2: Fractional concentrations of $\{Mo_{72}Fe_{30}\}^{i-}$ where i is the number of deprotonations for pHs of 2.5 (blue/solid) and 3.0 (orange/dotted).

the POM to represent a molecule that is reasonably polarisable. The charge on the modelled POMs is, in isolation, assumed to be spread uniformly over the surface, with the overall charge density distribution being altered by the presence of an electric field produced by other particles.

7.3.2 Dimer interactions

The initial interaction in the self-assembly of polyoxometalates is the coming together of two monomer POM structures to create a dimer, $2 \{Mo_{72}Fe_{30}\} \longrightarrow \{Mo_{72}Fe_{30}\}_2$. The formation of these dimers and other small oligomers is seen as the rate-determining step in the formation of blackberry structures [97]. For all calculations performed in this work, the dielectric constant, k_i , of the POMs is given an arbitrary value of 10. The charge states were chosen as $-1e$ and $-7e$ for POMs 1 and 2 respectively due to the increased effects of polarisation in interactions between systems with large charge asymmetry. For simplicity, the first calculations were performed in a vacuum or air with a dielectric constant

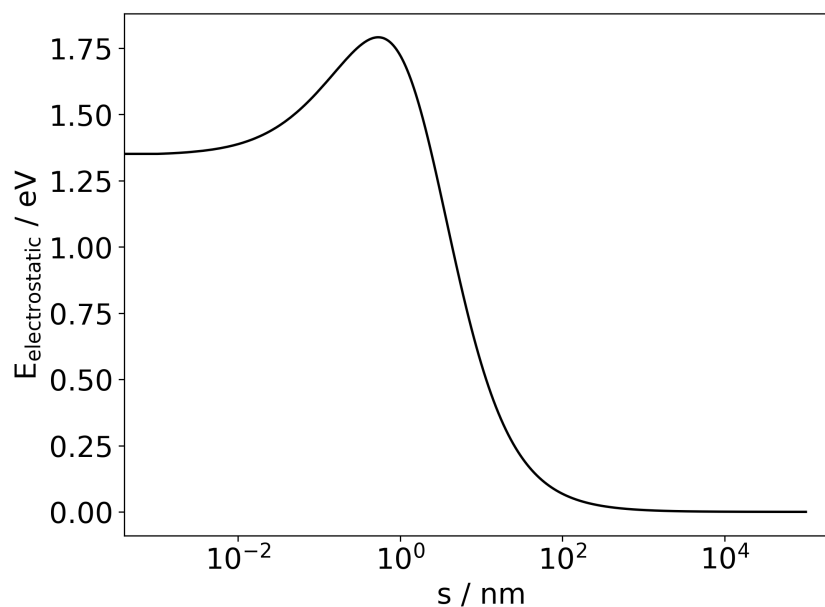


Figure 7.3: Interaction energy as a function of s between $\{Mo_{72}Fe_{30}\}^-$ and $\{Mo_{72}Fe_{30}\}^{7-}$ in a vacuum ($k_0 = 1$).

$k_0 = 1$ as a way of seeing what the interaction between the two particles is like without any solvent interference. This calculation gave rise to the energy profiles present in Figure 7.3.

In this profile, there is an evident attractive interaction between the two particles at very short separation (<0.7 nm), which would be expected in a self-assembling dimeric system; the size of the barrier that the particles need to overcome, on the other hand, is huge (> 75 kT at 298 K). This barrier would lead to the particles finding it impossible to ever get close enough to experience this attraction in a vacuum.

The dielectric constant of the medium, k_0 , reflects the tendency of the medium to shield charged species from each other, and is 1 in a vacuum, around 20 in acetone and 80 in water. Polar solvents, especially water, are very efficient at shielding the effective charges of ions in solution, reducing the size electrostatic forces between ions. Therefore, when the particles are placed in a more realistic environment, such as in water, $k_0 = 80$, there will be a shielding effect of the effective charges from the polar medium and therefore a reduction in the

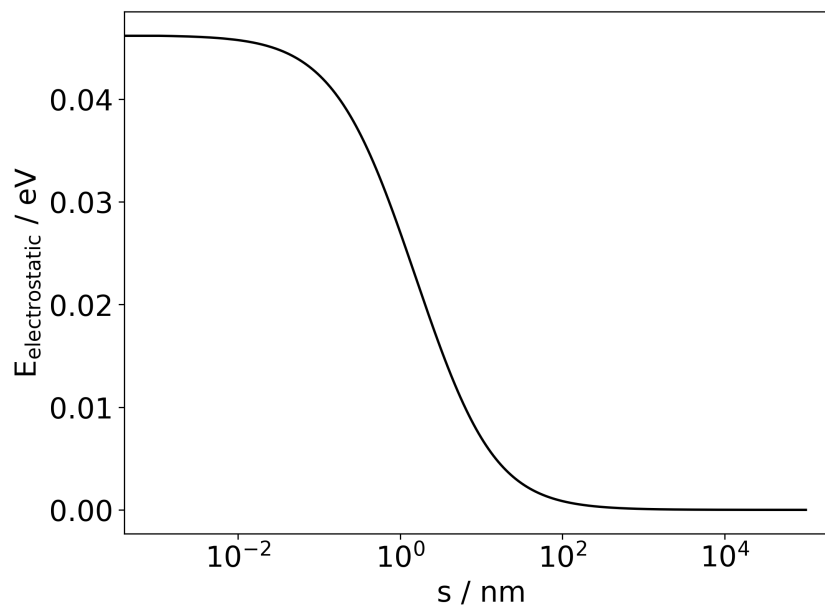


Figure 7.4: Interaction energy as a function of s between $\{Mo_{72}Fe_{30}\}^-$ and $\{Mo_{72}Fe_{30}\}^{7-}$ in water ($k_0 = 80$).

electrostatic interactions. The energy profile for the interaction between two $\{Mo_{72}Fe_{30}\}$ monomers in water is shown below in Figure 7.4.

This system shows a massive reduction in the electrostatic interactions present in the system due to the medium, which consequently leads to a substantial reduction in the size of the energy barrier needed for the POMs to come together with a maximum interaction energy of just over 2 kT. The issue with this energy profile is that it is completely repulsive, with no attractive region at short separation, unlike the interactions in a vacuum. This is due to the dielectric constant of the medium being much larger than that of the interacting POMs, therefore causing the medium to be more polarisable than the POMs.

Although the medium causes the electrostatic interaction to be reduced between the two interacting monomer units, there still seems to be an effect on the energy occurring due some form of polarisation effects. This increase in repulsion is caused due to the effects seen in [29], where the effect from polarisation is inverted due to the high polarisation of the medium. In this system, the polarisation effects lead to an increase in the repulsive energy of $\sim 25\%$, when compared to the expected coulombic interaction.

7.3.2.1 Counterion influence

The experimental data primarily suggests that the driving force for the self-assembling nature of POMs is the effect of the presence of counterions in the solution alongside the POMs [98–101, 104–106, 110–112]. The interactions between large metal-oxide polyanions and their counterions are seen to be significant in the self-assembling nature of macroanions in polar solvents due to the presence of a moderate ion-pairing effect and a loose distribution of the counterions around the macroions. This hints to the driving force for the self-assembly process being the interactions between macroanions and counterions.

Before any dimer interactions can be calculated with the counterion, the electrostatic interaction of the counterion association needs to be considered. The counterion used for the initial calculations was a Mg^+ ion, which has a hydrated radius of $\sim 0.4\text{nm}$ [17]. Counterions are generally thought to be more-or-less non-polarisable [107], therefore the dielectric constant for the counterions k_c used in this section are set to being equal to the dielectric constant of the medium k_0 , $k_c = k_0 = 80$. This interaction is shown in Figure 7.5.

Figure 7.5 shows the results that would be expected for the interaction of the association between a single POM and a counterion; the higher the charge of the POM, the stronger the association. An interesting observation is that the interaction between a POM with a charge of $-1e$, and a Mg^{2+} counterion has an attraction below kT at 298 K, providing a possible explanation for the lack of blackberry formation at low pH; in Figure 7.2 a low pH ~ 2.5 leads to the charges of the POMs being mainly between in the range of 0 and $-2e$, leading to an increased number of interactions between negative particles with no counterions which—as established in Figure 7.4—will not lead to an attractive interaction in water.

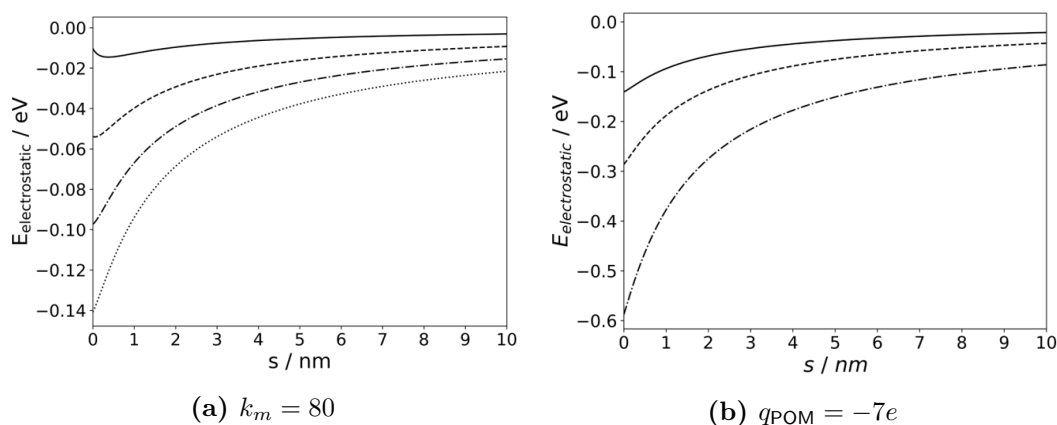


Figure 7.5: Interaction energy as a function of s for a range of POM-counterion interactions. (a) shows the interaction between a Mg^{2+} counterion with $\{\text{Mo}_{72}\text{Fe}_{30}\}^i$ with $i = -1e$ (solid), $-3e$ (dash), $-5e$ (dash-dot) and $-7e$ (dot) in water ($k_0 = 80$). (b) shows the interaction between a Mg^{2+} counterion with $\{\text{Mo}_{72}\text{Fe}_{30}\}^{7-}$ in a range of polar mediums. $k_0 = 80$ (solid), 40 (dash) and 20 (dash-dot).

From (7.1) we get $F_1 \propto 1/k_0$. A similar dependency was observed experimentally for the growth of blackberry radius (R_h) with the inverse of the dielectric constant. The polarisability of the medium k_0 is known to have significant effects on the formation of ‘blackberries’, with their size being inversely proportional to the dielectric constant of the medium. As a result, the effect of k_0 on counterion association is investigated. Fig. 7.6 shows the binding energy as a function of separation between the POM with the most abundant charge state at pH 3.0 $\{\text{Mo}_{72}\text{Fe}_{30}\}^{3-}$ and a single counterion ($\text{Mg}^{2+}/\text{K}^+$) interacting in mediums with varying polarisabilities.

Figure 7.7 shows the electrostatic interaction energy as a function of counterion position for a hypothetical configuration of two POMs with a charge of $-7e$ separated by a surface-to-surface separation of 1.5 nm and a single Mg^{2+} counterion. It gives an insight into the positional preference of counterions around the POMs in this configuration; while the most preferential position is that placed directly in between the POMs, there is also reasonably stable areas on the far sides of the POMs, indicating a stability for counterions to aggregate all over the POMs.

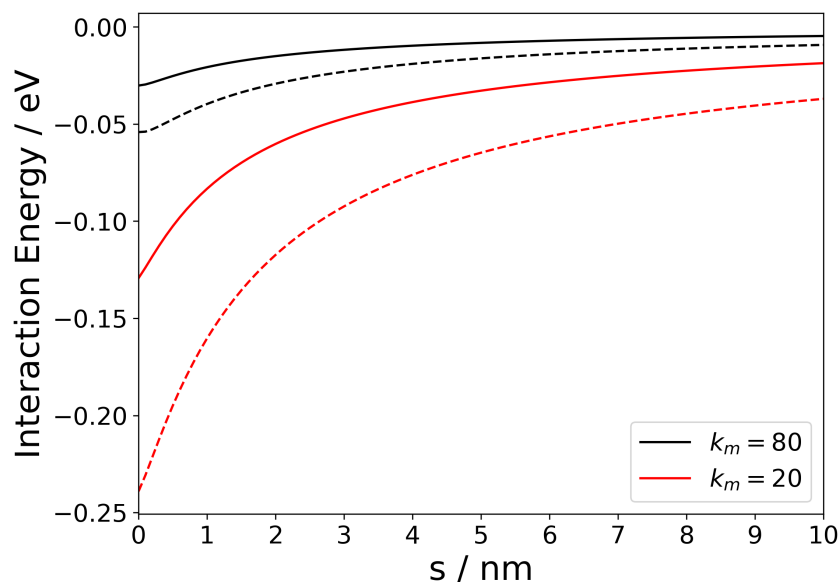


Figure 7.6: The effect of the dielectric constant of the medium on the binding energy between a pom and a counterion. $\{Mo_{72}Fe_{30}\}^{3-} + K^{+}$ (solid) and $\{Mo_{72}Fe_{30}\}^{3-} + Mg^{2+}$ (dashed) interaction, k_0 shown, $k_{POM} = 10$, $k_c = k_0 = 80$.

The charge density of POMs in solution is reduced by the presence of counterions association with the molecules. The number of counterions in solution is in a large excess when compared with the number of POMs, therefore the only limiting factor for binding is the energetics of the coordination of the counterions. The number of counterions aggregated to a POM varies depending on the POM's charge. Considered in Figure 7.8 is the relative abundance of POM-counterion aggregates with a certain overall charge, based on the binding energies of up to 7 Mg^{2+} counterions to $\{Mo_{72}Fe_{30}\}^{i-}$ molecules ($i = 0, 1, \dots, 9$). The location of counterions around the POM is chosen so that the energetics of the aggregates are minimised by placing them as far from each other on the surface as possible. The figure shows that, although there is a dynamic equilibrium between states, there is a clear energetic preference for the formation of overall positively charged aggregates.

The formation of a dimer requires an attraction between two aggregates. To produce an attractive interaction, aggregates of opposite charge are required. In this section only aggregates with overall charges of $+1e$ and $-1e$ were

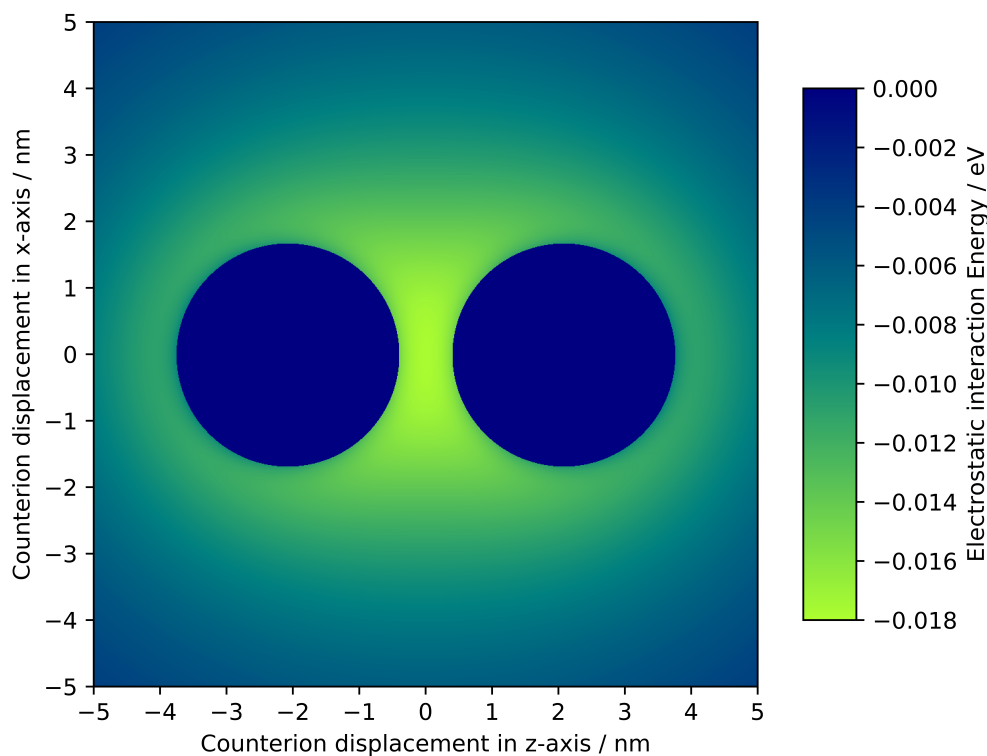


Figure 7.7: A contour plot of the electrostatic interaction energy as a function of Mg^{2+} counterion position in a system containing two $\{Mo_{72}Fe_{30}\}^{7-}$ ions separated by a surface-to-surface separation of 1.5 nm in water ($k_0 = 80$).

considered for simplicity. The charges of the POMs in each dimer formation was chosen to be equal in each of the interactions, with those charges being $-1e$, $-3e$, $-5e$ and $-7e$, and given the corresponding number of counterions to produce aggregates with both $+1e$ and $-1e$ overall charges. The counterions are arranged so that, in the dimer, they're positioned on the surface in a low energy configuration, with linear orientations ($-1e$ & $-3e$) as well as staggered trigonal planar and tetrahedral formations ($-5e$ & $-7e$ respectively) shown in Figure 7.9. This figure displays the interaction energy as a function of the separation between the surfaces of the POMs. The interesting observation of this figure is there is only small attraction between the monomer units ($\sim kT$) regardless of the charge of the POM, with the binding energy increasing as q_{POM} increases. The energy tends to converge for all pairs of monomer clusters as the separation increases, indicating the monomers approximate to $+1e$ and $-1e$ point charges at larger separations, regardless of q_{POM} . As previously

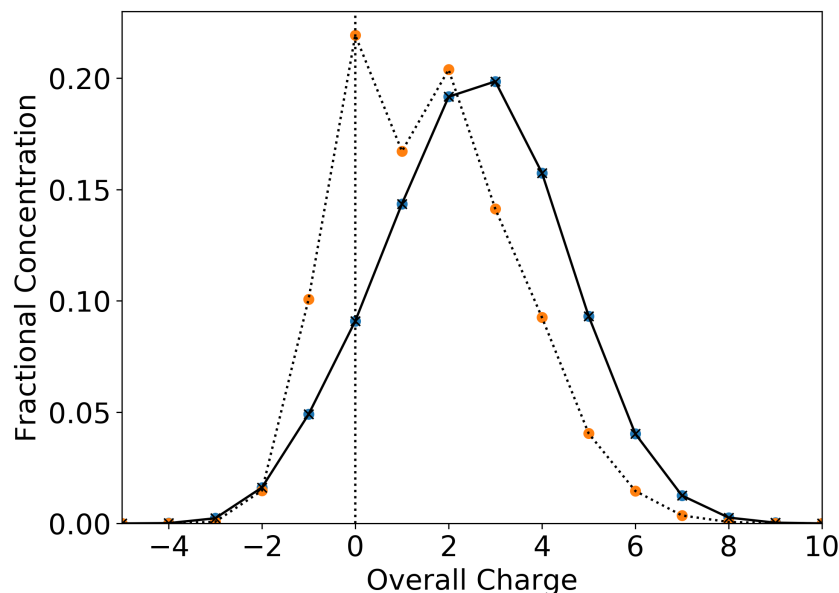


Figure 7.8: Fraction concentrations of $[Mg_x^{2+}\{Mo_{72}Fe_{30}\}^{i-}]^z$ for pHs of 2.5 (orange/dotted) and 3.0 (blue/solid).

stated, at pH=2.5—where no blackberries form—we can see from Figure 7.2 that the majority of the POMs have charge states between 0 and $-2e$; the smaller binding energy for these lower charges leads to the assumption that the formation of dimers and larger oligomers is much less likely in systems with a lower pH.

7.4 Concluding remarks

The work presented in this Chapter aims to develop a realistic model for the counterion driven formation of $\{Mo_{72}Fe_{30}\}$ dimers. It represents the POMs as uniformly charged and polarisable whereas the counterions are represented as uniformly charged and non-polarisable. The calculations for the interaction without counterions leads to purely repulsive interactions, with attraction only occurring once counterions are introduced to the system, which highlights the importance of counterions in the attraction, agreeing with the results expected from the literature.

It is clear that, for pairs of $[Mg_x^{2+}\{Mo_{72}Fe_{30}\}^{i-}]^z$ clusters with $z = +1e$ and

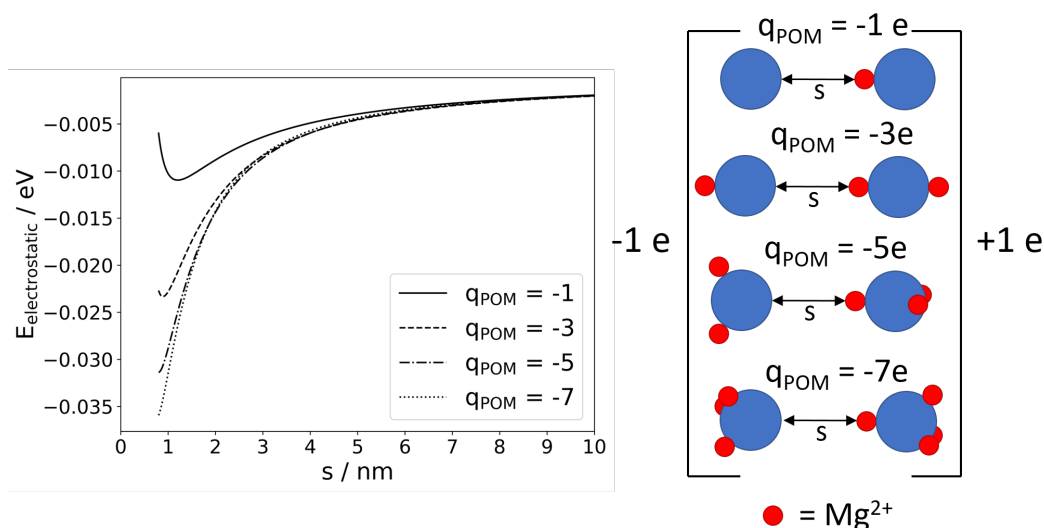


Figure 7.9: Energy as a function of s (left) for the 4 dimer systems considered (right).

$z = -1e$, that higher levels of deprotonation of $\{\text{Mo}_{72}\text{Fe}_{30}\}$ lead to a stronger interaction. This leads to the assumption that higher pHs will generally have a stronger dimer interaction due to their increased loss of protons, as shown in Figure 7.2, although this also translates to higher charged clusters in general which is likely be an electrostatic barrier to further growth past the dimer. Further calculations of the formation of larger oligomers are needed to verify this hypothesis.

Chapter 8

Conclusions and Future Work

8.1 Conclusions

The work in this thesis has tested the robustness and demonstrated the versatility of the many-body polarisable electrostatic solution proposed by Lindgren et al. [25] in 2018, with a clear focus on the recent developments involving the implementations of point charge surface distributions, Gaussian distributions and external electric fields.

Chapter 3 demonstrates a variety of trends, beginning with a wide range of two-body systems that show the fundamental interactions seen throughout the work in the thesis. Following this, the implementation of non-uniform charge distributions and their limitations were tested against the expected results from Coulomb's law and previous implementations. The implementation of the external electric field is tested against expected values from theory, such as the dipole-dipole interaction in Stone. After verifying the implementation, a dynamics simulation of 50 particles was performed; here, the stability and abundance of a range of microstructures within the final arrangement were analysed and compared.

In Chapter 4, a method was produced to compare the aggregation interactions

between a range of oxide particles with either other oxides, or large ice particles. The work showed that smaller particles only aggregate in opposite-charge or charge-neutral interactions, whereas small oxides interacting with large ice particles could also aggregate via like-charge interactions.

A pharmaceutical application was studied in Chapter 5 with regards to the electrostatic cohesion of pharmaceutical aerosols. The aim of the project was to investigate the aggregation behaviour of particles with sizes, charges and compositions similar to those found within dry powder inhalers, and from the BOLAR™. The general trend observed for the aggregation is for the asymmetrically-sized particles aggregating over a wider range of velocities and angles, which shows the preference of asymmetry in size for the majority of aggregations; this indicates a charge-scavenging mechanism which was the subject of dynamic simulations. These simulations showed the preference for the scavenging of particles with the highest charge-to-mass ratios, which tended to be the smallest particles due to the surface charge density staying relatively constant.

Chapter 6 represents a collaborative project with Prof. Alexander Böker at the Fraunhofer Institute for Applied Polymer Research looking in to the self-assembly behavior of oppositely charged inverse bi-patchy micro-colloids. The collaborators successfully fabricated oppositely charged polymeric patches on the surfaces of polymer MF particles. The electrostatic interactions between patchy microparticles observed were calculated theoretically, which demonstrated a significant prevalence of electrostatic energy over the energy of thermal motion (kT). The work was published in 2020 in the journal *Small*.

The final application in Chapter 7 considers the formation of dimers as a first step in to the investigation of the blackberry structure formation of poly-oxometalates. The Chapter emphasises the importance of the presence of

counterions in the system as it studies the interaction both with, and without counterions. The effect of pH and polarisability of the medium on the association of counterions was also investigated, with higher pHs leading to larger charges on the POMs, and aggregates with a higher charge, whereas a larger dielectric constant of the medium leads to a weaker interaction in general.

Chapters 4-7 demonstrate the versatility of the electrostatic model with a wide range of applications. The applicability of the model is tested in applications involving both polarisable (Chapters 6 & 7) and non-polarisable (Chapters 4 & 5) mediums, as well as interactions on different size scales, including the nanoscale (Chapters 4 & 7) and the mesoscale (Chapters 5 & 6).

8.2 Future Work

The work in this Thesis covers a wide range of applications, although with more time there are a large number of new topics and extensions to studied topics that would be of great interest with regards to the testing of the capabilities of the electrostatic model presented. Here, a selection of possible future work is presented for each Chapter.

Chapter 2

The current description of the force is only applicable to uniform surface charge distributions as it only considers the force as a translational force. In order to consider non-uniform charge distributions, there needs to be a separation of the force in to translational and rotational (torque) components. While this is enough for static calculations, when dynamic simulations are concerned, a range of additional problems need to be addressed, such as the rotational friction of particles colliding other particles, surfaces or rotating in a medium. These implementations would extend the applicability of the model much further than the span of this thesis.

Chapter 3

While a wide range of tests were covered here, there are a large number of additional tests that would be interesting to investigate. In addition to the tests in Chapter 3, it would be interesting to investigate the interactions involved in the interactions between many-body non-uniform charge distributions. One such idea would be to look at the interaction between endohedral fullerenes; the charge density distribution on the surfaces of these cages can be calculated using DFT, and using curve-fitting techniques it is possible to create a function that matches the distribution that can be input as the starting σ_s value in electrostatic simulations. This could be used with the existing model to analyse the formation of clusters and lattices, and be compared with uniform

distributions to give an insight in to the effect of non-uniform distributions on the interactions. Another test of non-uniform charge distributions is to look into systems containing Janus particles. These particles have two hemispheres with different properties that can be designed to aggregate into specific types of structures. This could be achieved using the flat nature of the higher-order Gaussian distributions to produce two hemispheres with different charges, although the dielectric nature of the two halves can't be defined as varying within a particle with current methods. In order to study the dynamics of these types of systems, the particles would need to be able to rotate freely which leads to the consideration of the torques discussed earlier to be an implementation that would greatly increase the range of applications that can be investigated. While the interactions between neutral particles in an external electric field has been studied in Section 3.3, the same types of studies with charged particles would be a very interesting topic to delve in to, with applications such as the melting of ionic lattice structures through the use of strong external electric fields.

Chapter 4

In Chapter 4, the work is fairly comprehensive in terms of the overall scope of the project; one thing that could be expanded upon would be to look at a wider range of materials, particle sizes and temperatures, which would allow a more nuanced discussion of the systems involved.

Chapter 5

The work in Chapter 5 covers a wide range of systems, from two-body interactions covering the fundamentals to large-scale dynamic simulations which observe and validate the two-body results, although there are more tests that could be added to further the depth of the study. Firstly, additional studies investigating a range of particle sizes, charges, impact angles and cluster sizes

would need to be added to the aggregation impaction section. The collision between two aggregates would also be an interesting topic to investigate to study the transfer or release of particles in collisions. Concerning the charge scavenging calculations, the sample size for each system was chosen to be 99, due to the computational cost of each simulation. While this gives a reasonable estimation for the overall charge scavenging mechanism, a larger sample size (i.e. 1000-2000) would give a more robust estimation. The shape and size of the cloud could also be modified to investigate the effect of cloud density, or to add many more particles to the system. While this is linearly scaling with respect to the number of particles, the number of particles needed to fully neutralise the particles in these systems would increase the computational cost substantially. It would also be very interesting to investigate the impact of having two clouds of particles pass over each other and to see the amount of aggregation that occurs between particles from the same and different clouds, this was something that I have wanted to investigate for a while, although the number of particles required (~ 500) would mean that the computational cost would be too high. Recent improvements in the computational speed of the calculations mean that this would now be an achievable project to perform.

Chapter 6

In Chapter 6, the patchy particles are represented as three spheres, a central neutral sphere representing the MF particles in between a pair of oppositely-charged spheres that represent the charged patches. While these give a good approximation of the interactions, our model has since been updated to include the capability to represent the charge distributions as non-uniform distributions. As the patches are printed on the surface uniformly, the ideal representation would be a higher-order Gaussian distribution as discussed in Section 3.2.1, this would give a much more realistic representation of the particles, with the Gaussian distributions being able to a closer the particles' actual compositions.

As the interactions in this work only consider purely electrostatic interactions, there are no considerations for interactions that could aid coalescence, such as van der Waals interactions; adding these types of attractive interactions could provide explanations for other observed interactions, such as the aggregations seen in systems with only monopatchy particles of the same charge, which our current model can't explain on its own.

Chapter 7

The work performed in the Chapter 7 solely considered the formation of polyoxometalate (POM) dimers, where all particles are treated as uniformly charged. One way of more realistically representing the charge density of the POMs would be to add the charge by placing small Gaussian distributions with charges of $-1e$ at i random Fe-O sites for each $\{\text{Mo}_{72}\text{Fe}_{30}\}^{i-}$ molecule. The size of the system was kept to the formation of a dimer; this was due to the high computational cost at the time of considering larger systems in a comprehensive fashion. With more time and with the recent lowering of computational cost in FMM calculations, larger systems would be able to be fully explored, allowing for the study of larger oligomers (trimer, tetramers and even larger 2D flakes). One potential way of lowering the computational cost even further would be to implement a method that treats the potential produced by the counterion as a point charge at the centre of the particle, as opposed to the current method of calculating the potential from a number of integration points across its surface, which equal to that of the POM. This would allow for the study of much larger POM systems such as POMs that form in to large spherical micelles with charges around $-300e$; these micelles come together to aggregate in to flat sheets at electrodes. The high charge on these micelles leads to the need for hundreds of counterions in the system to stabilise the interactions and drive the aggregation, which is extremely inefficient in the current implementation of the model due to the non-polarisable counterions

each having as many integration points as the micelles. Implementing this change and reducing the counterions to just a single integration point at the centre of the particle would drastically reduce the computational cost of these larger systems and would allow for thousands of counterions to be efficiently introduced into the system with very little computational cost. A final point is that the dissociation has only been calculated for deprotonations in water. Experimental results show that increasing the percentage of acetone in the solvent leads to the same outcome as lowering the pH of the solution [113]; both changes lead to less deprotonation and therefore POMs with lower charges. An effective way of calculating the dissociations of POMs in mixed solvents would be a good way of providing a more widely-reaching explanation of multiple trends seen with just one model.

Bibliography

- [1] Stephen Fry. *Mythos*. 2017. ISBN 9781405934138.
- [2] E. O. G. Turville-Petre. *Myth and Religion of the North: The Religion of Ancient Scandinavia*. Greenwood Press, 1964. ISBN 0837174201.
- [3] Kenneth S Schmitz. Chapter 1 - Philosophy of Science. pages 183–367. Elsevier, Boston, 2018. ISBN 978-0-12-800513-2. doi: 10.1016/B978-0-12-800513-2.00001-2.
- [4] Yıldız İlhami and Craig MacEachern. 1.2 Historical Aspects of Energy. pages 24–48. Elsevier, Oxford, 2018. ISBN 978-0-12-814925-6. doi: 10.1016/B978-0-12-809597-3.00102-4.
- [5] Michael R. Lynn. *Popular science and public opinion in eighteenth-century France*. Manchester Univ. Press, Manchester, 2006. ISBN 978-0-7190-7374-8.
- [6] P. Erik Gundersen. *The Handy Physics Answer Book*. Visible Ink Press, 1998. ISBN 978-1578596959.
- [7] Oak Ridge National Laboratory. *Review*. The Laboratory, 1996. URL https://books.google.co.uk/books?id=i_zLdWLLY2gC.
- [8] Abraham Wolf. *History of Science, Technology, and Philosophy in the Eighteenth Century*. Macmillan, New York, 1939. ISBN 9780367181345.
- [9] R. Home. Franklin’s Electrical Atmospheres. *The British Journal for the History of Science*, 6(2):131–151, 1972.
- [10] PBS LearningMedia. A Man-Made Ecological Disaster: The Dust Bowl. URL <https://www.pbslearningmedia.org/resource/ecological-disaster-ken-burns-dust-bowl/ken-burns-the-dust-bowl/>.
- [11] History.com. 10 Things You May Not Know About the Dust Bowl. URL <https://www.history.com/news/10-things-you-may-not-know-about-the-dust-bowl>.
- [12] Coulomb. Premier mémoire sur l’électricité et le magnétisme. In *Histoire de l’Académie Royale des Sciences*, pages 569–577. 1785.
- [13] David J Griffiths. *Introduction to Electrodynamics*. Cambridge University Press, Cambridge, 4 edition, 2017. ISBN 9781108420419. doi: DOI: 10.1017/9781108333511.

- [14] Daniel Fleisch. *A Student's Guide to Maxwell's Equations*. Cambridge University Press, Cambridge, 2008. ISBN 9780521877619. doi: DOI: 10.1017/CBO9780511984624.
- [15] M. Butt, H.; Graf, L.; Kappl. *Physics and Chemistry of Interfaces*. Wiley-VCH, Weinheim, Germany, 2nd edition, 2006. ISBN 978-3-527-40629-6.
- [16] Niels H de V. Heathcote. The early meaning of electricity: Some Pseudodoxia Epidemica—I. *Annals of Science*, 23(4):261–275, 1967. doi: 10.1080/00033796700203316.
- [17] Jacob N. Israelachvili. 5 - interactions involving the polarization of molecules. In Jacob N. Israelachvili, editor, *Intermolecular and Surface Forces (Third Edition)*, pages 91–106. Academic Press, San Diego, third edition edition, 2011. ISBN 978-0-12-375182-9. doi: 10.1016/B978-0-12-375182-9.10005-3.
- [18] A J Stone. *The Theory of Intermolecular Forces*. Oxford University Press, Oxford, 2nd ed. edition, 2013. ISBN 9780199672394.
- [19] Elena Bichoutskaia, Adrian L. Boatwright, Armik Khachatourian, and Anthony J. Stace. Electrostatic analysis of the interactions between charged particles of dielectric materials. *Journal of Chemical Physics*, 133(2):1–10, 2010. doi: 10.1063/1.3457157.
- [20] Armik Khachatourian, Ho-Kei Chan, Anthony J Stace, and Elena Bichoutskaia. Electrostatic force between a charged sphere and a planar surface: A general solution for dielectric materials. *The Journal of Chemical Physics*, 140(7):74107, 2014. doi: 10.1063/1.4862897.
- [21] Ivan N Derbenev, Anatoly V Filippov, Anthony J Stace, and Elena Besley. Electrostatic interactions between charged dielectric particles in an electrolyte solution. *The Journal of Chemical Physics*, 145(8):84103, 2016. doi: 10.1063/1.4961091.
- [22] Ivan N. Derbenev, Anatoly V. Filippov, Anthony J. Stace, and Elena Besley. Electrostatic interactions between charged dielectric particles in an electrolyte solution: constant potential boundary conditions. *Soft Matter*, 14(26):5480–5487, 2018. doi: 10.1039/c8sm01068d.
- [23] A V Filippov, X Chen, C Harris, A J Stace, and E Besley. Interaction between particles with inhomogeneous surface charge distributions: Revisiting the coulomb fission of dication molecular clusters. *The Journal of Chemical Physics*, 151(15):154113, 2019. doi: 10.1063/1.5119347.
- [24] Ivan N Derbenev, Anatoly V Filippov, Anthony J Stace, and Elena Besley. Electrostatic interactions between spheroidal dielectric particles. *The Journal of Chemical Physics*, 152(2):24121, 2020. doi: 10.1063/1.5129756.
- [25] Eric B Lindgren, Anthony J. Stace, E. Polack, Yvon Maday, Benjamin Stamm, and Elena Besley. An integral equation approach to calculate electrostatic interactions in many-body dielectric systems. *Journal of Computational Physics*, 371:712–731, 2018. doi: 10.1016/j.jcp.2018.06.015.

- [26] Eric B Lindgren, Benjamin Stamm, Yvon Maday, Elena Besley, and A J Stace. Dynamic simulations of many-body electrostatic self-assembly. *Philosophical Transactions of the Royal Society A: Mathematical, Physical and Engineering Sciences*, 376(2115), 2018.
- [27] Xiaojing Chen, Elena Bichoutskaia, and Anthony J Stace. Coulomb Fission in Dielectric Dication Clusters: Experiment and Theory on Steps That May Underpin the Electrospray Mechanism. *The Journal of Physical Chemistry A*, 117(19):3877–3886, 2013. doi: 10.1021/jp311950p.
- [28] Christopher Harris, Joshua Baptiste, Eric B Lindgren, Elena Besley, and Anthony J Stace. Coulomb fission in multiply charged molecular clusters: Experiment and theory. *The Journal of Chemical Physics*, 146(16):164302, 2017. doi: 10.1063/1.4981918.
- [29] E. B. Lindgren, I. N. Derbenev, A. Khachatourian, H.-K. Chan, A. J. Stace, and E. Besley. Electrostatic self-assembly: Understanding the significance of the solvent. *Journal of Chemical Theory and Computation*, 14:905–915, 2018.
- [30] Fatemeh Naderi Mehr, Dmitry Grigoriev, Rebecca Heaton, Joshua Baptiste, Anthony J Stace, Nikolay Puretskiy, Elena Besley, and Alexander Böker. Self-Assembly Behavior of Oppositely Charged Inverse Bipatchy Microcolloids. *Small*, 16(14):2000442, 2020. doi: 10.1002/smll.202000442.
- [31] J. Baptiste, C. Williamson, J. Fox, A. J. Stace, M. Hassan, S. Braun, B. Stamm, I. Mann, and E. Besley. The influence of surface charge on the coalescence of ice and dust particles in the mesosphere and lower thermosphere. *Atmospheric Chemistry and Physics*, 21(11):8735–8745, 2021. doi: 10.5194/acp-21-8735-2021.
- [32] Eric B Lindgren, Benjamin Stamm, Yvon Maday, Elena Besley, and Anthony J. Stace. Dynamic simulations of many-body electrostatic self-assembly. *Philosophical Transactions of the Royal Society A*, 376:20170143, 2018. doi: 10.1098/rsta.2017.0143.
- [33] E. Lindgren, A.J. Stace, E. Polack, Y. Maday, B. Stamm, and E. Besley. An integral equation approach to calculate electrostatic interactions in many-body dielectric systems. *J. Comp. Phys.*, 371:712–731, 2018.
- [34] Muhammad Hassan and Benjamin Stamm. An integral equation formulation of the N -body dielectric spheres problem. Part I: Numerical Analysis. *ESAIM: Math. Model. Numer. Anal.*, 2020. doi: 10.1051/m2an/2020030.
- [35] Bérenger Bramas, Muhammad Hassan, and Benjamin Stamm. An integral equation formulation of the N -body dielectric spheres problem. Part II: Complexity Analysis. *ESAIM: Math. Model. Numer. Anal.*, 2020. doi: 10.1051/m2an/2020055.
- [36] M. Hassan and B. Stamm. A linear scaling in accuracy numerical method for computing the electrostatic forces in the N -body dielectric spheres problem. *Commun. Comput. Phys.*, 29(2):319–356, 2021.

- [37] Ho-Kei Chan, Eric B Lindgren, Anthony J Stace, and Elena Bichoutskaia. A General Geometric Representation of Sphere-Sphere Interactions BT - Frontiers in Quantum Methods and Applications in Chemistry and Physics. pages 29–36, Cham, 2015. Springer International Publishing. ISBN 978-3-319-14397-2.
- [38] G L Squires. *Practical Physics*. Cambridge University Press, Cambridge, 4 edition, 2001. ISBN 9780521779401. doi: DOI:10.1017/CBO9781139164498.
- [39] A Parent, M Morin, and P Lavigne. Propagation of super-Gaussian field distributions. *Optical and Quantum Electronics*, 24(9):S1071–S1079, 1992. doi: 10.1007/BF01588606.
- [40] L. Megner, M. Rapp, and J. Gumbel. Distribution of meteoric smoke - Sensitivity to microphysical properties and atmospheric conditions. *Atmospheric Chemistry and Physics*, 6(12):4415–4426, 2006. doi: 10.5194/acp-6-4415-2006.
- [41] M Rapp, J M C Plane, B Strelnikov, G Stober, S Ernst, J Hedin, M Friedrich, and U.-P. Hoppe. In situ observations of meteor smoke particles (MSP) during the Geminids 2010: constraints on MSP size, work function and composition. *Ann. Geophys.*, 30(12):1661–1673, 2012. doi: 10.5194/angeo-30-1661-2012.
- [42] Ingrid Mann, Asta Pellinen-Wannberg, Edmond Murad, Olga Popova, Nicole Meyer-Vernet, Marlene Rosenberg, Tadashi Mukai, Andrzej Czechowski, Sonoyo Mukai, Jana Safrankova, and Zdenek Nemecek. Dusty plasma effects in near earth space and interplanetary medium. *Space Science Reviews*, 161(1):1–47, 2011. doi: 10.1007/s11214-011-9762-3.
- [43] J.S. Brooke, W. Feng, J.D. Carrillo-Sánchez, G.W. Mann, A.D. James, C.G. Bardeen, L. Marshall, S.S. Dhomse, and J.M. Plane. Meteoric smoke deposition in the polar regions: A comparison of measurements with global atmospheric models. *Journal of Geophysical Research: Atmospheres*, 122(20):11112–11130, 2017. doi: 10.1002/2017JD027143.
- [44] F.-J. Lübken. Thermal structure of the Arctic summer mesosphere. *Journal of Geophysical Research: Atmospheres*, 104(D8):9135–9149, 1999. doi: 10.1029/1999JD900076.
- [45] Mark Hervig, Robert E Thompson, Martin McHugh, Larry L Gordley, James M Russell III, and Michael E Summers. First confirmation that water ice is the primary component of polar mesospheric clouds. *Geophysical Research Letters*, 28(6):971–974, 2001. doi: 10.1029/2000GL012104.
- [46] Franz-Josef Lübken, Uwe Berger, and Gerd Baumgarten. On the Anthropogenic Impact on Long-Term Evolution of Noctilucent Clouds. *Geophysical Research Letters*, 45(13):6681–6689, 2018. doi: 10.1029/2018GL077719.

- [47] C G Bardeen, O B Toon, E J Jensen, D R Marsh, and V L Harvey. Numerical simulations of the three-dimensional distribution of meteoric dust in the mesosphere and upper stratosphere. *Journal of Geophysical Research: Atmospheres*, 113(D17), 2008. doi: 10.1029/2007JD009515.
- [48] L. Zhang, B. Tinsley, and L. Zhou. Parameterization of in-cloud aerosol scavenging due to atmospheric ionization: part 4. effects of varying altitude. *Journal of Geophysical Research: Atmospheres*, 124:13105–13126, 2019. doi: 10.1029/2018JD030126.
- [49] Anthony J Stace, Adrian L Boatwright, Armik Khachatourian, and Elena Bichoutskaia. Why like-charged particles of dielectric materials can be attracted to one another. *Journal of Colloid and Interface Science*, 354(1):417–420, 2011. doi: 10.1016/j.jcis.2010.11.030.
- [50] Eric B Lindgren, Benjamin Stamm, Ho-Kei Chan, Yvon Maday, Anthony J Stace, and Elena Besley. The effect of like-charge attraction on aerosol growth in the atmosphere of Titan. *Icarus*, 291:245–253, 2017. doi: 10.1016/j.icarus.2016.12.013.
- [51] J. Gumbel, D. E. Siskind, G. Witt, K. M. Torkar, and M. Friedrich. Influences of ice particles on the ion chemistry of the polar summer mesosphere. *Journal of Geophysical Research: Atmospheres*, 108:8436, 2003. doi: 10.1029/2002JD002413.
- [52] Christopher P Barrington-Leigh, Umran S Inan, and Mark Stanley. Identification of sprites and elves with intensified video and broadband array photometry. *Journal of Geophysical Research: Space Physics*, 106(A2): 1741–1750, 2001. doi: 10.1029/2000JA000073.
- [53] C. Baumann, M. Rapp, A. Kero, and C. F. Enell. Meteor smoke influences on the d-region charge balance—review of recent in situ measurements and one-dimensional model results. *Annales Geophysicae*, 31:2049–2062, 2013. doi: 10.5194/angeo-31-2049-2013.
- [54] C. Baumann, M. Rapp, M. Anttila, A. Kero, and P. T. Verronen. Effects of meteoric smoke particles on the d region ion chemistry. *Journal of Geophysical Research: Space Physics*, 120:10823–10839, 2015. doi: 10.1002/2015JA021927.
- [55] I Mann, T Gunnarsdottir, I Häggström, S Eren, A Tjulin, M Myrvang, M Rietveld, P Dalin, D Jozwicki, and H Trollvik. Radar studies of ionospheric dusty plasma phenomena. *Contributions to Plasma Physics*, 59(6):e201900005, 2019. doi: 10.1002/ctpp.201900005.
- [56] Mark E Hervig, Lance E Deaver, Charles G Bardeen, James M Russell, Scott M Bailey, and Larry L Gordley. The content and composition of meteoric smoke in mesospheric ice particles from SOFIE observations. *Journal of Atmospheric and Solar-Terrestrial Physics*, 84-85:1–6, 2012. doi: 10.1016/j.jastp.2012.04.005.

- [57] John M C Plane, Wuhu Feng, and Erin C M Dawkins. The Mesosphere and Metals: Chemistry and Changes. *Chemical Reviews*, 115(10):4497–4541, 2015. doi: 10.1021/cr500501m.
- [58] D Duft, M Nachbar, and T Leisner. Unravelling the microphysics of polar mesospheric cloud formation. *Atmos. Chem. Phys.*, 19(5):2871–2879, 2019. doi: 10.5194/acp-19-2871-2019.
- [59] J. Hedin, F. Giovane, T. Waldemarsson, J. Gumbel, J. Blum, R. M. Stroud, L. Marlin, J. Moser, D. E. Siskind, K. Jansson, R. W. Saunders, M. E. Summers, P. Reissaus, J. Stegman, J. M. C. Plane, and M. Horányi. The magic meteoric smoke particle sampler. *Journal of Atmospheric and Solar-Terrestrial Physics*, 118:127–144, 2014. doi: 10.1016/j.jastp.2014.03.003.
- [60] S Robertson, M Horányi, S Knappmiller, Z Sternovsky, R Holzworth, M Shimogawa, M Friedrich, K Torkar, J Gumbel, L Megner, G Baumgarten, R Latteck, M Rapp, U.-P. Hoppe, and M E Hervig. Mass analysis of charged aerosol particles in NLC and PMSE during the ECOMA/MASS campaign. *Ann. Geophys.*, 27(3):1213–1232, 2009. doi: 10.5194/angeo-27-1213-2009.
- [61] B Journaux, J M Brown, A Pakhomova, I E Collings, S Petitgirard, P Espinoza, T Boffa Ballaran, S D Vance, J Ott, F Cova, G Garbarino, and M Hanfland. Holistic approach for studying planetary hydrospheres: Gibbs representation of ices thermodynamics, elasticity, and the water phase diagram to 2,300 mpa. *Journal of Geophysical Research: Planets*, 125(1):e2019JE006176, 2020. doi: 10.1029/2019JE006176.
- [62] Arpa Hudait and Valeria Molinero. What Determines the Ice Polymorph in Clouds? *Journal of the American Chemical Society*, 138(28):8958–8967, 2016. doi: 10.1021/jacs.6b05227.
- [63] Jean C Sung, Brian L Pulliam, and David A Edwards. Nanoparticles for drug delivery to the lungs. *Trends in Biotechnology*, 25(12):563–570, 2007. doi: 10.1016/j.tibtech.2007.09.005.
- [64] Jennifer Wong, Hak Kim Chan, and Philip Chi Lip Kwok. Electrostatics in pharmaceutical aerosols for inhalation. *Therapeutic Delivery*, 4(8): 981–1002, 2013. doi: 10.4155/tde.13.70.
- [65] Jennifer Wong, Philip Chi Lip Kwok, Ville Niemelä, Desmond Heng, John Crapper, and Hak Kim Chan. Bipolar electrostatic charge and mass distributions of powder aerosols - Effects of inhaler design and inhaler material. *Journal of Aerosol Science*, 95:104–117, 2016. doi: 10.1016/j.jaerosci.2016.02.003.
- [66] D. Prime, C. Pang, and M. Hamilton. private communication.
- [67] Jaakko Yli-Ojanperä, Ari Ukkonen, Anssi Järvinen, Steve Layzell, Ville Niemelä, and Jorma Keskinen. Bipolar Charge Analyzer (BOLAR): A new aerosol instrument for bipolar charge measurements. *Journal of Aerosol Science*, 77:16–30, 2014. doi: 10.1016/j.jaerosci.2014.07.004.

- [68] Sharon S Y Leung, Thaigarajan Parumasivam, Fiona G Gao, Nicholas B Carrigy, Reinhard Vehring, Warren H Finlay, Sandra Morales, Warwick J Britton, Elizabeth Kutter, and Hak-Kim Chan. Production of Inhalation Phage Powders Using Spray Freeze Drying and Spray Drying Techniques for Treatment of Respiratory Infections. *Pharmaceutical Research*, 33(6): 1486–1496, 2016. doi: 10.1007/s11095-016-1892-6.
- [69] Rahul Bharadwaj, Carson Smith, and Bruno C. Hancock. The coefficient of restitution of some pharmaceutical tablets/compacts. *International Journal of Pharmaceutics*, 402(1):50–56, 2010. doi: 0.1016/j.ijpharm.2010.09.018.
- [70] Fatemeh Naderi Mehr, Dmitry Grigoriev, Nikolay Pureskiy, and Alexander Böker. Mono-patchy zwitterionic microcolloids as building blocks for pH-controlled self-assembly. *Soft Matter*, 15(11):2430–2438, 2019. doi: 10.1039/C8SM02151A.
- [71] Zhenli Zhang and Sharon C Glotzer. Self-Assembly of Patchy Particles. *Nano Letters*, 4(8):1407–1413, 2004. doi: 10.1021/nl0493500.
- [72] Étienne Duguet, Céline Hubert, Cyril Chomette, Adeline Perro, and Serge Ravaine. Patchy colloidal particles for programmed self-assembly. *Comptes Rendus Chimie*, 19(1):173–182, 2016. doi: 10.1016/j.crci.2015.11.013.
- [73] Niladri Patra and Alexei V Tkachenko. Programmable self-assembly of diamond polymorphs from chromatic patchy particles. *Physical Review E*, 98(3):32611, 2018. doi: 10.1103/PhysRevE.98.032611.
- [74] Erik W Edwards, Dayang Wang, and Helmuth Möhwald. Hierarchical Organization of Colloidal Particles: From Colloidal Crystallization to Supraparticle Chemistry. *Macromolecular Chemistry and Physics*, 208(5):439–445, 2007. doi: 10.1002/macp.200600655.
- [75] Emanuela Bianchi, Christos N Likos, and Gerhard Kahl. Self-Assembly of Heterogeneously Charged Particles under Confinement. *ACS Nano*, 7(5):4657–4667, 2013. doi: 10.1021/nm401487m.
- [76] S C Glotzer, M J Solomon, and N A Kotov. Self-assembly: From nanoscale to microscale colloids. *AIChE Journal*, 50(12):2978–2985, 2004. doi: 10.1002/aic.10413.
- [77] Ruohai Guo, Jian Mao, Xu-Ming Xie, and Li-Tang Yan. Predictive supracolloidal helices from patchy particles. *Scientific Reports*, 4(1):7021, 2014. doi: 10.1038/srep07021.
- [78] Shan Jiang and Steve Granick. A Simple Method to Produce Trivalent Colloidal Particles. *Langmuir*, 25(16):8915–8918, 2009. doi: 10.1021/la902152n.
- [79] Francesco Sciortino, Emanuela Bianchi, Jack F Douglas, and Piero Tartaglia. Self-assembly of patchy particles into polymer chains: A

- parameter-free comparison between Wertheim theory and Monte Carlo simulation. *The Journal of Chemical Physics*, 126(19):194903, 2007. doi: 10.1063/1.2730797.
- [80] Zhe Gong, Theodore Hueckel, Gi-Ra Yi, and Stefano Sacanna. Patchy particles made by colloidal fusion. *Nature*, 550(7675):234–238, 2017. doi: 10.1038/nature23901.
- [81] Lucero Sanchez, Paul Patton, Stephen M Anthony, Yi Yi, and Yan Yu. Tracking single-particle rotation during macrophage uptake. *Soft Matter*, 11(26):5346–5352, 2015. doi: 10.1039/C5SM00893J.
- [82] Yi Yi, Lucero Sanchez, Yuan Gao, and Yan Yu. Janus particles for biological imaging and sensing. *Analyst*, 141(12):3526–3539, 2016. doi: 10.1039/C6AN00325G.
- [83] Rémi Mérindol, Etienne Duguet, and Serge Ravaine. Synthesis of Colloidal Molecules: Recent Advances and Perspectives. *Chemistry – An Asian Journal*, 14(19):3232–3239, 2019. doi: 10.1002/asia.201900962.
- [84] Shuguang Zhang. Fabrication of novel biomaterials through molecular self-assembly. *Nat Biotech*, 21(10):1171–1178, 2003.
- [85] G. M. Whitesides and M. Boncheva. Beyond molecules: Self-assembly of mesoscopic and macroscopic components. *Proceedings of the National Academy of Sciences*, 99(8):4769–4774, 2002. doi: 10.1073/pnas.082065899.
- [86] M. Vendruscolo, J. Zurdo, C. E. MacPhee, and C. M. Dobson. Protein folding and misfolding: a paradigm of self-assembly and regulation in complex biological systems. *Philosophical Transactions of the Royal Society A: Mathematical, Physical and Engineering Sciences*, 361(1807):1205–1222, 2003. doi: 10.1098/rsta.2003.1194.
- [87] Christopher M Dobson. Principles of protein folding, misfolding and aggregation. *Seminars in Cell and Developmental Biology*, 15(1):3–16, 2004. doi: 10.1016/j.semcdb.2003.12.008.
- [88] Alan Sellinger, Pilar M Weiss, Anh Nguyen, Yunfeng Lu, Roger a Assink, Weiliang Gong, and C Jeffrey Brinker. That Mimic Nacre. *Nature*, 394 (July):256–260, 1998. doi: 10.1038/28354.
- [89] E Hückel and P Debye. The theory of electrolytes: I. lowering of freezing point and related phenomena. *Phys. Z*, 24:185–206, 1923.
- [90] Margaret Robson Wright. *An Introduction to Aqueous Electrolyte Solutions*. Wiley, 1st edition edition, 2007. ISBN 9780470842942,0470842946.
- [91] Ikuo S. Sogami (auth.) Norio Ise. *Structure Formation in Solution: Ionic Polymers and Colloidal Particles*. Springer-Verlag Berlin Heidelberg, 1 edition, 2005. ISBN 3540252711.

- [92] Shasha Xu, Yanhua Wang, Yue Zhao, Weilin Chen, Jiabo Wang, Lifei He, Zhongmin Su, Enbo Wang, and Zhenhui Kang. Keplerate-type polyoxometalate/semiconductor composite electrodes with light-enhanced conductivity towards highly efficient photoelectronic devices. *J. Mater. Chem. A*, 4(36):14025–14032, 2016. doi: 10.1039/C6TA03853K.
- [93] Chun Yi Sun, Chao Qin, Chun Gang Wang, Zhong Min Su, Shuang Wang, Xin Long Wang, Guang Sheng Yang, Kui Zhan Shao, Ya Qian Lan, and En Bo Wang. Chiral nanoporous metal-organic frameworks with high porosity as materials for drug delivery. *Advanced Materials*, 23(47):5629–5632, 2011. doi: 10.1002/adma.201102538.
- [94] Ivan V. Kozhevnikov. Catalysis by Heteropoly Acids and Multicomponent Polyoxometalates in Liquid-Phase Reactions. *Chemical Reviews*, 98(1): 171–198, 1998. doi: 10.1021/cr960400y.
- [95] Chun Yan Sun, Shu Xia Liu, Da Dong Liang, Kui Zhan Shao, Yuan Hang Ren, and Zhong Min Su. Highly stable crystalline catalysts based on a microporous metal-organic framework and polyoxometalates, 2009.
- [96] Noritaka Mizuno, Kazuya Yamaguchi, and Keigo Kamata. Epoxidation of olefins with hydrogen peroxide catalyzed by polyoxometalates. *Coordination Chemistry Reviews*, 249(17-18 SPEC. ISS.):1944–1956, 2005. doi: 10.1016/j.ccr.2004.11.019.
- [97] Panchao Yin, Dong Li, and Tianbo Liu. Solution behaviors and self-assembly of polyoxometalates as models of macroions and amphiphilic polyoxometalate–organic hybrids as novel surfactants. *Chemical Society Reviews*, 41(22):7368, 2012. doi: 10.1039/c2cs35176e.
- [98] Dawei Fan and Jingcheng Hao. Phase stability of Keplerate-type polyoxomolybdates controlled by added cationic surfactant. *Journal of Colloid and Interface Science*, 333(2):757–763, 2009. doi: 10.1016/j.jcis.2009.01.034.
- [99] Guang Liu and Tianbo Liu. Strong attraction among the fully hydrophilic {Mo₇₂Fe₃₀} macroanions. *Journal of the American Chemical Society*, 127(19):6942–6943, 2005. doi: 10.1021/ja0510966.
- [100] Joseph M. Pigga, Joseph A. Teprovich, Robert A. Flowers, Mark R. Antonio, and Tianbo Liu. Selective monovalent cation association and exchange around keplerate polyoxometalate macroanions in dilute aqueous solutions. *Langmuir*, 26(12):9449–9456, 2010. doi: 10.1021/la100467p.
- [101] Jie Zhang, Dong Li, Guang Liu, Kerney Jebrell Glover, and Tianbo Liu. Lag periods during the self-assembly of {Mo₇₂Fe₃₀} macroions: Connection to the virus capsid formation process. *Journal of the American Chemical Society*, 131(42):15152–15159, 2009. doi: 10.1021/ja903548m.
- [102] Joseph M. Pigga and Tianbo Liu. Stability of Keplerate polyoxometalate macroanionic assemblies in salt-containing aqueous solutions. *Inorganica Chimica Acta*, 363(15):4230–4233, 2010. doi: 10.1016/j.ica.2010.06.062.

- [103] Ethayaraja Mani, Jan Groenewold, and Willem K. Kegel. Properties of shell-like assemblies of weakly charged Keplerate-type polyoxometalates. *Inorganica Chimica Acta*, 363(15):4295–4298, 2010. doi: 10.1016/j.ica.2010.06.036.
- [104] Aletta A. Verhoeff, Melissa L. Kistler, Anish Bhatt, Joe Pigga, Jan Groenewold, Mark Klokkenburg, Sandra Veen, Soumyajit Roy, Tianbo Liu, and Willem K. Kegel. Charge regulation as a stabilization mechanism for shell-like assemblies of polyoxometalates. *Physical Review Letters*, 99(6):2–5, 2007. doi: 10.1103/PhysRevLett.99.066104.
- [105] Joseph M. Pigga, Melissa L. Kistler, Chwen Yang Shew, Mark R. Antonio, and Tianbo Liu. Counterion distribution around hydrophilic molecular macroanions: The source of the attractive force in self-assembly. *Angewandte Chemie - International Edition*, 48(35):6538–6542, 2009. doi: 10.1002/anie.200902050.
- [106] Zhuonan Liu, Tianbo Liu, and Mesfin Tsige. Elucidating the Origin of the Attractive Force among Hydrophilic Macroions. *Scientific Reports*, 6(January):26595, 2016. doi: 10.1038/srep26595.
- [107] Peter et al. Atkins. *Physical chemistry*. W.H. Freeman and Company, New York, 2010. ISBN 9781429218122.
- [108] Sandra J Veen. *Assemblies of Polyoxometalates*. PhD thesis, Universiteit Utrecht, 2009.
- [109] Fadi Haso, Dong Li, Somenath Garai, Joseph M. Pigga, and Tianbo Liu. Self-Recognition between Two Almost Identical Macroions during Their Assembly: The Effects of pH and Temperature, 2015.
- [110] Tianbo Liu. Supermolecular structures of polyoxomolybdate-based giant molecules in aqueous solution. *Journal of the American Chemical Society*, 124(37):10942–10943, 2002. doi: 10.1021/ja027045f.
- [111] Tianbo Liu, Brandon Imber, Ekkehard Diemann, Guang Liu, Katrina Cokleski, Huilin Li, Zhiqiang Chen, and Achim Müller. Deprotonations and charges of well-defined {Mo₇₂Fe₃₀} nanoacids simply stepwise tuned by pH allow control/variation of related self-assembly processes. *Journal of the American Chemical Society*, 128(49):15914–15920, 2006. doi: 10.1021/ja066133n.
- [112] Melissa L Kistler, Anish Bhatt, Guang Liu, Diego Casa, and Tianbo Liu. A Complete Macroion- “ Blackberry ” Assembly-Macroion Transition with Continuously Adjustable Assembly Sizes in { Mo 132 } Water / Acetone Systems. *Transition*, (10):6453–6460, 2007.
- [113] Melissa L. Kistler, Tianbo Liu, Pierre Gouzerh, Ana Maria Todea, and Achim Müller. Molybdenum-oxide based unique polyprotic nanoacids showing different deprotonations and related assembly processes in solution. *Dalton Transactions*, (26):5094, 2009. doi: 10.1039/b901505a.

- [114] S. Sauter and C. Schwab. *Boundary Element Methods*. Springer-Verlag, Berlin, 2010. ISBN 978-3-540-68093-2.
- [115] Muhammad Hassan. *Mathematical Analysis of Boundary Integral Equations and Domain Decomposition Methods with Applications in Polarisable Electrostatics*. PhD thesis, RWTH Aachen University, 3 2020.

Appendix A

Theory

A.1 Mathematical considerations

This section contains some additional mathematical considerations such as more details about our mathematical assumptions, the properties of the mathematical objects used in this thesis and a precise definition of the Galerkin approximation space that is used.

To begin with, we always assume that the external harmonic potential we consider satisfies $\Phi_{\text{ext}} \in H_{\text{loc}}^1(\mathbb{R}^3)$ with the associated external electric field $\mathbf{E}_{\text{ext}} := -\nabla\Phi_{\text{ext}} \in L_{\text{loc}}^2(\mathbb{R}^3)$, where $L_{\text{loc}}^2(\mathbb{R}^3)$ and $H_{\text{loc}}^1(\mathbb{R}^3)$ denote the spaces of locally square integrable functions and locally square integrable functions with locally square integrable first derivatives, respectively.

Next, we emphasise that, as is common in the mathematical literature, the solution to the PDE (2.8)-(2.11), i.e., the perturbed electrostatic function Φ , is typically understood as an element of the space $H^1(\Omega)$ and is therefore not, in general, continuous. Strictly speaking therefore, the transmission conditions in Equations (2.8)-(2.11) must be understood in the sense of so-called Dirichlet and Neumann traces in the Sobolev spaces $H^{\frac{1}{2}}(\lambda)$ and $H^{-\frac{1}{2}}(\lambda)$ respectively. A detailed description of trace operators and fractional Sobolev spaces is be-

yond the scope of this article and can, for instance, be found in [114, Chapter 2].

Concerning the mapping properties of the single layer potential and boundary operators, it can be shown that for any $s \in \mathbb{R}$, the mapping \mathcal{S} extends as a bounded linear map from the Sobolev space $H^s(\lambda)$ to $H_{\text{loc}}^{s+3/2}(\mathbb{R}^3)$ and the operator \mathcal{V} extends as an invertible, bounded linear map from $H^s(\lambda)$ to $H^{s+1}(\lambda)$ (see, e.g., [114, Chapter 2] for a concise exposition on Sobolev spaces and [114, Chapter 3] for precise definitions and properties of the single layer potential). “Local” versions of the single layer potential and boundary operators which we have used frequently in this thesis are formally defined as follows: For each $i \in \{1, \dots, N\}$, we have

$$\begin{aligned} (\mathcal{S}_i \sigma_i)(\mathbf{x}) &:= \int_{\lambda_i} \frac{\sigma_i(\mathbf{y})}{4\pi|\mathbf{x} - \mathbf{y}|} d\mathbf{y}, & \forall \mathbf{x} \in \Omega_i \cup \mathbb{R}^3 \setminus \overline{\Omega}_i, \quad \forall \sigma_i \in H^s(\lambda_i), \quad s \in \mathbb{R}, \\ (\mathcal{V}_i \sigma_i)(\mathbf{x}) &:= \int_{\lambda_i} \frac{\sigma_i(\mathbf{y})}{4\pi|\mathbf{x} - \mathbf{y}|} d\mathbf{y}, & \forall \mathbf{x} \in \lambda_i, \quad \forall \sigma_i \in H^s(\lambda_i), \quad s \in \mathbb{R}. \end{aligned}$$

In addition, we have used extensively in this article, the so-called Dirichlet-to-Neumann map, denoted DtN. Mathematically, the map $\text{DtN}: H^s(\Gamma) \rightarrow H^{s-1}(\lambda)$, $s \in \mathbb{R}$ is defined as follows: Given some boundary function $\lambda \in H^s(\lambda)$, let u_λ denote the harmonic extension of λ in Ω^- . Then $\text{DtN}\lambda \in H^{s-1}(\lambda)$ is the normal derivative of u_λ on the boundary λ . We emphasise that in contrast to the single layer potential and boundary operator, the DtN map is a purely local operator, i.e., for any $\lambda \in H^s(\lambda)$, $\text{DtN}\lambda|_{\lambda_i}$ depends only on $\lambda|_{\lambda_i}$.

Concerning the regularity of solutions to the BIE (2.13), we recall from Equations (2.8)-(2.11) that the point-charge contribution σ_p to the free surface charge is assumed to be a linear combination of Dirac delta distributions. It is possible to show therefore that σ_p is an element of the Sobolev space $H^r(\lambda)$ for every $r < -1$. In view of the regularising property of the single layer boundary operator \mathcal{V} , we can conclude that the right-hand side of the BIE (2.13) is, in general, an element of $H^r(\lambda)$ for every $r < 0$. This implies in particular that

solutions to the BIE (2.13) are not, in general, square integrable functions. On the other hand, we recall that $\sigma_s \in L^2(\lambda)$ by assumption so that solutions to the BIE (2.16) can be readily understood as elements of the Sobolev space $H^1(\lambda)$.

Finally, let us state the definition of the approximation space used in our proposed Galerkin discretisation.

Definition A.1 (Spherical Harmonics). *For every integer $\ell \in \mathbb{N} \cup \{0\}$ and $m \in \{-\ell, \dots, \ell\}$ we define $\mathcal{Y}_\ell^m: \mathbb{S}^2 \rightarrow \mathbb{R}$ as the real-valued L^2 -orthonormal spherical harmonic of degree ℓ and order m on the unit sphere \mathbb{S}^2 (see [115] for a precise, constructive definition).*

We remind the reader here that the set of spherical harmonics is dense in $L^2(\mathbb{S}^2)$ and is therefore well-suited for the choice of basis functions in the Galerkin discretisation of BIE (2.16).

Definition A.2 (Approximation Spaces). *Let $N \in \mathbb{N}$ be a discretisation parameter. First, on each sphere λ_i , $i = 1, \dots, N$ we define a local approximation space $W^N(\lambda_i)$ as*

$$W^N(\lambda_i) := \left\{ u: \lambda_i \rightarrow \mathbb{R} \right. \\ \left. \text{such that } u(\mathbf{x}) = \sum_{\ell=0}^N \sum_{m=-\ell}^{m=+\ell} [u]_\ell^m \mathcal{Y}_{\ell m}^i(\mathbf{x}) \quad \text{with } [u]_\ell^m \in \mathbb{R} \right\},$$

where we introduced for notational convenience the basis functions $\mathcal{Y}_{\ell m}^i: \lambda_i \rightarrow \mathbb{R}$ as

$$\mathcal{Y}_{\ell m}^i(\mathbf{x}) := \mathcal{Y}_\ell^m \left(\frac{\mathbf{x} - \mathbf{x}_i}{|\mathbf{x} - \mathbf{x}_i|} \right) \quad \forall \mathbf{x} \in \lambda_i.$$

Moreover, we define the global approximation space $W^N(\lambda)$ as

$$W^N(\lambda) := \left\{ u: \Gamma \rightarrow \mathbb{R} \text{ such that } \forall i \in \{1, \dots, N\}: u|_{\lambda_i} \in W^N(\lambda_i) \right\}.$$

A.2 Mathematical Proofs

In this section we provide proofs of ideas from Section 2.1.5, beginning with the proof of 2.31. This result shows that the definition of the interaction energy that we have provided in this article uses quantities of interest from the integral equation (2.13) and is consistent with the electric field-based definition of the interaction energy as derived directly from the PDEs (2.3)-(2.5) and (2.8)-(2.11). Throughout this section, we will use the notation and setting introduced in Sections 2.1.2, 2.1.3 and 2.1.5.

Proof. Let $j \in \{1, \dots, N\}$ and let \mathbb{B}_r be an open ball large enough so that $\Omega^- \subset \mathbb{B}_r$. We begin by defining precisely \mathbf{E}^{jj} , i.e., the electric field produced only due to the sphere λ_j in the absence of both the external field \mathbf{E}_{ext} as well as the other spheres. Maxwell's equations imply that $\mathbf{E}^{jj} := -\nabla\Phi^{jj}$ where the self-potential Φ^{jj} satisfies the PDE (c.f., Equation (2.8)-(2.11))

$$\begin{aligned}
 -\Delta\Phi^{jj} &= 0 && \text{in } \Omega_j \cup \mathbb{R}^3 \setminus \overline{\Omega_j} \\
 \llbracket\Phi^{jj}\rrbracket &= 0 && \text{on } \Gamma_j, \\
 \llbracket\kappa\nabla\Phi^{jj}\rrbracket &= \sigma_{s,j} + \sigma_{p,j} && \text{on } \Gamma_j, \\
 |\Phi^{jj}| &\rightarrow 0 && \text{as } |\mathbf{x}| \rightarrow \infty,
 \end{aligned} \tag{A.1}$$

where we remind the reader that $\sigma_{s,j} := \sigma_f|_{\lambda_j}$ and $\sigma_{p,j} := \sigma_p|_{\lambda_j}$.

Next, to aid the subsequent exposition, we define the auxiliary quantity

$$\begin{aligned}
 U_{\text{PDE,int}}^r &:= \int_{\mathbb{B}_r} \kappa(\mathbf{x})\mathbf{E}_{\text{tot}}(\mathbf{x}) \cdot \mathbf{E}_{\text{tot}}(\mathbf{x}) \, d\mathbf{x} \\
 &\quad - \sum_{j=1}^N \int_{\mathbb{B}_r} \kappa(\mathbf{x})\mathbf{E}^{jj}(\mathbf{x}) \cdot \mathbf{E}^{jj}(\mathbf{x}) \, d\mathbf{x} - \int_{\mathbb{B}_r} \kappa_0\mathbf{E}_{\text{ext}}(\mathbf{x}) \cdot \mathbf{E}_{\text{ext}}(\mathbf{x}) \, d\mathbf{x}. \tag{A.2}
 \end{aligned}$$

We may now use simple algebra and the fact that $\Phi_{\text{tot}} = \Phi + \Phi_{\text{ext}}$ (see Section

2.1.2) to deduce that

$$\begin{aligned} U_{\text{PDE,int}}^r &= \int_{\mathbb{B}_r} \kappa(\mathbf{x}) |\nabla \Phi(\mathbf{x})|^2 d\mathbf{x} + 2 \int_{\mathbb{B}_r} \kappa(\mathbf{x}) \nabla \Phi(\mathbf{x}) \cdot \nabla \Phi_{\text{ext}}(\mathbf{x}) d\mathbf{x} \\ &\quad - \sum_{j=1}^N \int_{\mathbb{B}_r} \kappa(\mathbf{x}) |\nabla \Phi^{jj}(\mathbf{x})|^2 d\mathbf{x} + \int_{\mathbb{B}_r} (\kappa(\mathbf{x}) - \kappa_0) |\nabla \Phi_{\text{ext}}(\mathbf{x})|^2 d\mathbf{x}. \end{aligned}$$

Next, we recall from the PDEs (2.3)-(2.5) and (2.8)-(2.11) that Φ is harmonic on $\Omega^- \cup \Omega^+$, Φ_{ext} is harmonic on \mathbb{R}^3 , and Φ^{jj} is harmonic on $\Omega_j \cup (\mathbb{R}^3 \setminus \overline{\Omega_j})$. Therefore we can appeal to Green's first identity to simplify the above integrals as

$$\begin{aligned} \int_{\mathbb{B}_r} \kappa(\mathbf{x}) |\nabla \Phi(\mathbf{x})|^2 d\mathbf{x} &= \int_{\lambda} [[\kappa \nabla \Phi]](\mathbf{x}) \Phi(\mathbf{x}) d\mathbf{x} + \int_{\partial \mathbb{B}_r} \kappa_0 \partial_n \Phi(\mathbf{x}) \Phi(\mathbf{x}) d\mathbf{x}, \\ 2 \int_{\mathbb{B}_r} \kappa(\mathbf{x}) \nabla \Phi_{\text{ext}}(\mathbf{x}) \cdot \nabla \Phi(\mathbf{x}) &= 2 \int_{\lambda} [[\kappa \nabla \Phi]](\mathbf{x}) \Phi_{\text{ext}}(\mathbf{x}) d\mathbf{x} \\ &\quad + 2 \int_{\partial \mathbb{B}_r} \kappa_0 \partial_n \Phi(\mathbf{x}) \Phi_{\text{ext}}(\mathbf{x}) d\mathbf{x}, \\ \int_{\mathbb{B}_r} \sum_{j=1}^N \kappa(\mathbf{x}) |\nabla \Phi^{jj}(\mathbf{x})|^2 d\mathbf{x} &= \sum_{j=1}^N \int_{\lambda_j} (\kappa_j - \kappa_0) \partial_n \Phi^{jj}(\mathbf{x}) \Phi^{jj}(\mathbf{x}) d\mathbf{x} \\ &\quad + \sum_{j=1}^N \int_{\partial \mathbb{B}_r} \kappa_0 \partial_n \Phi^{jj}(\mathbf{x}) \Phi^{jj}(\mathbf{x}) d\mathbf{x}, \\ \int_{\mathbb{B}_r} (\kappa(\mathbf{x}) - \kappa_0) |\nabla \Phi_{\text{ext}}(\mathbf{x})|^2 d\mathbf{x} &= \int_{\lambda} (\kappa(\mathbf{x}) - \kappa_0) \partial_n \Phi_{\text{ext}}(\mathbf{x}) \Phi_{\text{ext}}(\mathbf{x}) d\mathbf{x}. \end{aligned}$$

Recalling the interface conditions from the PDEs (2.8)-(2.11) and (A.1), we can further simplify several of these integral as

$$\begin{aligned} \int_{\lambda} [[\kappa \nabla \Phi]](\mathbf{x}) \Phi(\mathbf{x}) d\mathbf{x} &= (\sigma_s + \sigma_p + \sigma_{\text{ext}}, \Phi)_{L^2(\lambda)}, \\ 2 \int_{\lambda} [[\kappa \nabla \Phi]](\mathbf{x}) \Phi_{\text{ext}}(\mathbf{x}) d\mathbf{x} &= 2(\sigma_s + \sigma_p + \sigma_{\text{ext}}, \Phi_{\text{ext}})_{L^2(\lambda)}, \\ \sum_{j=1}^N \int_{\lambda_j} (\kappa_j - \kappa_0) \partial_n \Phi^{jj}(\mathbf{x}) \Phi^{jj}(\mathbf{x}) d\mathbf{x} &= \sum_{j=1}^N (\sigma_{s,j} + \sigma_{p,j}, \Phi^{jj})_{L^2(\lambda_j)}, \\ \int_{\lambda} (\kappa(\mathbf{x}) - \kappa_0) \partial_n \Phi_{\text{ext}}(\mathbf{x}) \Phi_{\text{ext}}(\mathbf{x}) d\mathbf{x} &= -(\sigma_{\text{ext}}, \Phi_{\text{ext}})_{L^2(\lambda)}, \end{aligned}$$

where we remind the reader that $\sigma_{\text{ext}} = -(\kappa - \kappa_0) \partial_n \Phi_{\text{ext}}$. Using the fact that

λ , λ_{ext} and λ^{jj} are the restrictions on the spheres of the potentials Φ , Φ_{ext} , and Φ^{jj} respectively, we can deduce that

$$\begin{aligned} U_{\text{PDE,int}}^r &= (\sigma_s + \sigma_p + \sigma_{\text{ext}}, \lambda)_{L^2(\lambda)} + 2(\sigma_s + \sigma_p, \lambda_{\text{ext}})_{L^2(\lambda)} + (\sigma_{\text{ext}}, \lambda_{\text{ext}}^N)_{L^2(\lambda)} \\ &\quad - \frac{1}{2} \sum_{j=1}^N (\sigma_{s,j} + \sigma_{p,j}, \lambda^{jj})_{L^2(\lambda_j)} \\ &\quad + \int_{\partial B_r} \kappa_0 \left(\partial_n \Phi(\mathbf{x}) \Phi(\mathbf{x}) - \sum_{j=1}^N \partial_n \Phi^{jj}(\mathbf{x}) \Phi^{jj}(\mathbf{x}) \right) d\mathbf{x} \\ &\quad + 2 \int_{\partial B_r} \kappa_0 \partial_n \Phi(\mathbf{x}) \Phi_{\text{ext}}(\mathbf{x}) d\mathbf{x} = U_{\text{int}}. \end{aligned}$$

Comparing this final expression with Equation (A.2) allows us to deduce the required result (2.31). \square

Next, we will prove that Equation (2.34) of the approximate electrostatic forces is consistent with the usual notion in the chemistry literature of the forces as the negative sphere-centered gradients of the electrostatic interaction energy. In order to present a concise and well-structured proof, we will first prove two lemmas.

Lemma A.1. *Let λ_N denote the solution to the Galerkin discretisation (2.25) for a given free charge $\sigma_f = \sigma_s + \sigma_p$ and external electric field \mathbf{E}_{ext} . Additionally, let σ_N denote the approximate induced surface corresponding to λ_N and let $\mathbf{E}_{\text{exc}}^i$, $i \in \{1, \dots, N\}$ denote the i -excluded electric fields generated by σ_N as defined through Definition 2.24. Then for each $i \in \{1, \dots, N\}$ it holds that*

$$\frac{1}{2} \nabla_{\mathbf{x}_i} \left(\sigma_s + \sigma_p + \sigma_{\text{ext}}, \lambda_N \right)_{L^2(\lambda)} = -\kappa_0 (\sigma_N, \mathbf{E}_{\text{exc}}^i)_{L^2(\lambda_i)} + (\nabla_{\mathbf{x}_i} \sigma_{\text{ext}}, \lambda_N)_{L^2(\lambda_i)}.$$

Proof. Let $i \in \{1, \dots, M\}$ be fixed. A simple application of the product rule yields that

$$\begin{aligned} \frac{1}{2} \nabla_{\mathbf{x}_i} \left(\sigma_s + \sigma_p + \sigma_{\text{ext}}, \lambda_N \right)_{L^2(\lambda)} &= \frac{1}{2} \left(\nabla_{\mathbf{x}_i} (\sigma_s + \sigma_p + \sigma_{\text{ext}}), \lambda_N \right)_{L^2(\lambda)} \\ &\quad + \frac{1}{2} \left(\sigma_s + \sigma_p + \sigma_{\text{ext}}, \nabla_{\mathbf{x}_i} \lambda_N \right)_{L^2(\lambda)}. \end{aligned}$$

Using the fact that both σ_s and σ_p are independent of changes in the locations $\{\mathbf{x}_i\}_{i=1}^N$ of the sphere centres locations (in the sense which is specified precisely in [115, Chapter 5]), we further obtain that

$$\begin{aligned} \frac{1}{2} \nabla_{\mathbf{x}_i} \left(\sigma_s + \sigma_p + \sigma_{\text{ext}}, \lambda_N \right)_{L^2(\lambda)} &= \frac{1}{2} \left(\nabla_{\mathbf{x}_i} \sigma_{\text{ext}}, \lambda_N \right)_{L^2(\lambda)} \\ &+ \frac{1}{2} \left(\sigma_s + \sigma_p + \sigma_{\text{ext}}, \nabla_{\mathbf{x}_i} \lambda_N \right)_{L^2(\lambda)}. \end{aligned}$$

Finally, it is straightforward to see that in fact

$$\frac{1}{2} \left(\nabla_{\mathbf{x}_i} \sigma_{\text{ext}}, \lambda_N \right)_{L^2(\lambda)} = \frac{1}{2} \left(\nabla_{\mathbf{x}_i} \sigma_{\text{ext}}, \lambda_N \right)_{L^2(\lambda_i)}$$

so that we obtain the expression

$$\begin{aligned} \frac{1}{2} \nabla_{\mathbf{x}_i} \left((\sigma_s + \sigma_p + \sigma_{\text{ext}}), \lambda_N \right)_{L^2(\lambda)} &= \frac{1}{2} \left(\nabla_{\mathbf{x}_i} \sigma_{\text{ext}}, \lambda_N \right)_{L^2(\lambda_i)} \quad (\text{A.3}) \\ &+ \frac{1}{2} \left((\sigma_s + \sigma_p + \sigma_{\text{ext}}), \nabla_{\mathbf{x}_i} \lambda_N \right)_{L^2(\lambda)}. \end{aligned}$$

Consequently, it remains to compute the sphere-centred gradient of λ_N . This is a slightly technical task so to aid the subsequent exposition, we first introduce some additional notation.

Notation: We define the vectors and matrices $\boldsymbol{\sigma}$, $\boldsymbol{\sigma}^{\text{ext}}$, \mathbf{DtN}^κ and \mathcal{V} as

$$\begin{aligned} [\boldsymbol{\sigma}_i]_\ell^m &:= (\sigma_s + \sigma_p, \mathcal{Y}_{\ell m}^i)_{L^2(\lambda_i)}, \\ [\boldsymbol{\sigma}_i^{\text{ext}}]_\ell^m &:= (\sigma_{\text{ext}}, \mathcal{Y}_{\ell m}^i)_{L^2(\lambda_i)}, \\ [\mathbf{DtN}_{ij}^\kappa]_{\ell\ell'}^{mm'} &:= \delta_{ij} \left(\frac{\kappa_j - \kappa_0}{\kappa_0} \mathbf{DtN} \mathcal{Y}_{\ell' m'}^j, \mathcal{Y}_{\ell m}^i \right)_{L^2(\lambda_i)}, \\ [\mathcal{V}_{ij}]_{\ell\ell'}^{mm'} &:= (\mathcal{V} \mathcal{Y}_{\ell' m'}^j, \mathcal{Y}_{\ell m}^i)_{L^2(\lambda_i)}, \end{aligned}$$

where $i, j \in \{1, \dots, N\}$, $\ell, \ell' \in \{0, \dots, N\}$ and $|m| \leq \ell$, $|m'| \leq \ell'$. Additionally, we recall that the Galerkin discretisation (2.25) is equivalent to the linear

system of equations

$$\mathbf{A}\boldsymbol{\lambda} := (\mathbf{I} - \mathcal{V}\mathbf{DtN}^\kappa)\boldsymbol{\lambda} = \mathbf{F}, \quad (\text{A.4})$$

where $\boldsymbol{\lambda}$ and \mathbf{F} are defined by (2.27) and (2.28) respectively.

Equipped with notation introduced above, we now take the gradient on both sides of Equation (A.4). Using the product rule together with the fact that the Dirichlet-to-Neumann map is independent of changes in the locations $\{\mathbf{x}_i\}_{i=1}^N$ of the sphere centers, we obtain that

$$\nabla_{\mathbf{x}_i}\boldsymbol{\lambda} + (\nabla_{\mathbf{x}_i}\mathcal{V})\mathbf{DtN}^\kappa\boldsymbol{\lambda} + \mathcal{V}\mathbf{DtN}^\kappa\nabla_{\mathbf{x}_i}\boldsymbol{\lambda} = \frac{1}{\kappa_0}(\nabla_{\mathbf{x}_i}\mathcal{V})(\boldsymbol{\sigma} + \boldsymbol{\sigma}^{\text{ext}}) + \frac{1}{\kappa_0}\mathcal{V}\nabla_{\mathbf{x}_i}\boldsymbol{\sigma}^{\text{ext}},$$

or equivalently, after collecting terms

$$\mathbf{A}\nabla_{\mathbf{x}_i}\boldsymbol{\lambda} = \frac{1}{\kappa_0}(\nabla_{\mathbf{x}_i}\mathcal{V})(\boldsymbol{\sigma} + \boldsymbol{\sigma}^{\text{ext}} - \kappa_0\mathbf{DtN}^\kappa\boldsymbol{\lambda}) + \frac{1}{\kappa_0}\mathcal{V}\nabla_{\mathbf{x}_i}\boldsymbol{\sigma}^{\text{ext}}. \quad (\text{A.5})$$

Next, recalling that σ_N satisfies Equation (2.33), it is easy to deduce that

$$\frac{1}{\kappa_0}(\nabla_{\mathbf{x}_i}\mathcal{V})(\boldsymbol{\sigma} + \boldsymbol{\sigma}^{\text{ext}} - \kappa_0\mathbf{DtN}^\kappa\boldsymbol{\lambda}) = (\nabla_{\mathbf{x}_i}\mathcal{V})\boldsymbol{\sigma},$$

where

$$[\boldsymbol{\sigma}_i]_\ell^m := (\sigma_N, \mathcal{Y}_{\ell m}^i)_{L^2(\lambda_i)},$$

with indices $i \in \{1, \dots, N\}$, $\ell \in \{0, \dots, N\}$ and $|m| \leq \ell$. We therefore conclude from Equation (A.5) that

$$\nabla_{\mathbf{x}_i}\boldsymbol{\lambda} = \mathbf{A}^{-1}((\nabla_{\mathbf{x}_i}\mathcal{V})\boldsymbol{\sigma}) + \frac{1}{\kappa_0}\mathbf{A}^{-1}(\mathcal{V}\nabla_{\mathbf{x}_i}\boldsymbol{\sigma}^{\text{ext}}).$$

Recalling now the last term on the right-hand side of Equation (A.3), we deduce

that

$$\begin{aligned}
\frac{1}{2} \left(\sigma_s + \sigma_p + \sigma_{\text{ext}}, \nabla_{\mathbf{x}_i} \lambda_N \right)_{L^2(\lambda)} &= \frac{1}{2} \left(\boldsymbol{\sigma} + \boldsymbol{\sigma}^{\text{ext}}, \nabla_{\mathbf{x}_i} \boldsymbol{\lambda} \right)_{\ell^2} \\
&= \frac{1}{2} \left(\boldsymbol{\sigma} + \boldsymbol{\sigma}^{\text{ext}}, \mathbf{A}^{-1} \left((\nabla_{\mathbf{x}_i} \mathcal{V}) \boldsymbol{\sigma} \right) \right)_{\ell^2} \\
&\quad + \frac{1}{2} \left(\boldsymbol{\sigma} + \boldsymbol{\sigma}^{\text{ext}}, \frac{1}{\kappa_0} \mathbf{A}^{-1} (\mathcal{V} \nabla_{\mathbf{x}_i} \boldsymbol{\sigma}^{\text{ext}}) \right)_{\ell^2} \\
&= \frac{1}{2} \left((\mathbf{A}^{\mathbf{T}})^{-1} (\boldsymbol{\sigma} + \boldsymbol{\sigma}^{\text{ext}}), (\nabla_{\mathbf{x}_i} \mathcal{V}) \boldsymbol{\sigma} \right)_{\ell^2} \\
&\quad + \frac{1}{2} \frac{1}{\kappa_0} \left((\mathbf{A}^{\mathbf{T}})^{-1} (\boldsymbol{\sigma} + \boldsymbol{\sigma}^{\text{ext}}), \mathcal{V} \nabla_{\mathbf{x}_i} \boldsymbol{\sigma}^{\text{ext}} \right)_{\ell^2}.
\end{aligned}$$

Next, a direct calculation and comparison with the Galerkin discretisation (2.25) and the definition of σ_N as given by Equation (2.32) reveals that

$$(\mathbf{A}^{\mathbf{T}})^{-1} (\boldsymbol{\sigma} + \boldsymbol{\sigma}^{\text{ext}}) = \kappa_0 \boldsymbol{\sigma}.$$

We thus obtain that

$$\begin{aligned}
\frac{1}{2} \left(\sigma_s + \sigma_p + \sigma_{\text{ext}}, \nabla_{\mathbf{x}_i} \lambda_N \right)_{L^2(\lambda)} &= \frac{1}{2} \kappa_0 \left(\boldsymbol{\sigma}, (\nabla_{\mathbf{x}_i} \mathcal{V}) \boldsymbol{\sigma} \right)_{\ell^2} + \frac{1}{2} \left(\boldsymbol{\sigma}, \mathcal{V} \nabla_{\mathbf{x}_i} \boldsymbol{\sigma}^{\text{ext}} \right)_{\ell^2} \\
&= \frac{1}{2} \kappa_0 \left(\boldsymbol{\sigma}, (\nabla_{\mathbf{x}_i} \mathcal{V}) \boldsymbol{\sigma} \right)_{\ell^2} + \frac{1}{2} \left(\boldsymbol{\lambda}, \nabla_{\mathbf{x}_i} \boldsymbol{\sigma}^{\text{ext}} \right)_{\ell^2} \\
&= \frac{1}{2} \kappa_0 \left(\sigma_N, (\nabla_{\mathbf{x}_i} \mathcal{V}) \sigma_N \right)_{L^2(\lambda)} + \frac{1}{2} \left(\lambda_N, \nabla_{\mathbf{x}_i} \sigma_{\text{ext}} \right)_{L^2(\lambda)} \\
&= \frac{1}{2} \kappa_0 \left(\sigma_N, (\nabla_{\mathbf{x}_i} \mathcal{V}) \sigma_N \right)_{L^2(\lambda)} + \frac{1}{2} \left(\lambda_N, \nabla_{\mathbf{x}_i} \sigma_{\text{ext}} \right)_{L^2(\lambda_i)}
\end{aligned} \tag{A.6}$$

Finally, a direct computation (see [115, Theorem 5.18] or [36, Supplementary Materials] for details) can be used to show that

$$\frac{1}{2} \kappa_0 \left(\sigma_N, (\nabla_{\mathbf{x}_i} \mathcal{V}) \sigma_N \right)_{L^2(\lambda)} = -\kappa_0 \left(\sigma_N, \mathbf{E}_{\text{exc}}^i \right)_{L^2(\lambda_i)}. \tag{A.7}$$

Combining therefore the developments (A.6) and (A.7) with Equation (A.3) now completes the proof. \square

Lemma A.2. For a given external electric field $\mathbf{E}_{\text{ext}} = -\nabla \Phi_{\text{ext}} \in L_{\text{loc}}^2(\mathbb{R}^3)$,

let $\sigma_{\text{ext}} = -(\kappa - \kappa_0)\partial_n\Phi_{\text{ext}}$, and let $\psi \in H^{\frac{1}{2}}(\lambda)$ be arbitrary. Then for each $i \in \{1, \dots, N\}$ it holds that

$$(\nabla_{\mathbf{x}_i}\sigma_{\text{ext}}, \Psi)_{L^2(\lambda_i)} = -(\kappa_i - \kappa_0) (\nabla_{\mathbf{x}_i}\lambda_{\text{ext}}, \text{DtN}\Psi)_{L^2(\lambda_i)}. \quad (\text{A.8})$$

Proof. Recall the notation $\lambda_{\text{ext}} := \Phi_{\text{ext}}|_{\lambda} \in H^{\frac{1}{2}}(\lambda)$ and let $[\lambda_{\text{ext},i}]_{\ell}^m$ and $[\Psi_i]_{\ell}^m$, $\ell \in \mathbb{N}_0$, $|m| \leq \ell$ denote the local spherical harmonics expansion coefficients of λ_{ext} and Ψ on the sphere λ_i . Since Φ_{ext} is harmonic in \mathbb{R}^3 and therefore in particular on $\overline{\Omega}_i$, it follows that we can write

$$\begin{aligned} (\nabla_{\mathbf{x}_i}\sigma_{\text{ext}}, \Psi)_{L^2(\lambda_i)} &= -(\kappa_i - \kappa_0) (\nabla_{\mathbf{x}_i}\partial_n\Phi_{\text{ext}}, \Psi)_{L^2(\lambda_i)} \\ &= -(\kappa_i - \kappa_0) (\text{DtN}\lambda_{\text{ext}}, \Psi)_{L^2(\lambda_i)} \\ &= -(\kappa_i - \kappa_0)r_i^2 \sum_{\ell=0}^{\infty} \sum_{m=-\ell}^{m=+\ell} \left(\nabla_{\mathbf{x}_i} \frac{\ell}{r_i} [\lambda_{\text{ext},i}]_{\ell}^m \right) [\Psi_i]_{\ell}^m \\ &= -(\kappa_i - \kappa_0)r_i^2 \sum_{\ell=0}^{\infty} \sum_{m=-\ell}^{m=+\ell} (\nabla_{\mathbf{x}_i} [\lambda_{\text{ext},i}]_{\ell}^m) \left(\frac{\ell}{r_i} [\Psi_i]_{\ell}^m \right) \\ &= -(\kappa_i - \kappa_0) (\nabla_{\mathbf{x}_i}\lambda_{\text{ext}}, \text{DtN}\Psi)_{L^2(\lambda_i)}. \end{aligned}$$

□

We are now ready to state the proof of Equation (2.35). Before proceeding to the proof, let us simply remark that the Equation (2.35) remains true if exact quantities are considered, i.e., if the force defined by (2.34) is built upon the exact induced charge σ being solution to the BIE (2.14) and where the energy corresponds to U_{int} as defined by (2.30).

Proof of Equation (2.35). Let $i \in \{1, \dots, N\}$ be fixed. By the definition of the

approximate electrostatic interaction energy, we have

$$\begin{aligned}
-\nabla_{\mathbf{x}_i} U_{\text{int}}^N &= \underbrace{-\frac{1}{2} \nabla_{\mathbf{x}_i} (\sigma_s + \sigma_p + \sigma_{\text{ext}}, \lambda_N)_{L^2(\lambda)}}_{:=\text{(I)}} \underbrace{-\nabla_{\mathbf{x}_i} (\sigma_s + \sigma_p, \lambda_{\text{ext}}^N)_{L^2(\lambda)}}_{:=\text{(II)}} \\
&\quad \underbrace{-\frac{1}{2} \nabla_{\mathbf{x}_i} (\sigma_{\text{ext}}, \lambda_{\text{ext}}^N)_{L^2(\lambda)}}_{:=\text{(III)}} + \underbrace{\frac{1}{2} \nabla_{\mathbf{x}_i} \sum_{j=1}^N (\sigma_{s,j} + \sigma_{p,j}, \lambda_N^{jj})_{L^2(\lambda_j)}}_{:=\text{(IV)}}.
\end{aligned}$$

We now simplify each of the terms (I), (II), (III), and (IV). First, we observe that self energy term (IV) is defined entirely through functions that are independent of changes in the location of the center \mathbf{x}_i of the sphere λ_i . Consequently, we obtain that (IV) $\equiv 0$.

Next, we use Lemmas A.1 and A.2 to write the term (I) as

$$\begin{aligned}
\text{(I)} &= -\frac{1}{2} \nabla_{\mathbf{x}_i} (\sigma_s + \sigma_p + \sigma_{\text{ext}}, \lambda_N)_{L^2(\lambda)} \\
&= \kappa_0 (\sigma_N, \mathbf{E}_{\text{exc}}^i)_{L^2(\lambda_i)} - (\nabla_{\mathbf{x}_i} \sigma_{\text{ext}}, \lambda_N)_{L^2(\lambda_i)} \quad (\text{Using Lemma A.1}) \\
&= \underbrace{\kappa_0 (\sigma_N, \mathbf{E}_{\text{exc}}^i)_{L^2(\lambda_i)}}_{:=\text{(IA)}} + \underbrace{(\kappa_i - \kappa_0) (\nabla_{\mathbf{x}_i} \lambda_{\text{ext}}, \text{DtN} \lambda_N)_{L^2(\lambda_i)}}_{:=\text{(IB)}}. \quad (\text{Using Lemma A.2})
\end{aligned} \tag{A.9}$$

Next, we simplify the term (IB). Indeed, a direct calculation shows that

$$\begin{aligned}
\text{(IB)} &= (\kappa_i - \kappa_0) (\nabla_{\mathbf{x}_i} \lambda_{\text{ext}}, \text{DtN} \lambda_N)_{L^2(\lambda_i)} = (\kappa_i - \kappa_0) \int_{\lambda_i} (\nabla_{\mathbf{x}_i} \Phi_{\text{ext}}) \text{DtN} \lambda_N \, d\mathbf{x} \\
&= (\kappa_i - \kappa_0) \int_{\lambda_i} (\nabla \Phi_{\text{ext}}) \text{DtN} \lambda_N \, d\mathbf{x} = -(\kappa_i - \kappa_0) \int_{\lambda_i} \mathbf{E}_{\text{ext}} \text{DtN} \lambda_N \, d\mathbf{x} \\
&= -(\kappa_i - \kappa_0) (\text{DtN} \lambda_N, \mathbf{E}_{\text{ext}})_{L^2(\lambda_i)}.
\end{aligned} \tag{A.10}$$

In order to simplify the term (II), we again recall that the free charges σ_s, σ_p are independent of changes in the location of the center \mathbf{x}_i of the sphere λ_i .

Consequently, we obtain

$$\begin{aligned} \text{(II)} &= -\nabla_{\mathbf{x}_i}(\sigma_s + \sigma_p, \lambda_{\text{ext}}^N)_{L^2(\lambda)} = -(\sigma_s + \sigma_p, \nabla_{\mathbf{x}_i} \lambda_{\text{ext}}^N)_{L^2(\lambda)} \\ &= -(\sigma_s + \sigma_p, \nabla_{\mathbf{x}_i} \lambda_{\text{ext}}^N)_{L^2(\lambda)_i}. \end{aligned} \quad (\text{A.11})$$

Therefore, using a calculation similar to the one used to obtain Equation (A.10), we deduce that

$$\text{(II)} = -(\sigma_s + \sigma_p, \nabla_{\mathbf{x}_i} \lambda_{\text{ext}}^N)_{L^2(\lambda)_i} = (\sigma_s^N + \sigma_p^N, \mathbf{E}_{\text{ext}})_{L^2(\lambda)_i}, \quad (\text{A.12})$$

where σ_s^N and σ_p^N are the best approximations in $W^N(\lambda)$ of σ_s and σ_p respectively.

Next, we attempt to simplify the term (III). A simple application of the product rule together with Lemma A.2 yields that

$$\begin{aligned} \text{(III)} &= -\frac{1}{2} \nabla_{\mathbf{x}_i}(\sigma_{\text{ext}}, \lambda_{\text{ext}}^N)_{L^2(\lambda)} = -\frac{1}{2} \nabla_{\mathbf{x}_i}(\sigma_{\text{ext}}, \lambda_{\text{ext}}^N)_{L^2(\lambda)_i} \\ &= -\frac{1}{2}(\nabla_{\mathbf{x}_i} \sigma_{\text{ext}}, \lambda_{\text{ext}}^N)_{L^2(\lambda)_i} - \frac{1}{2}(\sigma_{\text{ext}}, \nabla_{\mathbf{x}_i} \lambda_{\text{ext}}^N)_{L^2(\lambda)_i} \\ &= (\kappa_i - \kappa_0)(\text{DtN} \lambda_{\text{ext}}, \nabla_{\mathbf{x}_i} \lambda_{\text{ext}}^N)_{L^2(\lambda)_i} - \frac{1}{2}(\sigma_{\text{ext}}, \nabla_{\mathbf{x}_i} \lambda_{\text{ext}}^N)_{L^2(\lambda)_i} \\ &= -(\sigma_{\text{ext}}, \nabla_{\mathbf{x}_i} \lambda_{\text{ext}}^N)_{L^2(\lambda)_i}. \end{aligned}$$

Once again, a direct calculation of the form used to obtain Equation (A.10) allows us to conclude that

$$\text{(III)} = -(\sigma_{\text{ext}}, \nabla_{\mathbf{x}_i} \lambda_{\text{ext}}^N)_{L^2(\lambda)_i} = (\sigma_{\text{ext}}^N, \mathbf{E}_{\text{ext}})_{L^2(\lambda)_i}. \quad (\text{A.13})$$

Combining now Equations (A.9), (A.10), (A.12), and (A.13) we obtain that

$$\begin{aligned}
-\nabla_{\mathbf{x}_i} U_{\text{int}}^N &= (\text{IA}) + (\text{IB}) + (\text{II}) + (\text{III}) \\
&= \kappa_0 (\sigma_N, \mathbf{E}_{\text{exc}}^i)_{L^2(\lambda_i)} - (\kappa_i - \kappa_0) (\text{DtN}\lambda_N, \mathbf{E}_{\text{ext}})_{L^2(\lambda_i)} \\
&\quad + (\sigma_s^N + \sigma_p^N, \mathbf{E}_{\text{ext}})_{L^2(\lambda_i)} + (\sigma_{\text{ext}}^N, \mathbf{E}_{\text{ext}})_{L^2(\lambda_i)} \\
&= \kappa_0 (\sigma_N, \mathbf{E}_{\text{exc}}^i)_{L^2(\lambda_i)} + (- (\kappa_i - \kappa_0) \text{DtN}\lambda_N + \sigma_s^N + \sigma_p^N + \sigma_{\text{ext}}^N, \mathbf{E}_{\text{ext}})_{L^2(\lambda_i)} \\
&= \kappa_0 (\sigma_N, \mathbf{E}_{\text{exc}}^i)_{L^2(\lambda_i)} + \kappa_0 (\sigma_N, \mathbf{E}_{\text{ext}})_{L^2(\lambda_i)}.
\end{aligned}$$

where the last equality follows from Equation (2.33). This completes the proof \square